

# **Identification and Characterization of the Cell-Cell Communication System of a Multicellular Cyanobacterium**

**Dissertation**

der Mathematisch-Naturwissenschaftlichen Fakultät  
der Eberhard Karls Universität Tübingen  
zur Erlangung des Grades eines  
Doktors der Naturwissenschaften  
(Dr. rer. nat.)

vorgelegt von  
**Ann-Katrin Kieninger**  
aus Bietigheim-Bissingen

Tübingen  
2021



Gedruckt mit Genehmigung der Mathematisch-Naturwissenschaftlichen Fakultät der  
Eberhard Karls Universität Tübingen.

Tag der mündlichen Qualifikation:

09.12.2021

Dekan:

Prof. Dr. Thilo Stehle

1. Berichterstatter:

PD Dr. Iris Maldener

2. Berichterstatter:

Prof. Dr. Samuel Wagner

3. Berichterstatter:

Prof. Dr. Wolfgang R. Hess



## Erklärung

Ich erkläre hiermit, dass ich die zur Promotion eingereichte Arbeit mit dem Titel „Identification and characterization of the cell-cell communication system of a multicellular cyanobacterium“ selbständig verfasst, nur die angegebenen Quellen und Hilfsmittel benutzt und wörtlich oder inhaltlich übernommene Stellen/Zitate als solche gekennzeichnet habe. Eine detaillierte Abgrenzung meiner eigenen Leistungen von den Beiträgen meiner Kooperationspartner habe ich in 6.1.1 vorgenommen. Ich erkläre, dass die Richtlinien zur Sicherung guter wissenschaftlicher Praxis der Universität Tübingen (Beschluss des Senats vom 25.5.2000) beachtet wurden. Ich versichere an Eides statt, dass diese Angaben wahr sind und dass ich nichts verschwiegen habe. Mir ist bekannt, dass die falsche Abgabe einer Versicherung an Eides statt mit Freiheitsstrafe bis zu drei Jahren oder mit Geldstrafe bestraft wird.

Tübingen, den 03. Juli 2021



Ann-Katrin Kieninger

# Table of Content

<b>List of abbreviations</b> .....	<b>vi</b>
<b>1 Abstract</b> .....	<b>1</b>
<b>2 Zusammenfassung</b> .....	<b>2</b>
<b>3 Introduction</b> .....	<b>4</b>
3.1 Cyanobacteria: Ecological importance and diversity.....	4
3.2 The filamentous cyanobacterium <i>Anabaena</i> sp. PCC 7120 .....	5
3.3 Cell wall of filamentous cyanobacteria .....	6
3.4 Heterocyst differentiation.....	7
3.5 Cell-cell communication.....	10
3.5.1 Nanopore array drilled by amidases.....	11
3.5.2 Septal junctions and Fra proteins .....	14
<b>4 Research objectives</b> .....	<b>18</b>
<b>5 Materials and methods</b> .....	<b>19</b>
5.1 Cultivation of bacterial strains .....	19
5.2 Molecular cloning .....	20
5.2.1 Strains and plasmids .....	20
5.2.2 Construction of mutants.....	23
5.2.3 Triparental conjugation.....	25
5.3 Light and fluorescence microscopy .....	26
5.4 Immunolocalization .....	26
5.5 Nitrogen stepdown and staining of heterocysts .....	27
5.6 Measurement of cell-cell communication.....	28
5.6.1 Fluorescence recovery after photobleaching (FRAP) .....	28
5.6.2 FRAP assay after treatment with CCCP or other stress factors .....	28
5.6.3 Fluorescence recovery after multiple photobleaches (FRAMP <sub>x</sub> ).....	29
5.7 Analysis of the membrane potential, intracellular pH and intracellular Ca <sup>2+</sup> .....	29
5.8 Analysis of the septal nanopore array .....	30
5.8.1 Isolation of septal peptidoglycan discs .....	30
5.8.2 Transmission electron microscopy (TEM) .....	30
5.8.3 Septal PG analysis using FIJI scripts .....	31
5.9 Statistical analysis .....	31
5.10 Co-Immunoprecipitation (co-IP).....	31
5.11 SDS-PAGE and Western Blot .....	33
5.12 Protein expression and purification.....	34
5.13 Protein-protein interaction assays .....	35
5.13.1 Bacterial adenylate cyclase two-hybrid (BACTH) assay.....	35
5.13.2 Batch pulldown with purified proteins.....	36
5.13.3 Biolayer-interferometry.....	36

<b>6</b>	<b>Results</b> .....	<b>38</b>
6.1	Regulation of cell-cell communication .....	38
6.1.1	Publication 1: "Structure and Function of a Bacterial Gap Junction Analog" .....	38
6.1.2	Septal junctions are three-modular gated cell-cell communication channels .....	39
6.2	Mode of action of SJ gating .....	41
6.2.1	CCCP disrupts the membrane potential and the proton gradient in <i>Anabaena</i> .....	41
6.2.2	Several stress conditions trigger SJ gating .....	44
6.2.3	SJ gating is not synchronized within cells in a filament .....	47
6.3	Impact of FraD domains on cell-cell communication .....	50
6.3.1	Creation of partly complemented <i>fraD</i> mutants .....	50
6.3.2	Characterization of <i>fraD</i> mutants in view of communication and nanopore array .....	50
6.3.3	Characterization of <i>fraD</i> mutants in view of diazotrophic growth .....	53
6.3.4	Immunolocalization of FraD <sub>pp</sub> .....	56
6.3.5	Cryotomograms of the <i>fraD</i> <sub>TM</sub> strain revealed WT-like SJs .....	56
6.4	Identification and characterization of putative FraD interactors .....	57
6.4.1	Genomic localization and secondary structure prediction .....	58
6.4.2	SepN, Alr4788 and FraL localize to the septa .....	60
6.4.3	Intercellular communication and SJ gating are impaired in <i>sepN</i> and <i>fraL</i> mutants .....	63
6.4.4	The nanopore array is barely present in the <i>fraL</i> mutant .....	65
6.4.5	ECT reveals absence of plug and closed caps in SJs of a <i>sepN</i> mutant .....	67
6.4.6	Diazotrophic growth of mutants in putative FraD interactors .....	68
6.4.7	Mutual influences on localization of FraD and putative FraD interactors .....	73
6.4.8	Localization of AmiC-type amidases is reduced in the <i>fraL</i> mutant .....	74
6.4.9	FraD is the most abundant protein in a reverse co-IP with SepN-sfGFP as bait .....	75
6.4.10	Further investigated mutants .....	76
6.5	Protein-protein interaction studies with FraD and potential interactors .....	77
6.5.1	In vivo protein-protein interaction assay: BACTH .....	77
6.5.2	Purification of FraD <sub>pp</sub> and SepN <sub>pp</sub> .....	79
6.5.3	In vitro protein-protein interaction assays with FraD and SepN .....	80
<b>7</b>	<b>Discussion</b> .....	<b>83</b>
7.1	SJs are structurally distinct to cell junctions of metazoans and plants .....	83
7.2	SJs are gated cell-cell connections .....	85
7.3	SJ cap and plug modules are essential for gating .....	86
7.4	SJ gating is not synchronized within a filament .....	87
7.5	FraD is a structural SJ component .....	88
7.6	SepN is involved in formation of the SJ complex .....	89
7.7	FraL might be involved in formation of the nanopore array .....	91
7.8	Proteins with unclear impact on cell-cell communication .....	93
<b>8</b>	<b>Conclusions and outlook</b> .....	<b>95</b>
	<b>References</b> .....	<b>98</b>
	<b>Danksagung</b> .....	<b>107</b>
	<b>Appendix</b> .....	<b>108</b>

## List of abbreviations

5-CF	5-carboxy-fluorescein	LB	lysogeny broth
AC	affinity chromatography	LC-MS	liquid chromatography-mass spectrometry
AcOH	acetic acid		
AHT	anhydrotetracycline hydrochloride	MBP	maltose binding protein
AM	acetoxymethylester	MCS	multiple cloning site
Amp	ampicillin	NADP	nicotinamide adenine dinucleotide phosphate
ATP	adenosine triphosphate	ns	not significant
BACTH	bacterial adenylate cyclase two-hybrid	o/n	over night
BCECF	2',7'-bis(carboxethyl)-5(6)-carboxyfluorescein	PBS	phosphate-buffered saline
BLI	biolayer interferometry	PCC	Pasteur Culture Collection of Cyanobacteria
BSA	bovine serum albumin	PCR	polymerase chain reaction
cAMP	cyclic adenosine 3',5'-cyclic monophosphate	PG	peptidoglycan
CCCP	carbonyl cyanide 3-chlorophenylhydrazone	pH <sub>i</sub>	intracellular pH
Cm	chloramphenicol	pp	periplasmic part
co-IP	co-immunoprecipitation	PSI	photosystem I
DCCD	N,N-dicyclohexylcarbodiimide	PSII	photosystem II
DiBAC <sub>4</sub> (3)	bis-(1,3-dibutylbarbituric acid)trimethine oxonol	ROI	region of interest
DMSO	dimethyl sulfoxide	RT	room temperature
DNA	deoxyribonucleic acid	SDS-PAGE	sodium dodecyl sulfate-polyacrylamide gel electrophoresis
DR	double recombination	SEC	size exclusion chromatography
ds	downstream	sfGFP	superfolder green fluorescent protein
ECT	electron cryotomography	SJs	septal junctions
EtOH	ethanol	Sm	streptomycin
FITC	fluorescein isothiocyanate	Sp	spectinomycin
FRAMP	fluorescence recovery after multiple photobleaches	SR	single recombination
FRAP	fluorescence recovery after photobleaching	sRNAs	small RNA
GFP	green fluorescent protein	TB	Terrific Broth
GOGAT	glutamine-2-oxoglutarate aminotransferase	TCC	triphenyl tetrazolium chloride
GS	glutamine synthetase	TEM	transmission electron microscopy
HEP	heterocyst envelope polysaccharides	TM	transmembrane part
HGL	heterocyst glycolipids	TMD	transmembrane domain
IC	intercellular communication	us	upstream
IPTG	isopropyl β-D-1-thiogalactopyranoside	WT	wild type
Km	kanamycin	X-Gal	5-bromo-4-chloro-3-indolyl-β-D-galactopyranoside
		YFP	yellow fluorescent protein

# 1 Abstract

Around 2.5 billion years ago, cyanobacteria built the basis for life on Earth by raising the atmospheric oxygen level. Multicellularity among Cyanobacteria evolved very early and increased their fitness due to improved motility, economies of scale and faster adaptation to changing environmental conditions. The importance of multicellularity for evolution of life and complex life styles gives reason for performing research on these organisms. Of particular interest is the cell-cell communication system, which allows molecular exchange between cells of the organism via direct cell contact. Without such a system, a multicellular lifestyle with division of labor between specialized cells would be impossible.

The cell-cell communication system of the model organism *Anabaena* sp. PCC 7120 comprises a functional unit of a nanopore array in the septal peptidoglycan and of proteinaceous septal junctions (SJs). The SJs traverse the nanopores to connect the cytoplasm of adjacent cells. Little was known about the mode of action of this communication system and the structural protein components were obscure.

This work revealed the in situ architecture of SJs as three-modular complexes involving a cytoplasmic cap and a membrane-embedded plug module at both sites of a length-variable tube module. Furthermore, it could be demonstrated that SJs are gated channels whose caps undergo a structural rearrangement to switch from an open into a closed state, which does not allow cell-to-cell diffusion. Regulation of intercellular diffusion was observed as a response on various intracellular stress conditions.

Identification of the septum-localized membrane protein FraD as the first structural SJ component allowed the development of a co-immunoprecipitation using FraD as bait with the aim to discover further proteins of these complexes. By this, a so far hypothetical protein was identified as potential interaction partner of FraD and termed SepN. SJs of a mutant in this septal membrane protein lacked the plug module and exhibited a cap reminiscent to the closed state. Therefore, the function of the SJ plug was assumed to be important for holding the cap structure in its opened position as well as for SJ closure.

A mutant in another identified protein, FraI, showed a severely reduced communication, which was linked to a drastic reduction in the number of nanopores. A relation to amidases that drill the nanopore array was therefore suggested.

In this work, the complex network of proteins involved in cell-cell communication and the understanding of regulation of intercellular exchange were greatly extended. This includes the identification of two proteins that are essential to form the SJ complex, as well as the establishment of a microscopic assay to screen future mutants for their ability to regulate their communication, and the development of a workflow to identify further (membranous) SJ proteins.

## 2 Zusammenfassung

Vor ungefähr 2,5 Milliarden Jahren formten Cyanobakterien die Grundlage für das Leben auf der Erde, indem sie den atmosphärischen Sauerstoffgehalt erhöhten. Mehrzelligkeit unter Cyanobakterien entwickelte sich sehr früh und steigerte deren Fitness aufgrund einer verbesserten Beweglichkeit, aufgrund von Größenvorteilen und schnellerer Anpassung an sich ändernde Umweltbedingungen. Die Bedeutung der Mehrzelligkeit für die Evolution des Lebens und komplexer Lebensformen begründet die Erforschung dieser Organismen. Von besonderem Interesse ist das Zell-Zell-Kommunikationssystem, das den molekularen Austausch zwischen Zellen des Organismus durch direkten Zellkontakt erlaubt. Ohne ein solches System wäre eine mehrzellige Lebensform mit Arbeitsteilung zwischen spezialisierten Zellen nicht möglich.

Das Zell-Zell-Kommunikationssystem des Modellorganismus *Anabaena* sp. PCC 7120 umfasst eine funktionelle Einheit aus einem Nanoporen-Array im septalen Peptidoglykan und aus proteinösen Zellverbindungen (*septal junctions*, SJs). Diese durchqueren die Nanoporen und verbinden so das Zytoplasma benachbarter Zellen. Über die Wirkungsweise des Kommunikationssystems war wenig bekannt und beteiligte strukturelle Proteinkomponenten waren unklar.

Diese Arbeit zeigte die in situ Architektur der SJs als drei-modulare Komplexe auf, welche eine zytoplasmatische Kappe und ein in die Membran eingebettetes Stopfenmodul auf beiden Seiten des längen-variablen Röhrenmoduls umfassen. Des Weiteren wurde gezeigt, dass SJs gesteuerte Kanäle sind, deren Kappen eine strukturelle Umordnung durchlaufen. Damit wechseln sie von einer offenen in eine geschlossene Konformation, die keine Zell-zu-Zell-Diffusion erlaubt. Die Regulation der interzellulären Diffusion wurde als Reaktion auf verschiedene intrazelluläre Stressbedingungen beobachtet.

Die Identifikation des septum-lokalisierten Membranproteins FraD als die erste strukturelle SJ-Komponente erlaubte die Entwicklung einer Ko-Immünpräzipitation mit FraD als Antigen mit dem Ziel, weitere Proteine dieser Komplexe zu entdecken. So wurde ein bisher hypothetisches Protein als potentieller Interaktionspartner von FraD identifiziert und SepN benannt. SJs einer Mutante in diesem septalen Membranprotein fehlten die Stopfenmodule und wiesen eine Kappe ähnlich der des geschlossenen Zustands auf. Somit wurde die Funktion des SJ-Stopfens als wichtig für den Erhalt der offenen Kappenstruktur sowie für die SJ-Schließung vermutet.

Eine Mutante in einem weiteren identifizierten Protein, FraI, wies eine stark reduzierte Kommunikation auf, was in einer drastischen Reduktion der Nanoporenanzahl begründet war. Eine Verbindung zu Amidasen, die den Nanoporen-Array bohren, wurde daher vermutet.

In dieser Arbeit wurden das komplexe Netzwerk aus Proteinen, die an der Zell-Zell-Kommunikation beteiligt sind sowie das Verständnis der Regulation des interzellulären

Austauschs stark erweitert. Dies umfasst die Identifikation zweier Proteine, die für die Bildung des SJ-Komplexes essentiell sind, die Etablierung eines mikroskopischen Assays, um zukünftige Mutanten auf ihre Fähigkeit zur Regulierung ihrer Kommunikation zu untersuchen und die Entwicklung einer Vorgehensweise zur Identifikation weiterer (membranöser) SJ-Proteine.

### 3 Introduction

#### 3.1 Cyanobacteria: Ecological importance and diversity

“One of the most noticeable signs of life on Earth is produced by creatures so small that they are invisible to the human eye[. When we look] on Earth from afar our eyes are drawn to light blue patches beneath the white clouds. [...] The patterns and colors [...] are caused by photosynthetic plankton that wander across the seas” (Chimileski et al., 2018) (Figure 1). The prokaryotic part of the photosynthetic plankton, also referred to as phytoplankton, are cyanobacteria. About 2.5 billion years ago, the photosynthetic activity of cyanobacteria elevated the atmospheric oxygen and thereby created the conditions for the evolution of life as we know it today (Fay, 1992; Bekker et al., 2004; Schirrmeister et al., 2013). This fact reveals the great importance of these photoautotroph bacteria for the ecosystem, since as primary producers they convert light energy into biomass.

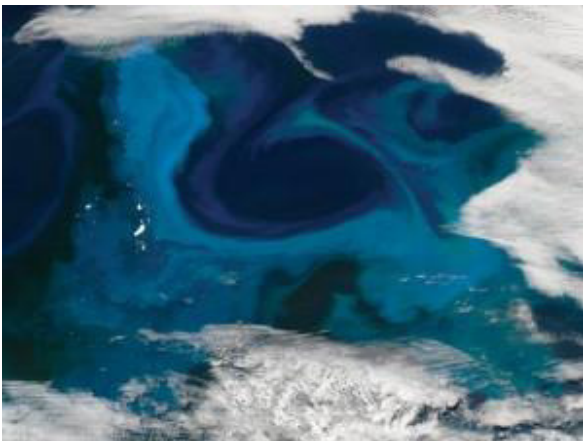


**Figure 1: Phytoplankton in the Southern Ocean.** Photograph of the Southern Ocean from space showing phytoplankton in light blue. Image from (Falkowski, 2012), credit: Lawrence Berkeley National Laboratory/Science Photo Library.

Cyanobacteria, the “inventors” of photosynthesis, were incorporated into plants as chloroplasts. This inheritance is known as endosymbiosis and renders plants capable of oxygenic photosynthesis (Sagan, 1967). In principal, photosynthesis generates chemical energy out of light energy in the photosystems I and II (PSI, PSII), which is in a second, light-independent step used to produce carbohydrates via the Calvin cycle (Vermaas, 2001). In cyanobacteria, sunlight as energy source is collected by light harvesting pigments, the phycobilisomes, predominantly localized on PSII in the thylakoid membranes (Liu, 2016). Here, water is split into protons and oxygen as a byproduct. Released electrons are transferred to PSI and a proton gradient is formed, which in turn fuels the ATP synthase (Vermaas, 2001; Liu, 2016). NADP is reduced to NADPH by receiving electrons from PSI. ATP and NADPH are then introduced into the Calvin cycle, in which CO<sub>2</sub> is converted into carbohydrates (Vermaas, 2001). Some cyanobacteria not only fix carbon but also atmospheric nitrogen and

therefore are diazotrophs. In conclusion, cyanobacteria highly contribute to carbon, oxygen and nitrogen cycles.

Beside the common photoautotrophic lifestyle, cyanobacteria built one of the morphologically most diverse prokaryotic phyla comprising unicellular, multicellular and cell differentiating species that live almost everywhere on Earth (Stanier & Cohen-Bazire, 1977; Rippka et al., 1979; Schirmer et al., 2013). Cyanobacterial orders have been classified into five subsections based on their morphology (Rippka et al., 1979): Whereas subsections I and II comprise the unicellular orders Chroococcales and Pleurocapsales, subsections III–V include the filamentous orders Oscillatoriales, Nostocales and Stigonematales, respectively. Members of subsection I divide by binary fission or budding. Additionally, members of subsection II perform multiple fission leading to small cells named baeocytes. Oscillatoriales (subsection III) feature only vegetative cells, while species of subsections IV and V can perform cell differentiation to nitrogen fixing heterocysts, spore-like akinetes or short motile hormogonia filaments. Reproduction of filamentous cyanobacteria happens via random filament (also trichome) breakage and intercalary cell division. Finally, Stigonematales (subsection V) are not limited to growth in linear filaments, but divide in more than one plane resulting in branched trichome patterns (Rippka et al., 1979).

In recent years, cyanobacteria gained more and more attention in biotechnological applications: production and synthesis of biofuels, biopolymers and pigments, synthesis of secondary metabolites as antimicrobials and herbicides or as food supply, to name just a few research fields (Angermayr et al., 2009; Martin & Lukas, 2015; Al-Haj et al., 2016; Mazard et al., 2016; Brilisauer et al., 2019). The special interest in cyanobacteria as host for industrial production is accounted for their autotrophic lifestyle. However, there are also some obstacles that need to be circumvented, for example the slow reproduction rate. Apart from their great biotechnological potential, negative attention is drawn to cyanobacteria because of cyanobacterial blooms in freshwater or marine environments. By release of toxins and depletion of oxygen, they impair the safety of drinking water and the stability of the ecological system (Huisman et al., 2018).

### 3.2 The filamentous cyanobacterium *Anabaena* sp. PCC 7120

A member of the order Nostocales of subsection IV (see 3.1 Cyanobacteria: Ecological importance and diversity) is the filamentous freshwater cyanobacterium *Anabaena* sp. PCC 7120 (also known as *Nostoc* sp. PCC 7120, hereafter *Anabaena*, see Figure 2A). *Anabaena* is a widely used model organism for cell differentiation, pattern formation, nitrogen fixation, multicellularity and cell-cell communication. In this work, *Anabaena* was the model organism to study regulation and proteins of cell-cell communication system.

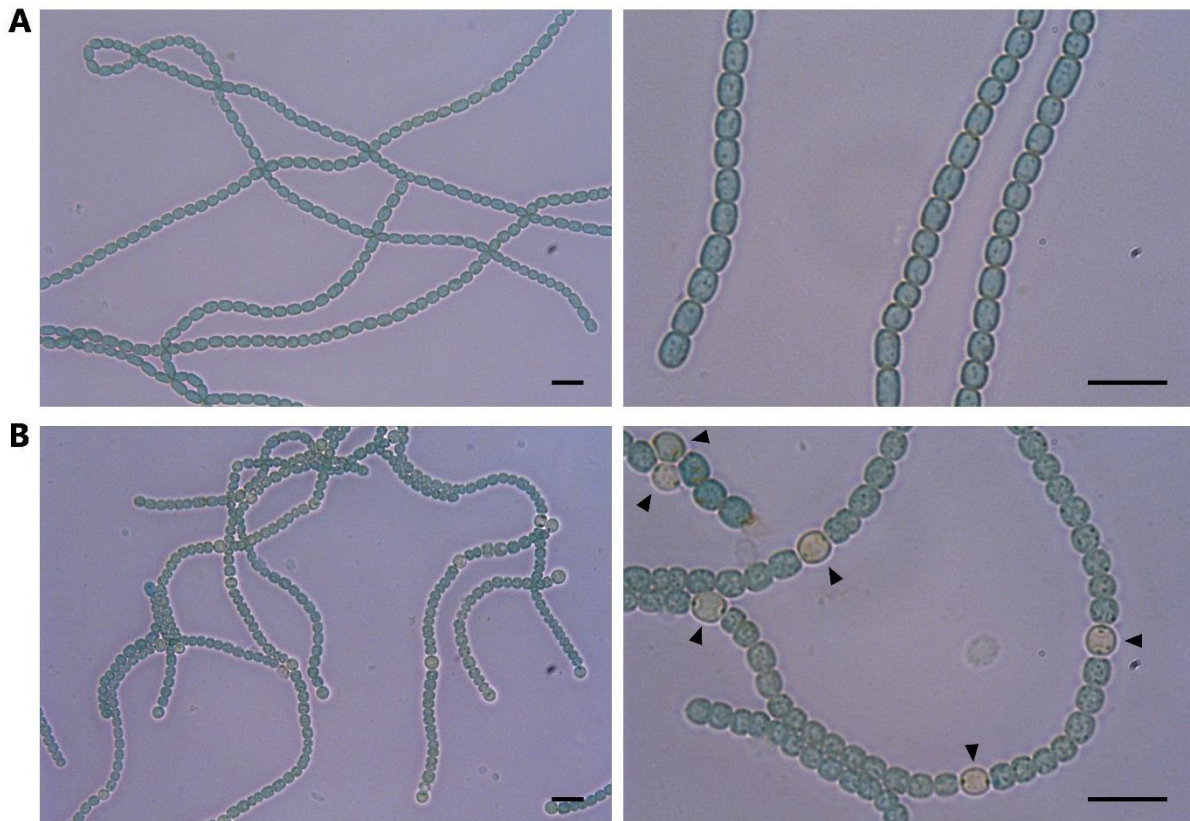


**Figure 2: Light micrographs of *Anabaena* sp. PCC 7120.** (A) *Anabaena* filaments consist of hundreds of vegetative cells. Two magnifications are shown. (B) Vegetative cells differentiate into heterocysts in the absence of combined nitrogen in a semi-regular pattern. Arrow heads point to heterocysts on the right image. Scale bar, 10  $\mu$ m.

The ability to differentiate heterocysts (see 3.4), specialized cells for nitrogen fixation, renders *Anabaena* a true multicellular bacterium (Figure 2B). Tools for genetic manipulation and full sequencing of its 6.4 Mbp genome makes *Anabaena* a suitable model strain (Kaneko et al., 2001). In addition to the chromosome, *Anabaena* harbors six plasmids ( $\alpha$ - $\zeta$ ) with sizes between 5.6-408 kbp (Kaneko et al., 2001). The reproducibility rate ranges from 19 h to 22 h depending on the nitrogen source and growth conditions like light, CO<sub>2</sub>, and temperature (Meeks et al., 1983).

### 3.3 Cell wall of filamentous cyanobacteria

Like all cyanobacteria, filamentous species are Gram-negative bacteria harboring a cytoplasmic membrane, a peptidoglycan (PG) or murein layer and an additional outer membrane. The outer membrane of filamentous cyanobacteria continuously encompasses the whole filament without entering the septal plane (Flores et al., 2006). In contrast, the peptidoglycan layer surrounds each cell within a filament, which leads to a giant peptidoglycan sacculus shared by neighboring cells (Lehner et al., 2013). The innermost layer is the cytoplasmic membrane, which encloses each individual cell.

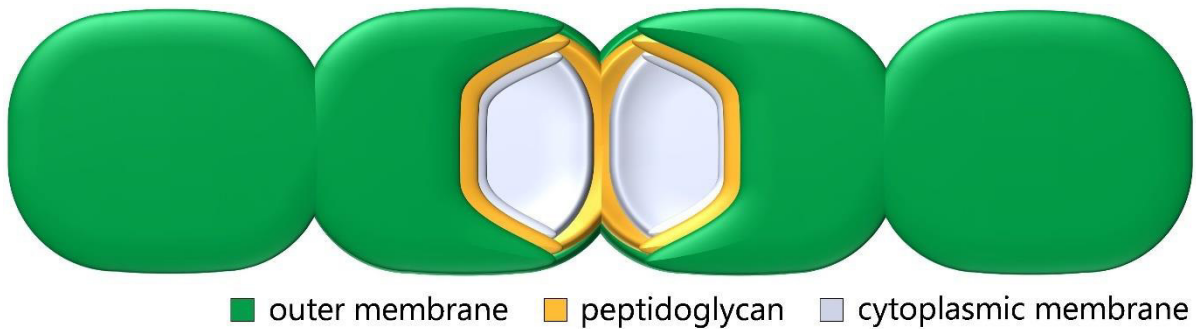


**Figure 3: Schematic view on a cyanobacterial filament.** A horizontal section through a filament is shown to illustrate the layers of the cell envelope. The continuous outer membrane (green) surrounds the whole filament without entering the septum between adjacent cells. Neighboring cells are connected via a giant peptidoglycan molecule (yellow) and separated through the cytoplasmic membrane (light grey). Modified from (Kieninger & Maldener, 2021).

In contrast to other Gram-negative bacteria, cyanobacteria exhibit a thicker and to a higher degree crosslinked PG reminiscent of Gram-positive bacteria (Hoiczky & Baumeister, 1995; Hoiczky & Hansel, 2000; Bok, 2020).

### 3.4 Heterocyst differentiation

Cell differentiation is characteristic for multicellular organisms and is performed by filamentous cyanobacteria of subsections IV and V (see 3.1). In these cyanobacteria, cell differentiation is initiated by environmental conditions for which metabolic and physical features are needed that cannot be provided by vegetative cells. Such features are fixation of nitrogen by heterocysts, adaption to nutrient limitation, resistance to desiccation or low temperatures by spore-like akinetes, and spreading via short motile hormogonia filaments. *Anabaena* has the ability to form heterocysts only. Therefore, and because its interconnection to intercellular communication, this cell type will be explained in more detail.

Bioavailable nitrogen is essential for proper growth of bacteria. Whereas most bacteria rely on combined nitrogen (in the form of ammonium or nitrate), filamentous cyanobacteria are able to grow diazotrophically by fixing atmospheric dinitrogen. Because of incompatibility of oxygen-sensitive  $N_2$  fixation and oxygen-evolving photosynthesis, these processes are spatially separated but occur simultaneously in heterocyst-forming cyanobacteria. In the absence of a combined nitrogen source, some vegetative cells of the filaments terminally differentiate into heterocysts in a semi-regular pattern (Fay et al., 1968; Buikema & Haselkorn, 1991a) (Figure 2B).

The purpose of heterocysts is fixation of atmospheric  $N_2$  into bioavailable nitrogen. This energy-consuming task is conducted by the nitrogenase enzyme, which is only expressed in heterocysts after creation of a micro-oxic environment. In some species, gene clusters need to be rearranged, like the *nif* (nitrogen fixation) gene cluster in *Anabaena* (Golden et al., 1985; Kumar et al., 2019). Nitrogenase-produced ammonium is directly incorporated into glutamate

by glutamine synthetase (GS), which produces glutamine (Wolk et al., 1976). However, heterocysts do not express the enzyme synthesizing glutamate from glutamine and 2-oxoglutarate, the glutamine-2-oxoglutarate aminotransferase (GOGAT) (Martin-Figueroa et al., 2000). Therefore, heterocysts need the product glutamate from vegetative cells (Thomas et al., 1977) (Figure 4).

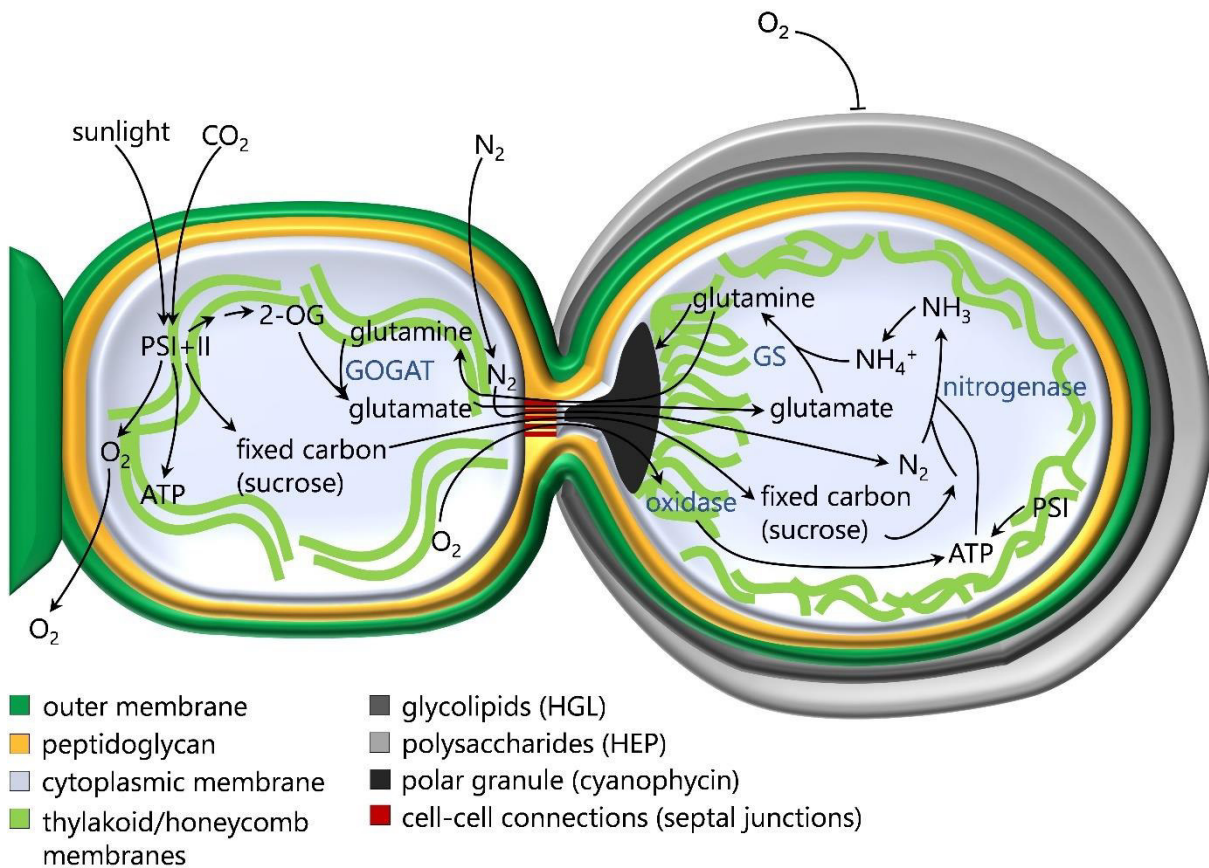


**Figure 4: Mutual dependence of vegetative cells and heterocysts.** A horizontal section through a vegetative cell (left) and an adjacent heterocyst (right) is illustrated. Major reactions and exchange of molecules are depicted. Compounds and molecules are in black letters, enzymes in blue. CO<sub>2</sub> is fixed via photosynthesis using sunlight as energy source in the vegetative cell. Products are O<sub>2</sub>, ATP and sucrose. The latter is transferred through cell-cell connections to the heterocyst and serves as reductants. In the vegetative cell, glutamate is synthesized from glutamine and 2-OG by GOGAT and transferred to the heterocyst for incorporation of fixed nitrogen in the form of ammonium by the GS. The resulting glutamine is either stored in cyanophycin (aspartate and arginine) or transferred to the vegetative cell. Nitrogen is fixed in the heterocyst by the oxygen-sensitive nitrogenase, fueled by ATP from PSI and respiration in the honeycomb membranes by respiratory oxidases. Note the lack of PSII. PS, photosystem; ATP, adenosine triphosphate; 2-OG, 2-oxoglutarate; GOGAT, glutamine-2-oxoglutarate aminotransferase; GS, glutamine synthetase. Modified from (Rascio & La Rocca, 2013).

The transformation from a vegetative cell into a mature heterocyst takes 24 h and involves extensive morphological, metabolic and genetical alterations in order to provide a micro-oxic environment (Flores & Herrero, 2010; Kumar et al., 2010; Muro-Pastor & Maldener, 2019). Before morphological changes are visible through a microscope, nitrogen limitation is sensed by increased levels of 2-oxoglutarate, which leads to activation of the global nitrogen regulator NtcA (reviewed in (Luque & Forchhammer, 2008; Huergo & Dixon, 2015)). In turn, NtcA induces the expression of the heterocyst-specific master regulator HetR (Frías et al., 1994;

Muro-Pastor et al., 2002; Golden & Yoon, 2003). While a highly complex activation and downregulation of various genes, *patS* and *hetN* expression is initiated in differentiating cells (reviewed in (Muro-Pastor & Maldener, 2019; Harish & Seth, 2020)). A pentapeptide cleaved from PatS and HetN negatively affects differentiation and laterally diffuses to neighboring cells creating a concentration gradient (Yoon & Golden, 1998; Callahan & Buikema, 2001; Corrales-Guerrero et al., 2013). Along the gradient, HetR decay is promoted by the PatS peptide in a concentration-dependent manner, and prevents heterocyst formation in close proximity to each other (Risser & Callahan, 2009). Heterocyst pattern formation along the filament is a tightly regulated process involving various proteins and also sRNAs (Álvarez-Escribano et al., 2018; Olmedo-Verd et al., 2019; He et al., 2020) with recent discoveries being HetL (Xu et al., 2020), the kinase PknH (Fukushima & Ehira, 2018), PatD (Wang et al., 2019) and the sRNA Yfr1 (Brenes-Álvarez et al., 2020), to name just a few. In depth, description of the differentiation process is reviewed in (Maldener et al., 2014; Herrero & Flores, 2019; Muro-Pastor & Maldener, 2019; Harish & Seth, 2020).

During the metabolic reprogramming from photoautotroph to photoheterotroph, heterocysts enhance their respiration to reduce entering oxygen and produce ATP (Jones & Haselkorn, 2002; Valladares et al., 2003). At the same time, they lose their oxygen-evolving PSII activity, whereas PSI is maintained for ATP production (Tel-Or et al., 1977; Giddings & Staehelin, 1979). As a consequence of degradation of phycobiliproteins, heterocysts do not autofluoresce and appear in a pale color under the light microscope (Wood & Haselkorn, 1980; Kumazaki et al., 2013). Furthermore, heterocysts exhibit two additional layers deposited on the outer membrane to hamper the entry of oxygen (Figure 4). The outermost layer consists of polysaccharides (heterocyst envelope polysaccharides, HEP) and is the first observable morphological change during heterocyst differentiation (Cardemil & Wolk, 1979; Maldener et al., 2014). The HEP layer functions in mechanical protection of the underneath following laminated glycolipid layer (heterocyst glycolipids, HGL), which is poorly permeable for gases and solutes (Walsby & Fogg, 1985; Murry & Wolk, 1989). In order to minimize oxygen entry from neighboring vegetative cells, the heterocyst septum is restricted by the HEP layer and therefore harbors fewer cell-cell connections (Giddings & Staehelin, 1978; Maldener et al., 2014). Additionally, intercellular exchange is decelerated and the gas entry is reduced by cyanophycin granules located in the heterocyst poles (Mullineaux et al., 2008; Nürnberg et al., 2015), which serve as storage for fixed nitrogen in the form of aspartate and arginine. So-called honeycomb membranes, consisting of reorganized thylakoid membranes, adjoin this polar granules and harbor specific oxidases for oxygen respiration (Lang & Fay, 1971; Valladares et al., 2003).

The division of labor between photosynthetically active vegetative cells and nitrogen-fixing heterocysts causes mutual dependence. This means, vegetative cells provide heterocysts with carbon reductants in the form of sucrose and glutamate (Wolk, 1968; Jüttner, 1983). In

turn, heterocysts supply neighboring vegetative cells with fixed nitrogen in the form of  $\beta$ -aspartyl-arginine and glutamine (Thomas et al., 1977; Burnat et al., 2014). This emphasizes the dependence of a multicellular lifestyle on a cell-cell communication system.

### 3.5 Cell-cell communication

Multicellularity allows division of labor by differentiating specialized cells (see 3.4) and depends on intercellular exchange of molecules and metabolites between mutually dependent cell types. Fixed carbon was one of the first compounds shown to directly move from vegetative cells into heterocysts via filament-autoradiography studies (Wolk, 1968). Stewart and coworkers suggested that fixed nitrogen is transferred from heterocysts to adjacent vegetative cells (Stewart et al., 1969). Two feasible routes have been supposed for this kind of molecular exchange: via the periplasmic continuum (Montesinos et al., 1995; Flores et al., 2006) or via cell-cell connections (Lang & Fay, 1971), the septal junctions (SJs, Figure 5A), formerly known as microplasmodesmata (see 3.5.2).

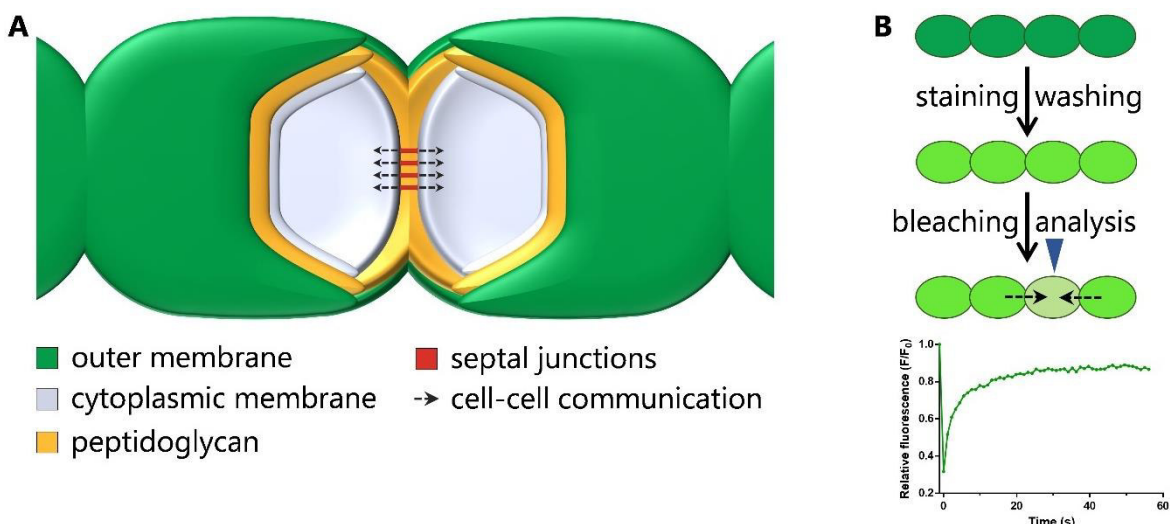


**Figure 5: Route of intercellular communication and its measurement.** (A) Septal junctions, the cell-cell connecting structures are illustrated in red. The dotted arrows show the route of molecular exchange. Modified from (Kieninger & Maldener, 2021). (B) Experimental overview of the fluorescence recovery after photobleaching (FRAP) method. Filaments are stained with a fluorescent tracer by incubation and washing periods. Then, the dye of a specific cell is bleached by a high intensity laser (blue arrow head) and recovery of the fluorescence in the bleached cell is monitored. A representative fluorescence recovery curve (relative fluorescence over time) is shown.

Diffusion through the periplasm involves export from the cytoplasm of one cell and import by another cell. ABC-type transporters were suggested to play a role in this process (Flores et al., 2006). Periplasmic movement of GFP (green fluorescent protein) along an *Anabaena* filament proved the continuous nature of the periplasm and thereby supported a periplasmic communication route (Mariscal et al., 2007). Contradictory, another study showed diffusion of GFP only within one cell, but not across cell borders (Zhang et al., 2008). Discrepancy between these observations remained elusive. Transfer of GFP from the cytoplasm of a heterocyst to a vegetative cell or vice versa did not occur (Yoon & Golden, 1998; Mariscal et al., 2007).

However, an approximately 40 times smaller fluorophore, calcein (623 Da vs. 27 kDa of GFP), moved between cytoplasm of adjacent cells and was traced via fluorescence recovery after photobleaching (FRAP) experiments (Mullineaux et al., 2008) (Figure 5B). For this, filaments were incubated with the hydrophobic acetoxymethylester derivative of calcein, which easily penetrates the cell membranes. Once inside the cells, the compound is hydrolyzed by esterases producing a hydrophilic, fluorescent calcein. Using a high intensity laser, a specific cell within the filament is photobleached and recovery of the fluorescence in the bleached cell is monitored. Irreversible bleaching as well as absence of spontaneous dye recovery and biological inertness towards proteins make calcein an appropriate tracer for FRAP experiments (Mullineaux et al., 2008). Further suitable fluorophores are the similar but smaller 5-carboxfluorescein (376 Da) and the sucrose analog esculin (340 Da) (Nürnberg et al., 2015). Since intracellular calcein cannot pass membranes anymore, the periplasmic route of communication was unlikely (Mullineaux et al., 2008). Exchange of fluorescent tracers was exclusively observed down the concentration gradient, which argues for a simple diffusion process (Mullineaux et al., 2008). Diffusion as mechanism for intercellular exchange without consumption of energy was supported by direct proportionality between temperature and rate of molecular exchange (Nieves-Mori3n et al., 2017b).

Molecular exchange between cells within a filament seems to be particularly important during diazotrophic growth. Strikingly, the rate of intercellular communication (IC) between heterocyst and vegetative cell is reduced in comparison to vegetative cells in heterocyst promoting conditions, which can partly be explained by the cyanophycin plug in the heterocyst pole and the reduced septa at the interface between heterocyst and vegetative cell (Mullineaux et al., 2008) (see Figure 4). IC in non-heterocyst-forming *Oscillatoria* could not be measured by FRAP studies (Mullineaux et al., 2008), although cell-cell communication structures were observed (Hagedorn, 1961).

### 3.5.1 Nanopore array drilled by amidases

First piece of evidence for a direct communication route from cell to cell was already obtained in 1955, when pores in the septal PG of various filamentous cyanobacteria were observed (Metzner, 1955; Palinska & Krumbein, 2000). Purification of septal PG discs from *Nostoc punctiforme* (hereafter *Nostoc*), another filamentous heterocyst-forming cyanobacterium, revealed semi-regularly spaced nanopores of 20 nm in diameter (Lehner et al., 2013) (Figure 6A). Connection of this so called nanopore array with intercellular molecular exchange was proven by an *amiC2* mutant in *Nostoc* that lacked the nanopore array and at the same time did not communicate, which led to an aberrant filament morphology and loss of cell differentiation (Lehner et al., 2011; Lehner et al., 2013; Maldener & Forchhammer, 2015) (Figure 6C). The disrupted gene *amiC2*, which encodes a *N*-acetyl-muramyl-L-alanine amidase, is homologous to amidases in *Escherichia coli* (*E. coli*). In *E. coli*, amidases are responsible for

daughter cell separation during cell division (Priyadarshini et al., 2007) by hydrolyzing the amide bonds between PG stem peptides and the glycan strands (Vollmer et al., 2008). Interestingly, members of the order Nostocales code for two AmiC homologs (Lehner et al., 2011). Whereas AmiC2<sub>Nostoc</sub> drills nanopores in the septal PG as a framework for the cell-cell communication machinery, the function of the essential AmiC1 enzyme is still unknown, since mutation of *amiC1* was not feasible (Lehner et al., 2011) (Table 1). The nanopore array was also found in *Anabaena* (Figure 6B), but harbors with average 80 pores per septum a smaller amount of nanopores in comparison to about 150 pores in *Nostoc* (Nürnberg et al., 2015). Nanopores in *Anabaena* are also drilled by amidases, but here, AmiC1 and AmiC2 were shown to have related functions and single amidase disruptions did not lead to a complete loss of the nanopore array (Berendt et al., 2012; Bornikoel et al., 2017). Mutants deficient in only one of the amidases harbored reduced numbers of nanopores with impaired cell-cell communication and showed no diazotrophic growth (Bornikoel et al., 2017) (Table 1). However, AmiC1 seems to be the more important amidase in *Anabaena*, since loss of AmiC2 can be compensated by AmiC1 (Bornikoel et al., 2017).

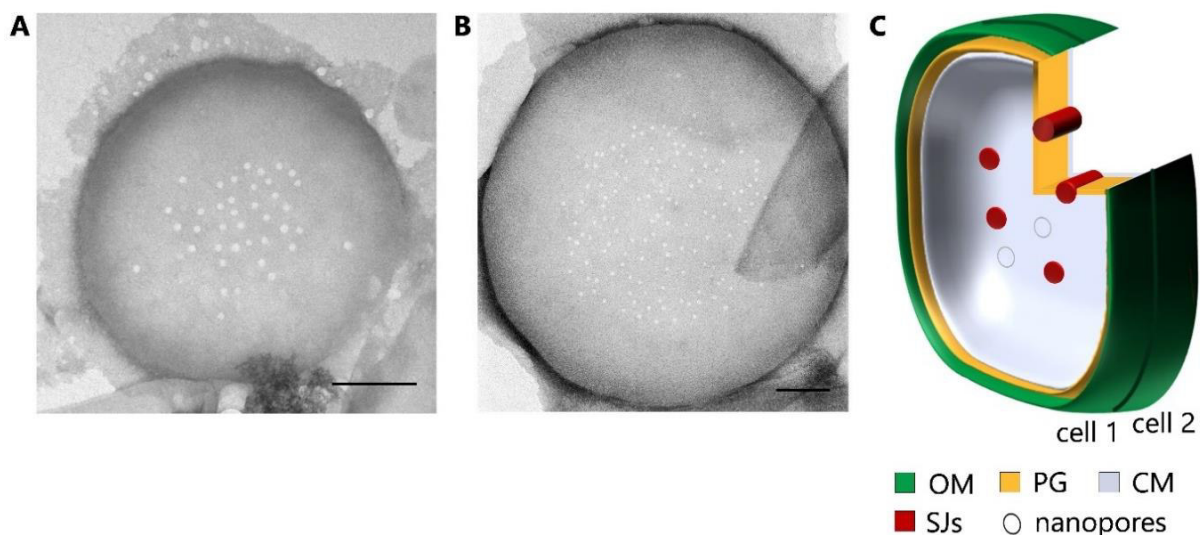


**Figure 6: The nanopore array in the septal peptidoglycan serves as framework for SJs.** (A) Transmission electron microscopic images of a purified septal PG disc of *Nostoc* and (B) *Anabaena*. Scale bar, 250 nm. (C) Schematic view from the side on the septum of two adjacent cells. The SJs traverse the PG through the nanopores. OM, outer membrane; PG, peptidoglycan; CM, cytoplasmic membrane; SJs, septal junctions. Modified from (Kieninger & Maldener, 2021).

The hydrolytic activity of the nanopore drilling amidase needs to be strictly controlled in order to avoid lysis of the cell (Berendt et al., 2012). In *E. coli*, the amidase is held in its inactive form by an  $\alpha$ -helix that blocks the active site until removed via a conformational change triggered by the LytM factor NlpD (Uehara et al., 2010). However, this inhibitory  $\alpha$ -helix is lacking in AmiC2 of *Nostoc* and raises the question about its spatiotemporal regulation mechanism (Büttner et al., 2016). Despite the absence of the inhibitory  $\alpha$ -helix in AmiC of filamentous cyanobacteria, an open reading frame (ORF) homologous to *nlpD* of *E. coli* is present: *alr3353* in *Anabaena*. The essential protein Alr3353 enhances the hydrolytic activity of AmiC1 via direct

interaction and thereby positively influences nanopore formation, cell-cell communication and nitrogen fixation (Bornikoel et al., 2018) (Table 1). Besides a PG-binding domain, a SH3 motif is present in Alr3353, which probably mediates interaction with further proteins of the cell-cell communication machinery (Bornikoel et al., 2018).

**Table 1: Influence of various proteins on the nanopore array.**

Mutant in	Nanopore array	Function of protein	Reference
<i>amiC1</i> <i>Nostoc</i>	not investigated	essential for growth	Lehner et al. 2011
<i>amiC2</i> <i>Nostoc</i>	none	drilling of nanopores	Lehner et al. 2013
<i>amiC1</i>	reduced to ~50 %	drilling of nanopores, influence on localization of SepJ, partly redundant to AmiC2	Bornikoel et al. 2017
<i>amiC2</i>	reduced to ~30 %	drilling of nanopores, partly redundant to AmiC1	Bornikoel et al. 2017
<i>alr3353</i>	reduced to ~50 %	enhancement of hydrolytic activity of AmiC1 via direct interaction	Bornikoel et al. 2018
<i>sjcF1</i>	increased nanopore diameter	interaction with FraC and SepJ	Rudolf et al. 2015
<i>fraC/fraD</i>	strongly reduced	septal junction proteins?	Nürnberg et al. 2015
<i>fraE</i>	unaltered	heterocyst maturation	Arévalo et al. 2015
<i>sepJ</i>	strongly reduced	septal junction protein?	Nürnberg et al. 2015
<i>sepI</i>	strongly reduced	interaction with SepJ and divisome proteins	Springstein et al. 2020
<i>glsC</i>	reduced to ~50 %	influence on localization of SepJ	Nieves-Morión et al. 2017
<i>glsP, hepP</i>	unaltered	interaction with SepJ	Nieves-Morión et al. 2017

If not stated otherwise, mutants and proteins in *Anabaena* are described.

The PG-binding protein SjcF1 (septal junction channel formation protein) has impact on the regulation of the nanopore diameter (Table 1), since a *sjcF1* (*all1861*) mutant showed significant larger nanopores compared to wild type *Anabaena* (Rudolf et al., 2015). Additionally, SjcF1 links nanopore formation to SJs, since protein-protein interaction with the putative SJ proteins FraC and SepJ (see 3.5.2) was shown and is mediated through the SH3 domain of SjcF1 and the SH3 binding motifs in FraC and SepJ (Rudolf et al., 2015).

Recently, SepI, the gene product of *alr3364*, was described to play a role in nanopore formation (Table 1) and cell-cell communication. SepI was shown to interact with components of the divisome and the putative SJ protein SepJ, linking cell division with cell-cell communication (Springstein et al., 2020). A mutant in *sepI* showed filament fragmentation, reduced cell-cell communication due to fewer nanopores and inability of heterocyst differentiation (Springstein et al., 2020).

As already mentioned, the sucrose analog esculin can be used for FRAP experiments and is taken up via subunits of glucoside transporters consisting of the ATP-binding subunit GlcC (Alr4781), the permease subunit GlcP (All0261) and the major facilitator superfamily protein HepP (All1711) (Nieves-Morión et al., 2017a). Vegetative cells of mutants in one of the

respective genes are impaired in molecular exchange of esculin, which might be caused by the interplay of the proteins with SepJ: GlsC is relevant for proper localization of SepJ, whereas GlsP and HepP interact with the latter (Nieves-Mori3n et al., 2017a) (Table 1).

Recently, purified septal discs in heterocyst-enriched samples revealed nanopores, which were approximately 1.3-fold larger than in septa between two vegetative cells, but relation between the nanopore arrays in both types of septal discs was suggested (Ar3valo & Flores, 2021).

The broad variety of proteins influencing nanopore drilling (summarized in Table 1) and the interconnected processes of septum maturation and SJ formation argue for the cell-cell communication being a complex and important invention of multicellular organisms.

### 3.5.2 Septal junctions and Fra proteins

Decades ago, cell-cell connecting structures traversing the PG were revealed by electron microscopy of ultrathin sections and freeze-fracture electron microscopy, and based on plasmodesmata of plants termed “microplasmodesmata” (Hagedorn, 1961; Lang & Fay, 1971; Giddings & Staehelin, 1981). Electron tomography analysis of the septal region suggested that the microplasmodesmata consist of proteins instead of membranes (Wilk et al., 2011). Therefore, they were named “septosomes” (Wilk et al., 2011) and “channels” (Omairi-Nasser et al., 2014), but eventually the term “septal junctions” (SJs) gained acceptance (Mariscal, 2014; Flores et al., 2016; Flores et al., 2019). As mentioned above, these SJ complexes were suggested to penetrate the nanopores in the PG and together form the cell-cell communication machinery of filamentous cyanobacteria (Lehner et al., 2013) (Figure 6C). Cyanobacterial SJs were compared with metazoan gap junctions, but show an obvious difference: cytoplasmic membranes are in a defined proximity at the sites of gap junctions, which is not the case for SJs (Mullineaux et al., 2008). However, both kind of cell connecting junctions allow diffusion of small molecules (Nieves-Mori3n et al., 2017b). Furthermore, it was suggested that SJs could be closed similarly to gap junctions, since communication was depleted between vegetative cells and senescent heterocysts (N3rnberg et al., 2015). Although genes coding for gap junction protein homologs are absent in cyanobacteria (Flores et al., 2016), several proteins were described to play a role in establishing the cell-cell connecting structures. The most prominent proteins in this respect are FraC (Alr2392), FraD (Alr2393) and FraG (Alr2338), which is also named SepJ. These proteins got their name from their severe fragmentation phenotype especially in nitrate-depleted conditions and were initially identified as genes involved in aerobic nitrogen fixation (Buikema & Haselkorn, 1991b; Bauer et al., 1995; Flores et al., 2007; Nayar et al., 2007; Merino-Puerto et al., 2010). Because disruption of *amiC* in a *fraCfraD* or *sepJ* mutant background rescued filament fragmentation, fragmentation could arise from a poorly controlled AmiC activity, which results in septal PG splitting (Bornikoel et al., 2017). Mutants in *fraC* and *fraD* rarely differentiate mature heterocysts (Bauer et al., 1995) whose nitrogenase

activity develop slowly (Merino-Puerto et al., 2010). In contrast, a *sepJ* mutant did not show nitrogenase activity, since mature heterocysts cannot evolve due to hampered heterocyst glycolipids synthesis (Flores et al., 2007; Nayar et al., 2007). The genes *fraC* and *fraD* are constitutively expressed at a low level from an operon to which also *fraE* (see below) belongs (Merino-Puerto et al., 2010).

The cytoplasmic membrane proteins FraC and FraD comprise three or four and five transmembrane domains, respectively (Bauer et al., 1995; Merino-Puerto et al., 2011b) (Figure 7A). The C-terminal part of FraD harbors two coiled-coil motifs and faces the periplasm (Merino-Puerto et al., 2010; Merino-Puerto et al., 2011b). A coiled-coil domain was also predicted in the N-terminal part of the membrane protein SepJ, which ranges to the periplasm (Flores et al., 2007). A proline/serine/threonine-rich linker connects this part to its C-terminus, which shows sequence similarity to an export permease (Flores et al., 2007) (Figure 7A). Furthermore, SepJ strongly interacts with itself forming multimers and was supposed to be part of cell-cell connecting channels (Ramos-León et al., 2015; Ramos-León et al., 2017).

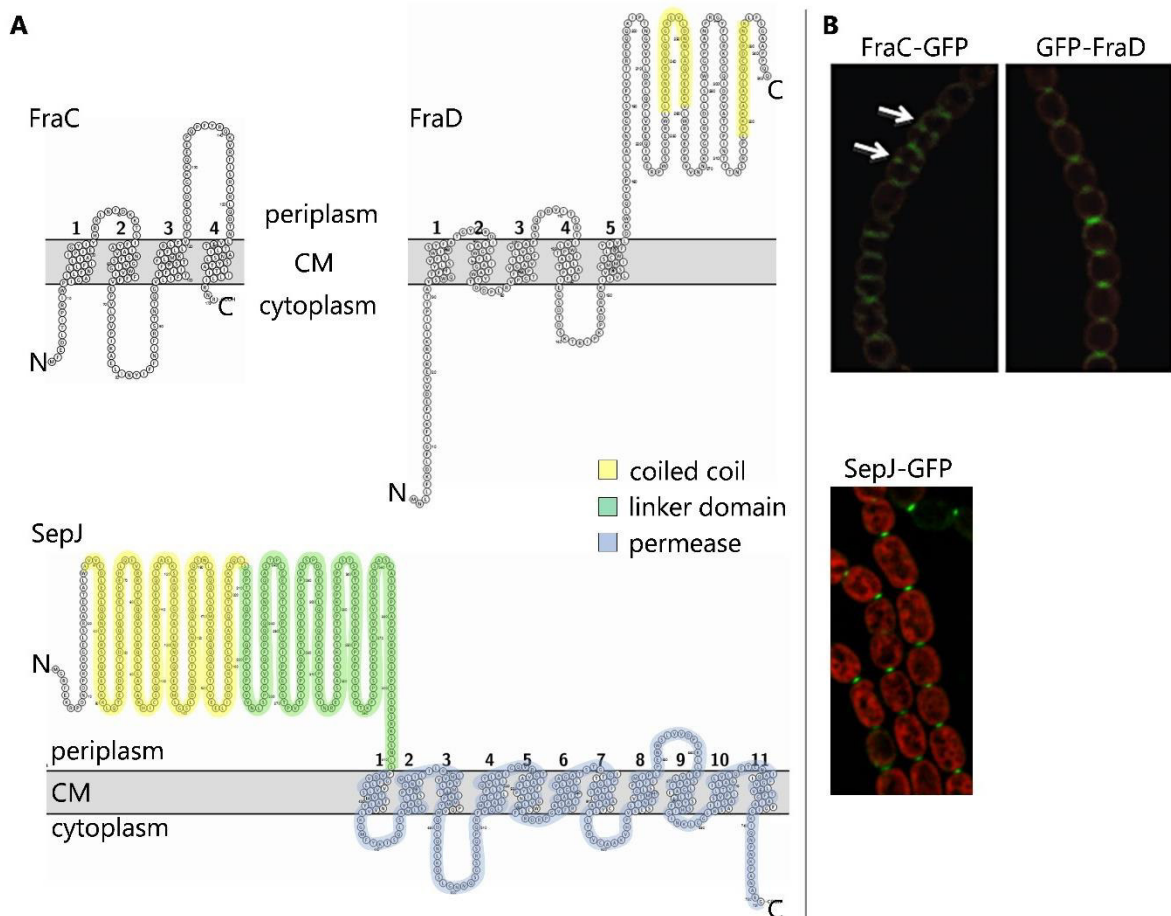


**Figure 7: Secondary structure prediction and localization of Fra proteins.** (A) Predicted secondary structure of FraC, FraD and SepJ. Coiled coil domains are marked in yellow, the linker domain of SepJ in green and its permease domain in blue. The topology images are derived from Protter webinterface after (Merino-Puerto et al., 2011b) in case of FraD and (Herrero et al., 2016) in case of SepJ. N, N-terminus; C, C-terminus; CM, cytoplasmic membrane. (B) Fluorescence micrographs show the localization of Fra proteins fused to GFP. Arrows point to dividing cells in the *fraC-gfp* strain. FraC-GFP and GFP-FraD images were modified from (Merino-Puerto et al., 2010).

FraC, FraD and SepJ are localized at the intercellular septa (Figure 7B), however, fluorescence was described to be most focused to a spot in the middle of the septum in the case of SepJ-GFP (Flores et al., 2007). A less focused localization was observed for GFP-FraD and distribution over the whole septum for FraC-GFP (Merino-Puerto et al., 2010). In contrast to FraD, both, FraC and SepJ, are moving with the Z-ring of dividing cells during septum constriction (Flores et al., 2007; Merino-Puerto et al., 2010; Merino-Puerto et al., 2011b). Interaction of SepJ with the divisome is mediated through direct interaction with FtsQ, a downstream divisome protein of FtsZ (Ramos-León et al., 2015). Furthermore, SepJ loses its focused localization in the absence of FraC, FraD or AmiC1 (Merino-Puerto et al., 2010; Bornikoel et al., 2017). Nevertheless, localization to the mid-cell ring during cell division is unaltered (Merino-Puerto et al., 2010). Additionally, localization of FraD is dependent on FraC but not on SepJ (Merino-Puerto et al., 2011b). These mutual dependencies in proper localization of the Fra proteins emphasizes the complexity of the interaction network.

For this work, the Fra proteins are especially important because their suggested involvement in cell-cell communication (reviewed in (Kieninger & Maldener, 2021)). Interestingly, reduced IC was observed in *fraC*, *fraD* and *sepJ* deletion mutants (Mullineaux et al., 2008; Merino-Puerto et al., 2010), which was reflected in a reduced amount of nanopores in the septal PG (Nürnberg et al., 2015) (Table 1). Strikingly, molecular exchange of calcein and 5-CF was differently impaired in *fraCfraD* and *sepJ* mutants, which led to the suggestion that two types of septal junctions exist (Merino-Puerto et al., 2011b; Flores et al., 2019). This assumption would also explain remaining SJs in *sepJ* and *fraCfraD* mutants, but not in the triple mutant. In summary, FraD and SepJ were suggested to build cell-cell joining complexes, whereas FraC was ascribed as a coordinator of other proteins (Flores et al., 2007; Merino-Puerto et al., 2010; Merino-Puerto et al., 2011b). Nevertheless, a related function of FraC and FraD was supposed, since the proteins are expressed from the same operon and the deletion mutants showed a similar phenotype (Merino-Puerto et al., 2011b; Flores et al., 2019). The diazotrophic growth phenotype of *fraC* and *fraD* mutants was suggested to be not directly linked to these proteins (Bauer et al., 1995; Merino-Puerto et al., 2010), but the role of SepJ could be dual (Flores et al., 2007; Nayar et al., 2007). Interaction between FraC, FraD and SepJ was supposed but could not be proven yet (Flores et al., 2019). Furthermore, functional relation between the Fra proteins and AmiC1 was suggested, which links nanopore drilling as scaffold for cell-cell communication with SJ complexes as intercellular exchange mediating channels (Bornikoel et al., 2017).

The *fra* proteins FraE and FraH were ascribed to the development of heterocysts, since nitrogenase activity was undetectable under oxic and very low under anoxic conditions (Merino-Puerto et al., 2010). FraE localizes mainly to heterocyst poles after 24 h incubation in heterocyst-inducing conditions and is important for formation of the restricted heterocyst neck (Merino-Puerto et al., 2011b; Arévalo & Flores, 2021). Whereas IC and the nanopore array

between vegetative cells in a *fraE* mutant are similar to the WT (except for enlarged nanopore diameter), both are reduced between heterocyst and vegetative cell (Merino-Puerto et al., 2010; Arévalo & Flores, 2021). Expression of *fraH* is enhanced dependent on NtcA and HetR in heterocyst-promoting conditions (Merino-Puerto et al., 2010) and its gene product is involved in the reorganization of intracellular membranes during heterocyst differentiation, but does not interfere with IC (Merino-Puerto et al., 2011a).

Another *fra* gene, *fraF*, which is encoded on the antisense DNA strand of the *fraCDE* operon, partially overlaps with *fraE* and is induced in the absence of nitrate (Merino-Puerto et al., 2013). In contrast to other Fra proteins, deletion of *fraF* results in prolonged filaments instead of filament fragmentation (Merino-Puerto et al., 2013).

In conclusion, various proteins are involved in the establishment of the nanopore array and the formation of SJs (reviewed in (Herrero et al., 2016; Kieninger et al., 2019; Kieninger & Maldener, 2021)). Yet their detailed interplay as well as their spatial and temporal regulation is still poorly understood. Nevertheless, it is obvious that proper establishment of the nanopore array is essential for accurate constitution and action of the SJs (Flores et al., 2019). Most likely, a lot of proteins involved in cell-cell communication are still unknown and their disclosure will contribute further knowledge about this essential system for multicellularity.

## 4 Research objectives

Intercellular communication is a highly complex system interconnected with cell division and cell differentiation. Multicellular cyanobacteria like *Anabaena* sp. PCC 7120 and *Nostoc punctiforme* ATCC 29133 harbor perforated septal PG discs drilled by amidases and traversed by proteinaceous septal junction protein complexes. Although extensively studied during the last decades, the process of nanopore formation and septal junction incorporation, the architecture and protein identity of septal junctions as well as the potential regulation of metabolite exchange remained poorly understood. Regulation of IC seems to be essential to maintain the life of a filament especially in emergency situation. Interruption of molecular exchange with a neighboring cell is necessary when single cells within a filament are disrupted by shear force, filament breakage or senescence or are attacked by predators. Inability to cease IC in such cases would lead to leakage of the whole filament and in consequence to the death of the organism.

The overall aim of this work is to broaden the knowledge about the cell-cell communication system in *Anabaena* consisting of nanopores and septal junctions. In order to address the question of a potential regulation mechanism of cell-cell communication, molecular exchange is monitored under various stress conditions. By establishing an assay for the study of the potential regulation of IC, previously described mutants in septal junction proteins are examined to identify proteins involved in this regulation. This molecular analysis is coupled to imaging of septal junctions via electron cryotomography performed by collaboration partners.

The establishment of the confocal microscopic assay to monitor regulation of IC is linked to another major aim of this research, which is the identification of structural septal junction proteins and clarification of the contribution of FraC, FraD and SepJ. Mutants in potential structural septal junction components or proteins otherwise involved in cell-cell communication should be generated and physiologically characterized.

## 5 Materials and methods

### 5.1 Cultivation of bacterial strains

*Escherichia coli* (*E. coli*) strains were cultivated in liquid lysogeny broth (LB) medium (Bertani, 1951) or on LB medium solidified with 1.5 % (w/v) agar-agar at 37 °C in the dark. For protein expression, *E. coli* was cultured in Terrific Broth (TB) medium (Tartof & Hobbs, 1987). The composition of LB and TB media is described in Table 2. Respective antibiotics were used at concentrations of 50 µg mL<sup>-1</sup> kanamycin (Km), 100 µg mL<sup>-1</sup> spectinomycin (Sp), 25 µg mL<sup>-1</sup> streptomycin (Sm), 25 µg mL<sup>-1</sup> chloramphenicol (Cm), and 100 µg mL<sup>-1</sup> ampicillin (Amp).

**Table 2: Composition of cultivation media for *E. coli*.**

LB medium		TB medium			
Component	g/L	Broth	g/L	10x TB salts	mM
Tryptone	10	Tryptone	12	KH <sub>2</sub> PO <sub>4</sub>	170
Yeast extract	5	Yeast extract	24	K <sub>2</sub> HPO <sub>4</sub>	72
NaCl	10	Glycerol	5	autoclave, add 100 mL to	
		ddH <sub>2</sub> O to 900 mL, autoclave		TB medium	

*Anabaena* sp. PCC 7120 strains were cultured in 100 mL Erlenmeyer flasks with 50 mL BG11 medium (Rippka et al., 1979) at 28 °C, constant illumination at 30-40 µE m<sup>-2</sup> s<sup>-1</sup> and shaking at 100-140 rpm or were grown on BG11 plates solidified with 1.5 % (w/v) Bacto agar (Becton Dickinson and Company). Stock cultures were kept on BG11 and nitrate-depleted BG11<sub>0</sub> agar plates. For co-IP experiments, *Anabaena* was cultivated in 700 mL BG11 medium bubbled with ambient air and 2 % CO<sub>2</sub>. The composition of BG11 medium is summarized in Table 3. Respective antibiotics were added at concentrations of 50 µg mL<sup>-1</sup> neomycin (Nm), 5 µg mL<sup>-1</sup> streptomycin, and 5 µg mL<sup>-1</sup> spectinomycin. All bacterial strains used in this work are summarized in Table 5 in 5.2.1.

**Table 3: Composition of BG11 cultivation medium for *Anabaena*.**

Component	µM	Component	µM
MgSO <sub>4</sub> x 7H <sub>2</sub> O	304	H <sub>3</sub> BO <sub>4</sub>	46
CaCl <sub>2</sub> x 2H <sub>2</sub> O	245	MnCl <sub>2</sub>	9.2
Na <sub>2</sub> CO <sub>3</sub>	180	ZnSO <sub>4</sub>	0.77
K <sub>2</sub> HPO <sub>4</sub>	175	Na <sub>2</sub> MoO <sub>4</sub>	1.6
citric acid	31	CuSO <sub>4</sub>	0.32
ferric(III)-citrate	24	CoCl <sub>2</sub>	0.2
Na <sub>2</sub> EDTA x 2H <sub>2</sub> O	3.4	NaNO <sub>3</sub> (omitted in Bg11 <sub>0</sub> )	17.6 x10 <sup>3</sup>

## 5.2 Molecular cloning

Amplification of DNA fragments for creation of plasmids was performed via polymerase chain reaction (PCR) in a SensoQuest Labcycler using the Q5 high-fidelity DNA polymerase (New England Biolabs) according to the manufacturer's protocol. For PCR reactions that only served for verification of inserts, the RedTaq Mastermix (Genaxxon) was used. DNA was separated via gel electrophoresis at 120-130 V using 1 % agarose gels in TAE buffer (50 mM Tris pH 8, 1 mM EDTA). 0.9  $\mu$ L Midori Green Advanced (Nippon Genetics) were added to 20 mL of agarose solution and GenLadder 1 kb (Genaxxon) was used as DNA ladder. Vectors were linearized by overnight digest at 37 °C with restriction enzymes ordered from Thermo Fisher Scientific, and heat-inactivated for 20 min at 80 °C. Table 4 shows the restriction enzymes used for digest of the respective plasmids.

**Table 4: Linearization of vectors with restriction enzymes.**

Vector	Enzymes	Buffer
pRL1049	EcoRI, BamHI	2x Tango
pRL277	XhoI, PstI	Red
pET28a	XhoI, 2x NdeI	Red
pASK15	EcoRI, 2x BamHI	2x Tango
pMalc2x	XmnI, 2x PstI	1x Tango
pKT25	2x XbaI, EcoRI	2x Tango
pUT18	XbaI, HindIII	2x Tango
pUT18C	XbaI Fast digest	Fast Digest
	2x XbaI, EcoRI (for pIM845)	2x Tango

Enzymes and buffers from Thermo Fisher Scientific.

All plasmids created in this work (Table 6) were assembled using isothermal Gibson Assembly Cloning (Gibson et al., 2009). Eight  $\mu$ L of a 20  $\mu$ L reaction mix were introduced into electrocompetent *E. coli* cells (strain NEB 10- $\beta$ ) via electroporation (1.8 kV, 25  $\mu$ F, 200  $\Omega$ ) using a Gene Pulser (Bio-Rad). Plasmids were sequenced by Eurofins Genomics and compared to reference sequences derived from the KEGG database (Kanehisa & Goto, 2000).

For PCR clean-up, gel clean-up, and plasmid isolation, the Monarch Kit Systems (New England Biolabs) and the ExtractMe Kit systems (Blirt, Poland) were used. Concentration of purified DNA was determined via measurement of the absorbance at 260 nm using a NanoPhotometer (Implen).

### 5.2.1 Strains and plasmids

All strains and plasmids used and created in this work are described in Table 5 and Table 6, respectively.

**Table 5: *Anabaena* sp. PCC 7120 and *E. coli* strains used in this work.**

<i>Anabaena</i> sp.		
PCC 7120 strain	Relevant characteristics	Reference
PCC 7120	wild type	Rippka et al., 1979
7120.800	$P_{fraCDE}$ - <i>gfpmut2</i> , Sm <sup>r</sup> , Sp <sup>r</sup>	This study
AFS-I- <i>sjcF1</i>	<i>sjcF1</i> ( <i>all1861</i> )::pCVS3	Rudolf et al., 2015
CSVM34	$\Delta$ <i>sepJ</i> ( <i>alr2338</i> )	Mariscal et al., 2011
CSVT2	$\Delta$ <i>fraD</i> ( <i>alr2393</i> )	Merino-Puerto et al., 2010
CSVT2.768	$\Delta$ <i>fraD</i> , $P_{fraCD}$ - <i>fraD</i> , Sm <sup>r</sup> , Sp <sup>r</sup>	Weiss et al., 2019
CSVT2.769	$\Delta$ <i>fraD</i> , $P_{fraCD}$ - <i>fraD</i> <sub>TM</sub> , Sm <sup>r</sup> , Sp <sup>r</sup>	This study
CSVT2.779	$\Delta$ <i>fraD</i> , $P_{fraCD}$ - <i>gfpmut2</i> - <i>fraD</i> , Sm <sup>r</sup> , Sp <sup>r</sup>	Weiss et al., 2019
CSVT2.824	$\Delta$ <i>fraD</i> , $P_{fraCD}$ - <i>fraD</i> - <i>Tat-FraDpp</i> , Sm <sup>r</sup> , Sp <sup>r</sup>	This study
CSVT2.837	$\Delta$ <i>fraD</i> , $P_{fraCD}$ - <i>fraD</i> <sub>2TM</sub> , Sm <sup>r</sup> , Sp <sup>r</sup>	This study
CSVT2.SR834	$\Delta$ <i>fraD</i> ( <i>alr2393</i> ), <i>all4109</i> -5xGS- <i>sfgfp</i> , Sm <sup>r</sup> , Sp <sup>r</sup>	This study
CSVT22	$\Delta$ <i>fraCfraD</i> ( <i>alr2392/alr2393</i> )	Merino-Puerto et al., 2011
CSVT22.768	$\Delta$ <i>fraCfraD</i> , $P_{fraCD}$ - <i>fraD</i> , Sm <sup>r</sup> , Sp <sup>r</sup>	Weiss et al., 2019
DR814	<i>all3826</i> ::C.K3t4, Nm <sup>r</sup>	This study
DR823	<i>fral</i> ( <i>alr4714</i> )::C.K3t4, Nm <sup>r</sup>	This study
DR823.847	<i>fral</i> ::C.K3t4, $P_{alr4714}$ - <i>alr4714</i> , Nm <sup>r</sup> , Sm <sup>r</sup> , Sp <sup>r</sup>	This study
DR823.851	<i>fral</i> ::C.K3t4, $P_{alr4714}$ -SS-5xGS- <i>sfgfp</i> - <i>fral</i> , Nm <sup>r</sup> , Sm <sup>r</sup> , Sp <sup>r</sup>	This study
DR825	<i>sepN</i> ( <i>all4109</i> )::C.K3t4, Nm <sup>r</sup>	This study
DR825.848	<i>sepN</i> ::C.K3t4, $P_{all4110/4109}$ - <i>sepN</i> , Nm <sup>r</sup> , Sm <sup>r</sup> , Sp <sup>r</sup>	This study
DR833	<i>alr4788</i> ::C.K3t4, Nm <sup>r</sup>	This study
SR477	<i>amiC1</i> ( <i>alr0092</i> )::pIM477, Sm <sup>r</sup> , Sp <sup>r</sup>	Berendt et al., 2012
SR834	<i>all4109</i> :: <i>all4109</i> -5xGS- <i>sfgfp</i> , Sm <sup>r</sup> , Sp <sup>r</sup>	This study
SR835	<i>alr4788</i> :: <i>alr4788</i> -5xGS- <i>sfgfp</i> , Sm <sup>r</sup> , Sp <sup>r</sup>	This study
SR840	<i>alr4714</i> :: <i>alr4714</i> -5xGS- <i>sfgfp</i> , Sm <sup>r</sup> , Sp <sup>r</sup>	This study
<i>Escherichia coli</i>		
strain		
BTH101	$F'$ , <i>cya</i> -99, <i>araD139</i> , <i>galE15</i> , <i>galK16</i> , <i>rpsL1</i> ( <i>Str<sup>R</sup></i> ), <i>hsdR2</i> , <i>mcrA1</i> , <i>mcrB1</i> , <i>relA1</i>	Euromedex
HB101	$F^-$ , <i>thi</i> -1, <i>hsdS20</i> ( $r_B^-$ , $m_B^-$ ), <i>supE44</i> , <i>recA13</i> , <i>ara</i> -14, <i>leuB6</i> , <i>proA2</i> , <i>lacY1</i> , <i>galK2</i> , <i>rpsL20</i> ( <i>str<sup>r</sup></i> ), <i>xyl</i> -5, <i>mtl</i> -1	Sambrook et al., 1989
J53 (RP-4)	R+, <i>met</i> , <i>pro</i> (RP-4: <i>Ap</i> , <i>Tc</i> , <i>Km</i> , <i>Tra<sup>+</sup></i> , <i>IncP</i> )	Wolk et al., 1984
Lemo21 (DE3)	<i>fhuA2</i> [ <i>lon</i> ] <i>ompT gal</i> ( $\lambda$ DE3) [ <i>dcm</i> ] $\Delta$ <i>hsdS</i> / <i>pLemo</i> ( <i>Cm<sup>r</sup></i> ), $\lambda$ DE3 = $\lambda$ <i>sBamH1o</i> $\Delta$ <i>EcoRI</i> - <i>B int</i> :( <i>lacI</i> :: <i>PlacUV5</i> :: <i>T7 gene1</i> ) <i>i21</i> $\Delta$ <i>nin5</i> , <i>pLemo</i> = <i>pACYC184-PrhaBAD</i> - <i>lysY</i>	NEB

NEB 10-β	<i>Δ(ara-leu) 7697 araD139 fhuA ΔlacX74 galK16 galE15 e14- Φ80dlacZΔM15 recA1 relA1 endA1 nupG rpsL (Sm<sup>r</sup>) rph spoT1 Δ(mrr-hsdRMS-mcrBC)</i>	NEB
Rosetta2 (DE3)	<i>F<sup>-</sup> ompT hsdS<sub>B</sub>(r<sub>B</sub><sup>-</sup> m<sub>B</sub><sup>-</sup>) gal dcm (DE3) pRARE2 (Cm<sup>r</sup>)</i>	Sigma Aldrich

DR: double recombination; SR: single recombination.

**Table 6: Plasmids used and created in this work.**

Plasmids for <i>Anabaena</i>		
pRL1049	Self-replicating plasmid, Sm <sup>r</sup> , Sp <sup>r</sup>	Black and Wolk, 1994
pRL277	Integrative vector, <i>sacB</i> , Sm <sup>r</sup> , Sp <sup>r</sup>	Black <i>et al.</i> , 1993
pIM660.2	C-terminal <i>alr3353</i> -fragment fused to 5xGS-linker and <i>sfgfp</i> in pRL277, Sm <sup>r</sup> , Sp <sup>r</sup>	Bornikoel, unpublished
pIM768	<i>P<sub>fraCD</sub>-fraD (alr2393)</i> in pRL1049, Sm <sup>r</sup> , Sp <sup>r</sup>	Weiss <i>et al.</i> , 2019
pIM769	<i>P<sub>fraCD</sub>-fraD<sub>TM</sub></i> (transmembrane part of <i>fraD</i> ) in pRL1049, Sm <sup>r</sup> , Sp <sup>r</sup>	This study
pIM779	<i>P<sub>fraCDE</sub>-gfpmut2-fraD</i> in pRL1049, Sm <sup>r</sup> , Sp <sup>r</sup>	Weiss <i>et al.</i> , 2019
pIM800	<i>P<sub>fraCDE</sub>-gfpmut2</i> in pRL1049, Sm <sup>r</sup> , Sp <sup>r</sup>	This study
pIM814	C.K3t4 flanked by us and ds fragments of <i>all3826</i> in pRL277, Sm <sup>r</sup> , Sp <sup>r</sup> , Km <sup>r</sup>	This study
pIM823	C.K3t4 flanked by us and C-terminal fragment of <i>alr4714</i> in pRL277, Sm <sup>r</sup> , Sp <sup>r</sup> , Km <sup>r</sup>	This study
pIM824	<i>P<sub>fraCD</sub>-Tat-fraD<sub>pp</sub></i> (periplasmic part of <i>fraD</i> ) in pRL1049, Sm <sup>r</sup> , Sp <sup>r</sup>	This study
pIM825	C.K3t4 flanked by us and C-terminal fragment of <i>all4109</i> in pRL277, Sm <sup>r</sup> , Sp <sup>r</sup> , Km <sup>r</sup>	This study
pIM833	C.K3t4 flanked by us and C-terminal fragment of <i>alr4788</i> in pRL277, Sm <sup>r</sup> , Sp <sup>r</sup> , Km <sup>r</sup>	This study
pIM834	C-terminal <i>all4109</i> -fragment fused to 5xGS- <i>sfgpf</i> in pRL277, Sm <sup>r</sup> , Sp <sup>r</sup>	This study
pIM835	C-terminal <i>alr4788</i> -fragment fused to 5xGS- <i>sfgpf</i> in pRL277, Sm <sup>r</sup> , Sp <sup>r</sup>	This study
pIM837	<i>P<sub>fraCD</sub>-fraD<sub>2TM</sub></i> (M1-L80 of <i>fraD</i> ) in pRL1049, Sm <sup>r</sup> , Sp <sup>r</sup>	This study
pIM840	C-terminal <i>alr4714</i> -fragment fused to 5xGS- <i>sfgpf</i> in pRL277, Sm <sup>r</sup> , Sp <sup>r</sup>	This study
pIM847	<i>P<sub>alr4714</sub>-alr4714</i> in pRL1049, Sm <sup>r</sup> , Sp <sup>r</sup>	This study
pIM848	<i>P<sub>all4110/4109</sub>-all4109</i> in pRL1049, Sm <sup>r</sup> , Sp <sup>r</sup>	This study
pIM851	<i>P<sub>alr4714</sub></i> -signal sequence (SS)-5xGS- <i>sfgfp</i> - <i>alr4714</i> in pRL1049, Sm <sup>r</sup> , Sp <sup>r</sup>	This study

Continued on next page.

Plasmids for <i>E. coli</i>		
pRL528	Helper plasmid for mobilization used in triparental mating, Aval/Eco47II methylases, Cm <sup>r</sup>	Wolk <i>et al.</i> , 1984
pKT25	P <sub>lac</sub> -T25-MCS, Km <sup>r</sup>	Karimova <i>et al.</i> , 2001
pKNT25	P <sub>lac</sub> -MCS-T25, Amp <sup>r</sup>	Karimova <i>et al.</i> , 2005
pUT18	P <sub>lac</sub> -MCS-T18, Amp <sup>r</sup>	Karimova <i>et al.</i> , 2001
pUT18C	P <sub>lac</sub> -T18-MCS, Km <sup>r</sup>	Karimova <i>et al.</i> , 2001
pASK15	StrepII fusion tag, Amp <sup>r</sup>	IBA
pET28a	His <sub>6</sub> fusion tag, Km <sup>r</sup>	Addgene
pMalc2x	Maltose binding protein (MBP) fusion tag, Amp <sup>r</sup>	NEB
pIM597	T25- <i>fraD</i> <sub>pp</sub> in pKT25, Km <sup>r</sup>	F. Treppke, J. Bornikoel, 2015 (unpublished)
pIM812	Strep- <i>fraD</i> <sub>pp</sub> in pASK15, Amp <sup>r</sup>	This study
pIM813	MBP-Strep- <i>fraD</i> <sub>pp</sub> in pMalc2x, Amp <sup>r</sup>	This study
pIM826	T18- <i>all4109</i> in pUT18C, Amp <sup>r</sup>	E. Lorenz, 2020
pIM827	His <sub>6</sub> - <i>all4109</i> <sub>pp</sub> (D28-end) in pET28a, Km <sup>r</sup>	This study
pIM829	T18- <i>all4109</i> <sub>pp</sub> in pUT18C, Amp <sup>r</sup>	E. Lorenz, 2020
pIM831	T18- <i>alr4788</i> in pUT18C, Amp <sup>r</sup>	E. Lorenz, 2020
pIM832	T25- <i>fraD</i> in pKT25, Km <sup>r</sup>	E. Lorenz, 2020
pIM836	<i>alr4714</i> -T18 in pUT18, Amp <sup>r</sup>	E. Lorenz, 2020
pIM845	<i>all4109</i> <sub>opt</sub> (optimized for <i>E. coli</i> ) in pUT18C, Amp <sup>r</sup>	This study
pIM846	<i>fraD</i> <sub>opt</sub> (optimized for <i>E. coli</i> ) in pKT25, Km <sup>r</sup>	This study
pIM849	<i>Alr4714</i> -T25 in pKNT25, Km <sup>r</sup>	This study
pIM850	T25- <i>all4109</i> <sub>opt</sub> (optimized for <i>E. coli</i> ) in pKT25, Km <sup>r</sup>	This study
pIM852	T25- <i>alr4714</i> <sub>Δaa1-57</sub> in pKT25, Km <sub>r</sub>	This study

Elisabeth Lorenz (E. Lorenz) did her bachelor thesis under my supervision; us, upstream; ds, downstream; MCS, multiple cloning site.

## 5.2.2 Construction of mutants

Oligonucleotides were ordered from Sigma-Aldrich (Merck KGaA) and are listed in Table 7 with indication of the resulting PCR products.

**Table 7: Oligonucleotides used for amplification of DNA fragments.**

Plasmid	Product	Template	Oligo	Sequence 5'-3'
pIM769	$P_{fraCD}$		1998	GATATCCCGCAAGAGGCCCTTTCGTCTTCAAGAATTCTGCCGTTCTTGCATCTG
			2041	GTAACCTAACCGAGTGTAGCAAGACACTCAACAAAAAGGGAAAC
	<i>fraD</i> <sub>TM</sub>		2008	CACTATAGGGAGACACAACGGTTCCCTCTACCGGGATCCTTATTCTTGTAAACCATTTATCCA
			2040	CCCTTTTTGTTGAGTGTCTTGTAACTCGTTAAGTTAC
pIM814, pIM823, pIM825, pIM833	C.K3t4		1383	TCTAGAGGATCTCAATGAATA
			1384	ATGCTTGTAAACCGTTTTG
pIM800	$P_{fraCDE-gfpmut2}$	pIM779	1998	GATATCCCGCAAGAGGCCCTTTCGTCTTCAAGAATTCTGCCGTTCTTGCATCTG
			2235	CCACAACGGTTCCCTCTACCGGGATCCGGTATTGTATAGTTCATCCATGCCATGTCG
pIM814	<i>all3826</i> us		2320	ATGGCAGAAATTCGATATCTAGATCTCGAGTACCTGCGCGGCAAAAT
			2321	ATTCATTGAGATCCTCTAGAAGCAATTACTGCACTTGA
	<i>all3826</i> ds		2322	ACAAAACGGTTTACAAGCATACAGCATCCGCCGACAAAC
			2323	AATAGTTTGCACAACGTTGTTGCCATTGCTGCAGCAATTGCCTCACAC
pIM823	<i>atr4714</i> us		2410	ATGGCAGAAATTCGATATCTAGATCTCGAGTGAAGCAGCCAGCATC
			2411	ATTCATTGAGATCCTCTAGATCGTGGAACAGTGAG
	<i>atr4714</i> ds		2412	ACAAAACGGTTTACAAGCATCCAGCAACCAAAACAC
			2413	TAGTTTGCACAACGTTGTTGCCATTGCTGCAGAGCAACATGGCAGAAC
pIM824	$P_{fraCDE-tat}$	pIM802	1998	GATATCCCGCAAGAGGCCCTTTCGTCTTCAAGAATTCTGCCGTTCTTGCATCTG
			2409	AAACTGAAGCCAGCAACTTTTGGCAATAGTGGCATG
	<i>fraD</i> <sub>pp</sub>		1199	CTGCAGGCAGTGTGGCTTCAAGT
			2009	CAACGGTTCCCTCTACCGGGATCCTACTGCTGCGTTACGGTGGCGCTGC
pIM825	<i>all4109</i> us		2399	ATGGCAGAAATTCGATATCTAGATCTCGAGTGTGCTGATGCGATTATTG
			2397	ATTCATTGAGATCCTCTAGATGGTCACTACTCTAGTC
	<i>all4109</i> ds		2398	CAAAACGGTTTACAAGCATATTGGACTTATGCCCTACC
			2400	TAATAGTTTGCACAACGTTGTTGCCATTGCTGCAGGTTGTCAGTTGCCAGTTG
pIM833	<i>atr4788</i> us		2440	ATGGCAGAAATTCGATATCTAGATCTCGAGCAGCACTGAAGGAAGAAG
			2441	ATTCATTGAGATCCTCTAGAGAATTCGGGAGTGAAATG
	<i>atr4788</i> ds		2442	TTTTTACAAAACGGTTTACAAGCATGGAAATAGTGTGCTGTTGG
			2443	TAGTTTGCACAACGTTGTTGCCATTGCTGCAGCGCTCAACAACGCTGAA
pIM834	<i>all4109</i> C-terminal		2450	ATGGCAGAAATTCGATATCTAGATCTCGATTGGTGTATCTTATATATT
			2451	ACCGGATCCACTACCGGATCCACTACCTTTTTTATCCAGGGTAGG
pIM834, pIM835, pIM840	5xGS- <i>sfGFP</i>	pIM660.2	1444	TAGTGGATCCGGTAGTGGATCCGGTAGCGCATCAAAGGTGAAGAATTATTTAC
pIM835	<i>atr4788</i> C-terminal		2448	ATGGCAGAAATTCGATATCTAGATCTCGAAACAATAAACACTATTC
			2449	ACCGGATCCACTACCGGATCCACTACCTCTCCGTCATTATGAC
pIM837	$P_{fraCDE-fraD}$ <sub>2TM</sub>	pIM768	2455	GGTTTCCCTCTACCGGGATCCTTAAAGGGGTCACTAGTTGT
			1998	GATATCCCGCAAGAGGCCCTTTCGTCTTCAAGAATTCTGCCGTTCTTGCATCTG
pIM840	<i>atr4714</i> C-terminal		2489	ATGGCAGAAATTCGATATCTAGATCTCGTTACTGTTAAGCCGGGTAC
			2490	ACCGGATCCACTACCGGATCCACTACTGCTGGCGACCACGTA
pIM847	$P_{atr4714-atr4714}$		2509	AGAGGCCCTTTCGTCTTCAAGAATTATATTAGACCCAGTGTG
			2510	GACCACAACGGTTTCCCTCTACCGGTTATGCTGGCGACCAC
pIM848	$P_{all4109/4109}$		2511	AGAGGCCCTTTCGTCTTCAAGAATTTTCCGCTCAGGCTTAG
			2512	TGGTCAGTACTCCTAGTATGATGAGTATACCCGAAACTT
	<i>all4109</i>		2513	ATGACTAGGAGTACTGACC
			2514	GACCACAACGGTTTCCCTCTACCGGTTATTCTTTTTATTCCAGGGTAG
pIM851	$P_{atr4714-SS}$		2509	AGAGGCCCTTTCGTCTTCAAGAATTATATTAGACCCAGTGTG
			2526	CCACTACCGGATCCACTACTGAGTATACGATAGTACCAATC
	5xGS- <i>sfGFP</i>		1444	TAGTGGATCCGGTAGTGGATCCGGTAGCGCATCAAAGGTGAAGAATTATTTAC
			2454	GGTCATGAGATTATCAAAGGATCTTATTATATAATTATCCATACC
	<i>atr4714</i>	2527	GTATGGATGAATTATATAAACTGTTCCAGCGATTTTATC	
		2510	GACCACAACGGTTTCCCTCTACCGGTTATGCTGGCGACCAC	
pIM812	<i>fraD</i> <sub>pp</sub>		2297	AAGGGCTCCCGAGACCGGCTCCGGAATTGCAAGAATATCTAGTTTATTAG
			2298	GTCCCTTGCAGGTCGACCTCGAGGGATCCTTACTGCTGCGGTGGCG
pIM813	Strep- <i>fraD</i> <sub>pp</sub>	pIM812	2299	CAATAACAACAACCTCGGATCGAGGGAAGGGCTAGCTGGAGCCACCCG
			2300	GTAACAACGACGGCAGTGGCAAGCTTGCCTGCACTACTGCTGCGGTGGCGCTG
pIM826	<i>all4109</i>		2421	GGTACCCGGGATCCTCTAGATTATTCTTTTTATTCCAGGGTAG
			2422	AACGCCACTGCAGGTCGACTACTAGGAGTACTGACCAAAA
pIM827	<i>all1409</i> <sub>pp</sub>		2429	GCCTGGTCCCGCGGACCCATATGGATGCCATTGATGATCGC
			2406	GATCTCAGTGGTGGTGGTGGTGGTCTCGAGTATTCTTTTTATTCCAGGGTAG
pIM829	<i>all1409</i> <sub>pp</sub>		2420	GGTATGGATGAATTATATAAACTAGGAGTACTGACCAAAA
			2421	GGTACCCGGGATCCTCTAGATTATTCTTTTTATTCCAGGGTAG
pIM830	<i>all4260</i>		2430	AACGCCACTGCAGGTCGACTATGCTTATTGTAATTCA
			2431	GGTACCCGGGATCCTCTAGCTAGCGCGCAATAGGT
pIM831	<i>atr4788</i>		2432	AACGCCACTGCAGGTCGACTATGGCTAACATAACAACC
			2433	GGTACCCGGGATCCTCTAGTACTCTCCGTCATTATGAC
pIM832	<i>fraD</i>		2423	GGCGGGCTGCAGGTCGACTAATTTATTTAAAGACCTTTTCGG
			2438	GACGTTGTAAAACGACGGCCGAATTTACTGCTGCGGTGGC
pIM836	<i>atr4714</i>		2435	GAGCTCGTACCCGGGATCCTCTGCTGGCGACCAGCT
			2439	AACAGCTATGACCATGATTACGCCAATGTTTTACTGTTAAGCCG
pIM849	<i>atr4714</i>		2519	TCACACAGGAACAGCTATGTTTTACTGTTAAGCCG
			2520	TGATGCGATTGTCATGTTGCTGGCGACCAGCT
pIM850	<i>all4109</i> <sub>opt</sub>	pIM845	2517	GGCGGGCTGCAGGTCGACTACCCGTAGCACCCGATCA
			2518	TGAAAACGACGGCCGAATTTACTTTTTTTGTTCCAAGGC
pIM852	<i>atr4714</i> <sub>Δaa1-57</sub>		2522	GGCGGGCTGCAGGTCGACTCTTTGTGGCGGTTAAT
			2523	TGAAAACGACGGCCGAATTTATGCTGGCGACCAGCTA

Unless stated otherwise, *Anabaena* cells were used as template for PCR; ds, downstream; us, upstream.

Disruption of specific genes was achieved by genomic insertion of the cassette C.K3t4 via double homologous recombination using the shuttle vector pRL277. The cassette encodes for a kanamycin/neomycin resistance under the control of the strong promoter  $P_{psbA}$  and was previously described as C.K3 (Elhai & Wolk, 1988). A translational tandem stop and a transcriptional terminator were C-terminally cloned downstream of the BamHI restriction site and derived from the bacteriophage T4 gene 32 (Krisch & Allet, 1982). The C.K3t4 construct was ordered as a synthetic gene from Eurofins Genomics (Bornikoel, unpublished). For genomic integration, the cassette was flanked by ~800 bp homologous regions up- and downstream (see Table 7) to the integration site. Internal fragments were ligated into the vector pRL277 for single homologous recombination. As a result, the whole plasmid is inserted into the genome.

Insertional mutants were tested for segregation via colony PCR using oligonucleotides up- and downstream of the insertion site. Integration of plasmids in single recombinant mutant strains was verified using an oligo, which binds within the plasmid, and another, which binds up- or downstream of the insertion site. Oligonucleotides used for these PCRs are summarized in Table 8 and agarose gels of segregation PCRs are shown in Appendix 1.

**Table 8: Oligonucleotides used for test on segregation and integration.**

Strain	Oligo	Sequence 5'-3'
DR823	2418	CTTCGGGAATAGGAACAG
	2419	GCTGGTTCTAGCTTGAG
DR825, SR834,	2446	GCTTTGCAGGCGTGAG
SR855	2447	TCGCACTGGACGTTATC
SR834	2446	GCTTTGCAGGCGTGAG
(integration)	890	ACCTATCTCAGCGATCTGTC
DR833, SR835	2444	TGACTGGGAAGGCTTAG
	2445	AGATTCGGCTTGTCAC
SR835	2444	TGACTGGGAAGGCTTAG
(integration)	890	ACCTATCTCAGCGATCTGTC
SR840	2418	CTTCGGGAATAGGAACAG
	2419	GCTGGTTCTAGCTTGAG
SR840	2418	CTTCGGGAATAGGAACAG
(integration)	890	ACCTATCTCAGCGATCTGTC
SR855	2446	GCTTTGCAGGCGTGAG
(integration)	890	ACCTATCTCAGCGATCTGTC
DR814	2347	TATGGCTGGCTCCAAAAG
	2348	CCGTCAAGAGTCCATCAG

### 5.2.3 Triparental conjugation

Triparental conjugation was performed to introduce plasmids (see Table 6) into *Anabaena* sp. using the *E. coli* strains J53 (RP-4) (Wolk et al., 1984) and the cargo plasmid-carrying strain HB101 (pRL825) (Wolk et al., 1984; Sambrook et al., 1989) as described in (Elhai & Wolk, 1988). In short, 50 mL LB cultures with the respective antibiotics were inoculated 1:100 with o/n

cultures of each *E. coli* strain. After growth for 4 h at 37 °C, the two strains were mixed and washed two times with LB medium. The cells were resuspended in 900 µL LB medium and incubated 1 h at 28 °C in the dark. 200 µL of the combined *E. coli* strains were mixed with 200 µL of an exponentially growing *Anabaena* culture and dispersed with glass beads (2.85-3.45 mm, Carl Roth GmbH) on a 0.45 µm HATF filter (Merck Millipore Ltd.) placed on top of a BG11 agar plate without antibiotics. After incubation for 1-3 d under standard growth conditions, the filter was transferred to a BG11 plate supplemented with respective antibiotics.

### 5.3 Light and fluorescence microscopy

To avoid movement of the cells during light and fluorescence microscopy, microscope slides (Menzel Gläser) were coated with agarose. For this, 1 mL of a boiled 2 % agarose solution (w/v in ddH<sub>2</sub>O) was dispersed per slide and dried at RT o/n. For microscopy, 10-15 µL culture was placed on the coated microscope slide.

Light microscopy was performed using a Leica DM2500 B microscope with a Leica DFC420C camera. A 100x/1.3 oil objective of a Leica DM5500 B microscope coupled to a Leica DFC360FX camera was used for fluorescence microscopy. BP470/40 nm and BP535/50 nm filters were used for excitation of GFP and chlorophyll fluorescence, respectively. Emission was detected using a BP525/50 nm or BP610/75 nm filter, respectively. The exposure time was set to 15 ms for bright field images, 50 ms for autofluorescence and 70-150 ms for excitation in the GFP channel.

To perform three-dimensional blind deconvolution with the built-in function of the Leica ASF software (10 iterations), z-stacks with 0.1 µm intervals were taken. To quantify fluorescence signals, each xy pixel of 20 slices of a raw (not deconvoluted) z-stack was summed into one image with ImageJ, and the mean intensity of septal ROIs (regions of interest) was measured. The averaged mean intensity of identical ROIs in the cytoplasm were subtracted from every single septum measurement as background signal. Background-subtracted values were normalized to the average of the background fluorescence.

### 5.4 Immunolocalization

Immunolocalization of FraD and AmiC was performed as described previously (Büttner et al., 2016) with minor changes. Three days old cells grown on BG11 agar plates were resuspended to OD<sub>750</sub>=1 in 1 mL PBS pH 7.4. Cells were washed three times and fixed with 1 mL HistoChoice Tissue Fixative (Sigma-Aldrich) for 10 min at RT and 30 min at 4 °C. After three further washing steps, the cells were washed once with 70 % -20 °C-cold EtOH and again with PBS. To ease accessibility of the cells by the antibodies, cells were incubated for 5 min at RT with 1 mg lysozyme in 1 mL GTE buffer (50 mM glucose, 20 mM Tris-HCl pH 7.5, 10 mM EDTA). Next, cells were resuspended in 200 µL PBS and dropped onto a Polysine slide

(Thermo Fisher Scientific). Cells were dried at RT, rehydrated with 200  $\mu$ L PBS for 5 min and blocked for 20 min using 200  $\mu$ L 2 % (w/v) BSA in PBS.  $\alpha$ -FraD (10  $\mu$ g/mL, see 5.10) or  $\alpha$ -AmiC antibodies (1:500) in BSA-PBS were applied o/n in a wet chamber at 4 °C. AmiC-antibodies were raised against the enzymatic domains of AmiC1 and AmiC2 of *Nostoc punctiforme* (Büttner et al., 2016). However, high sequence similarity of these proteins with *Anabaena* amidases allows the usage in *Anabaena*. The next day, the microscope slides were washed five times with PBS, followed by incubation for 2 h at RT in the dark with FITC-coupled  $\alpha$ -rabbit antibodies (1:200 in BSA-PBS, Sigma Aldrich). After washing and drying, one drop of Vectashield Mounting Medium H-1200 (Vector Laboratories, USA) was applied, covered with a coverslip and sealed with nail polish. Fluorescence microscopy was performed as described above (5.3), using a BP470/40 nm excitation and a BP525/50 nm emission filter for FITC fluorescence. 3D-deconvolution (Leica ASF software) was performed on z-stacks with 0.1  $\mu$ m intervals. Quantification of raw fluorescence data was performed as described in 5.3.

## 5.5 Nitrogen stepdown and staining of heterocysts

Differentiation of heterocysts is triggered by the absence of a combined nitrogen source. The removal of the latter is named nitrogen stepdown. For this, cells growing in nitrate-supplemented BG11 medium were washed three times with BG11<sub>0</sub> medium void of nitrate and resuspended in BG11<sub>0</sub> to the original volume. Heterocyst development was checked at indicated timepoints via light microscopy.

The heterocyst polysaccharide layer was stained by mixing cells in a ratio of 1:200 with a 1.5 % (w/v in ddH<sub>2</sub>O) Alcian Blue solution (McKinney, 1953) and analyzed via light microscopy. Incubation of cells with 0.01 % triphenyl tetrazolium chloride (TCC, in ddH<sub>2</sub>O) for 15-20 min in the dark results in a brownish precipitate in micro-oxic conditions (Fay & Kulasooriya, 1972), which was visualized with light microscopy. The fluorescent dye boron-dipyrromethene difluoride 493/503 (BODIPY, Thermo Fisher Scientific) was used to stain the heterocyst glycolipid layer (Perez et al., 2016). Cells were washed with PBS pH 7.4 and mixed 1:500 with a 1 mg/mL BODIPY stock (in DMSO). Cells were analyzed via fluorescence microscopy in the GFP channel after incubation for 30 min at RT in the dark.

A nitrogen stepdown agar drop assay was performed to check diazotrophic growth of *Anabaena* strains. For this, 3 d old cells were scratched from an BG11 agar plate, washed three times with nitrate-depleted medium and resuspended to OD<sub>750</sub>=10. From this stock, a 10-fold solution series was prepared. 10  $\mu$ L of each concentration were spotted onto BG11<sub>0</sub> and BG11 (as control) agar plates and imaged after growth for 7 d under standard conditions.

## 5.6 Measurement of cell-cell communication

### 5.6.1 Fluorescence recovery after photobleaching (FRAP)

Cell-cell communication was measured based on the fluorescent tracer calcein as described previously (Mullineaux et al., 2008; Merino-Puerto et al., 2011b). *Anabaena* strains were cultivated for 3 d on BG11 agar plates, resuspended and washed with BG11 medium, and were then resuspended in 500  $\mu\text{L}$  BG11 to  $\text{OD}_{750}=1.2$ . The cells were incubated for 90 min at 28 °C in the dark under gentle agitation with 8-10  $\mu\text{L}$  of 1 mg/mL calcein acetoxymethylester (AM) (Chemodex, in DMSO). After three washing steps with fresh medium, another 90 min incubation period followed before 10  $\mu\text{L}$  of the stained cells were spotted onto a thin BG11 agar plate. When the liquid was dried, the agar spot was excised and transferred upside down onto a cover slip. All measurements were performed using a Zeiss LSM 800 confocal microscope (Carl Zeiss AG) with the ZEN 2.3 blue edition software. Images were taken through a 63x/1,4 oil-immersion objective and a 191  $\mu\text{m}$  confocal pinhole to yield a  $\sim 3$   $\mu\text{m}$  z-directed point-spread as described previously (Bornikoel et al., 2017). The 488 nm line (0.2 % intensity) of a 10 mW laser was used to simultaneously excite chlorophyll and calcein. Emission was detected at 650-700 nm and 400-530 nm, respectively. Five pre-bleached images were taken before the laser intensity was shortly increased to 3.5 % in a defined region of 1  $\mu\text{m}$  in diameter to irreversibly bleach calcein fluorescence using the “fast-bleach” option. Fluorescence recovery was captured with images at 1 s intervals over a time of 40-150 s.

Derived time series image stacks were analyzed using the Time Series Analyzer V3 plugin of ImageJ version 1.51j and GraphPad Prism 6 as described previously (Bornikoel et al., 2017). The rate of molecular exchange in the bleached cell ( $c_B$ ) was quantified using the formula  $c_B = c_0 + c_R(1 - e^{-2Rt})$ , which assumes constant fluorescence in neighboring cells, described with the fluorescence recovery rate constant  $R$  (Mullineaux et al., 2008; Merino-Puerto et al., 2011b).

### 5.6.2 FRAP assay after treatment with CCCP or other stress factors

To analyze the gating ability of septal junctions, cells were treated with the protonophore carbonyl cyanide 3-chlorophenylhydrazone (CCCP) prior to FRAP measurements as described in (Weiss et al., 2019). Unless stated otherwise, 50  $\mu\text{M}$  CCCP (in DMSO, Sigma Aldrich), 50  $\mu\text{M}$  DCCD (in DMSO, Sigma Aldrich) or 10 mM  $\text{H}_2\text{O}_2$  was added at the beginning of the second 90 min incubation step during loading the cells with calcein (see 5.6.1). When indicated, cells were then washed three times with fresh medium and incubated for 2.5-3 h at RT in the light. The prepared samples were processed in FRAP measurements as described above. Cells were mixed with the indicated concentration of acetic acid or 200 mM KCl for 5-15 min after the cells were stained with calcein directly prior to FRAP measurements. The

influence of various temperatures was tested by incubating the stained cells at the stated temperature prior to FRAP measurements.

Treatment with CCCP and other stress-inducers led to the appearance of four distinct FRAP responses. Each FRAP experiment was therefore assigned to one of the groups “full recovery” (usual FRAP recovery curve), “slow increase” (delayed and only minimal recovery), “only two” (communication with just one neighbor), and “no communication” (no fluorescence recovery) and represented as fraction of total bleached cells (Weiss et al., 2019).

### 5.6.3 Fluorescence recovery after multiple photobleaches (FRAMP<sub>x</sub>)

In principal, there are no differences between FRAP and FRAMP, except for the bleaching procedure. For bleaching of a region of 1 µm in diameter, the laser intensity was increased to 5 % using the “fast-bleach” option. Bleaching of the same region was subsequently repeated 3, 5 or 10 times. Data were processed and analyzed as described above (5.6.2).

## 5.7 Analysis of the membrane potential, intracellular pH and intracellular Ca<sup>2+</sup>

For analysis of the membrane potential, cells grown for three days on a BG11 agar plate were resuspended in BG11 medium to OD<sub>750</sub>=1.2. The cells were then treated for 90 min either with 50 µM CCCP (in DMSO) or with pure DMSO. As positive control, cells were boiled for 20 min at 99 °C. Next, the samples were incubated for 30 min in the dark with 5 µM of the membrane potential probe Bis-(1,3-dibutylbarbituric acid)trimethine oxonol (DiBAC<sub>4</sub>(3) in DMSO, AAT Bioquest). Cells were imaged with a 100x/1.3 oil objective of a Leica DM5500 B microscope coupled to a Leica DFC360FX camera. YFP fluorescence was excited using an ET500/20x filter and emission was detected with an ET535/30 nm filter.

For comparing the intracellular pH before and after CCCP-treatment, OD-adjusted cells (see above) were incubated for 60 min in the dark with 10 µM of the pH indicator 2',7'-bis(carboxyethyl)-5(6)-carboxyfluorescein acetoxymethyl ester (BCECF AM, in DMSO) (Cyaman Chemical). Afterwards, cells were washed three times with medium and treated with 50 µM CCCP or DMSO as described above. As control, cells were resuspended after washing in 1 M Tris pH 9 or acetic acid was added to a final concentration of 5 mM, respectively. Imaging was performed as described for DiBAC<sub>4</sub>(3) using a 40x/0.75 objective. Additionally, BCECF-emission was measured at 535 nm using a Tecan Spark 10M Reader (Tecan Trading AG) after transferring 200 µL of the samples into a 96 well plate. Excitation was performed at 490 nm and 440 nm, the ratio of the two values was calculated and normalized to stained, untreated cells.

Changes of intracellular Ca<sup>2+</sup> levels were monitored with the fluorescent dye Fluo4 (AAT Bioquest). Cells (OD<sub>750</sub>=1.2) were incubated with 5 µM Fluo4 AM for 1 h in the dark. After three washing steps, cells were treated with 50 µM CCCP or 200 mM KCl for 30 min before

measurement. Alternatively, cells were incubated for further 30 min after washing. Then, cells were supplemented either with CCCP or KCl followed by direct measurement of the fluorescence. For measurement, 200  $\mu$ L of the samples were transferred into a 96 well plate and measured with a Tecan Reader using 488 nm for excitation and 516 nm for emission.

## 5.8 Analysis of the septal nanopore array

### 5.8.1 Isolation of septal peptidoglycan discs

Isolation of septal peptidoglycan (PG) discs was performed after Kühner et al with some changes (Kühner et al., 2014). All solutions were filtered through a 0.22  $\mu$ m PVDF filter (Carl Roth). Cells grown for 3 d on Bg11 agar plates were resuspended in 700  $\mu$ L 0.1 M Tris-HCl pH 6.8. After sonication (Branson Sonifier 250) for 2 min at a duty cycle of 50 % and output control 1, 300  $\mu$ L 10 % SDS were added to the samples. Membranes were melted by incubation of the samples at 99 °C for 30 min under shaking at 300 rpm. The suspension was washed two times with ddH<sub>2</sub>O (5 min, 10000 rpm) and incubated for 30 min in a sonifier water bath (RK100, Bandelin electronic, Berlin). The cell debris were washed with ddH<sub>2</sub>O and resuspended in 1 mL 50 mM Na<sub>3</sub>PO<sub>4</sub> pH 6.8. To digest proteins, the samples were incubated for 3 h with 300  $\mu$ g  $\alpha$ -Chymotrypsin at 37 °C under gentle agitation. Then, the addition of  $\alpha$ -Chymotrypsin was repeated followed by o/n incubation. After heat inactivation of the enzyme for 3 min at 99° C and washing with ddH<sub>2</sub>O, the isolated PG was again sonicated for 30-90 s.

A 10  $\mu$ L sample was mixed with 0.1  $\mu$ L of fluorescent vancomycin (Vancomycin, BODIPY FL conjugate, 100  $\mu$ L/mL in DMSO, Invitrogen) to check the presence and purity of PG septa under a fluorescence microscope (see above). If necessary, the sample was again sonicated and washed before the isolated septa were resuspended in 50-500  $\mu$ L ddH<sub>2</sub>O.

### 5.8.2 Transmission electron microscopy (TEM)

Isolated PG discs were visualized via transmission electron microscopy (TEM) as described before (Lehner et al., 2013). For this, formvar/carbon film-coated copper grids (Science Services GmbH, Munich, Germany) were activated by UV-irradiation for 16 h. Then, 10  $\mu$ L of a septum sample (see above) was dropped onto the grid and incubated for 30 min. Carefully, the liquid was soaked using a filter paper and the grid was washed four times with ddH<sub>2</sub>O. Grid-loaded septa were stained with 1 % (w/v in ddH<sub>2</sub>O) uranyl acetate for 1:30 min. Imaging was performed with a Philips Tecnai10 electron microscope at 80 kV connected to a Rio Camera (Gatan).

Preparation and electron microscopy of ultrathin sections was performed as described previously (Fiedler et al., 1998). Cells were fixed with glutaraldehyde followed by potassium

permanganate and stained with uranyl acetate and lead citrate as described before (Lehner et al., 2013). Imaging with TEM was performed as described above.

### 5.8.3 Septal PG analysis using FIJI scripts

Analysis of transmission electron micrographs of septal PG discs was performed with ImageJ version 1.51j. In order to analyze nanopores and the septum diameter in a fast and little user biased approach, two scripts in the ImageJ Macro language were created and used. For proper functioning of the scripts, it is important to use an ImageJ version including the BioVoxel Toolbox (Brocher, 2015). The scripts and a step by step walkthrough can be found in Appendix 2.

In short, for counting and measuring the nanopores, a region containing the nanopores needs to be selected. Then, a threshold to perform rolling ball background subtraction specific to each image needs to be chosen and applied to yield a binary mask. The selected particles (the nanopores) need to be checked and potentially edited. As result, a list with Feret and MinFeret values for each nanopore is printed. The average of these two values represent the diameter of a nanopore. The second script helps to measure the diameter of the septal disc. At least three lines traversing the septum center and ending at the septum rim need to be drawn to calculate the average diameter.

### 5.9 Statistical analysis

In general, statistical analysis was done with GraphPad Prism version 6.01. Significant difference testing of two groups was performed using an unpaired Student's *t*-test. To compare multiple groups, an ordinary one-way ANOVA followed by Dunnett's multiple comparison test was performed. Significance values *P* are indicated with asterisks: \*:  $P \leq 0.05$ ; \*\*:  $P \leq 0.01$ ; \*\*\*:  $P \leq 0.001$ ; \*\*\*\*:  $P \leq 0.0001$ ; ns (not significant):  $P > 0.05$ .

### 5.10 Co-Immunoprecipitation (co-IP)

Co-Immunoprecipitation (co-IP) was performed to identify proteins that are involved in cell-cell communication using  $\alpha$ -GFP or  $\alpha$ -FraD antibodies coupled to magnetic beads, and FraD as bait. *Anabaena* strains were cultivated in 700 mL BG11 medium with supply of 2 % CO<sub>2</sub> for 7-10 d at 28 °C in constant light. Cells were harvested, washed with PBS pH 7.4 and resuspended in 15/20 mL PBS to OD<sub>750</sub>=15/25 ( $\alpha$ -GFP/ $\alpha$ -FraD co-IP). Some of the samples were crosslinked with 1 % glutaraldehyde for 30 min at RT. For this step, cells were diluted in 30 mL buffer. In one of the  $\alpha$ -GFP immunoprecipitations crosslinking was performed with 0.6 % formaldehyde for 30 min at RT followed by two wash steps and incubation for 10 min with 1 % glutaraldehyde at RT.

Glutaraldehyde-treated cells were washed and resuspended in 20 mL PBS. A protease inhibitor cocktail tablet (cOmplete™, Roche) was added to avoid protein degradation before cells were broken via three passages through a French pressure cell press (SIM-AMINCO, Spectronic Instruments) at 20,000 psi. The samples were centrifuged at 1,780 g for 4 min to get rid of whole cells followed by ultra-centrifugation at 48,000-70,000 g at 4 °C for 1 h. The supernatant was discarded and the membranes were carefully resuspended in either 500 µL Tris buffer (10 mM Tris-HCl, 100 mM NaCl pH 8) for  $\alpha$ -GFP co-IPs or in PBS pH 7.4 for  $\alpha$ -FraD co-IPs. The samples were supplemented with 1 % *N*-lauroylsarcosine and 1 mg/mL lysozyme and incubated for 1 h at RT under gentle rotation to solubilize membranes and to digest peptidoglycan. The supernatant derived after centrifugation at 21,000 g and 4 °C for 25 min was used for co-IP.

Co-IPs with  $\alpha$ -GFP magnetic beads (GFP-Trap®\_MA, Chromotek) were performed following the supplier's instructions. Tris-buffer (see above) equilibrated magnetic beads were incubated with the solubilized membranes for 1:30 h under slow rotation at 4 °C. Elution of bound proteins was achieved by resuspension in 70 µL 2x SDS loading dye in Tris buffer and boiling at 95 °C for 10 min. For  $\alpha$ -FraD co-IPs, Dynabeads™ Protein G (Invitrogen) were coupled to  $\alpha$ -FraD antibodies as suggested by the supplier. A monospecific peptide antibody was raised for 90 d against the peptide sequence NH<sub>2</sub>-IWTGPTANPRGYFLRKSC-CONH<sub>2</sub> in the C-terminal part of FraD (Pineda Antikörper-Service, Berlin). 10 µg purified  $\alpha$ -FraD antibodies were incubated for 10 min at RT with 50 µL of the magnetic beads, followed by incubation for 1:30 h at 4 °C under gentle rotation with 500 µL solubilized membranes. Bound proteins were eluted with 40 µL 50 mM glycine pH 2.8 and 20 µL 6x SDS loading dye. Samples were boiled for 10 min at 70 °C and neutralized with 5 µL 1 M Tris pH 9. Elution fractions were separated via 13 % SDS-PAGE (see 5.11). The gel was stained over night with InstantBlue (Abcam), lanes were excised and sent to the Proteome Center Tübingen for LC-MS/MS analysis. In short, the samples were digested with trypsin and analyzed using a linear 60 min gradient and an Easy-nLC 1200 system coupled to a Q Exactive HF mass spectrometer (Thermo Fisher Scientific, Germany).

Proteins with a  $\geq 100$  times increased abundance in the sample compared to the control were considered as possible candidates. The taxonomic distribution of these proteins was examined using STRING version 11 (Szklarczyk et al., 2019) and HmmerWeb version 2.41.1. Proteins were considered as good candidates for cell-cell communication related proteins, if their taxonomic distribution was similar to the one of FraD, meaning that they were only conserved within filamentous cyanobacteria. The UniProt database (The UniProt UniProt Consortium, 2020) was used to retrieve information about Pfam and InterPro entries.

## 5.11 SDS-PAGE and Western Blot

Proteins were separated via denaturing sodium dodecyl sulfate-polyacrylamide gel electrophoresis (SDS-PAGE) after Laemmli (Laemmli, 1970). If not stated otherwise, protein samples were mixed with SDS-PAGE loading dye (Table 9) to a final concentration of 1x and boiled at 95 °C for 10 min. The separation was performed at 150-200 V for 45-60 min in 1x SDS-PAGE running buffer. BlueStar Prestained Protein Ladder (Nippon Genetics) was used as protein ladder. All buffers and the composition of the polyacrylamide gels are summarized in Table 9. After the run, the gel was either stained for 1 h o/n at RT with InstantBlue Coomassie Protein Stain (Abcam) or processed via Western Blotting.

**Table 9: Buffers for (A) SDS-PAGE and Western Blot and (B) composition of polyacrylamide gels.**

<b>A</b>	Component	Concentration	
5x SDS-PAGE loading dye	Tris-HCl pH 6.8	250 mM	
	SDS	10%	
	glycerol	3%	
	β-mercaptoethanol	5%	
	bromophenol blue	0.02%	
	10x SDS-PAGE running buffer	Tris base	250 mM
		glycine	1.92 M
		SDS	1%
	Friendly Towbin	Tris-HCl pH 8.5	25 mM
		glycine	192 mM
2-propanol		5%	
PBS pH 7.4	NaCl	137 mM	
	KCl	2.7 mM	
	Na <sub>2</sub> HPO <sub>4</sub>	10 mM	
	KH <sub>2</sub> PO <sub>4</sub>	1.8 mM	
PBS-T20	PBS pH 7.4		
	Tween20	0.1%	
Blocking solution	powdered milk	5%	
	PBS-T20		
Washing solution	powdered milk	0.5%	
	PBS-T20		

<b>B</b>	Component	Stacking gel (5 %, 3 mL)	Separating gel (12 %, 10 mL)	Separating gel (13 %, 10 mL)
	ddH <sub>2</sub> O	2.1 mL	3.3 mL	2.96 mL
	Rotiphorese Gel 30 (Carl Roth)	500 µL	4 mL	4.33 mL
	acrylamide/bisacrylamide			
	1 M Tris-HCl pH 6.8	380 µL		
	1.5 M Tris-HCl pH 8.8		2.5 mL	2.5 mL
	10% SDS	30 µL	100 µL	100 µL
	10% APS	30 µL	100 µL	100 µL
	TEMED	3 µL	4 µL	4 µL

To identify specific proteins, semi-dry electroblotting after Towbin et al. (Western Blot) was performed (Towbin et al., 1979). In principal, proteins are transferred from a gel onto a membrane and then detected via specific antibodies. A sandwich of Friendly Towbin-soaked (Table 9) thin and thick Whatman Gel Blotting papers (GE Healthcare), an ethanol-activated and Firendly Towbin equilibrated PVDF membrane (0.45  $\mu\text{m}$  pore size, Carl Roth), a SDS-PAGE gel and again Gel Blotting papers was built. The transfer was performed at 30 V for 30 min. Afterwards, the membrane was transferred into a 50 mL conical Falcon tube and incubated under gentle agitation with 3 mL Blocking solution (Table 9) for 1 h at RT. Next, the membrane was incubated with 1:2000  $\alpha$ -GFP (Sigma Aldrich) or 1:200  $\alpha$ -FraD (animal 1, Pineda Antikörper-Service) in 3 mL Washing solution o/n at 4 °C under gentle agitation. The next day, the membrane was washed three times with Washing solution followed by incubation with 1:10,000  $\alpha$ -rabbit IgG coupled to horseradish peroxidase (Thermo Fisher Scientific) in Washing solution for 2 h at RT. Afterwards, the membrane was washed three times with PBS-T20 and two times with ddH<sub>2</sub>O. Detection was performed using the Lumi-Light Western Blotting Substrate (Roche) and 10 s-3 min exposure with a Gel Logic 1500 Imaging System (Kodak).

## 5.12 Protein expression and purification

Periplasmic parts (pp) excluding the TMDs of both, FraD and All4109, fused to different tags were overexpressed in *E. coli* for purification. For this, plasmids pIM812 (Strep-FraD<sub>pp</sub>), pIM813 (MBP-Strep-FraD<sub>pp</sub>) and pIM827 (His-All4109<sub>pp</sub>) were cloned as described in 5.2.1. MBP-Strep-FraD<sub>pp</sub> was overexpressed in *E. coli* Lemo21 (DE3). *E. coli* Rosetta2 (DE3), which allows the translation of rare arginine codons, was used as expression host for Strep-FraD<sub>pp</sub> and His-All4109<sub>pp</sub>.

For overexpression, two 2 L chicane flasks with 400 mL TB medium each were inoculated to OD<sub>600</sub>=0.05 from o/n LB cultures. The cultures were grown at 37 °C under constant shaking at 140 rpm. Protein expression was induced at OD<sub>600</sub>=0.5-0.6 with 200  $\mu\text{g/L}$  AHT (pIM812) or 0.3 mM IPTG (pIM827, pIM828). The cells were harvested after 3 h at 37 °C (30 °C for MBP-Strep-FraD<sub>pp</sub>) and stored at -80 °C until further processing. Strep-FraD<sub>pp</sub> was only poorly soluble and therefore not processed further.

Frozen cells were resuspended in 30 mL of the respective binding buffer (Table 10) supplemented with 3 u DNase I, 100  $\mu\text{g/mL}$  lysozyme and a protease inhibitor cocktail tablet (cOmplete, Roche) and incubated under slow rotation for 30 min at 4 °C. The suspensions were sonified for three times 2 min at a duty cycle of 50 % and output control 3 (Branson Sonifier 250). After centrifugation for 1 h and 20,000 rpm in a JA-25.50 rotor at 4 °C, the lysates were filtered through a 0.45  $\mu\text{m}$  PVDF syringe filter (Carl Roth GmbH) and purified via affinity chromatography followed by size exclusion chromatography.

**Table 10: Composition of buffers used for protein purification.**

Buffer	Composition	Purification of
Binding buffer 1	20 mM Na <sub>2</sub> HPO <sub>4</sub> pH 8, 500 mM NaCl, 40 Mm imidazole	His-All4109 <sub>pp</sub>
Elution buffer 1	20 mM Na <sub>2</sub> HPO <sub>4</sub> pH 8, 500 mM NaCl, 500 Mm imidazole	His-All4109 <sub>pp</sub>
Binding buffer 2	20 mM Tris-HCl pH 7.4, 200 mM NaCl, 1 mM EDTA, 1 mM DTT	MBP-Strep-FraD <sub>pp</sub>
Elution buffer 2	20 mM Tris-HCl pH 7.4, 200 mM NaCl, 1 mM EDTA, 1 mM DTT, 10 mM maltose	MBP-Strep-FraD <sub>pp</sub>
SEC buffer	50 mM Na <sub>2</sub> HPO <sub>4</sub> pH 8, 150 mM NaCl	all proteins

The lysate containing His-All4109<sub>pp</sub> was then loaded onto a 1 mL HisTrap HP column (GE Healthcare) via a ÄKTApurifier system (GE Healthcare) with a flowrate of 0.8 mL/min. The column was washed with 10 mL Binding buffer 1 before a 0-100 % gradient with Elution buffer 1 (Table 10) over 30 mL was started. Then, the column was washed with 5 mL Elution buffer 1. Fractions of 1 mL were sampled throughout the run. Pooled elution fractions were concentrated to 500 µL using an Amicon Ultra-15 Centrifugal Filter (10 kDa cutoff, Merck KGaA). Size exclusion chromatography (SEC) was performed on a Superdex 75 10/300 column using 1.5 CV SEC buffer (Table 10) as running buffer. The purified protein was stored in 20 % glycerol at -80 °C with a concentration of 25 µM.

The lysate derived from MBP-Strep-FraD<sub>pp</sub> overexpression was loaded onto a 1 mL MBPTrap HP (GE Healthcare) using an ÄKTApurifier with a flowrate of 0.5 mL/min and Binding and Elution buffers 2 (Table 10). Pooled and concentrated (to 2 mL) elution fractions were applied to SEC using a HiLoad 16/60 Superdex 200 pg (GE Healthcare) and SEC buffer. The purified protein was stored in 9 % glycerol with a concentration of 25 µM at -80 °C.

Concentration of purified proteins was measured after Bradford (Bradford, 1976). For this, 1 µL of a protein solution was mixed with 800 µL buffer and 200 µL of a 5x Roti-Quant solution (Carl Roth) in a 1 mL cuvette. The absorbance of the protein-bound dye was measured at 595 nm using a Helios spectrophotometer (Thermo Fisher Scientific). The concentration was determined by comparison to a BSA standard curve.

## 5.13 Protein-protein interaction assays

### 5.13.1 Bacterial adenylate cyclase two-hybrid (BACTH) assay

Heterologous protein-protein interaction in *E. coli* was investigated with the BACTH system following the protocol of Battesti and Bouveret (Battesti & Bouveret, 2012). In principal, two proteins of interest were translationally fused to the T25 and T18 parts of the adenylate cyclase domain from *Bordetella pertussis*, each encoded on a plasmid. The two plasmids were introduced into a adenylate cyclase-deleted *E. coli* strain (BTH101) via electroporation.

Multiple 3 mL LB-cultures containing 0.5 mM IPTG were inoculated with randomly picked transformants and grown at 30 °C o/n. Then, 2 µL of each culture were dropped onto LB agar plates containing 40 µg/mL X-Gal (5-bromo-4-chloro-3-indolyl-β-D-galactopyranoside) and 0.5 mM IPTG or onto MacConkey plates containing lactose (Difco MacConkey Agar). The plates were incubated up to 72 h at 30 °C or 20 °C. Reconstitution of the adenylate cyclase parts is achieved, when the proteins are in close proximity due to interaction. This reconstitution leads to the synthesis of cAMP (cyclic AMP), which in turn regulates the transcription of various genes. The activation of the *lactose* and *maltose* operons can be detected by a colorimetric signal of the colonies on the detection plates. A strain transformed with the two plasmids not coding a protein-fusion served as negative control. For positive control, strongly interacting leucine zipper regions of the GCN4 yeast protein were introduced on the two plasmids. Plasmids created and the combinations used for the BACTH assay are described in Table 6 and Table 13, respectively.

#### 5.13.2 Batch pulldown with purified proteins

Batch pulldown with purified proteins was performed after Scholl et al. with some modifications (Scholl et al., 2020). 500 nM of the two proteins of interest were incubated for 30 min at 28 °C in 100 µL binding buffer (used buffers are summarized in the results section) under gentle shaking. 15 µL of this mixture served as input control. Because the beads were very sticky towards the tube wall and the pipette tip after incubation with the proteins, all binding buffers were supplemented with 0.02 % NP-40. The remaining 80 µL of the protein mixture was added to 5 µL buffer equilibrated Ni-NTA MagBeads (Genaxxon) and incubated for further 15 min. A 20 µL sample of the supernatant was taken to detect unbound protein. After three washing steps with binding buffer, the beads were transferred into a new tube and eluted for 10 min at RT with regular vortexing with 40 µL elution buffer (20 mM Na<sub>2</sub>HPO<sub>4</sub> pH 8, 500 mM NaCl, 500 mM imidazole). All samples were mixed with SDS loading dye, boiled for 10 min at 95 °C and separated via 13 % SDS-PAGE.

#### 5.13.3 Biolayer-interferometry

Biolayer-interferometry (BLI) is an optical analytical method to investigate the interaction between two proteins. Changes in the interference pattern of reflected light from a reference layer and the ligand-bound sensor tip are measured. Interaction of the ligand with an analyte in solution changes the biolayer thickness on the biosensor tip, which can be measured as shift in the interference pattern. BLI was performed with an Octet K2 system (FortéBio). The binding assays were performed either in 50 mM Tris-HCl pH 8.5, 100 mM MgCl<sub>2</sub>, 0.02 % NP-40 or in 1x PBS pH 7.4, 0.02 % NP-40. 50 nM purified His-All4109<sub>pp</sub> (see above) were bound as ligand to Ni-NTA sensor tips (FortéBio), and the baseline was adjusted over 60 s. In a 300-400 s association step, the All4109-bound sensors were incubated in buffer containing either MBP-

Strep-FraD<sub>pp</sub> or MBP (purified by Jan Bornikoel) as control in concentrations of 500 nM or 1  $\mu$ M. Dissociation was monitored for 300 s by putting the sensors in buffer without protein. As further control, sensor tips not loaded with His-All4109<sub>pp</sub> were used.

## 6 Results

### 6.1 Regulation of cell-cell communication

#### 6.1.1 Publication 1: "Structure and Function of a Bacterial Gap Junction Analog"

Chapter 6.1.2 is a summary of the article "Structure and function of a bacterial gap junction analog", which was published in 2019 in *Cell* 178, 374-384.

DOI: <https://doi.org/10.1016/j.cell.2019.05.055>.

References to figures in section 6.1.2 refer to the figures of this publication (hereafter Publication 1). Publication 1 can be found in Appendix 6.

Authors: Gregor L. Weiss,<sup>1,3</sup> **Ann-Katrin Kieninger**,<sup>2,3</sup> Iris Maldener,<sup>2\*</sup> Karl Forchhammer,<sup>2</sup> and Martin Pilhofer<sup>1,4,\*</sup>

<sup>1</sup>Department of Biology, Institute of Molecular Biology & Biophysics, Eidgenössische Technische Hochschule Zürich, Otto-Stern-Weg 5, 8093 Zürich, Switzerland

<sup>2</sup>Interfaculty Institute of Microbiology and Infection Medicine Tübingen, Organismic Interactions, University of Tübingen, Auf der Morgenstelle 28, 72076 Tübingen, Germany

<sup>3</sup>**These authors contributed equally**

<sup>4</sup>Lead Contact

Declaration of personal contribution:

I established a confocal microscopy-based assay through which gating of the cell-cell connections was demonstrated. I designed, performed, analyzed and interpreted all FRAP experiments including FRAP experiments after treatment with CCCP, H<sub>2</sub>O<sub>2</sub>, and incubation in darkness. ATP determination and CCCP/H<sub>2</sub>O<sub>2</sub> recovery assays were performed by me. Furthermore, I designed and cloned the plasmids pIM768, pIM779 and pIM759, and created the *Anabaena* mutant strains CSVT22.768, CSVT2.768 and CSVT2.779. All graphs and figures that show FRAP-data, agar drop assay and ATP data, as well as movie 3 were created by me. Gregor Weiss designed, performed and analyzed ECT data. The manuscript was written by me and Gregor Weiss under the supervision of Prof. Martin Pilhofer, PD Iris Maldener and Prof. Karl Forchhammer. MP, IM and KF considerably contributed to the conceptualization of the study. All authors participated in the revision process. Gregor Weiss and I are equally contributing authors.

### 6.1.2 Septal junctions are three-modular gated cell-cell communication channels

Electron cryotomography (ECT) bridges the resolution gap between light microscopy and X-ray crystallography and therefore is suitable to visualize macromolecular complexes (Celler et al., 2013; Oikonomou & Jensen, 2017). Using ECT, protein complexes can be analyzed in a near-native state, since cells get plunge-frozen in their hydrated form (Oikonomou & Jensen, 2017). Thin lamella of the frozen cells suitable for ECT were obtained via cryo-focused ion beam milling. For this work, ECT was performed by our collaboration partners of the ETH Zurich.

As described in the introduction, cell-cell connecting channels were observed in electron tomograms decades ago (Hagedorn, 1961; Lang & Fay, 1971; Giddings & Staehelin, 1981; Wilk et al., 2011). Unexpectedly, electron cryotomograms revealed a more complex architecture than just cell-cell connecting channels (Publication 1, Figure 1). The PG-traversing tube ended on both sites in a plug-like module embedded in the cytoplasmic membrane. On the cytoplasmic site of the cell, the tube was covered with a five-fold symmetric cap module, which featured lateral openings (Figure 8A). Furthermore, the length of the tubes was variable and adjusted to the thickness of the PG, which implies the involvement of polymerizing protein subunits.

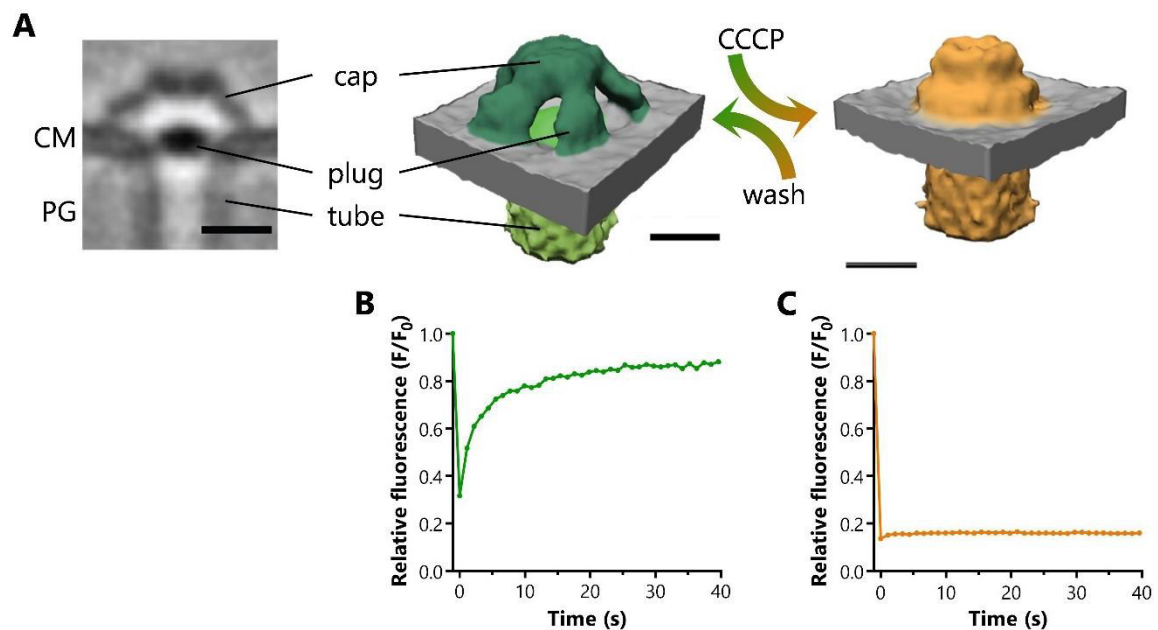


**Figure 8: Gated SJs comprise cap, plug and tube modules.** (A) Subtomogram average of a SJ half derived from ECT with indicated cap, plug and tube modules (left). Surface representation of subtomogram averages of open, untreated SJ (middle) and closed, CCCP-treated SJ (right). Scale bar, 10 nm. (B) Fluorescence recovery curve derived from a FRAP experiment of untreated cells and (C) FRAP response of a CCCP-treated, non-communicating cell. Figure was modified from (Weiss et al., 2019).

The unexpected complexity of SJ architecture and the presence of a cap module suggested an associated function in terms of regulation of cell-to-cell diffusion. Intercellular communication (IC) can be traced in calcein-stained filaments via FRAP experiments (see 3.5). Bleached cells in nitrate-grown WT cultures recovered their fluorescence after photobleaching, as already described earlier (Mullineaux et al., 2008). This finding fits to the observed SJ structures with

openings in the cap structure (Figure 8A, B). To challenge the cells with a stress condition, cells were treated with the protonophore carbonyl cyanide 3-chlorophenylhydrazone (CCCP). CCCP transports protons across the membrane, which causes disruption of both, the membrane potential (Novo et al., 1999) and the proton gradient (Hopfer et al., 1968). The majority of CCCP-treated cells (83 %) did not recover their fluorescence after bleaching, the IC ceased (Figure 8C; Publication 1, Figure 2). The fraction of non-communicating cells was proportional to increasing CCCP concentrations and reached a plateau at 50  $\mu$ M CCCP. In some cells, the fluorescence recovered very slowly or delayed, and only reached low levels compared to the initial fluorescence. This FRAP response was referred to as "slow increase". Occasionally, the bleached cell only exchanged the fluorescent tracer with one neighboring cell, forming the "only two cells" group. ECT analysis of CCCP-treated cells revealed a rearranged SJ cap module (Publication 1, Figure 3) in which the five-fold symmetry as well as the lateral openings were absent (Figure 8A). This closed state was in line with the non-communication phenotype observed in the CCCP-FRAP assay. Ceasing of molecular exchange and conformational rearrangement of the cap structure was also observed when the cells suffered from oxidative stress (addition of hydrogen peroxide) or incubation for 24-28 h in the dark (Publication 1, Figure S7) and was accomplished within a few seconds to minutes after addition of CCCP to the cells (Publication 1, Figure S4). Interestingly, communication was resumed after incubation in protonophore-free medium independently of protein biosynthesis (Publication 1, Figure 2), and the cap module reversed back into the opened state (Publication 1, Figure S4I-L).

Due to macromolecular alteration of cell-cell connections in order to stop cell-to-cell diffusion, these data led to the conclusions that (i) SJs are gated cell-cell connections with functional analogy to eukaryotic gap junctions, (ii) the cap module is essential for the regulation of molecular exchange, and (iii) disruption of the proton motive force is a trigger for SJ closure.

Next, we wondered, if the proteins earlier reported to be involved in cell-cell communication (see 3.5) are structural SJ components. To address this question, mutants in these proteins were investigated physiologically via the established CCCP-FRAP assay and structurally via ECT. Surprisingly, deletion of SepJ did only lead to a slight reduction of SJ closure and the architecture of the few present SJs looked like in the WT (Publication 1, Figure 4). Likewise, the *sjcF1* and *amiC1* mutants did not show an altered gating behavior and the SJs' architecture was identical to WT SJs. We concluded the respective proteins were not structurally involved in formation of SJs, but rather play a coordinator role in nanopore formation. Structural participation of SjcF1 and AmiC1 was also not expected, since SjcF1 was described as regulating factor of nanopore formation (Rudolf et al., 2015) and AmiC1 functions in drilling of the nanopores (Lehner et al., 2013; Nürnberg et al., 2015; Bornikoel et al., 2017).

In contrast, a *fraCfraD* double mutant never showed a “no communication” response in CCCP-FRAP experiments (Publication 1, Figure 5D). Also, the fraction of non-communicating cells upon treatment with CCCP in the *fraC* and *fraD* single mutants was severely reduced compared to the WT. This was a first hint that mutation in both or one of those proteins has a structural influence on SJ formation. Indeed, the inability to cease intercellular exchange was explained by the absence of cap and plug modules in the double and the *fraD* single mutant via ECT (Publication 1, Figure 5A, B). Deletion of *fraC*, however, resulted in a mixed phenotype comprising missing cap and plug modules, deformed caps or WT-like SJs (Publication 1, Figure 5C). We therefore proposed a rather regulatory or coordinating role for FraC in line with a previous suggestion (Merino-Puerto et al., 2011b). Via N-terminal fusion of GFP to FraD, we confirmed FraD as structural SJ component. Cap and plug modules missing in the *fraD* mutant were restored in the GFP-FraD complemented strain and GFP was observed as extension of the plug module inside the tube lumen in an ECT subtomogram average (Publication 1, Figure 6A, B). Additionally, communication in the GFP-FraD strain was almost ten-fold reduced compared to the WT, which could be explained by GFP that occupies a major part of the diffusion area (Publication 1, Figure 6E). Furthermore, the *gfp-fraD* strain did allow closure of SJs upon treatment with CCCP. However, the efficacy of SJ reopening was strongly reduced (Publication 1, Figure 6D).

Taken together, we demonstrated that IC can be abolished upon stress conditions and showed that SJs comprise tube, plug and cap modules. Whereas the role of the plug module remained unclear, the cap is essential for SJ gating by changing its conformation. Additionally, FraD was verified as the first structural SJ component and its deletion led to loss of cap and plug modules, which resulted in inability of SJ gating. The capability to regulate IC renders the cyanobacterial SJs functional analogs to eukaryotic gap junctions and most likely serves as survival strategy in situations when single cells within a filament are disrupted or die.

## 6.2 Mode of action of SJ gating

### 6.2.1 CCCP disrupts the membrane potential and the proton gradient in *Anabaena*

The dual effect of the protonophore CCCP in depolarizing the membrane and impairing the proton motive force was shown before for example in *E. coli*, *Staphylococcus aureus* or in phospholipid bilayers (Hopfer et al., 1968; Novo et al., 1999). To test if CCCP, as applied here, destroys these two processes also in *Anabaena*, cells were stained with the membrane potential probe Bis-(1,3-dibutylbarbituric acid)trimethine oxonol (DiBAC<sub>4</sub>(3)) or with the pH indicator 2',7'-bis-(2-carboxyethyl)-5-(and-6)-carboxyfluorescein (BCECF) and analyzed via fluorescence microscopy.

While the membrane potential is intact, the anionic dye DiBAC<sub>4</sub>(3) cannot pass the cytoplasmic membrane and fluorescence is low. However, upon depolarization of the

membrane potential, the dye enters the cell, which increases its fluorescence. In line with this, boiled *Anabaena* cells exhibited a strong fluorescence signal, because the membrane potential collapsed (Figure 9A). In contrast, most of the mock-treated (DMSO, solvent of CCCP) cells showed no fluorescence signal due to an intact membrane potential. Treatment of cells with CCCP led to influx of the dye and therefore indicated a depolarized membrane potential. Cells that were washed after CCCP-treatment and incubated in fresh medium for 2.5 h, resumed intercellular communication (6.1.2), which implied restored membrane potential. Strikingly, these cells were more fluorescent than mock-treated cells. However, in a part of the cells, fluorescence was less intense than upon treatment with CCCP. This suggested a slow and inhomogeneous redevelopment of the membrane potential.

Similar to calcein acetoxymethylester (AM), the hydrophobic pH indicator BCECF AM penetrates the cell membrane. Intracellularly, the dye is processed into its fluorescent and hydrophilic form by esterases, which prevents its passage out of the cell. The fluorescence of BCECF increases with increasing pH values. Therefore, cells incubated in Tris buffer with pH 9 as positive control showed a bright fluorescence signal (Figure 9B). Overall, the fluorescence was reduced when shortly incubated with 5 mM acetic acid. DMSO-treated cells exhibited a fluorescence intensity between those two controls. Upon treatment with CCCP, most of the cells did not fluoresce, which indicated a reduced intracellular pH ( $\text{pH}_i$ ).

Summed up, this led to the conclusion that, also in *Anabaena*, CCCP dissipates the membrane potential and lowers the  $\text{pH}_i$ . It therefore remained unknown, if the collapse of the membrane potential or changing the  $\text{pH}_i$  or potentially a combination of both served as trigger for SJ closure.

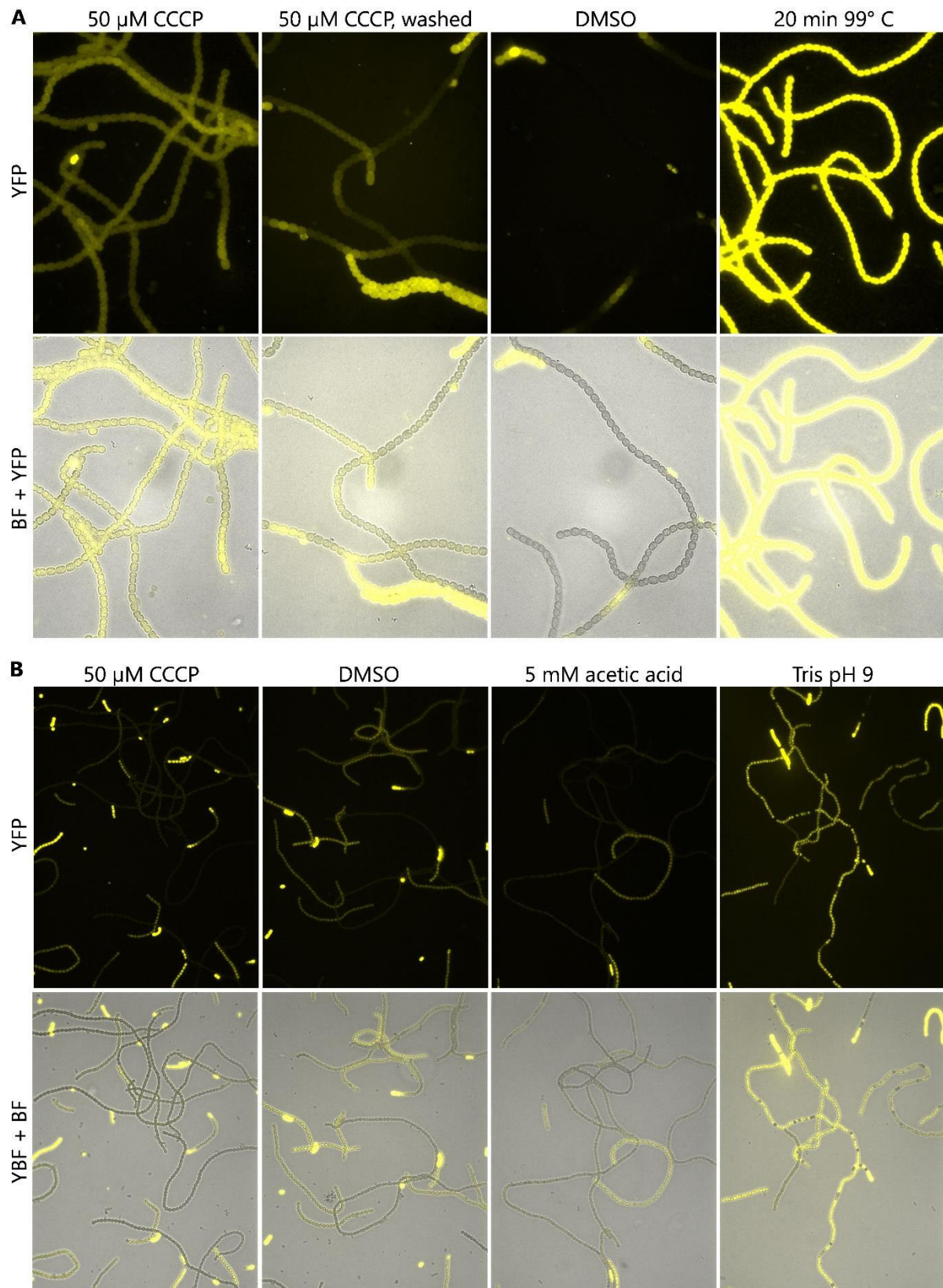


**Figure 9: CCCP impairs the membrane potential and the intracellular pH.** (A) The membrane potential probe DiBAC<sub>4</sub>(3) enters depolarized cells, which increases its fluorescence. Cells were treated as indicated and after staining analyzed via fluorescence and bright field microscopy. Images were taken with a 100x objective. (B) The higher the pH, the higher the fluorescence of the pH indicator BCECF. Stained cells were treated as stated and imaged through a 40x objective. YFP, yellow fluorescent protein channel; BF, bright field channel.

### 6.2.2 Several stress conditions trigger SJ gating

Since CCCP disrupts the membrane potential and at the same time the proton gradient, the actual trigger for SJ closure remained unknown. Also, oxidative stress induced with hydrogen peroxide as well as incubating cells in the dark for 24-28 h led to partly closure of SJs (Weiss et al., 2019). To gain further insights into the regulation of IC, cells were exposed to several stress conditions. Another compound that challenges the proton motive force is *N,N*-dicyclohexylcarbodiimide (DCCD). It is a widely used inhibitor of the F-ATPase, which generates ATP from ADP under usage of the proton gradient. DCCD also depolarizes the membrane potential, probably due to the inhibited proton extrusion (Apte & Thomas, 1986).

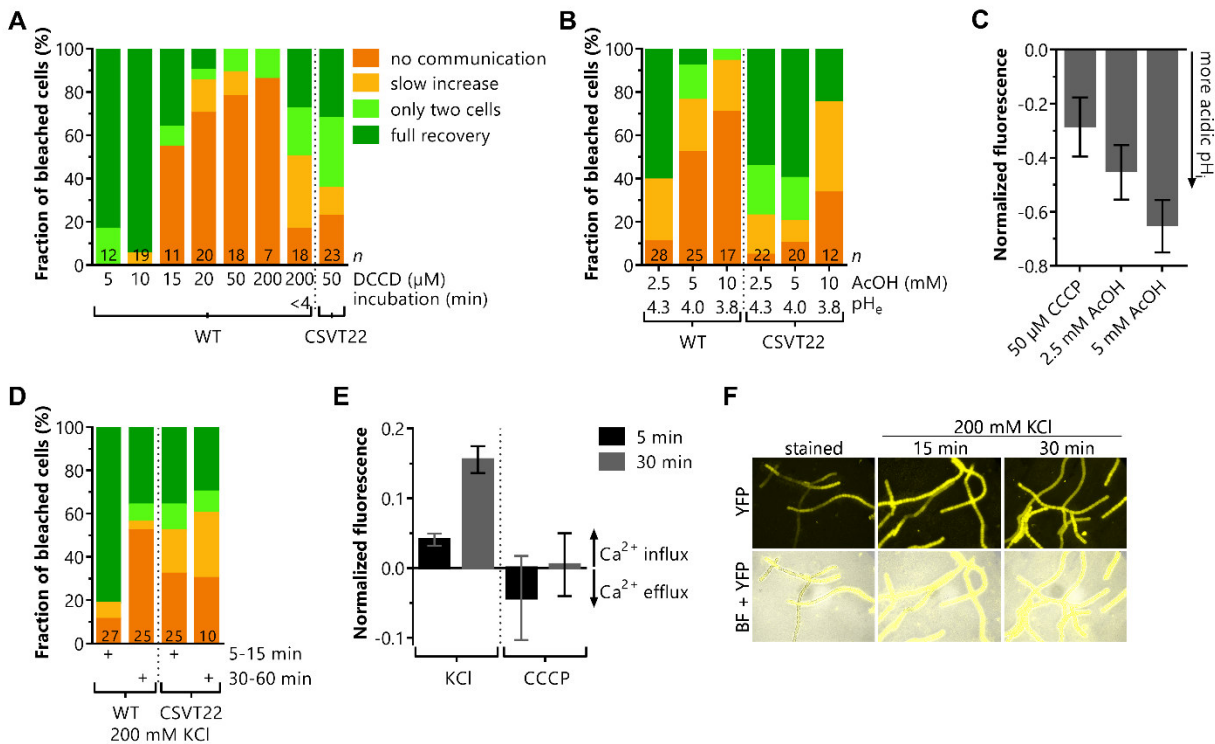


**Figure 10: Changes in the proton motive force impairs intercellular communication.** (A) Cells were treated with the indicated concentrations of DCCD for 90 min prior to FRAP measurements, unless stated otherwise. FRAP responses were assigned to one of the four groups described earlier. CSVT22, *fraDfraD* mutant. (B) Cells were treated with the indicated concentration of acetic acid (AcOH) for 5-15 min directly prior to FRAP measurements. The external pH (pH<sub>e</sub>), which resulted from the treatment is stated below. Color scheme is identical to A. (C) Changes of the pH<sub>i</sub> were monitored by pH-dependent fluorescence of cells stained with the fluorophore BCECF. Stained cells were treated like indicated for 10 min before emission at 535 nm was measured. A ratio of excitation at 440 nm over 490 nm was calculated and normalized to untreated, stained cells. Negative values indicate a more acidic pH<sub>i</sub>. (D) Cells were treated with 200 mM KCl for the indicated time prior to FRAP measurements. Color scheme is identical to A. (E) Changes of intracellular levels of Ca<sup>2+</sup> upon treatment with 200 mM KCl or 50 μM CCCP for 5 min or 30 min were monitored via the fluorophore Fluo4. The fluorescence intensities were normalized to untreated, stained cells. Fluo4 has an enhanced fluorescence upon intracellular binding to Ca<sup>2+</sup> ions. (F) The membrane potential before and after treatment with 200 mM KCl was visualized with the fluorophore DiBAC<sub>4</sub>(3). A collapsed membrane potential causes higher fluorescence of the dye.

IC of WT cells was severely impaired upon treatment of the cells with concentrations above 10 μM DCCD for 90 min (Figure 10A). Interestingly, the effect of DCCD on molecular exchange was slower than with CCCP. After incubation for 4 min with DCCD, only 17 % of

the cells showed a “no communication” response (Figure 10A), whereas 54 % did upon CCCP-treatment (Publication 1, Figure S4I). IC was also affected in the *fraCfraD* mutant CSVT22 upon a 90 min DCCD treatment to a level similar to the 4 min treatment of WT cells. Since no alteration of ATP-levels were observed after treatment of the cells with CCCP (Publication 1, Figure S3D), influence of the energy state on SJ gating was excluded (Weiss et al., 2019). Therefore, inhibition of cell-to-cell diffusion by DCCD is probably related to secondary harms like depolarization of the membrane potential. This could also explain the slower reaction of the cells to stop intercellular diffusion compared to the rapid action of CCCP.

CCCP transports protons across membranes and thereby acidifies the  $\text{pH}_i$  (see Figure 9B). Therefore, the influence of 5-15 min incubation with 2.5-10 mM acetic acid (AcOH) on intercellular diffusion was investigated as a further stress condition (Figure 10B). Indeed, the fraction of non-communicating cells increased with increase of AcOH molarity and therefore with acidification of the medium. Compared to the WT,  $\Delta\text{fraCfraD}$  cells (CSVT22) were less impaired in communication, especially below 10 mM AcOH. Treatment with AcOH indeed lowered the  $\text{pH}_i$  compared to untreated cells, which was confirmed by using the fluorophore BCECF (Figure 10C). A more acidic  $\text{pH}_i$  resulted from treatment of the cells with AcOH than with CCCP, indicated by a lower fluorescence of the fluorophore. Strikingly, however, the majority of CCCP-treated cells showed a non-communication phenotype because of SJ closure, whereas only 11 % did when exposed to 2.5 mM AcOH. This might be a hint, that disruption of the membrane potential has a higher impact on triggering SJ closure.

As a further stress condition, cells were challenged with a high concentration of potassium ions in the medium. This was described to depolarize the membrane as a result of  $\text{Ca}^{2+}$ -influx (Thermo Fisher Scientific, 2021). Therefore, the cultures were supplemented with 200 mM KCl for either 5-15 min or 30-60 min. In the WT, longer incubation with an increased potassium concentration led to a “no communication” response in FRAP measurements in about 52 % of analyzed cells (Figure 10D). In contrast, after short incubation times, this number dropped to 11 %. However, even the short potassium treatment impaired IC in the strain CSVT22. Sixteen to 30 % of the cells ceased communication, but a large fraction of cells showed a “slow increase” response after bleaching. The negative effect of potassium on IC might therefore be of SJ-independent nature. Changes of the intracellular calcium levels upon treatment of cells with either KCl or CCCP were monitored via the fluorophore Fluo4. The fluorescence emitted by Fluo4 increases upon binding to  $\text{Ca}^{2+}$ . Stained cells were again treated with KCl or CCCP and the fluorescence was compared to non-treated cells. As shown in Figure 10E, KCl-treatment led to an enhanced fluorescence, which increased with incubation time, and therefore suggested an elevated level of intracellular  $\text{Ca}^{2+}$ . In comparison, intracellular  $\text{Ca}^{2+}$  levels were not altered after incubation with CCCP, regardless of the incubation time. As suggested previously, treatment of cells with KCl indeed depolarized the membrane potential. This was verified with the fluorophore DiBAC<sub>4</sub>(3), which showed an increased fluorescence in

KCl-treated compared to untreated cells (Figure 10F). Albeit the membrane potential was depolarized, only half of the WT-cells ceased intercellular communication. This argues for a combined action of membrane potential and proton gradient to induce SJ closure.

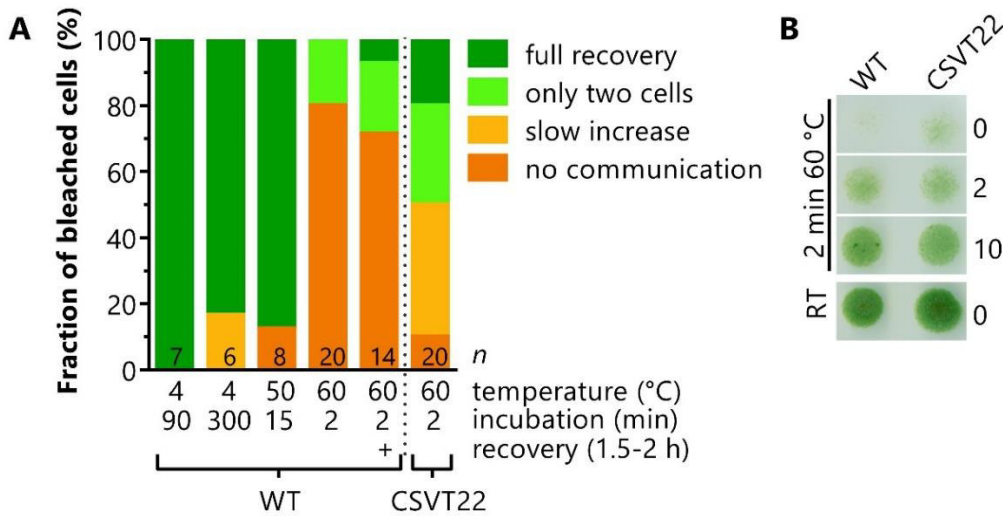


**Figure 11: Influence of temperature on SJ gating.** (A) Calcein-stained cells were incubated at 4 °C, 50 °C or 60 °C for the indicated time prior to FRAP measurements. (B) 10  $\mu$ L of the 60 °C samples were spotted onto a BG11 agar plate to check for viability. Numbers on the right indicate concentration of the sample. 0 times concentrated equals OD<sub>750</sub>=1.2 used for FRAP experiments. Image was taken after incubation under normal growth conditions for three days. CSVT22, *fraCfraD* mutant.

Since cyanobacteria are exposed to varying temperatures in nature, influence of temperature on SJ gating was investigated. For this, calcein-stained cells were incubated at a specific temperature for a defined time period before FRAP experiments. However, incubation of the cells at 4 °C for up to 5 h did not trigger closure of SJs (Figure 11A), although decrease of the membrane potential at 4 °C was reported as result of inhibited Na<sup>+</sup>-influx in other *Anabaena* species (Reed et al., 1981; Apte & Thomas, 1986). Also, 15 min exposure to 50 °C only led to a “no communication” response in about 13 % of the analyzed cells and incubation at 40 °C did not have any effect (data not shown). Two minutes at 60 °C was sufficient to induce a no-communication FRAP response in 80 % of analyzed WT cells, whereas only 10 % of CSVT22 cells ( $\Delta$ *fraC* $\Delta$ *fraD*) ceased intercellular exchange completely. However, recovery of the cells after the heat shock for 1.5-2 h did not restore cell-cell communication (Figure 11A). Therefore, interruption of diffusion might be an indirect effect caused by denatured SJ cap proteins. In order to verify that cells were still alive after the heat shock, 10  $\mu$ L of cells incubated for 2 min at 60 °C were spotted onto a BG11 agar plate and incubated for three days under normal growth conditions (Figure 11B). In comparison to cells incubated at RT (bottom panel), heat-treated cells were severely reduced in growth. Either a fraction of the cells died due to the temperature shift or growth was slowed down, because denatured proteins had to be resynthesized.

### 6.2.3 SJ gating is not synchronized within cells in a filament

As described above (6.1.2), SJs regulate the diffusion of molecules between cells via gating. In the previous performed FRAP experiments, the whole culture was exposed to the respective stress. However, filament fragmentation or predation of filaments from one end at first affects single cells of the organism. Is IC regulated on the cellular level or is SJ gating synchronized within a whole filament? To address this question, mechanical disruption of a single cell with a glass needle (200 nm, 1  $\mu$ m or 2  $\mu$ m in diameter) coupled to a microinjection device was attempted. To do so, *Anabaena* cells needed to be fixed on a glass slide in a living state. Different compounds used for cell attachment were tested: agar, gelatin, polyethylenimine, poly-L-lysine and 3-aminopropyl triethoxysilan (APTES). However, when a cell fixed with any of those compounds was touched with the glass needle, the filament moved instead of the cell was crushed. In conclusion, none of these coatings were feasible to tightly fix the cells. Thus, this approach to mechanically disrupt single cells was not successful.

Instead, an altered FRAP experiment was established and named FRAMP (fluorescence recovery after multiple photobleaches). A single cell was stressed via multiple, sequential photobleaches and the recovery of fluorescence in the bleached and the adjacent cells was monitored (Figure 12A). Resulting FRAMP responses were assigned to one of the four groups described before. Additionally, a response named “abnormal recovery” appeared in some of the WT cells. The fluorescence recovery curve of responses assigned to this group was reminiscent to two successive “full recovery” curves (Figure 12B, yellow-green dotted line). In some cases, the first part of the curve was missing and full recovery took place after 30-50 s after the last bleach. None of the analyzed *fraCfraD* mutant cells showed this abnormal recovery.

When cells were bleached five times in a row, only 24 % of WT cells, but 76 % of *fraCfraD* mutant cells showed a “full recovery” response of fluorescence (Figure 12C). After ten bleaches, almost none of the WT cells showed a “full recovery” response, whereas still 65 % of mutant cells did. About 20 % of five or ten times bleached WT cells showed an abnormal recovery of fluorescence. The increasing fraction of non-communicating cells with increasing number of bleaches in the WT but not in the *fraCfraD* mutant suggested, that multiple bleaching is sensed as stress by the cell. In order to investigate if just the SJs of the bleached cell or also SJs of neighboring cells closed, the neighboring cells of cells in the “no communication” group (marked with  $\blacklozenge$  in Figure 12A) were analyzed via FRAP (Figure 12C,  $\blacklozenge$ ). The majority (86 %) of cells adjacent to multiple bleached cells showed a “full recovery” response. This led to the suggestion, that closure of SJs is not synchronized within a filament, but decided on the single cell level.

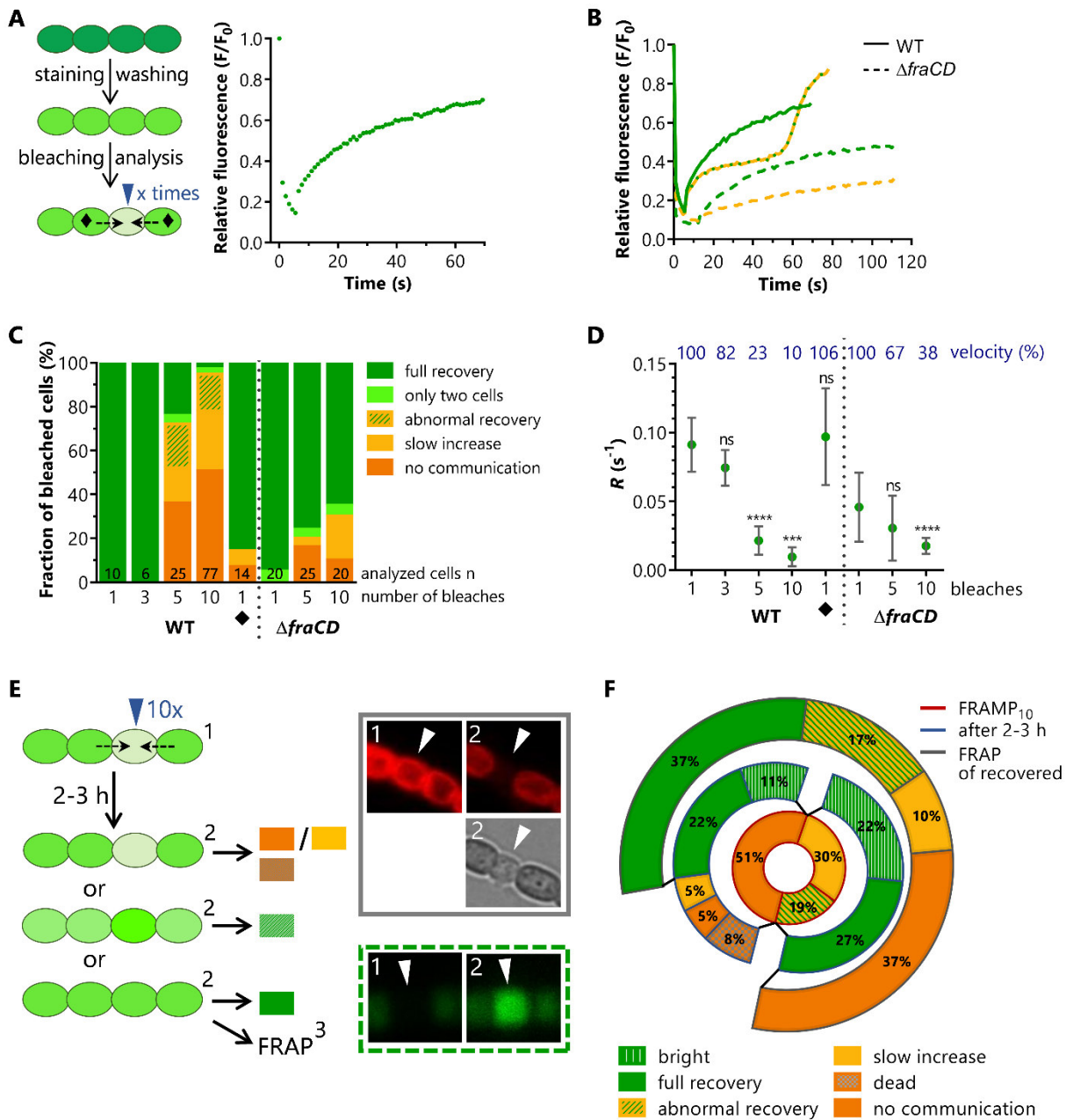


**Figure 12: FRAMP experiments revealed unsynchronized SJ closure.** (A) Experimental outline of the FRAMP (fluorescence recovery after multiple photobleaches) experiment. Cells were stained with calcein as described for FRAP experiments. Then, a single cell was bleached either 3, 5 or 10 times before recovery of the fluorescence was monitored. Adjacent cells are marked with  $\blacklozenge$ . (B) Representative fluorescence recovery curves of “full recovery” and “abnormal recovery/slow increase” responses after 5 bleaches (WT, solid curves) or 10 bleaches (mutant, dotted curves), respectively, are shown. (C) Cells with the indicated number of bleaches were assigned to one of five groups depending on their response after the last bleach. Shown are cumulated results from three independent experiments. Additionally, FRAP was performed on the cells adjacent to the ten times bleached ones ( $\blacklozenge$ ). (D) The fluorescence recovery rate constant  $R$  was calculated for cells showing a “full recovery” response. The relative velocity compared to one time bleached cells is indicated in blue.  $\blacklozenge$ , adjacent cells. (E) Experimental outline of the FRAMP reversibility experiment. After FRAMP<sub>10</sub> (1), the cells were incubated for 2-3 h on the microscopic slide. Then, the fluorescence in the previously bleached cell was checked and assigned to one of the indicated groups (2). Fully recovered cells were investigated by normal FRAP (3). Representative images of newly arising groups “dead” (top) and “very bright” (bottom) are shown. (F) Cumulated results of two independent FRAMP reversibility experiments. The inner circle (red border) shows the distribution of FRAMP<sub>10</sub> responses (step 1 in E). The middle circle halves (blue border) depict the status of beforehand non-communicating (left) or slowly recovering (right) cells after 2-3 h incubation (step 2 in E). The outer circle (grey border) summarizes FRAP responses of recovered cells (step 3 in E).

Figure 12D shows the fluorescent recovery rate constant  $R$ , which was calculated for bleached cells that showed a “full recovery” response. Interestingly, higher numbers of bleaches led to a reduced velocity of fluorescence recovery. This effect was more pronounced in the WT compared to the mutant: Whereas the mutant communicated with 67 % of total velocity after 5 bleaches, the WT only recovered with 23 % of total velocity. An explanation could give the fact that during repeated bleaching, the neighboring cells already lose some of their fluorescence to the bleached cell. After the last bleach, more cells than just the bleached cell is less fluorescent as at the start of the experiment. The bleached cell gets its fluorescence from its neighboring cells, but also the neighboring cells and the neighboring cells of these need to recover. As a consequence, the recovery rate of the initial bleached cell may be reduced. This effect might be less severe in the mutant, because its filaments are much shorter.

Since denaturing of septal proteins due to repeated bleaches with a high intensity laser could not be excluded, the reopening of SJs after a 2-3 h incubation period was examined. The experimental outline of this analysis is depicted in Figure 12E. The fluorescence level of ten times bleached WT cells was checked after 2-3 h incubation on the agar pad on the microscope slide. According to their fluorescence level, cells were assigned to one of the before mentioned groups. Some cells were dead after the incubation time, which was visible in bright field and the autofluorescence channel. The group “bright” comprises cells that showed a higher fluorescence as the neighboring cells (Figure 12E).

The result of the reversibility experiment is shown in Figure 12F. Half of the cells that showed a “no communication” response after FRAMP<sub>10</sub> (Figure 12F, inner circle with red border) recovered their fluorescence during the 2-3 h incubation time (green part of middle circle, left). This suggests, that initial closure of SJs after the repetitive bleaching was indeed reversible in a fraction of cells. Further 11 % of the cells showed a brighter fluorescence as their neighboring cells and were therefore assigned to the group “bright”. The reason for this uneven distribution of fluorescence is elusive. The fluorescence level of all cells that were assigned to the “slow increase” or “abnormal recovery” group after FRAMP<sub>10</sub> (inner circle), showed a fully recovered or very bright fluorescence (middle circle, right). In the next step, cells that had fully or brightly recovered their fluorescence after the incubation period were investigated by normal FRAP (outermost circle, grey border). About 40 % of those cells showed a “full recovery” response after the single bleach. Therefore, SJs of those cells were still able to gate after recovering from the repetitive bleaching. This led to the conclusion, that FRAMP<sub>10</sub> is a suitable method to study synchronization of gating. Nevertheless, cells that showed a bright fluorescence after an incubation period following FRAMP<sub>10</sub> did never fully recover in FRAP.

In summary, the experiment showed that SJ closure is a decision on the cellular level and not synchronized within the cells in a filament.

### 6.3 Impact of FraD domains on cell-cell communication

#### 6.3.1 Creation of partly complemented *fraD* mutants

As part of this work, the septal protein FraD was confirmed as structural SJ protein with localization to the plug module (see 6.1.2, (Weiss et al., 2019)). Disruption of *fraD* led to SJs without plug and cap modules. To gain deeper insight into the role of FraD in SJ formation, a *fraD* mutant was complemented with various parts of FraD.

Secondary structure predictions ascribe five transmembrane domains (TMDs) to FraD. The C-terminal part of the protein stretches into the periplasm (Merino-Puerto et al., 2011b), whereas the N-terminus of FraD was observed in the SJ tube lumen (Weiss et al., 2019). Based on these data, Figure 13A shows a projection of FraD onto a SJ ECT subtomogram average. In the following, the impact of the transmembrane part (TM), only the first two TMDs (2TM), and the periplasmic part (pp) of FraD on communication, gating and diazotrophic growth (not for FraD<sub>2TM</sub>) was investigated. Therefore, the *fraD* mutant strain CSVT2 was complemented with either full-length *fraD* (CSVT2.768), *fraD*<sub>TM</sub> (CSVT2.769), *fraD*<sub>2TM</sub> (CSVT2.837) or *fraD*<sub>pp</sub> (CSVT2.824) (Figure 13B). All introduced genes were encoded on a self-replicating plasmid under the control of the native *fraCDE* operon promoter. To ensure periplasmic localization of FraD<sub>pp</sub>, a Tat signal sequence was cloned upstream of *fraD*<sub>pp</sub>.

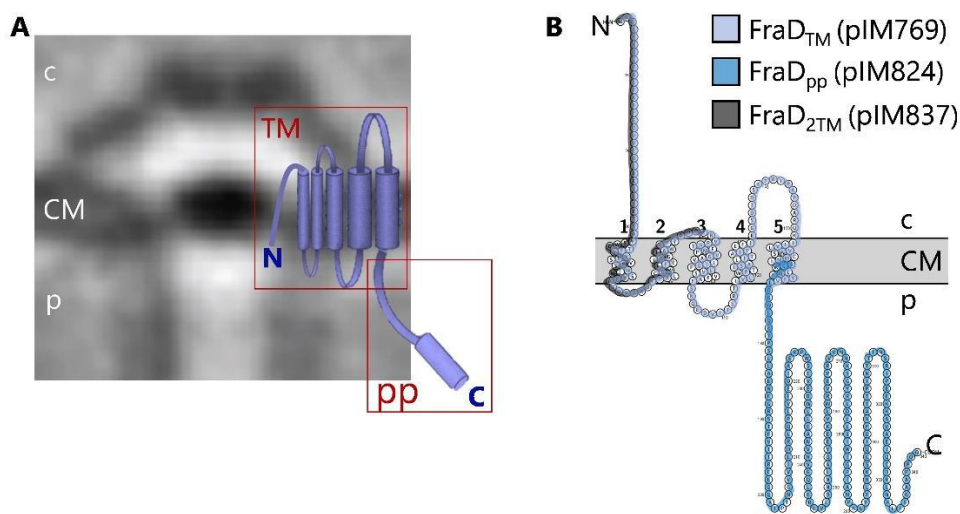


**Figure 13: Projection of the secondary structure of FraD.** (A) The predicted secondary structure of FraD is projected onto a SJ ECT subtomogram average. FraD comprises a transmembrane part (TM) and a periplasmic part (pp). The N-terminus faces the SJ tube lumen, whereas the C-terminal part reaches into the periplasm. Representation of FraD was modified from (Mariscal, 2014), the SJ average was modified from (Weiss et al., 2019). (B) Parts of FraD used for partial complementation of the *fraD* mutant are marked. The structure was predicted and illustrated using Protter (Omasits et al., 2013). CM, cytoplasmic membrane; c, cytoplasm; p, periplasm.

#### 6.3.2 Characterization of *fraD* mutants in view of communication and nanopore array

As described above (6.1.2), most cells of the *fraD* mutant communicated despite treatment with CCCP, because only the SJ tubes were present (Weiss et al., 2019). To investigate the impact of either the transmembrane part or the periplasmic part of FraD on gating, the partly

complemented *fraD* mutants (see 6.3.1) were analyzed via CCCP-FRAP experiments (Figure 14A). As a positive control, the mutant complemented with full-length *fraD* was included and proved a proper expression of the plasmid-encoded gene due to WT-like gating. Interestingly, SJ closure could be restored when *fraD<sub>TM</sub>* was introduced, but resumption of communication after removal of CCCP was highly impaired. In contrast, expression of *fraD<sub>pp</sub>* did not restore the gating ability in comparison to the *fraD* mutant. From this, a function of FraD<sub>pp</sub> in SJ reopening could be hypothesized, whereas FraD<sub>TM</sub> seemed to be important for cap recruitment and therefore closure of SJs.

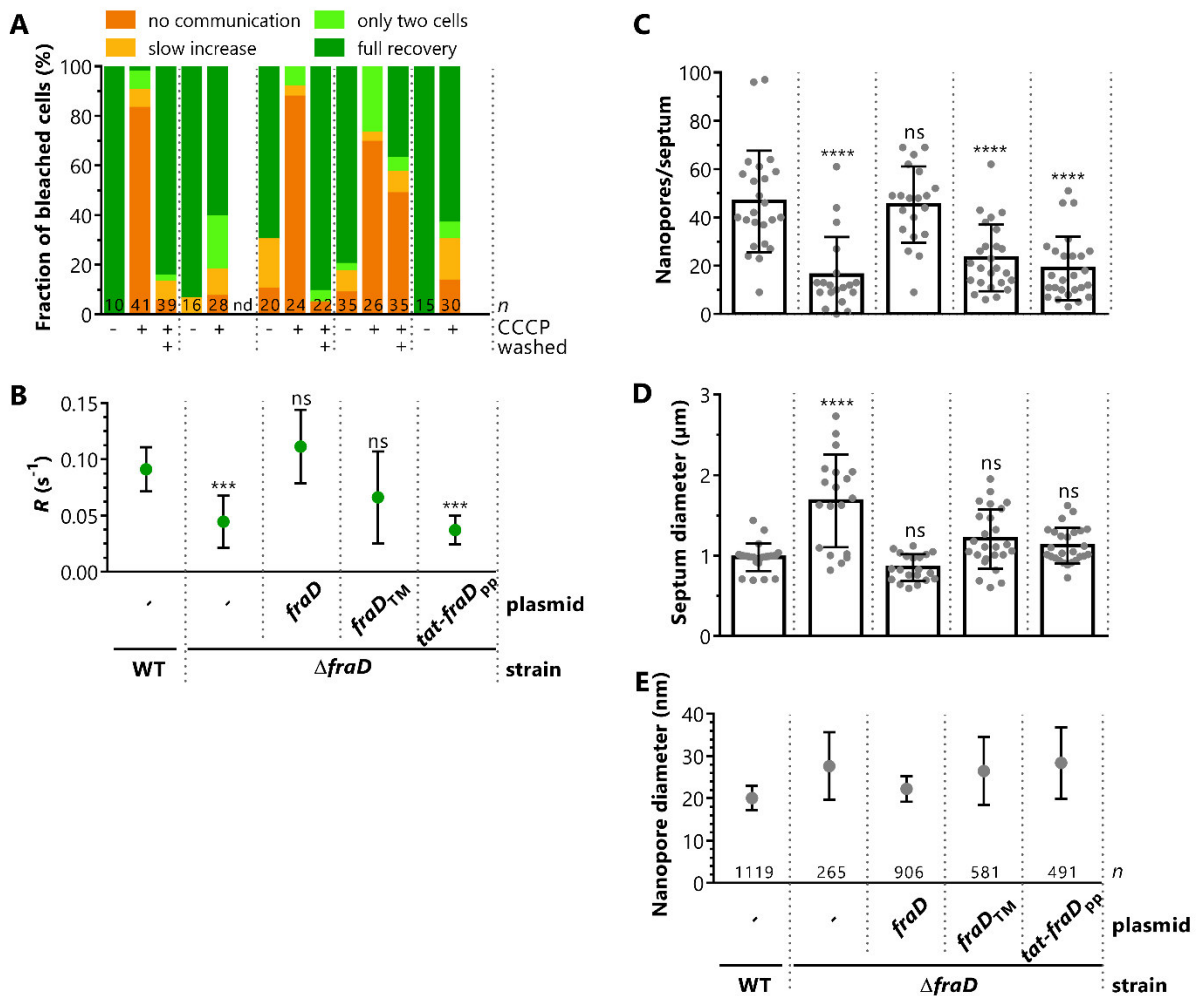


**Figure 14: Impact of FraD domains on intercellular communication and the nanopore array.** (A) SJ gating was investigated via a CCCP-FRAP assay in the mutants indicated in B. The FRAP responses were assigned to one of the indicated groups and depicted as fractions of total. Cumulated results of at least two independent cultures are shown. The numbers in the bars indicate the number *n* of analyzed cells. Data for WT, the *fraD* mutant and the mutant complemented with *fraD* was taken from Weiss et al. (2019). (B) The fluorescence recovery rate constant was calculated of cells assigned to the “full recovery” group and compared to the WT. (C-E) Purified septal PG discs were imaged with a transmission electron microscope to analyze the nanopore array. Strains are indicated in E. (C) Nanopores per septum were counted. Each grey dot represents an analyzed septum (*n*=14-25). (D) The septum diameter was measured for *n*=14-25 septa. (E) The diameter of each single pore was measured. Shown is the mean of all nanopores from all analyzed septa. The number *n* of nanopores is stated at the bottom of the graph.

Next, the fluorescence recovery rate constant was calculated for fully recovering, untreated cells and is shown in Figure 14B. Complementation of the *fraD* mutant with *fraD<sub>TM</sub>* led to a

communication rate between WT and the mutant. No significant differences of  $R$  to the WT, nor to  $\Delta fraD$  was observed because of the large standard deviation in the  $fraD_{TM}$  strain. Expression of  $fraD_{PP}$  did not lead to an accelerated communication rate in comparison to the  $fraD$  mutant. These results suggested an impact of FraD<sub>TM</sub> but not of FraD<sub>PP</sub> on communication.

Since the communication rate is dependent on the amount of nanopores per septum, septal PG discs were purified and imaged with a transmission electron microscope (TEM) to check, if the somewhat enhanced communication rate in the  $fraD_{TM}$  strain is caused by more nanopores. Whereas the  $fraD$  mutant showed significantly less nanopores, complementation of the latter with  $fraD$  restored a WT-like nanopore array (Figure 14C). Strikingly, neither the transmembrane nor the periplasmic part of FraD alone could restore the nanopore array. Although no significant difference in the number of nanopores between  $\Delta fraD$  and the partly complemented mutants was detected, the mean of nanopores in the  $fraD_{TM}$  strain was enhanced. This fits to the somewhat increased recovery rate constant observed for this strain. The septum diameter in the absence of FraD was highly enlarged compared to the WT (Figure 14D). This phenotype was rescued by both partly complemented strains, whereas the nanopore diameter was similarly to the  $fraD$  mutant enlarged (Figure 14E).

Taken together, these results suggested an essential role for FraD<sub>TM</sub> in SJ closure and therefore, probably in plug formation and cap recruitment. Since SJ reopening did not occur when complemented with  $fraD_{TM}$ , a role of FraD<sub>PP</sub> in this process might be possible. For proper formation of the nanopore array full-length FraD seemed to be important. Nevertheless, restriction of the septum was achieved in the presence of either part of FraD.

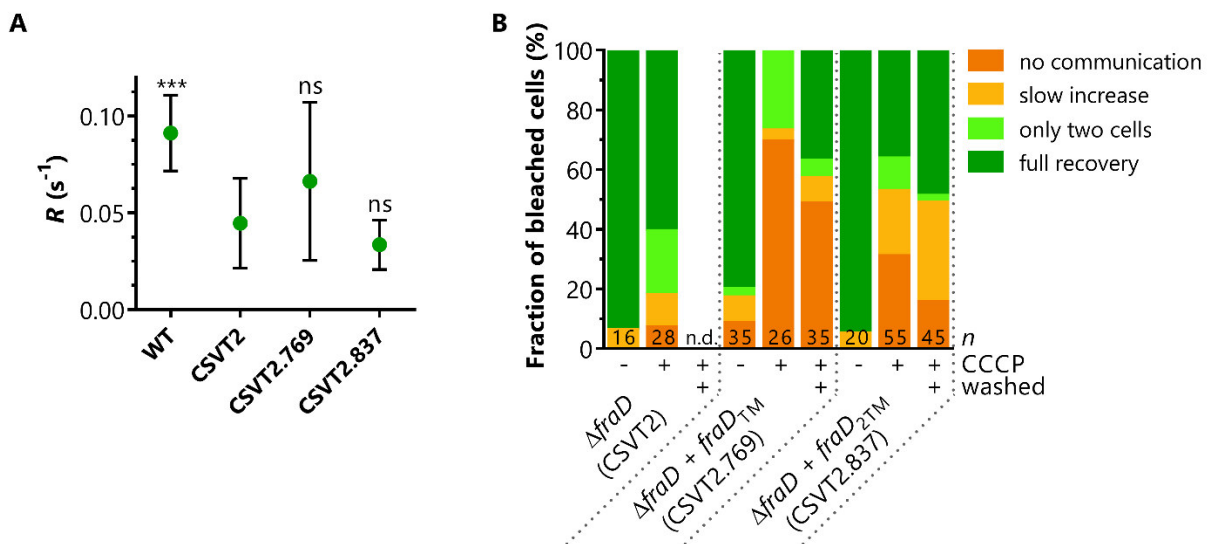


**Figure 15: Cell-cell communication in the  $fraD$  mutant complemented with FraD<sub>2TM</sub>.** (A) The fluorescence recovery rate constant  $R$  was not altered upon complementation of CSVT2 with pIM837 ( $fraD_{2TM}$ ). Significance was calculated in comparison to CSVT2. (B) CCCP-FRAP assay showed 31 % non-communicating cells in strain CSVT2.837 upon CCCP-treatment and an increased fraction of the “slow increase” group compared to CSVT2 and CSVT2.769 ( $fraD_{TM}$ ).

As shown above, FraD<sub>TM</sub> is sufficient to allow closure of SJs upon treatment of the cells with CCCP (Figure 14A). In order to further investigate the impact of the five transmembrane domains, the *fraD* mutant was complemented with only the first two TMDs of FraD (FraD<sub>2TM</sub>, strain CSVT2.837, see Figure 13B). The rate of IC resembled the *fraD* mutant and was lower than in the presence of all TMDs (CSVT2.769, Figure 15A). Furthermore, SJ closure upon CCCP-treatment was reduced by 38 % in comparison to the *fraD*<sub>TM</sub> strain (Figure 15B). Nevertheless, a larger fraction of cells ceased communication in comparison to the full mutant and the fraction of cells assigned to the “slow increase” group was increased. Similar to the *fraD*<sub>TM</sub> strain, reopening of SJs was impaired in CSVT2.837.

In conclusion, just the first two TMDs of FraD allowed approximately one third of the cells to stop IC upon CCCP-treatment, whereas the rate of communication was uninfluenced. It could therefore be speculated that the C-terminal part of FraD interacts with other proteins to establish the nanopore array, whereas the N-terminal part of FraD is important for formation of the plug module and therefore probably cap recruitment.

### 6.3.3 Characterization of *fraD* mutants in view of diazotrophic growth

The *fraD* mutant differentiates some heterocysts with reduced nitrogenase activity, but cannot grow diazotrophically (Bauer et al., 1995; Merino-Puerto et al., 2010). Because cell differentiation is strongly influenced by the interconnected process of cell-cell communication, a role for FraD in heterocyst differentiation was suggested to be rather indirect (Merino-Puerto et al., 2010). Expression of FraD<sub>TM</sub> in the  $\Delta$ *fraD* background led to a communication rate between the full mutant and the WT and restored closing of SJs upon CCCP-treatment (see 6.3.2). To check if the partially restored gating was sufficient to allow diazotrophic growth and heterocyst differentiation, a drop plate assay after nitrogen-stepdown was performed.

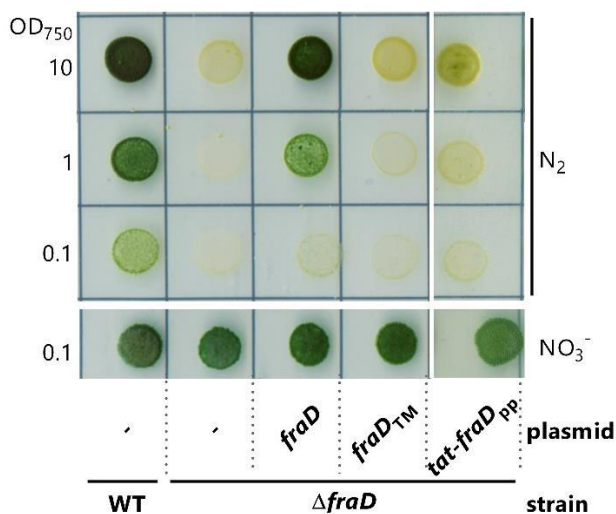


**Figure 16: Partly complemented  $\Delta$ *fraD* strains cannot grow diazotrophically.** Nitrate-grown cultures were washed with nitrate-depleted medium, resuspended to OD<sub>750</sub>=10 and spotted as serial 10-fold dilutions on a BG11<sub>0</sub> agar plate. As a control, the strains were also grown on a plate supplemented with nitrate (bottom lane). The image was taken after 7 d incubation under standard growth conditions.

Cells grown under standard conditions were washed with medium depleted of nitrate and spotted onto an agar plate without a source of combined nitrogen. The plate was imaged after seven days and is shown in Figure 16. The mutants expressing either FraD<sub>TM</sub> or FraD<sub>PP</sub> did not survive when solely dependent on atmospheric nitrogen, although communication and SJ gating was partly restored in the *fraD*<sub>TM</sub> mutant.

To further investigate the development of heterocysts in the strains, liquid cultures were shifted to nitrate-free medium and analyzed via light microscopy at different timepoints. Heterocyst exopolysaccharides were stained with Alcian blue and micro-oxid conditions in the heterocysts were visualized with the redox indicator triphenyl tetrazolium chloride (TTC). Representative micrographs are shown in Figure 17.

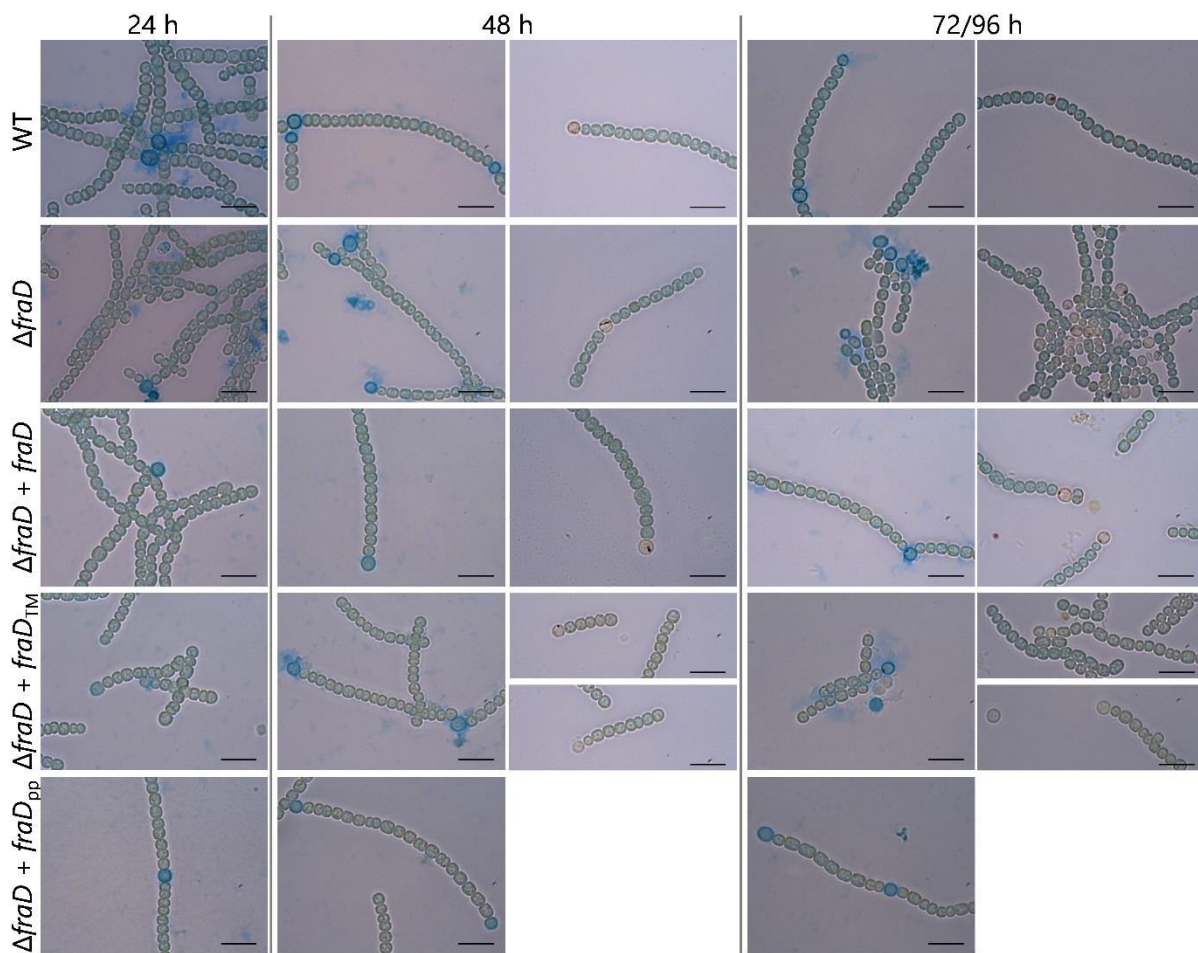


**Figure 17: Light micrographs of developing heterocysts in *fraD* mutants.** Representative micrographs of Alcian blue (24 h, 48 h and 72/96 h left column) and TTC stained (48 h and 72/96 h right column) samples of the indicated mutant strains are shown. Scale bar, 10  $\mu$ m.

As reported previously, the *fraD* mutant developed some heterocysts within 24 h growth on N<sub>2</sub> that could be stained with Alcian blue (Merino-Puerto et al., 2010). Furthermore, a micro-oxic environment in the heterocysts was established when tested after 48 h growth on N<sub>2</sub>. Introduction of *fraD*<sub>PP</sub> led to a phenotype very similar to  $\Delta$ *fraD*. Strikingly, heterocyst development in the mutant complemented with *fraD*<sub>TM</sub> was delayed compared to  $\Delta$ *fraD*, since

mature heterocysts were only observed after 48 h dependence on N<sub>2</sub>. Additionally, heterocysts often appeared palely and TTC only formed precipitates in few heterocysts. Expression of FraD<sub>TM</sub> compounded the ability of diazotrophic growth in comparison to  $\Delta fraD$ . This behavior is astonishing, when the partly restored communication rate and gating ability are considered (compare Figure 14AB). In contrast to the WT, the *fraD*<sub>TM</sub> strain was impaired in reopening SJs after washing off CCCP. Consequently, the need for SJ gating at a specific timepoint during heterocyst differentiation was hypothesized.

Merino-Puerto et al. reported a wider septum in *fraD* and *fraC* mutants between heterocyst and vegetative cell due to a shift of the heterocyst cytoplasmic membrane further into the heterocyst neck (Merino-Puerto et al., 2011b). To check if one part of FraD is sufficient to rescue this phenotype, the heterocyst ultrastructure of the partly complemented mutants was examined via TEM. Representative images are shown in Figure 18. The septum between heterocyst-vegetative cell was broadened in the  $\Delta fraD$  strain (Figure 18A, E) compared to the WT (Figure 18D, H), as previously reported. This phenotype could not be restored by the expression of either of the parts of FraD (Figure 18B, C, F, G). A wider heterocyst-vegetative cell septum with very long SJs was visible in both strains. Full-length FraD might therefore have an important influence on heterocyst septum formation. Alternatively, proper SJ gating is essential for heterocyst differentiation.

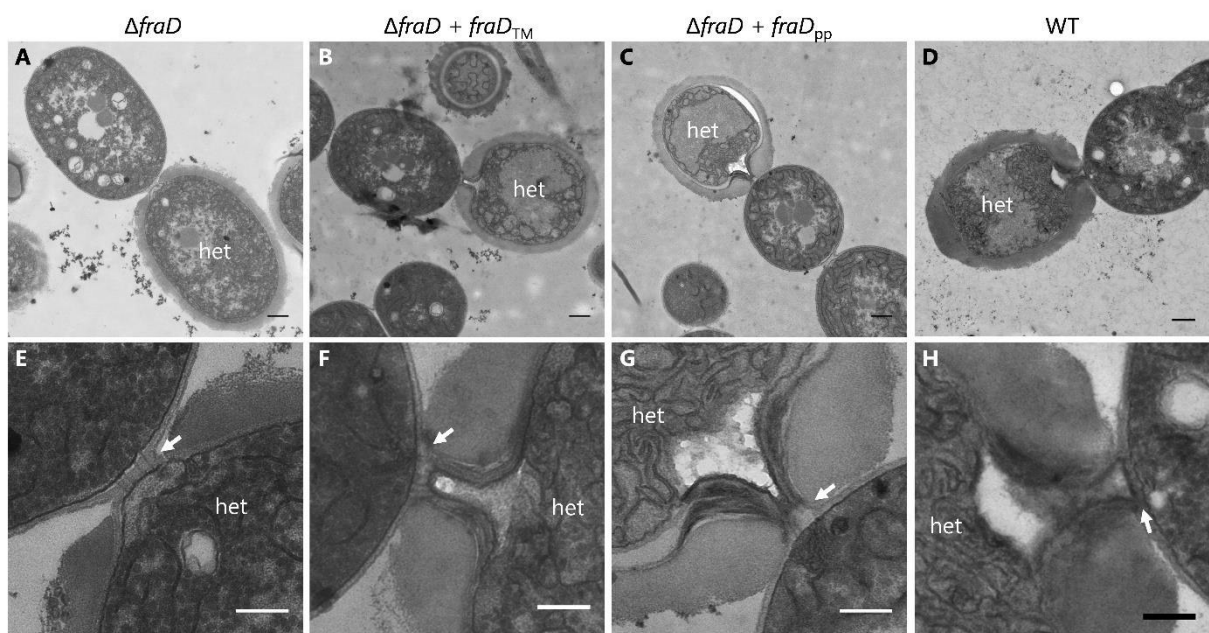


**Figure 18: Ultrastructure of *fraD* mutant heterocysts.** The indicated strains were grown 48 h on agar plates without nitrate before cells were fixed, ultrathin sections prepared and imaged via TEM. (A-D) Terminal heterocysts adjacent to their neighboring vegetative cells. Scale bar, 500 nm. (E-H) Magnified view on the heterocyst-vegetative cell septum, indicated by white arrows. Scale bar, 250 nm. Het, heterocyst.

### 6.3.4 Immunolocalization of FraD<sub>pp</sub>

How FraD finds its place to the septum is not known. Since SJ closure upon treatment with CCCP was restored in the majority of cells that expressed FraD<sub>TM</sub> (compare Figure 14A), it can be assumed that FraD localizes correctly without its C-terminal periplasmic part. To check the subcellular localization of FraD<sub>pp</sub>, immunolocalization was performed using peptide antibodies raised against a C-terminal region in FraD.

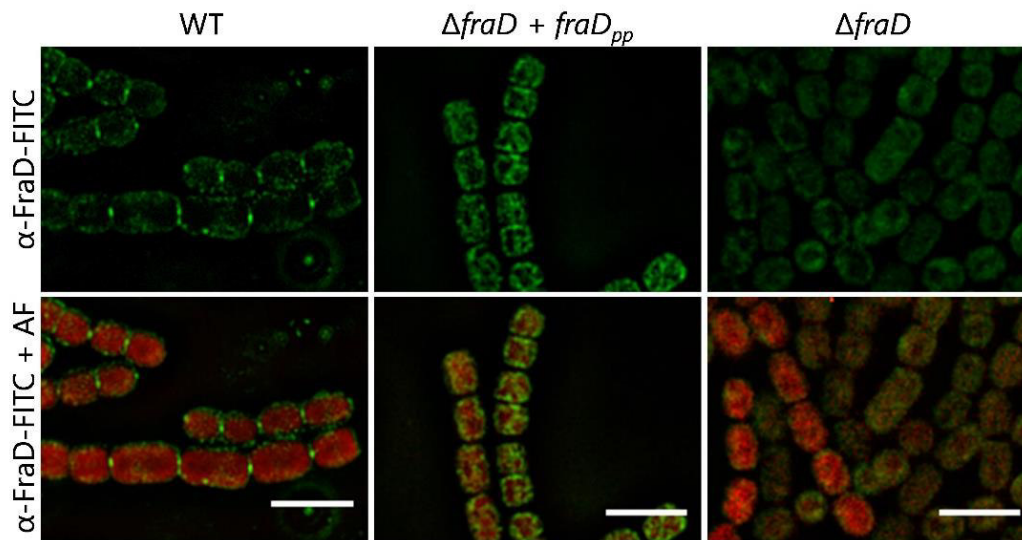


**Figure 19: FraD<sub>pp</sub> does not localize to the septum.** Immunolocalization using  $\alpha$ -FraD and secondary  $\alpha$ -rabbit antibodies coupled to FITC showed septal localization of FraD in WT cells, but not of FraD<sub>pp</sub>. The *fraD* mutant served as negative control. AF, autofluorescence. Scale bar, 5  $\mu$ m.

As a positive control, immunolocalization of FraD was performed in WT cells and showed clear septal localization as already reported previously (Merino-Puerto et al., 2010; Merino-Puerto et al., 2011b). Unfortunately, despite the Tat signal sequence, FraD<sub>pp</sub> was not transported to the periplasmic space and did not localize to the septum (Figure 19).

This observation led to the conclusions that (i) the N-terminus or the transmembrane part of FraD promotes septal localization and (ii) that the results obtained with the FraD<sub>pp</sub> strain need to be considered with caution.

### 6.3.5 Cryotomograms of the *fraD*<sub>TM</sub> strain revealed WT-like SJs

Restoration of SJ closure but not reopening after removal of stress conditions in the *fraD*<sub>TM</sub> strain raised the question, how the architecture of its SJs look like. To address this question, this strain was analyzed by FIB-milling and ECT (Pilhofer group).

Electron cryotomograms and a subtomogram average of SJs revealed no obvious difference to SJs in the WT (Figure 20A, B). The transmembrane part of FraD therefore is the crucial part for formation of the plug domain and recruitment of the cap structure. The five arches of the cap module seemed to be smaller and more vertical in a 3D-representation of the subtomogram average compared to the WT (Figure 20C). However, minor structural changes

could also be an artefact caused by the small data set, which led to a low quality of the subtomogram average (Piotr Tokarz, personal communication).

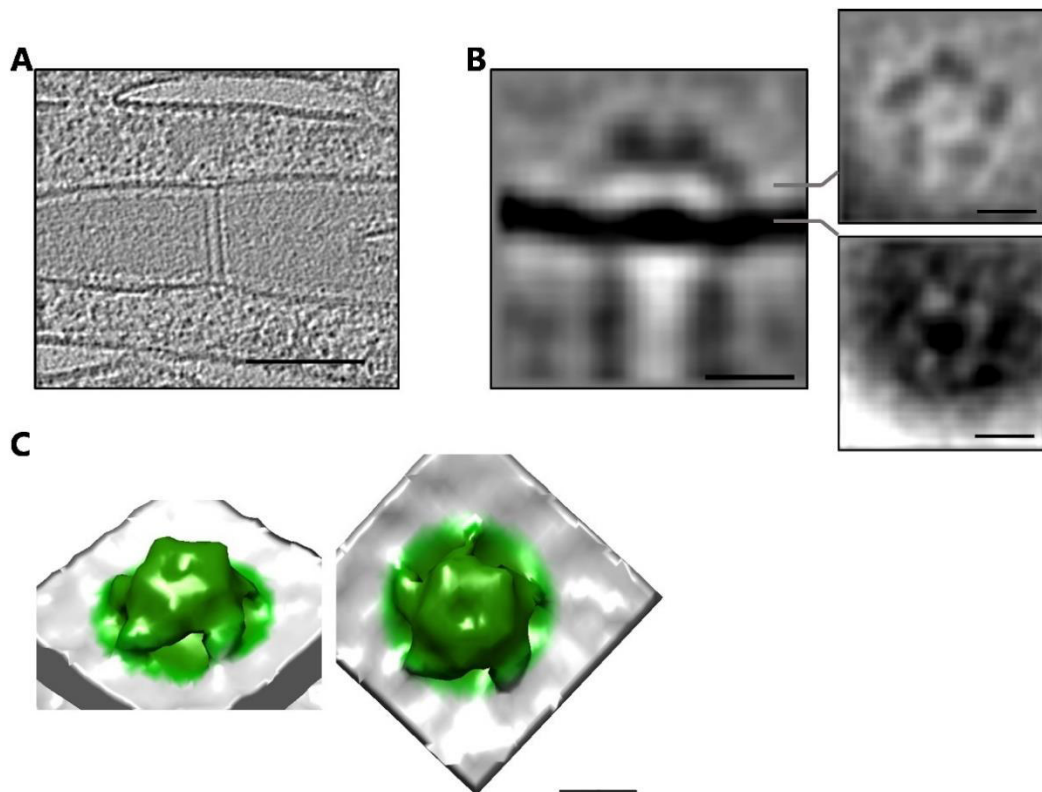


**Figure 20: ECT of SJs in the *fraD*<sup>TM</sup> strain.** (A) Section through an electron cryotomogram shows a SJ of the *fraD*<sup>TM</sup> strain CSVT2.769. Scale bar, 100 nm. (B) Subtomogram average and cross-sectional slices at the indicated heights. Scale bar, 10 nm. (C) 3D-representation of the subtomogram average from the site (left) and from the top (right). Scale bar, 10 nm. Data by Piotr Tokarz, Pilhofer group, ETH Zurich.

#### 6.4 Identification and characterization of putative FraD interactors

The identification of FraD as structural SJ component in the first part of this work (6.1.2) opened the way to identify further SJ proteins via co-immunoprecipitation (co-IP) using FraD as bait. Proteins that interact with FraD are most likely themselves structurally or coordinately involved in the establishment of the cell-cell communication system. After the development of a co-IP workflow with membrane proteins, in total six independent co-IPs directed against either GFP-FraD or wild-type FraD were performed as described in 5.9. Detected proteins with at least 100 times abundance in the sample over the control were further evaluated. Out of the resulting 50-230 proteins in each dataset, only those were considered as candidates that showed a similar taxonomic distribution as FraD. Therefore, proteins with conservation in sections of filamentous cyanobacteria and absence in other sections and phyla were favored as possible candidates. Table 11 summarizes putative FraD interactors that were abundant in at least three of the six co-IPs after the beforehand described filtering. Two times detected proteins are listed in Appendix 4.

**Table 11: Putative FraD interactors (candidate proteins) detected in several co-IPs.**

Antibody	Co-IP	Sample	Control	Candidate proteins*
$\alpha$ -GFP	1	CSVT2.779	CSVT2.779	<b>All4109</b>
		no crosslinking	no crosslinking	
		CSVT2.779	empty beads	<b>All4109, Alr4788, All0157</b>
	2	GA crosslinking		
		CSVT2.779	7120.800	<b>All4109</b>
		no crosslinking	no crosslinking	<b>All4109, Alr4788, All0157</b>
	3	GA crosslinking		
		CSVT2.779	CSVT2.779	
		GA+FA crosslinking	GA+FA crosslinking	<b>All4109, Alr4788, Alr4714</b>
$\alpha$ -FraD	1	WT	WT	
		GA crosslinking	GA crosslinking	<b>All4109, All0157</b>
		pre-immunserum	pre-immunserum	
	2	WT	CSVT2	<b>All4109, Alr4788, Alr4714</b>
		GA crosslinking		
			GA crosslinking	<b>All4109, Alr4788, Alr4714</b>

\*At least detected in three independent co-IPs; investigated proteins are in bold.

CSVT2.779:  $\Delta$ *fraD* + *p(gfpmut2-fraD)*; 7120.800: WT + *p(gfpmut2)*; CSVT2:  $\Delta$ *fraD*.

The most promising candidate was All4109, since corresponding peptides were detected in all samples (crosslinked and non-crosslinked) in all co-IPs among the most abundant proteins (Table 11). Alr4788 was detected with one exception in all crosslinked samples, but not in samples without glutaraldehyde. Alr4714 was identified in three co-IPs in cells treated with glutaraldehyde. Strikingly, although transcribed in the same operon as FraD, FraC was never detected in any of the performed co-IPs. Other cell-cell communication related proteins like SepJ, All1861, and AmiC have not been pulled down neither.

All0157 was detected in three independent co-IPs in crosslinked samples, but in two of three samples, only one peptide for All0157 with low sequence coverage was detected by LC-MS/MS. This rendered All0157 unlikely as real hit and therefore was not investigated.

#### 6.4.1 Genomic localization and secondary structure prediction

The gene *all4109* is the second in a predicted operon downstream of *all4110* (MicrobesOnline Operon Prediction, Figure 21A). However, transcription start sites were reported to be upstream of *all4109* within *all4110* and internally within *all4109* (Mitschke et al., 2011). Therefore, transcription of *all4109* as single gene might be possible. The upstream gene product, All4110, is annotated as magnesium transport protein CorA, which mediates the influx of magnesium ions. *all4109* is translated into an unknown protein comprising 235 aa and a single transmembrane domain between amino acids 7-29 (InterPro, Figure 21B). The short N-terminus faces the cytoplasm, whereas the C-terminal part is predicted to localize in

the periplasm (Protter). Poor similarity of the N-terminal part to an Apo-citrate lyase phosphoribosyl-dephospho-CoA transferase (E-value 0.0049) was found in the Pfam database. Furthermore, even less similarities to ABC-2 family transporter proteins (E-value 0.14) and to a NTF2-like N-terminal transpeptidase domain (E-value 0.12) were found. A domain of known activity or functions is therefore not encoded by *all4109*. Interestingly, All4109 was described as a signature protein for the order Nostocales (Gupta & Mathews, 2010) and gene co-occurrence with FraD is stated by the STRING database. The STRING database reports conserved homologs of *all4109* in the filamentous cyanobacteria clades *Oscillatoriothycidae*, *Nostocaceae*, and *Stigonematales*.

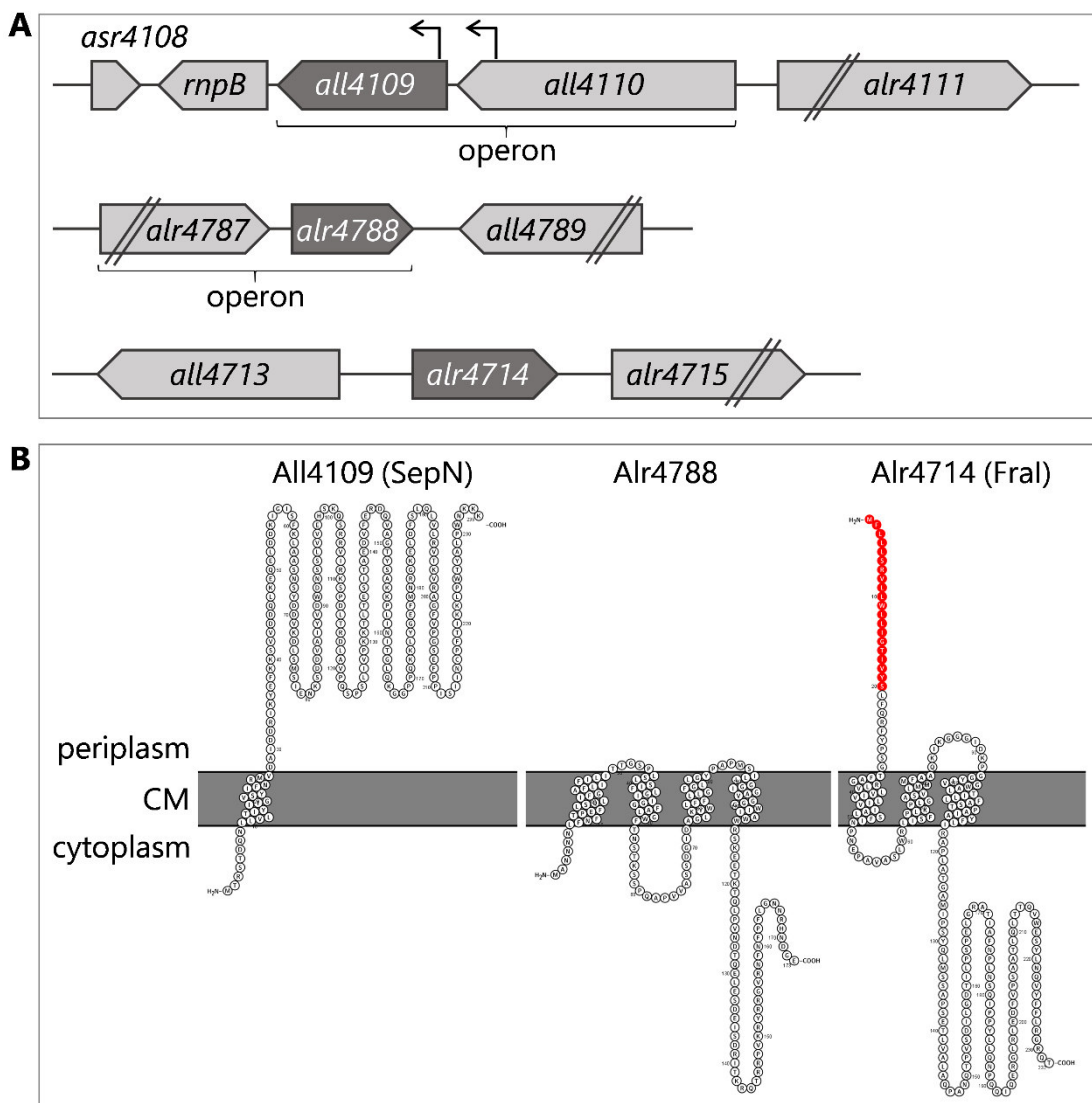


**Figure 21: Genes *all4109*, *alr4788* and *alr4714* encode integral membrane proteins.** (A) Genomic localization of *all4109*, *alr4788* and *alr4714* (dark grey) as annotated in the KEGG database. ORFs and intergenic regions are represented in the original ratio. Transcription start sites for *all4109* are depicted as arrows (Mitschke et al., 2011). (B) The secondary structures were predicted using Protter (Omasits et al., 2013). N-termini are depicted on the left. A signal sequence (red) is predicted for Alr4714. CM, cytoplasmic membrane.

Alr4788 is encoded as the second gene in a predicted operon with *alr4787* (MicrobesOnline Operon Prediction). The 173 aa protein is unknown and does not show any significant

similarity to known domains, but was described as a signature protein for Nostocales (Gupta & Mathews, 2010). Alr4788 is a predicted membrane protein with four transmembrane domains comprising the amino acid regions 7-29, 35-52, 73-90, and 96-113 (Protter). Both termini are predicted to face the cytoplasm (Protter, Figure 21B).

The 232 aa signature protein of Nostocales and Oscillatoriales (Gupta & Mathews, 2010), Alr4714, is predictably transcribed as single gene. Alr4714 is unknown, but its mRNA was reported as one of the predicted targets for the sRNA Yfr1 (Brenes-Álvarez et al., 2020). Besides repression of various outer membrane and cell wall-related proteins, expression of AmiC2 is positively influenced by Yfr1 (Brenes-Álvarez et al., 2020). According to secondary structure predictions, Alr4714 comprises three transmembrane domains with the C-terminal part located in the cytoplasm (Protter). A signal peptide for transportation into the periplasm is predicted at the N-terminus. Interestingly, gene co-occurrence with *all4109* and *fraD* is stated by the STRING database.

Taken together, All4109, Alr4714 and Alr4788 are hypothetical proteins without similarities to known domains and similar taxonomic distribution and conservation in filamentous cyanobacteria like FraD. Importantly, also FraD and FraC are signature proteins in Nostocales and Oscillatoriales (Gupta & Mathews, 2010). Hereafter, All4109 will be referred to as SepN because of its septal localization (see 6.4.2), and Alr4714 as FraI due to its strong fragmentation phenotype (see 6.4.6).

#### 6.4.2 SepN, Alr4788 and FraI localize to the septa

Proteins involved in cell-cell communication are expected to localize to the septum, as it was reported for example for FraC, FraD and SepJ (Flores et al., 2007; Nayar et al., 2007; Merino-Puerto et al., 2010). To visualize the subcellular localization of SepN, Alr4788 and FraI, the respective open reading frames (ORFs) were exchanged via single homologous recombination for a recombinant copy in which the gene was C-terminally fused to the superfolder version of *gfp* (*sfgfp*). Expression of the fusion genes was thus under the control of their native promoter to avoid overexpression artefacts. Fully segregated mutant clones were examined via fluorescence microscopy. Indeed, defined fluorescence foci in the septum between vegetatively growing cells were observed when sfGFP was fused to SepN (SR834) or Alr4788 (SR835) (Figure 22A). In comparison to the weak septal signal observed for GFPmut2-FraD (CSVT2.779) (see also (Merino-Puerto et al., 2010)), fluorescence foci in SR834 and SR835 were more reminiscent to the focused localization described for SepJ-GFP (Flores et al., 2007; Nayar et al., 2007). Due to its septal localization All4109 was named SepN.

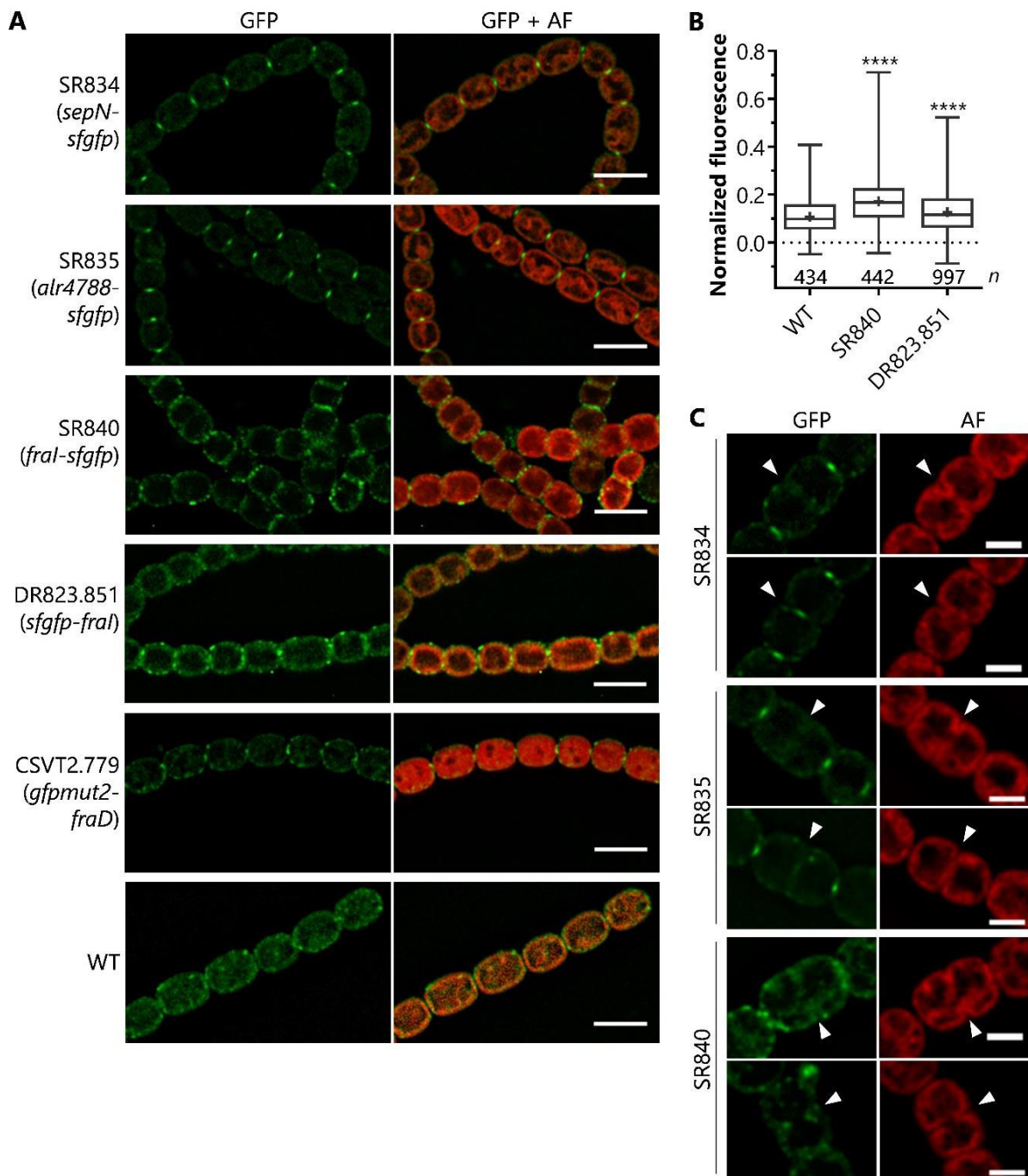


**Figure 22: Subcellular localization of putative FraD interactors in vegetative cells.** (A) 3D-deconvoluted fluorescence micrographs of the indicated GFP-fusion strains. WT cells were included as negative control. Scale bar, 5  $\mu$ m; GFP, GFP channel; AF, autofluorescence channel. (B) Quantification of the fluorescence signal of summed z-stacks in the septum as described in methods. *n* indicates the number of analyzed septa. Data from five clones of two independent conjugations were cumulated for strain DR823.851. (C) Subcellular localization of GFP-tagged proteins in the indicated strains was analyzed in immature or freshly formed septa. Arrow heads point to the septa. Scale bar, 2  $\mu$ m.

Less distinct was the localization of FraI-sfGFP in strain SR840 (Figure 22A). Broad septal fluorescence was detected in some, but not in all cells. Furthermore, fluorescence was not restricted to the septum, but occasionally also occurred in the lateral cell wall. However, quantification of the septal fluorescence in comparison to the WT not expressing GFP revealed significantly increased septal fluorescence (Figure 22B). To exclude localization artefacts due

to sfGFP fused to the C-terminus, a plasmid-encoded N-terminal sfGFP-fusion was created. For this, a 270 bp fragment including the predicted promoter region and signal sequence of *alr4714* were cloned upstream of *sfgfp* translationally fused to *alr4714*. The self-replicating plasmid pIM851 was introduced in the *alr4714* knockout mutant DR823 (see below), which resulted in strain DR823.851. However, localization of sfGFP-FraI was similar to the C-terminal fusion protein (Figure 22A). Also, quantification stated a significant difference in emitted fluorescence compared to the WT, although the mean fluorescence of DR823.851 was lower than of SR840 (Figure 22B). Assuming that fusion to GFP does not interfere with localization at both termini of FraI, FraI seems to occupy the whole septal plane and sometimes is found in the lateral cell wall.

As mentioned above (3.5.2), FraC and SepJ move with the Z-ring during septum constriction in dividing cells, whereas FraD does not (Flores et al., 2007; Merino-Puerto et al., 2010; Merino-Puerto et al., 2011b). Like FraD, SepN and Alr4788 appeared in completely closed septa, but did not move with the Z-ring (Figure 22C). Some of the dividing cells of SR840 exhibited fluorescent foci at constriction sites, where the new septum was formed. Therefore, FraI might migrate with the Z-ring during septum constriction.

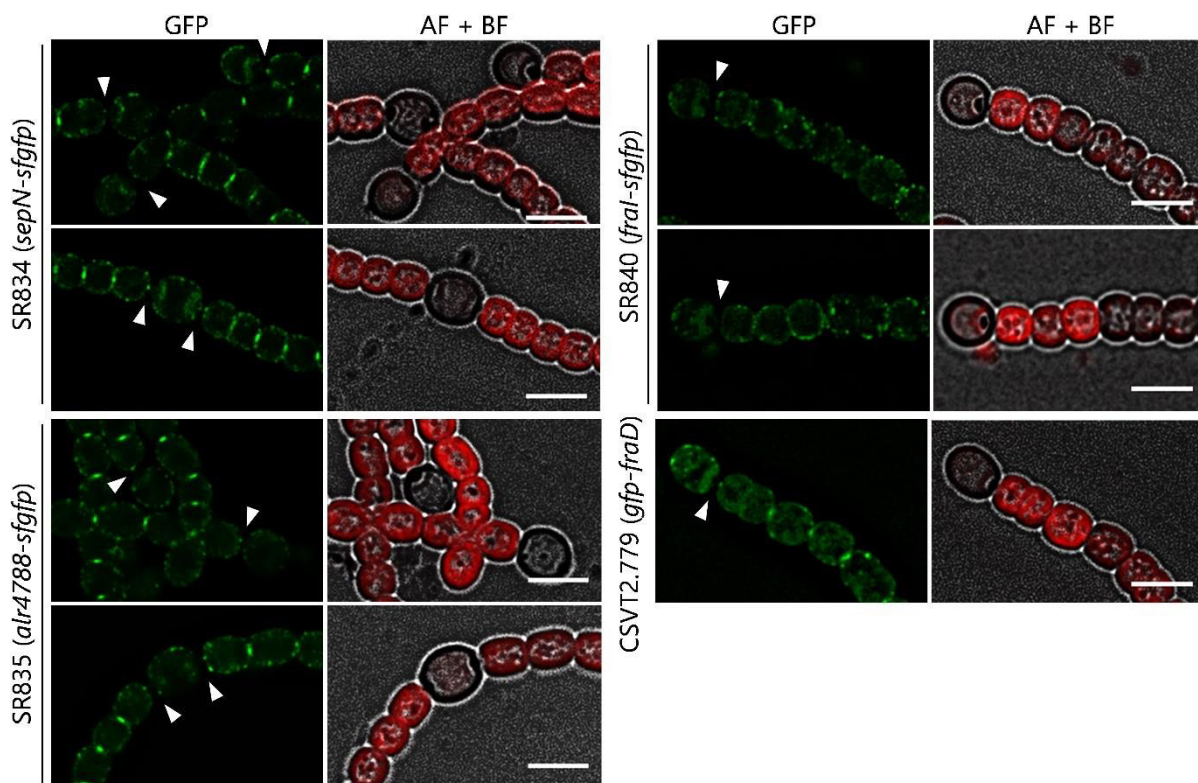


**Figure 23: Localization of putative FraD interactors in diazotroph conditions.** SR834 (*sepN-sfgfp*), SR835 (*alr4788-sfgfp*), SR840 (*fraI-sfgfp*) and CSV2.779 (*gfpmut2-fraD*) were grown for three days on BG11<sub>0</sub> agar plates before imaging via fluorescence microscopy. Representative micrographs of 3D-deconvoluted z-stacks are shown. Contrast of GFP-images was enhanced after 3D-deconvolution by histogram stretching for better visualization. Arrow heads point to the septum between heterocyst and vegetative cell. GFP, GFP channel; AF, autofluorescence channel; BF, bright field channel; scale bar, 5  $\mu$ m.

Localization of the investigated proteins was also monitored in diazotrophically growing filaments. The strains were grown for three days on nitrate-free agar plates and were then analyzed via fluorescence microscopy. Localization of SepN and Alr4788 in the septa of vegetative cells was similar to cultures growing with supplement of nitrate. Tiny fluorescence foci in the septum between heterocyst and vegetative cell were detectable (Figure 23). SepN-sfGFP was additionally detected at the rim of the honeycomb membranes in the heterocyst poles. In contrast, FraI-sfGFP was barely detectable when grown under diazotrophic conditions in both, vegetative-vegetative and heterocyst-vegetative septa.

### 6.4.3 Intercellular communication and SJ gating are impaired in *sepN* and *fral* mutants

Septal localization of the putative FraD interactors (see above) made their involvement in IC further presumable. To address this hypothesis, the exchange rate of the fluorescent tracer calcein and SJ gating were analyzed in mutants in *sepN*, *alr4788* and *fral* by FRAP experiments. Mutants in the respective genes were created by insertion of the neomycin resistance cassette C.K3t4 including a transcriptional terminator into the respective ORFs via double homologous recombination. All three mutants were fully segregated, which excludes that SepN, FraI or Alr4788 are essential (Appendix 1).

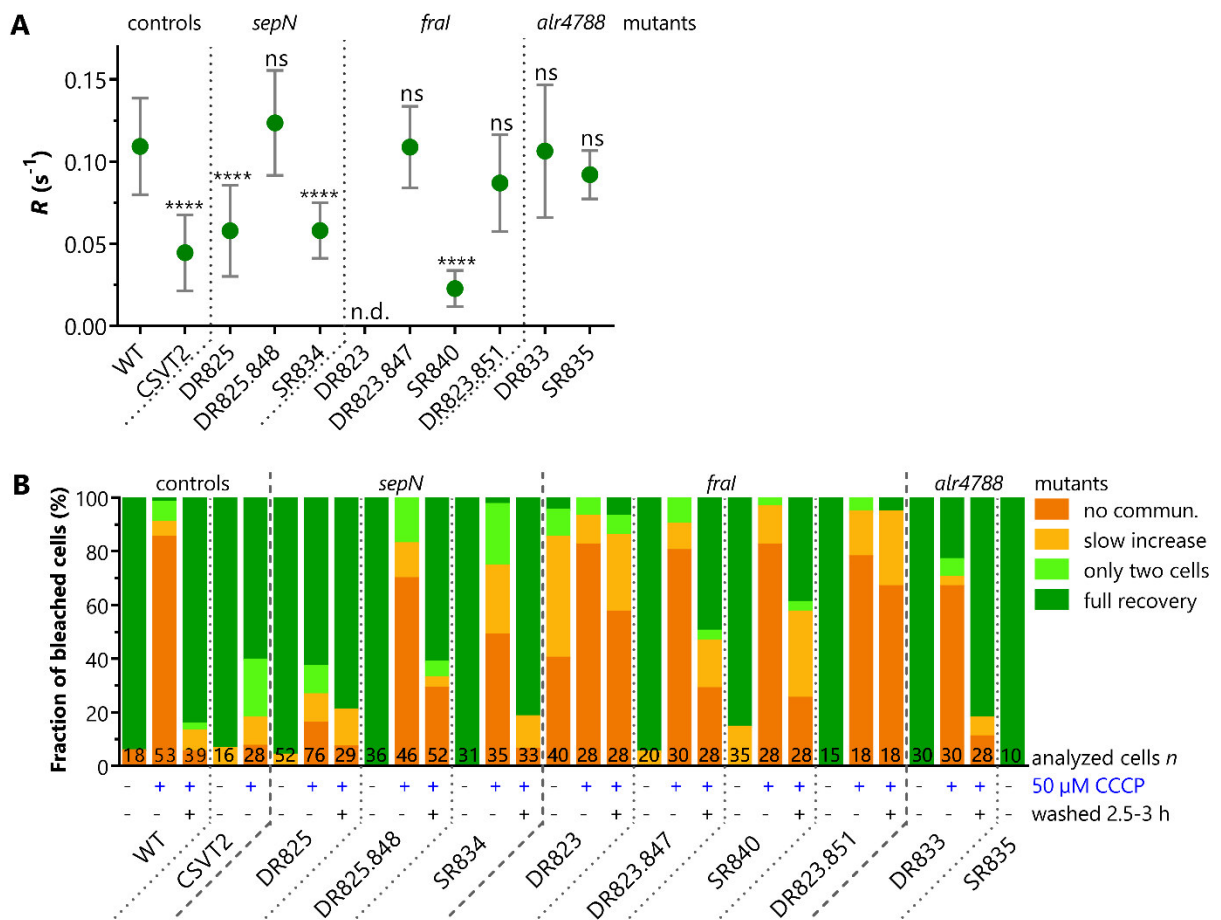


**Figure 24: Intercellular communication and SJ gating in *sepN*, *fral* and *alr4788* mutants.** FRAP experiments with and without CCCP-treatment were performed with calcein-stained filaments. (A) The fluorescence recovery rate constant  $R$  was calculated from fully recovering, untreated cells. The mean, SD and significant difference compared

to the WT from at least two independent cultures (except for SR835) are depicted.  $R$  could not be calculated for DR823 (n.d.). (B) Cells bleached in CCCP-FRAP experiments were assigned to one of four groups dependent on their FRAP response. Cumulated results of at least two independent cultures (except for SR835) are shown. Data from three different DR825 and DR825.848 mutant clones were cumulated.

Figure 24A shows the fluorescence recovery rate constant  $R$  in comparison to the communication rates of the WT and the *fraD* mutant CSVT2. The rate of molecular exchange was significantly reduced in the *sepN* mutant DR825. Likewise, a C-terminal fusion of GFP to SepN reduced the rate of molecular exchange to almost 50 % of the WT's rate. Complementation of DR825 with plasmid-encoded SepN (pIM848) rescued the phenotype. Disruption of *fraI* (DR823) led to a severe impairment of IC, which is why  $R$  could not be calculated for this strain. Introduction of plasmid pIM847 coding for FraI complemented the mutant phenotype, which was reflected in a WT-like fluorescence recovery rate constant of DR823.847. Interestingly, a genome-inserted C-terminal fusion of GFP to FraI (SR840) only allowed very decelerated communication, whereas a plasmid-encoded N-terminal GFP-fusion (DR823.851) rescued the phenotype of DR823 concerning  $R$ . Disruption of *alr4788* or fusion to *sfgfp* did not interfere with IC.

In a next step, gating of SJs in these mutants was examined via the CCCP-FRAP assay, the results of which are summarized in Figure 24B. As described previously, treatment of cells with CCCP resulted in non-communicating WT-cells and uninfluenced, communicating cells in the *fraD* mutant (Weiss et al., 2019). CCCP-treatment of cells with disrupted *sepN* only led to a minor fraction (16 %) of non-communicating cells, similar to cells in which *fraD* was disrupted. This observation led to the hypothesis, that SepN might indeed act as structural SJ component or is important for the assembly of the protein complex. Reintroduction of *sepN* on a plasmid under the control of its native promoter into DR825 complemented the gating phenotype. However, reopening of SJs in DR825.848 was not as efficient as in the WT. Nevertheless, restoration of SJ closure confirms disrupted *sepN* as the cause of the observed non-closing phenotype. Although  $R$  was reduced when *sepN* was exchanged for its C-terminal *gfp*-fusion, gating was possible to some extent. In this strain, the fraction of cells in the "slow increase" group was enlarged by about 20 % in comparison to the WT. This led to conclude that C-terminal fusion of GFP to SepN influences IC, but allows SJ gating.

IC was severely impaired in the *fraI* mutant DR823 (Figure 24B). Even in the absence of CCCP, only 5 % of the analyzed cells showed a "full recovery" response, whereas 40 % and 45 % showed a "slow increase" or a "no communication" response, respectively. Nevertheless, the fraction of non-communicating cells was further increased upon protonophore-treatment, suggesting that before communicating cells were able to close their SJs' caps. Also, reopening after removal of CCCP to the level of communicating cells before CCCP-treatment was observed. As mentioned above, intercellular exchange was restored in the complemented mutant DR823.847. Like in strain DR825.848, reopening of closed SJs in the complemented *fraI* mutant was slightly less efficient than in the WT. Whereas SJ gating in the *fraI-sfgfp* strain

(SR840) was similar to the complemented mutant (DR823.847), N-terminal fusion to GFP (DR823.851) strongly impaired SJ reopening. The fraction of non-communicating cells in the *alr4788* mutant DR833 was slightly reduced in comparison to the WT, but comparable to the *sepJ* mutant described earlier (Weiss et al., 2019).

In conclusion, FRAP analyses gave the hypothesis of SepN being a structural SJ component further evidence. In contrast, FraI might rather be involved in nanopore formation, because of the severely impaired molecular exchange but ability to gate communication. Fusion of GFP to the C-terminus of FraI strongly reduced cell-to-cell diffusion compared to the WT and SJ gating was possible. In contrast, N-terminal fusion to GFP led to a WT-like communication rate and closure of SJs, but not to their reopening. Hence, protein-protein interactions of FraI mediated by the C-terminus might be important for nanopore formation, whereas a free N-terminus seems to play a role in SJ reopening. Since no communication-related abnormalities were observed upon disruption of *alr4788*, the corresponding protein probably is not involved in IC or only plays a minor role.

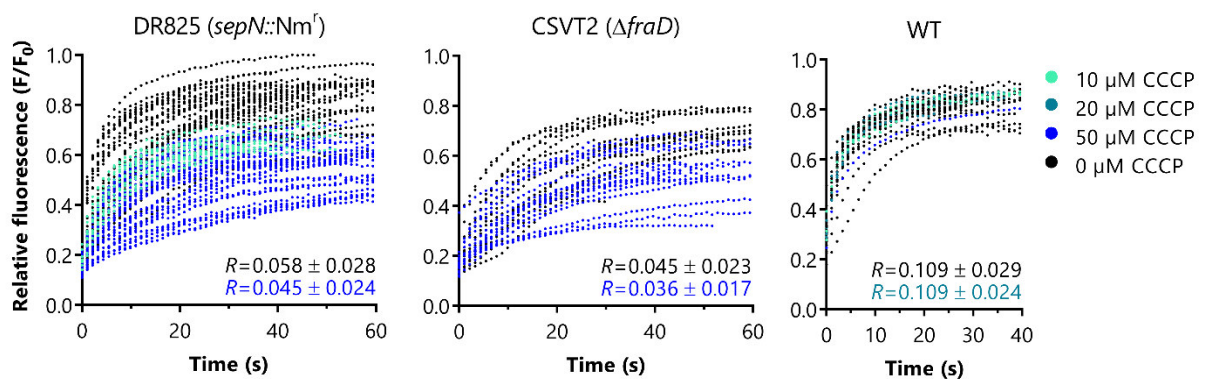


**Figure 25: CCCP-treatment reduces fluorescence recovery in the *sepN* mutant DR825.** Normalized fluorescence recovery curves after bleaching of cells assigned to the “full recovery” group of untreated (black) or CCCP-treated (blue) cells.  $R$  of untreated and CCCP-treated (50 μM in DR825 and CSVT2, 20 μM in WT) are stated. Student’s  $t$ -test showed no significant differences in all strains.

During the analysis of FRAP responses of the *sepN* mutant, it was striking, that fluorescence recovery curves of CCCP-treated cells were flatter and  $R$  slightly reduced in comparison to untreated cells (Figure 25). In the *fraD* mutant, the tendency was the same, but the effect was not as strong as in DR825. Unfortunately, only few recovery curves of CCCP-treated WT cells could be analyzed, since the majority of WT cells ceased communication in this condition. Nevertheless, no difference in the recovery responses between treated and untreated cells was observed in WT cells. A possible reason for this phenomenon will be discussed later (7.3).

#### 6.4.4 The nanopore array is barely present in the *fraI* mutant

The nanopore array is directly linked to the rate of IC. To address the question if reduced molecular exchange in some of the mutants is related to a decreased nanopore array, septal PG discs of vegetative cells were isolated and analyzed via TEM. Representative electron

micrographs of septal discs are shown in Figure 26A. Nanopores per septum were determined and averaged (Figure 26B). As already reported for the *fraCfraD* double mutant (Nürnberg et al., 2015), single deletion of *fraD* resulted in a severely reduced nanopore array and was reflected by a decreased molecular diffusion rate (see above). Surprisingly, the nanopore array of the *sepN* mutant DR825 was unaltered compared to the WT (Figure 26B), although *R* was significantly reduced (Figure 24A). Therefore, SepN seems to influence intercellular diffusion in a nanopore-independent way, which further strengthened the hypothesis, that SepN is a SJ component.

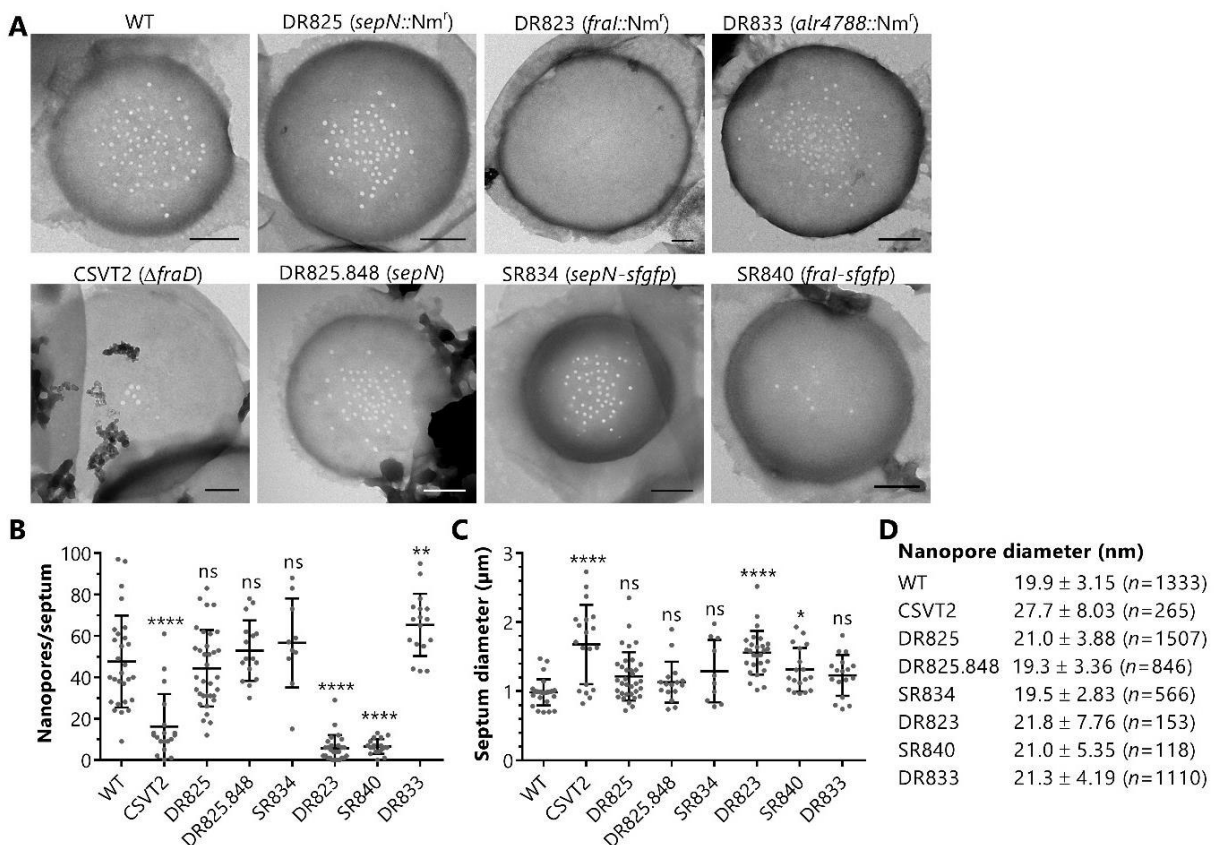


**Figure 26: The nanopore array in purified septal PG discs of *sepN*, *fraI* and *alr4788* mutants.** Septal PG discs of the indicated strains were purified and imaged via TEM. (A) Representative septal discs are shown. Scale bar, 250 nm. (B) Nanopores per septum were counted and (C) septa diameter were measured. Each dot represents an analyzed septal disc. Shown are mean, SD and significance in comparison to the WT. (D) The average diameter of *n* nanopores cumulated from all septal discs was calculated. Data for DR825 are cumulated from two independent mutant clones.

A dramatically reduced, often even to zero, nanopore array was drilled in PG discs of the *fraI* mutant DR823 (Figure 26B). The low numbers of nanopores explain the severe impairment in IC observed in FRAP experiments (Figure 24A). Additionally, disruption of *fraI* enhanced the average septum diameter significantly (Figure 26C). Since the nanopore array in the GFP-fusion strain SR840 was comparable to the mutant, a free C-terminus of FraI might be important for interaction with other proteins. If the rate of molecular change would be reduced because of GFP blocking the diffusion area, a WT-like nanopore array is expected. Although

disruption of *alr4788* did not cause detectable changes in molecular exchange, the number of nanopores per septum was slightly increased compared to the WT.

The diameter of single nanopores was slightly larger compared to the WT in all strains, except for SR834 and the complemented *sepN* mutant DR825.848 (Figure 26D). However, none of the pores were as large as in the *fraD* deletion strain.

#### 6.4.5 ECT reveals absence of plug and closed caps in SJs of a *sepN* mutant

Insensitivity of the *sepN* mutant towards treatment with CCCP was elucidated above (6.4.3) and strongly suggested a structural alteration in the SJ modules. To gain insights into the SJ architecture in the absence of SepN, ECT was performed by Piotr Tokarz, Pilhofer group (ETH Zurich).

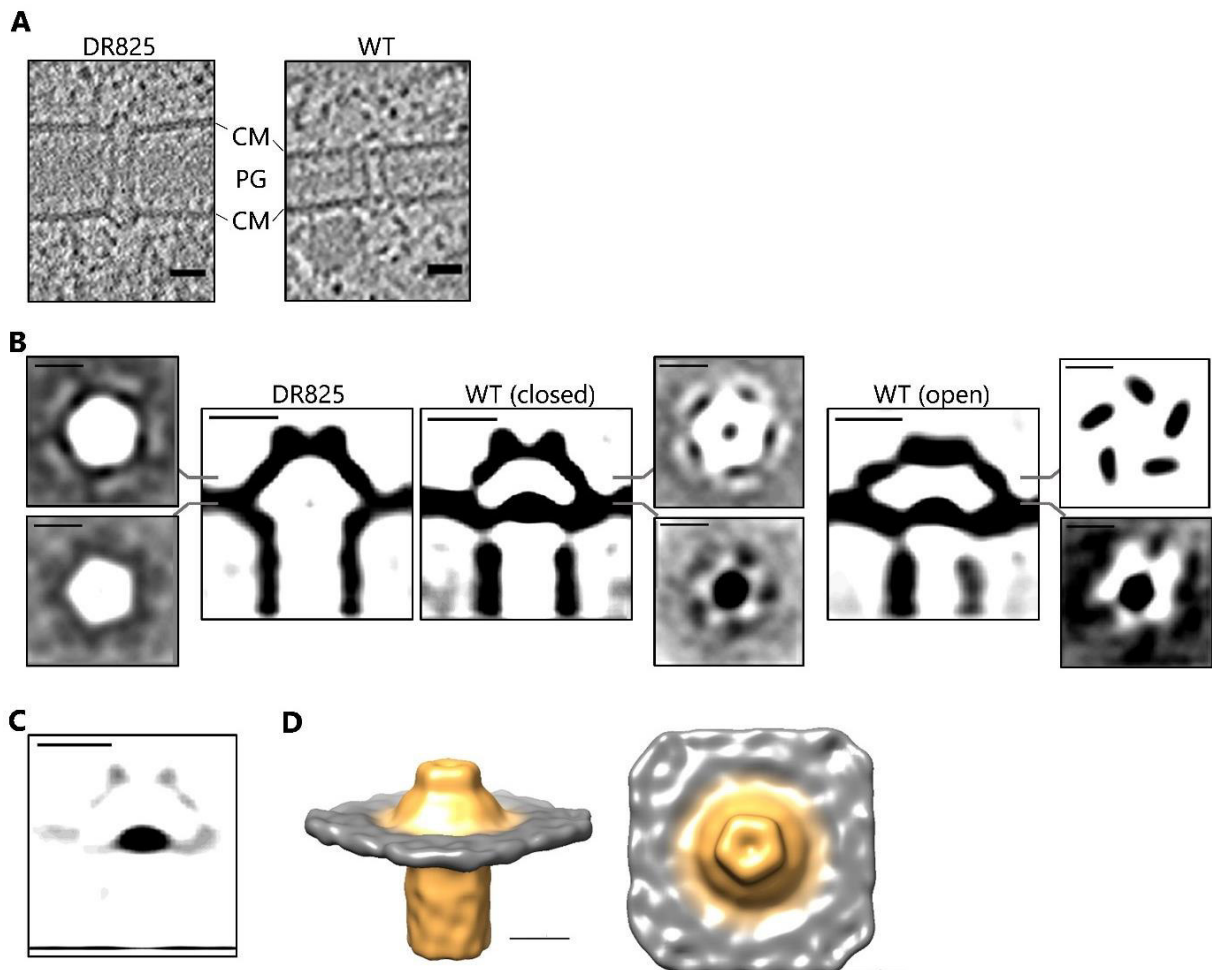


**Figure 27: SJs of the *sepN* mutant lack the plug module and exhibit closed caps.** ECT of FIB-milled DR825 (*sepN::Nm<sup>+</sup>*) cells was performed by Piotr Tokarz, Pilhofer group (ETH Zurich). (A) Slice of cryotomograms of DR825 and the WT. WT image was modified from (Weiss et al., 2019). Scale bar, 20 nm. CM, cytoplasmic membrane; PG, peptidoglycan. (B) Subtomogram averages of SJs and cross-sectional slices at the indicated heights. WT closed state is averaged from CCCP-treated cells. Scale bar, 10 nm (C) Difference map between subtomogram averages of SJs of the WT in the closed conformation and the *sepN* mutant. Scale bar, 10 nm. (D) Surface representation of the subtomogram average of SJs from DR825 from the side (left) and the top (right). Scale bar, 10 nm.

As described earlier (Weiss et al., 2019), ECT was performed after FIB-milling of septal regions of the *sepN* mutant DR825. Surprisingly, in cryotomograms and the subtomogram average, the density referred to as the plug module was absent in SJs of the *sepN* mutant (Figure 27A, B). This was further verified by a calculated difference map of subtomogram averages of SJs between the WT in the closed conformation and the *sepN* mutant, in which only the plug module was identified as different (Figure 27C). Strikingly, the cap module was narrower than expected for the open position in the absence of SepN and therefore reminiscent of the closed cap in WT cells after treatment with CCCP (compare Publication 1, Figure 3D). Indeed, absence of the five-fold symmetric cap openings was obvious in the surface representation of the DR825 subtomogram average (Figure 27D, compare with WT in Figure 8A).

In conclusion, SepN might indeed be a structural SJ component with probable localization to the plug module. However, indirect involvement of SepN in assembly of the SJs might also be possible. The absence of the plug but not the cap module allows elucidation of the plug's role in communication and SJ gating and will be discussed below (7.3).

#### 6.4.6 Diazotrophic growth of mutants in putative FraD interactors

Differentiation of heterocysts is dependent on proper cell-cell communication. For this reason, the ability of mutants in putative FraD interactors to grow on atmospheric nitrogen was investigated. An agar drop assay after a N<sub>2</sub>-stepdown revealed diazotrophic growth of the *sepN* (DR825) and *alr4788* (DR833) mutants, but not of the *fraI* mutant (DR823, Figure 28A). However, the WT had a little growth advantage over DR825 as manifested in the last sample of the dilution series. C-terminal fusion of GFP to FraI (SR840) did not allow diazotrophic growth, whereas N-terminal fusion did (DR823.851).

To get further insights into the development of specialized cells for nitrogen fixation, nitrate-depleted cultures were examined via light microscopy. Heterocysts developed in both, *sepN* and *alr4788* mutants. In contrast, heterocysts were barely observed in the *fraI* mutant strain DR823, even after 48 h (Figure 28B) or 72 h growth in nitrate-free medium. This absence of differentiated cells is probably related to the strongly impaired IC and explains the inability of this mutant to grow on N<sub>2</sub>. The heterocyst polysaccharide layer was present in the heterocysts of all mutants, as indicated via Alcian blue staining. Furthermore, severe filament fragmentation was observed in the absence of FraI. A major fraction of 91 % of the filaments consisted of ten or less cells after 72 h in nitrate-free medium (Figure 28C). Albeit 51 % of the filaments were of ten or less cells already in nitrate-supplemented medium, depletion of nitrate further increased the amount of strongly fragmented filaments. In contrast, filament fragmentation was not observed in the *sepN* and *alr4788* mutants (not statistically determined for the latter).

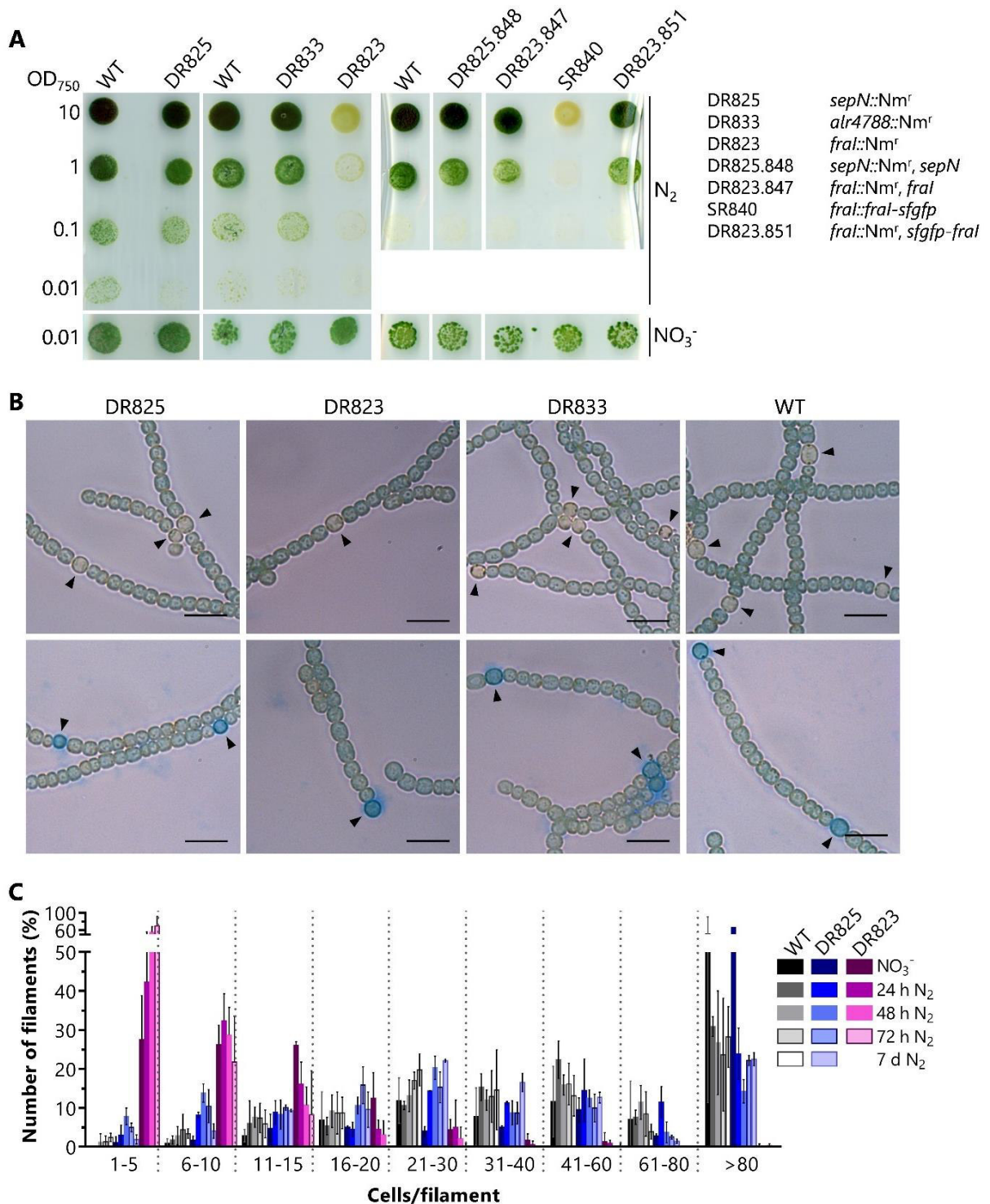


**Figure 28: Diazotrophic growth and heterocyst development.** (A) Nitrogen stepdown agar drop assay was performed as described in methods. As growth control, the last sample of the dilution series was spotted onto an agar plate supplemented with nitrate. The image was taken after 7 d under standard cultivation conditions. Mutants are specified on the right. (B) Liquid cultures of the indicated strains were grown for 48 h in nitrate-depleted medium and analyzed via light microscopy. The heterocyst polysaccharide layer was stained with Alcian blue (bottom row). Heterocysts are indicated with arrow heads. Scale bar, 10  $\mu$ m. (C) Cells per filament were counted before and at indicated time points after the shift into nitrate-free medium. At least 100 filaments per replicate and timepoint were counted. Mean values and SD from 2-3 independent replicates are depicted.

The *sepN* mutant DR825 exhibited an instable phenotype concerning SJ gating after a while, although the mutant was still fully segregated (Appendix 1). This is why the C.K3t4 resistance

cassette was inserted into the ORF of *sepN* in two independent recombination events after conjugation, yielding a DR825 clone from the first conjugation and two clones from the second conjugation. The two *sepN* mutant clones from the second conjugation will be referred to as DR825<sub>new</sub> in the following. The inability to close SJs after CCCP-treatment was confirmed in both clones from the second conjugation. Differences between the mutants were only observed in terms of the number of vegetative cells, which separate two heterocysts, and heterocyst morphology (see below). The reason for this discrepancy is elusive.

Especially after 24 h under diazotrophic conditions, the interval between heterocysts of the first mutant clone were noticeably enlarged compared to the WT (Figure 29A). After 72 h in nitrate-free medium heterocysts showed a similar pattern as in the WT. Micrographs that show the different number of vegetative cells between heterocysts in the *sepN* mutant compared to the WT after 48 h on N<sub>2</sub> are shown in Figure 29B. This difference to the WT in heterocyst pattern development was not observed in the two later mutant clones (Figure 29A, DR825<sub>new</sub>). In contrast, a higher fraction of contiguous heterocysts were observed for DR825<sub>new</sub> after 48 h and 72 h in nitrate-free medium compared to the WT (Figure 29A, C).

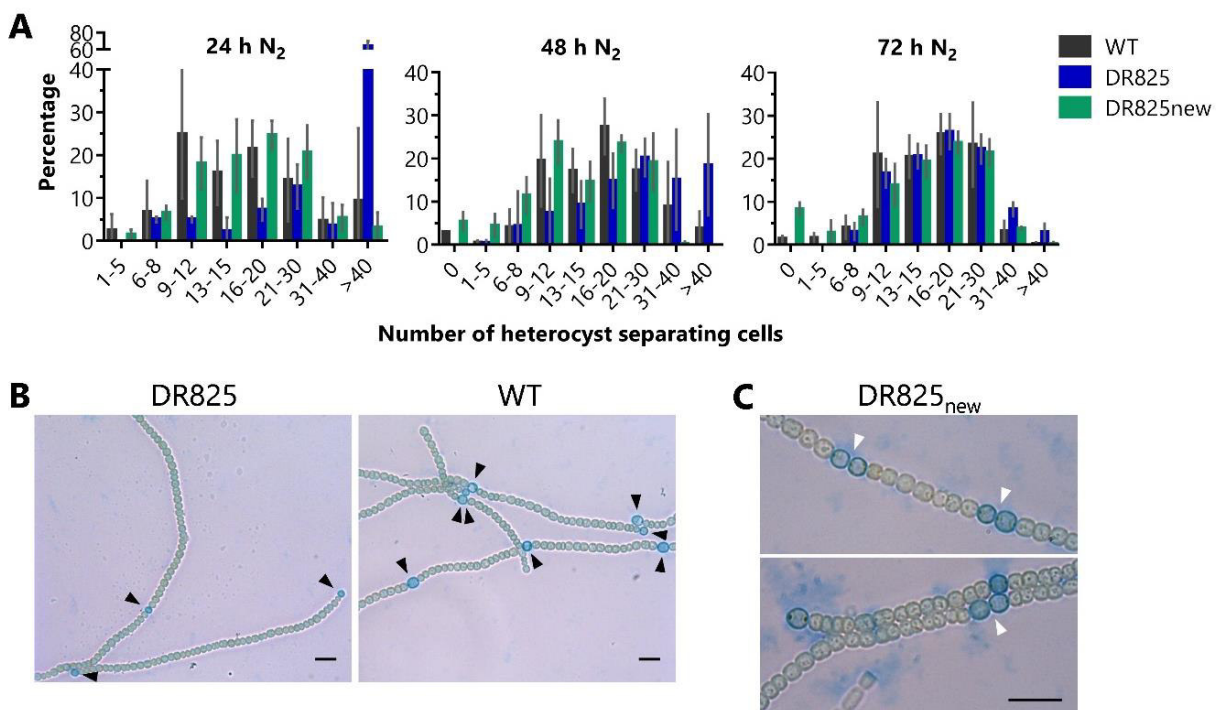


**Figure 29: Heterocyst pattern in different *sepN* mutant clones.** Nitrogen stepdown with two independent *sepN* mutant clones (DR825 and DR825<sub>new</sub>) was performed and the number of vegetative cells between two heterocysts was statistically enumerated. (A) Vegetative cells that separate two heterocysts were counted at different time points after nitrate depletion. At least 100 intervals between two heterocysts were counted per replicate. Mean values with SD of 4 replicates for each strain are depicted. (B) Light microscopic images were taken after 48 h growth in nitrate-free medium. Arrow heads point to heterocysts stained with Alcian blue. Scale bar, 10  $\mu$ m. (C) Directly adjacent heterocysts were more abundant in DR825<sub>new</sub> than in the WT (interval of 0 in A). Microscopic images were taken after 48 h after stepdown. White arrow heads point to contiguous heterocysts. Scale bar, 10  $\mu$ m.

To have a closer look on potential morphological alterations of the heterocysts in comparison to the WT, ultrathin sections of heterocysts were analyzed via TEM. For this, the WT and two

DR825 clones from independent conjugations were grown on nitrate-free agar plates for two days before fixation, sectioning and TEM analysis.

Surprisingly, heterocysts of the two *sepN* mutant clones showed morphological differences (Figure 30A). Most heterocysts of the earlier mutant clone showed a short heterocyst neck and the septal PG was not restricted to this neck region (Figure 30A, middle panel). Note, that perpendicular structures, probably SJs, were not only found in the neck septum, but also adjacent to the neck. Most of the heterocysts seemed immature, since the cyanophycin plug and the glycolipid layer were absent. The short heterocyst neck and surrounding PG could therefore represent an earlier development stage. A minor fraction of observed heterocysts looked similar to WT heterocysts. In contrast, no morphological differences between heterocysts of the newer mutant clone and the WT were observed (bottom panel).

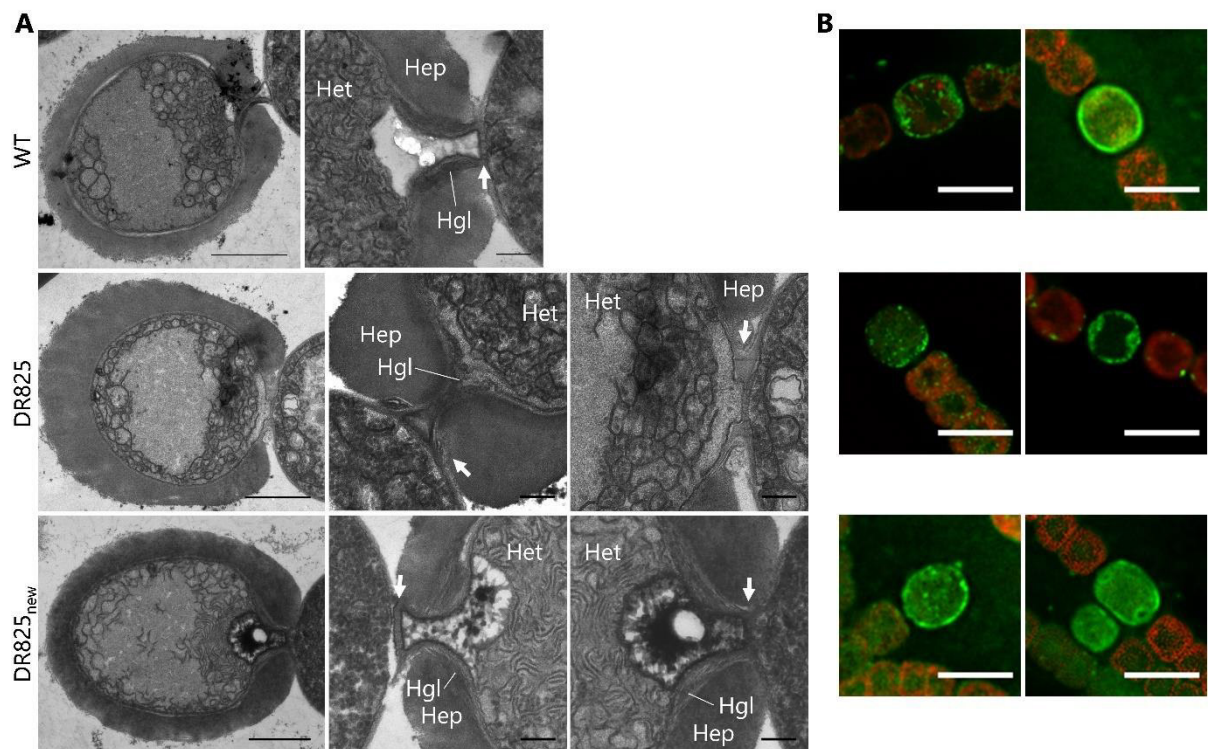


**Figure 30: Heterocyst ultrathin sections and glycolipid staining.** (A) Ultrathin sections for TEM analysis were prepared from cells that were grown for 2 d on BG11<sub>0</sub> agar plates. Het, heterocyst; Hep, heterocyst exopolysaccharides; Hgl, heterocyst glycolipid layer. Scale bar in images with whole heterocyst 1  $\mu\text{m}$ ; in magnified images 250 nm. Arrows point to the heterocyst-vegetative cell septum. (B) Heterocyst glycolipids were stained with BODIPY after growth for 2 d on BG11<sub>0</sub> agar plates. Two replicates for each strain (indicated in A) are shown. Scale bar, 5  $\mu\text{m}$ .

BODIPY staining of the heterocyst glycolipids was performed on cells grown for two days on nitrate-depleted agar plates (Figure 30B). Whereas the majority of heterocysts of the WT and DR825<sub>new</sub> were nicely stained with the dye, a minor fraction was in the earlier mutant clone. This reflected the observations made in TEM analysis.

The growth rate of the *sepN* mutant in medium with and without combined nitrogen was measured and compared to the WT (Figure 31A). The data shown here were derived from

the more recent mutant clones. Whereas no difference was observed in vegetatively growing cultures, the mutant strain suffered from a growth disadvantage after two days in nitrate-free medium in comparison to the WT. In parallel, the mutant cultures exhibited a yellowish color from the first day until the third day after shift into nitrate-free medium (Figure 31B). In the WT, this initial bleaching caused by the degradation of phycobilisomes only lasted for one day and cells re-greened at the second day. Additionally, whereas the autofluorescence was only reduced in differentiating cells of the WT, also adjacent cells exhibited lower autofluorescence after 24 h and 48 h on  $N_2$  in the *sepN* mutant (Figure 31C).

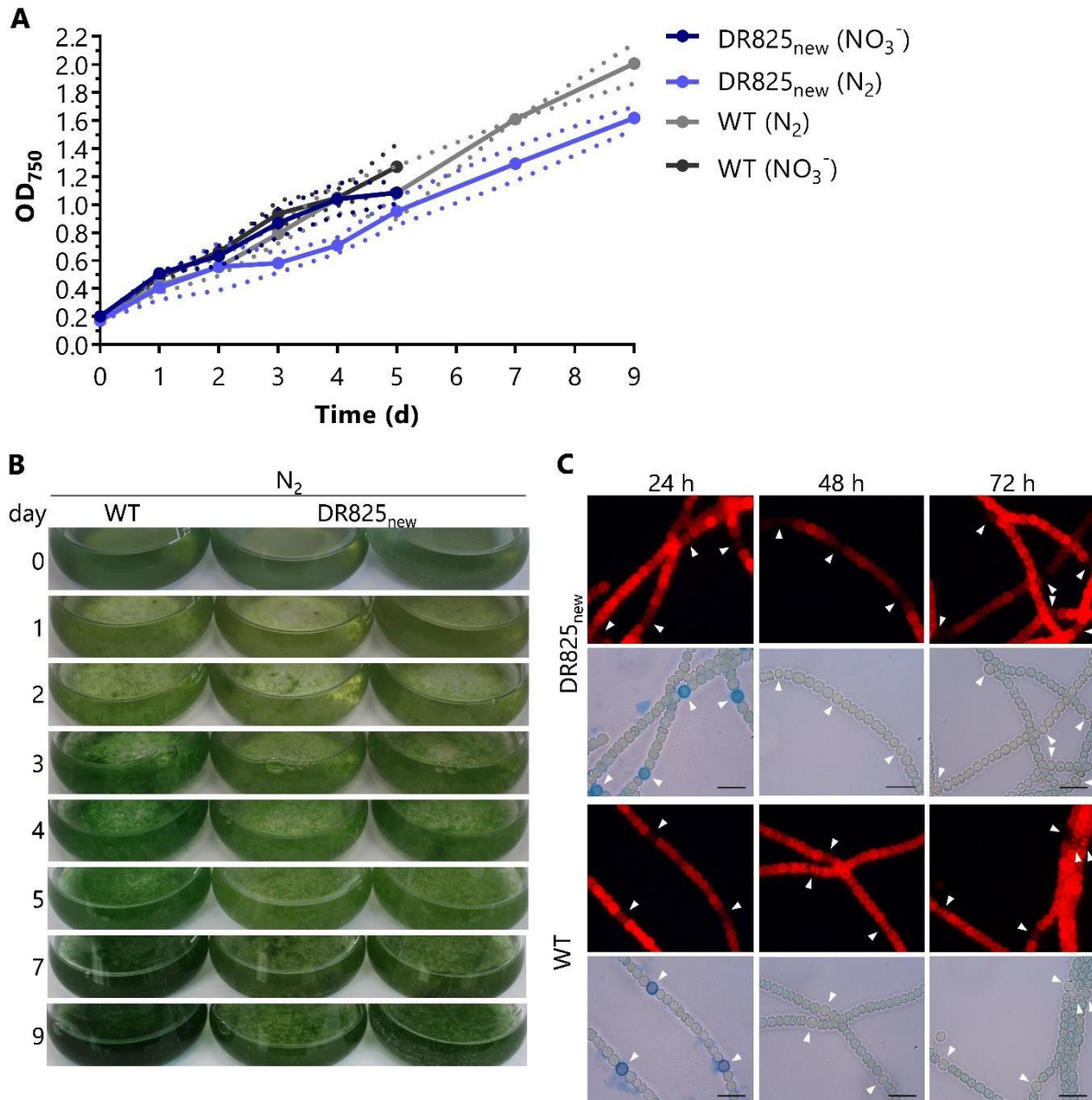


**Figure 31: Growth rate in diazotrophic conditions is decelerated in a *sepN* mutant.** Nitrate-grown cultures were washed with nitrate-free medium and inoculated to OD<sub>750</sub>=0.15 in 20 mL. (A) OD was measured at the indicated time points. The growth of WT and two independent mutant clones (DR825<sub>new</sub>) were monitored in duplicates. SD is shown as dotted lines. (B) Images of the culture flasks show faster re-greening of the WT than of the mutant cultures. (C) Microscopic images after the indicated timepoints after shift into nitrate-free medium. Autofluorescence channel and bright field are shown. Arrow heads point to heterocysts. Heterocysts after 24 h were stained with Alcian blue. Scale bar, 10  $\mu$ m.

Taking together the results of the *sepN* mutant clones, heterocyst development seemed to be slightly decelerated compared to the WT. The reason for the discrepancy between the mutant clones concerning heterocyst development remained elusive.

#### 6.4.7 Mutual influences on localization of FraD and putative FraD interactors

SepN, FraI and Alr4788 were co-eluted with FraD in co-IPs and were therefore expected to interact with the latter. Proper localization of proteins often depends on their interaction. To address the question, if the localization of FraD is dependent on one of the knocked-out proteins, it was immunolocalized in the different mutant backgrounds. Secondary  $\alpha$ -rabbit antibodies coupled to the fluorochrome fluorescein isothiocyanate (FITC) were used to detect  $\alpha$ -FraD antibodies via fluorescence microscopy.

FraD in the *sepN* mutant DR825 showed a similar septum-located fluorescence signal as in the WT (Figure 32). Also, FraD-localization was unaltered in the *alr4788* mutant DR833. A septum-localized signal for FraD was also detected in the absence of FraI, however, the fluorescence intensity appeared lower in most of the analyzed septa (Figure 32A). Indeed, quantification of fluorescence revealed a significant drop of septal fluorescence normalized to the cytoplasmic background in comparison to the WT (Figure 32B).

The experiment led to the conclusion that localization of FraD is independent of the presence or absence of SepN and Alr4788. Lower fluorescence signal of FraD in the *fraI* mutant could either be caused by dependence on FraI for proper localization of FraD or by the severely reduced nanopore array in the *fraI* mutant (compare 6.4.4).

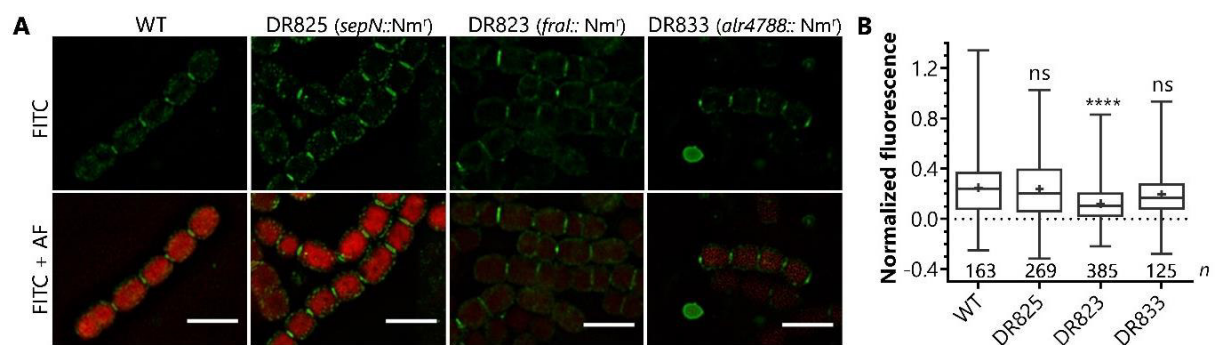


**Figure 32: Immunolocalization of FraD in mutants of putative FraD interactors.** (A) FraD was localized using  $\alpha$ -FraD followed by  $\alpha$ -rabbit-FITC antibodies in the indicated mutant strains. Representative 3D-deconvoluted fluorescence micrographs of the FITC channel and merged with autofluorescence (AF) are shown. Scale bar, 5  $\mu$ m. (B) Quantification of the fluorescence signal in the septum was performed as described in methods. Values are depicted as box (25<sup>th</sup>-75<sup>th</sup> percentile) and whiskers (min to max). The median is indicated by a line, the mean as +. Background-subtracted values were normalized to the average of background fluorescence in the cytoplasm. The number of analyzed septa is stated below the boxes (n).

Deletion of FraD resulted in SJs that lack cap and plug modules (Weiss et al., 2019). Therefore, the question arose, if SepN is still localized in the septum in the absence of these SJ modules. To address this question, a plasmid coding for *sepN-sfgfp* was single recombinantly inserted into the respective genomic site in the *fraD* mutant background. The resulting strain was

referred to as CSVT2.SR834 and analyzed via fluorescence microscopy in comparison to the localization of SepN-sfGFP in WT background (Figure 33). As a negative control, the GFP-free strain CSVT2 was imaged. Interestingly, SepN-sfGFP could barely be visualized in the septum or was even absent in a part of the *fraD* mutant cells. Also, quantification of the fluorescence signal stated a significant difference to strain SR834 and similar values as in the negative control (Figure 33B).

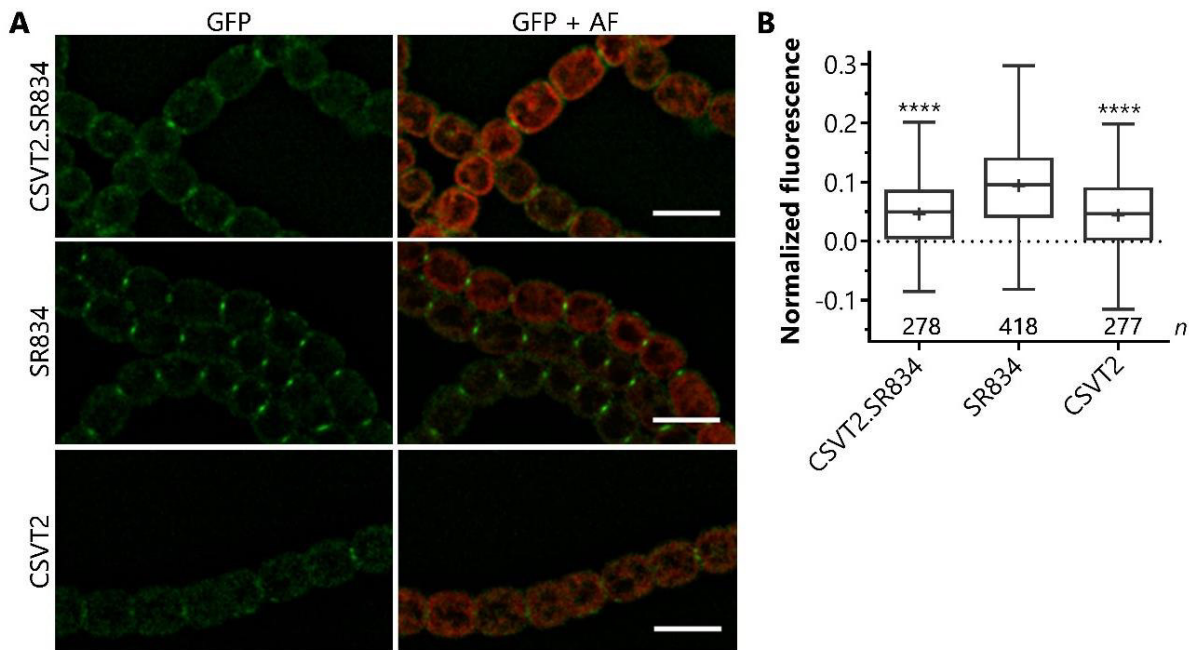


**Figure 33: Localization of SepN-sfGFP in the *fraD* mutant and WT background.** A single recombinant insertion of *sepN-sfgfp* into the genome of the *fraD* mutant CSVT2 or the WT was analyzed via fluorescence microscopy. (A) Representative 3D-deconvoluted micrographs of the indicated strains are shown. Scale bar, 5  $\mu$ m. (B) The septal fluorescence was quantified and normalized to the background fluorescence in the cytoplasm. Septal localization of SepN was significantly reduced in CSVT2.SR834. Box (25<sup>th</sup>-75<sup>th</sup> percentile) and whiskers (min to max) are shown with the median as horizontal line. Mean is indicated as +. The number of analyzed septa (*n*) is stated below the boxes.

Two possibilities could explain the low abundance of SepN in the septum in the absence of FraD. First, localization of SepN might depend on the presence of FraD or the cap and plug modules of the SJ complex. Second, since the nanopore array and therefore the presence of SJs is strongly reduced in the *fraD* mutant, the fluorescence signal emitted by the potential SJ-protein SepN might be below the detection limit.

#### 6.4.8 Localization of AmiC-type amidases is reduced in the *fraI* mutant

As elucidated above (6.4.4), the nanopore array in the *fraI* mutant was severely reduced or absent in isolated septal PG discs. Since the amidases AmiC1 and AmiC2 drill the nanopore array in *Anabaena* (Bornikoel et al., 2017), a relation between FraI and one of the amidases was hypothesized. To address this issue, subcellular localization of the two amidases was investigated via immunolocalization using antibodies directed against a common C-terminal part. The antibodies were raised against AmiC in *Nostoc punctiforme* (Büttner et al., 2016), but

because of high sequence similarity to *Anabaena* amidases, the antibodies are suitable to also detect the latter. Indeed, the fluorescence signal derived from FITC-conjugated AmiC in the *fraI* mutant was different from that in the WT (Figure 34A). The fluorescence in the septum was more focused and less intense in the absence of FraI. Quantification revealed a significantly reduced fluorescence signal derived from AmiC in DR823 compared to the WT (Figure 34B).

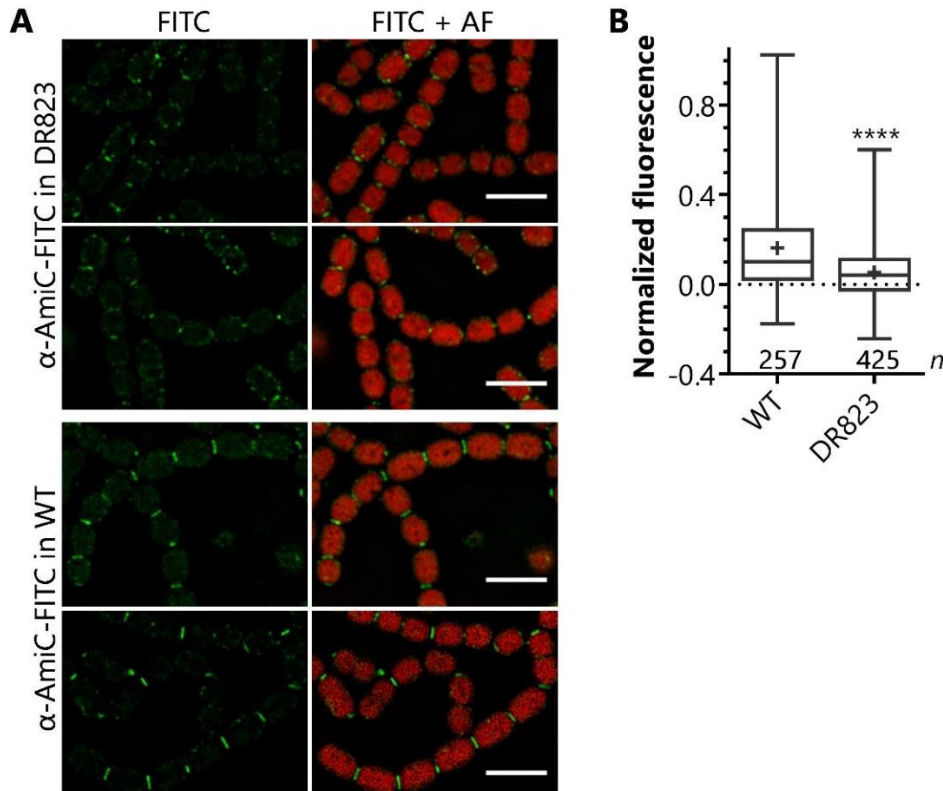


**Figure 34: Immunolocalization of amidases in the *fraI* mutant and the WT.** Immunolocalization was performed using primary antibodies directed against the C-terminal part of AmiC1 and AmiC2, followed by  $\alpha$ -rabbit secondary, FITC-coupled antibodies. (A) FITC and autofluorescence (AF) channels of two representative 3D-deconvoluted images for each strain are shown. Scale bar, 5  $\mu$ m. (B) Septal fluorescence in  $n$  septa was quantified as described in methods and normalized to the background fluorescence. Student's  $t$ -test revealed a significant lower AmiC-derived fluorescence in the absence of *fraI* compared to the WT.

In conclusion, a direct or indirect influence of FraI on localization of one or both of the amidases might be possible.

#### 6.4.9 FraD is the most abundant protein in a reverse co-IP with SepN-sfGFP as bait

To verify the putative interaction between FraD and SepN, a reverse co-IP using SepN-sfGFP as bait was performed as described for co-IPs with GFP-FraD. The most abundant protein after SepN indeed was FraD in both, samples with and without glutaraldehyde crosslinking (Table 12). Interestingly, the second most abundant peptide was FraI, followed at position four by Alr4788 in the non-crosslinked or vice versa in the crosslinked sample. Even more interesting was the detection of FraC among the 20 most abundant proteins, since it was never detected in co-IPs with FraD as bait.

**Table 12: Most abundant proteins in co-IPs with SepN.**

#	Glutaraldehyde crosslinking	
	-	+
1	FraD	FraD
2	Fral	Alr4788
3	Alr0761	Alr0761
4	Alr4788	Fral
5		Alr7326
7		FraC
11	Alr7326	
20	FraC	

Moreover, the two proteins Alr0761 and Alr7326 attracted attention, because their high abundancy in both samples. Alr7326 was also detected in two of the crosslinked  $\alpha$ -FraD co-IPs (Appendix 4). Both proteins are unknown and predicted to be periplasmic proteins harboring a signal peptide at the N-terminus (Protter). Whereas Alr7326 is only conserved in few Nostocales, Alr0761 is also conserved in Oscillatoriales and some other phyla including Proteobacteria. Alr7326 does not contain similarities to a known domain, whereas Alr0761 shows weak similarity to a pre-peptidase domain (E-value 0.039, Pfam database). It was reported, that Alr0761 is differentially expressed dependent on calcium concentrations (Walter et al., 2016) and transcribed together with a hydrogenase gene cluster (Sjöholm et al., 2007), which makes its direct involvement in cell-cell communication questionable.

The reverse co-IP gave further evidence to an interaction between FraD and SepN. Furthermore, SepN could be the missing link between FraD and FraC.

#### 6.4.10 Further investigated mutants

Peptides corresponding to All3520 were identified in one of the GFP-FraD co-IPs and in the co-IP using SepN-sfGFP as bait in both, crosslinked and non-crosslinked sample. However, the abundancy and number of peptides for All3520 were low in both co-IPs. A mutant in *all3520* was created earlier (FQ211) and a regulating function in heterocyst development was assigned to All3520 (Lechno-Yossef et al., 2011). This is, because expression of All3520 was upregulated early after shift to nitrate-free medium and a mutant could not grow on N<sub>2</sub> under aerobic conditions and sometimes showed internally divided heterocysts (Lechno-Yossef et al., 2011). All3520 is unique to heterocyst-forming cyanobacteria and predicted as a periplasmic protein (Lechno-Yossef et al., 2011). In FRAP-experiments, the *all3520* mutant FQ211 showed a reduced fluorescence recovery rate constant (Figure 35A), but WT-like SJ gating properties (Figure 35B). Interestingly, the nanopore array in isolated septal PG discs was not significantly different to the WT (Figure 35C) except that 20 % of the analyzed septa exhibited less than 20 nanopores per septum.

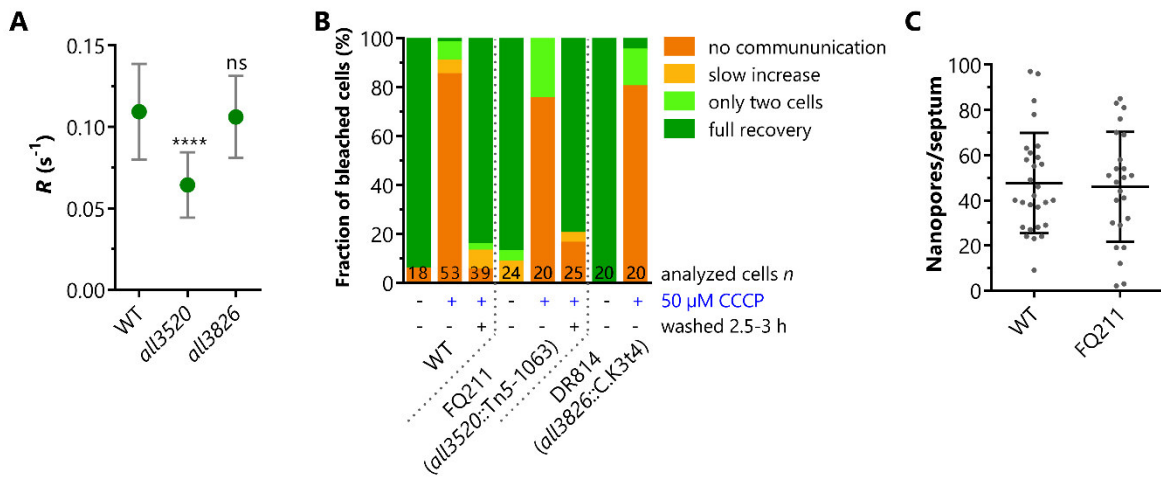


**Figure 35: Analysis of communication in further mutants.** (A) A mutant in *all3520* showed a reduced fluorescence recovery rate constant in FRAP experiments. (B) CCCP-FRAP assay with *all3520* and *all3826* mutants revealed no differences in comparison to the WT. (C) Septal PG discs of the *all3520* mutant were isolated and analyzed via TEM.

Peptides corresponding to All3826 were only detected in the crosslinked sample of one of the GFP-FraD co-IPs. The unknown, predicted periplasmic protein was considered as interesting, because the STRING database states gene co-occurrence with SjcF1, and All3826 comprises two PG-binding domains (Pfam database). In cyanobacteria, *all3826* is only conserved in filamentous strains, but it's also present in other bacteria, especially in Firmicutes and some eukaryotes and archaea. The ORF of *all3826* was exchanged by the C.K3t4 cassette via double homologous recombination, yielding strain DR814. Neither the fluorescence recovery rate constant nor gating of SJs was altered in the mutant compared to the WT (Figure 35A, B). Therefore, All3826 is probably not involved in the cell-cell communication network.

## 6.5 Protein-protein interaction studies with FraD and potential interactors

### 6.5.1 In vivo protein-protein interaction assay: BACTH

First hints on protein-protein interactions can be obtained via a bacterial adenylate cyclase two hybrid (BACTH) system in *E. coli*. The genes for two proteins are fused to two parts of an adenylate cyclase domain from *B. pertussis* that only synthesizes cyclic adenosine 3',5'-monophosphate (cAMP) when the two parts are in close proximity (Battesti & Bouveret, 2012). In the original host, interaction of the two parts of the adenylate cyclase is mediated via calmodulin, a protein only present in eukaryotes. In the BACTH system, the interaction of the cyclase parts is mediated by the two proteins of interest fused to those parts. Thereby synthesized cAMP activates, among others, the transcription of the lactose and maltose operons, which can be detected by a color change of colonies on indicator plates. All via the BACTH system tested protein combinations are summarized in Table 13. Additional to interaction of FraD with SepN, FraI or Alr4788, SepN self-interaction and interaction of SepN with FraI and Alr4788 were investigated. Because the *fraD* and *sepN* sequences contain some

codons that are rarely used by *E. coli*, codon optimized synthetic genes were ordered to ensure proper expression in the heterologous host (GeneArt Synthesis, Thermo Fisher Scientific, see Appendix 5).

**Table 13: Protein-protein interactions investigated via the BACTH system.**

Protein pair	Plasmid 1: genotype	Plasmid 2: genotype	Scheme
FraD - SepN	pIM832: T25- <i>alr2393</i>	pIM826: T18- <i>all4109</i>	
FraD <sub>opt</sub> - SepN <sub>opt</sub>	pIM846: T25- <i>alr2393</i> <sub>opt</sub>	pIM845: T18- <i>all4109</i> <sub>opt</sub>	
FraD <sub>pp</sub> - SepN <sub>pp</sub>	pIM597: T25- <i>alr2393</i> <sub>pp</sub>	pIM829: T18- <i>all4109</i> <sub>pp</sub>	
SepN <sub>opt</sub> - SepN <sub>opt</sub>	pIM850: T25- <i>all4109</i> <sub>opt</sub>	pIM845: T18- <i>all4109</i> <sub>opt</sub>	
FraD - Alr4788	pIM832: T25- <i>alr2393</i>	pIM831: T18- <i>alr4788</i>	
FraD - FraI	pIM832: T25- <i>alr2393</i>	pIM836: <i>alr4714</i> - T18	
SepN <sub>opt</sub> - Alr4788	pIM850: T25- <i>all4109</i> <sub>opt</sub>	pIM831: T18- <i>alr4788</i>	
SepN <sub>opt</sub> - FraI	pIM850: T25- <i>all4109</i> <sub>opt</sub>	pIM836: <i>alr4714</i> - T18	
FraI <sub>Δaa 1-57</sub> - SepN <sub>opt</sub>	pIM852: T25- <i>alr4714</i> <sub>Δaa 1-57</sub>	pIM845: T18- <i>all4109</i> <sub>opt</sub>	

Opt, codon optimized for *E. coli*; pp, periplasmic part. Blue square, T25 tag; green square, T18 tag; p, periplasm; c, cytoplasm; \*, native localization in the periplasm.

Unfortunately, a positive interaction signal was detected in none of the combinations, neither during incubation at 28 °C nor at 20 °C for 1-3 days. However, negative results in BACTH assays do not necessarily mean that two proteins do not interact. Since *E. coli* is not the native host, *Anabaena* proteins could be instable or misfolded. Also, different intercellular conditions compared to the native host or missing proteins that mediate the interaction might be an issue.

### 6.5.2 Purification of FraD<sub>pp</sub> and SepN<sub>pp</sub>

To perform in vitro protein-protein interaction studies, the periplasmic parts (pp) of FraD and SepN without the transmembrane domains were overexpressed in *E. coli* for purification. Strep-FraD<sub>pp</sub> (pIM812) was only poorly soluble (data not shown), additional fusion to maltose binding protein (MBP, pIM813) rendered the protein more soluble. SepN<sub>pp</sub> could only be expressed by *E. coli* Rosetta2 cells and was soluble with a N-terminal His-tag (pIM827). The first purification step was performed using affinity chromatography (AC) as described in the methods. Then, pooled elution fractions were further purified via size exclusion chromatography (SEC).

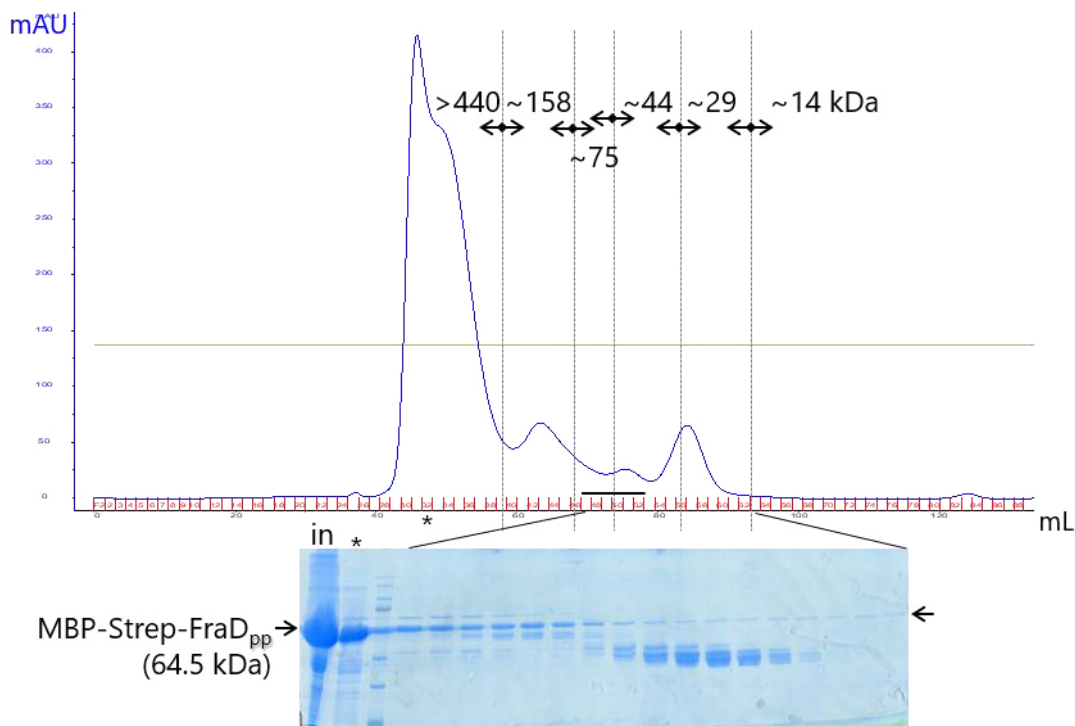


**Figure 36: SEC to purify MBP-Strep-FraD<sub>pp</sub>.** Elution fractions derived from AC were further purified via SEC using a HiLoad 16/60 Superdex 200 pg column. The chromatogram and a 13 % SDS-PAGE gel of indicated fractions are shown. The expected elution range of proteins with the indicated molecular weights derived from the Gel Filtration Calibration Kits Product booklet (GE Healthcare) are indicated with arrows and vertical dotted lines. Black lines in the chromatogram and below the gel mark fractions that were pooled as purified protein. in, injected sample; \*, fraction of the first peak also marked below the chromatogram.

Figure 36 shows the chromatogram of the SEC-based purification of MBP-Strep-FraD<sub>pp</sub>. The corresponding peak in the UV-chromatogram for pure MBP-Strep-FraD<sub>pp</sub> (64.5 kDa) at the expected elution volume was very low. Most of the protein was eluted with several contaminants in the >400 kDa range. Anyway, elution fractions indicated with a black line were stored at -80 °C until usage.

Similarly, His-SepN<sub>pp</sub> was eluted with several contaminants closely to the aggregate peak and at a higher molecular weight range than expected for a monomer (25.8 kDa; Figure 37). Furthermore, the protein precipitated prior to injection onto the SEC column during

concentration of the elution fractions from AC. Nevertheless, fractions marked with a black line were combined and stored at -80 °C.

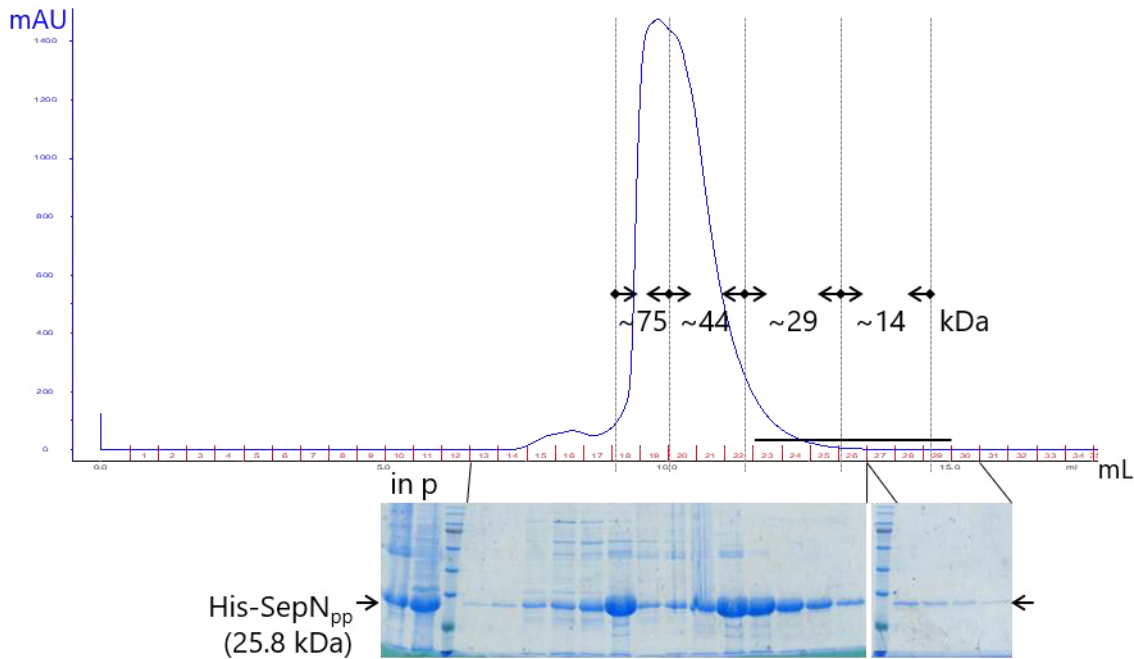


**Figure 37: SEC to purify His-SepN<sub>pp</sub>.** SEC with elution fractions from AC were injected to a Superdex 75 10/300 GL column. Vertical dotted lines and arrows in the chromatogram indicate the expected elution range of proteins with the indicated molecular weights derived from the Gel Filtration Calibration Kits Product booklet (GE Healthcare). Black lines in the chromatogram and below the gel indicate fractions that were stored as the purified protein. in, injection; p, precipitate within the injection sample.

Only small amounts of both proteins were detected in the elution fractions corresponding the weight of the monomers. This might be caused by either polymerization into macromolecules or by aggregation of misfolded or instable proteins due to the missing transmembrane domains.

### 6.5.3 In vitro protein-protein interaction assays with FraD and SepN

To investigate a possible interaction between SepN and FraD in vitro, the purified periplasmic parts of these proteins (see 6.5.2) were first applied to batch pulldown experiments. His-SepN<sub>pp</sub> was preincubated with MBP-Strep-FraD<sub>pp</sub> before the mixture was incubated with Ni-NTA magnetic beads. If the two periplasmic protein parts interact in vitro, MBP-Strep-FraD<sub>pp</sub> would be detected additionally to His-SepN<sub>pp</sub> in the elution fraction as pulled down protein.

Since the beads got very sticky towards the tube wall and the pipette tips, 0.02 % NP-40 was included in all buffers, which helped to overcome the problem. Interaction of the two proteins was investigated in sodium phosphate and Tris buffers with different concentrations of either NaCl, KCl or MgCl<sub>2</sub> in a pH range between 7.4 and 8.5. Buffers are described in Table 14.

**Table 14: Composition of buffers used in protein-protein interaction studies.**

Binding buffer	Composition	pH
1	50 mM Na <sub>2</sub> HPO <sub>4</sub> , 150 mM NaCl, 0.02 % NP-40	8.0
2	50 mM Na <sub>2</sub> HPO <sub>4</sub> , 50 mM NaCl, 0.02 % NP-40	8.0
3	50 mM Na <sub>2</sub> HPO <sub>4</sub> , 150 mM KCl, 0.02 % NP-40	8.0
4	50 mM Na <sub>2</sub> HPO <sub>4</sub> , 150 mM NaCl, 0.02 % NP-40	7.4
5	50 mM Na <sub>2</sub> HPO <sub>4</sub> , 50 mM NaCl, 0.02 % NP-40	7.4
6	50 mM Tris-HCl, 100 mM NaCl, 0.02 % NP-40	8.5
7	50 mM Tris-HCl, 50 mM NaCl, 0.02 % NP-40	8.5
8	50 mM Tris-HCl, 100 mM MgCl <sub>2</sub> , 0.02 % NP-40	8.5
9	1x PBS, 0.02 % NP-40	7.4

Only a very faint band for MBP-Strep-FraD<sub>pp</sub> was detected in the elution fraction in some of the tested conditions (Figure 38A). However, background binding of MBP-Strep-FraD<sub>pp</sub> to the beads was also occurring in the absence of His-SepN<sub>pp</sub> (i.e. in Buffer 1). Furthermore, detection of a faint band was not always reproducible (see Buffer 6).

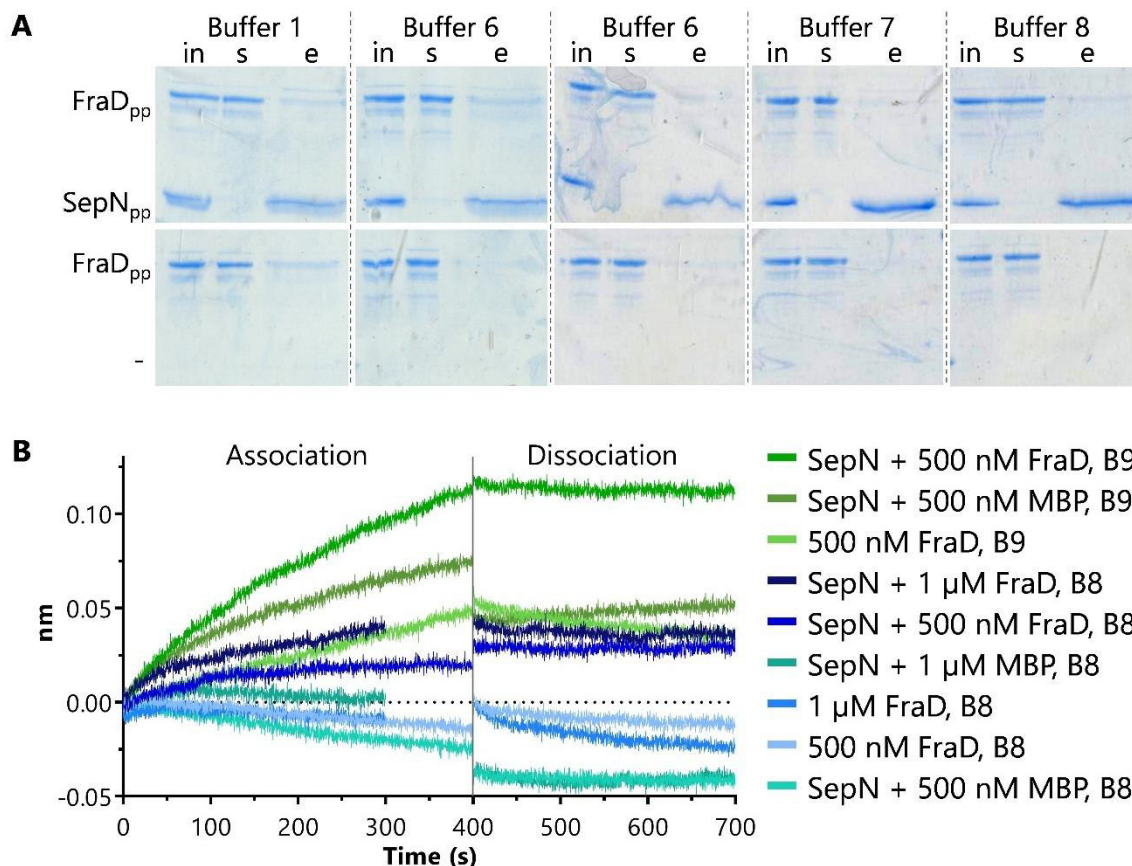


**Figure 38: In vitro protein-protein interaction assays with His-SepN<sub>pp</sub> and MBP-Strep-FraD<sub>pp</sub>.** (A) Batch pull-downs using Ni-NTA magnetic beads with 500 nM His-SepN<sub>pp</sub> and 500 nM MBP-Strep-FraD<sub>pp</sub> (upper panel) or MBP-Strep-FraD<sub>pp</sub> alone (lower panel) in the indicated buffers (input, in). After incubation with the beads, a sample of the supernatant (s) was taken and bound proteins were eluted (e) after washing. Fractions were separated via 13 % SDS-PAGE. (B) Interaction of 50 nM His-SepN<sub>pp</sub> with 500 nM/1 μM MBP-Strep-FraD<sub>pp</sub> or MBP was investigated via Biolayer-interferometry using the indicated buffers (Bx). Association was monitored for 300-400 s, followed by dissociation for 300 s.

As an additional approach, the purified protein parts were investigated via Biolayer-interferometry. 50 nM His-SepN<sub>pp</sub> were bound to Ni-NTA sensor tips. Association of 500 nM or 1  $\mu$ M MBP-Strep-FraD<sub>pp</sub> was monitored as shown in Figure 38B. Likewise to the batch pull-downs, only minimal interaction signals were detected as minimal shifts in the interference pattern. Background association of SepN<sub>pp</sub> with MBP in Buffer 9 was high, which rendered Buffer 9 inapplicable for this experiment. Background interaction was suppressed in Buffer 8. However, only minimal changes in the interference pattern were detected for SepN<sub>pp</sub> and FraD<sub>pp</sub> in a molar ratio of 1:10 and 1:20.

Taken together, interaction of the periplasmic parts of the two proteins is unlikely, at least under the conditions investigated here. Stability of protein complexes that are removed from defined intracellular conditions is often an issue (Mourão et al., 2014), especially, when the protein complex is integrated into membranes or located in different compartments (Oikonomou & Jensen, 2017). Septal junction protein complexes meet these criteria, since they are located in the periplasm and the cytoplasm and integrated into the cytoplasmic membrane.

## 7 Discussion

### 7.1 SJs are structurally distinct to cell junctions of metazoans and plants

Already 60 years ago, channels connecting neighboring cells in filamentous cyanobacteria were observed (Hagedorn, 1961; Lang & Fay, 1971). Soon, these cell connections were assumed to build a communication route to exchange carbon and nitrogen fixation products between vegetative cells and heterocysts (Wolk, 1968). Initially, the communication system was thought to be reminiscent of plasmodesmata in plants. There, cytoplasmic symplasts are formed by fusion of the cytoplasmic membranes of neighboring cells, and stretches of the endoplasmic reticulum, known as desmotubule, penetrate the channels (Figure 39A) (Nicolas et al., 2017).

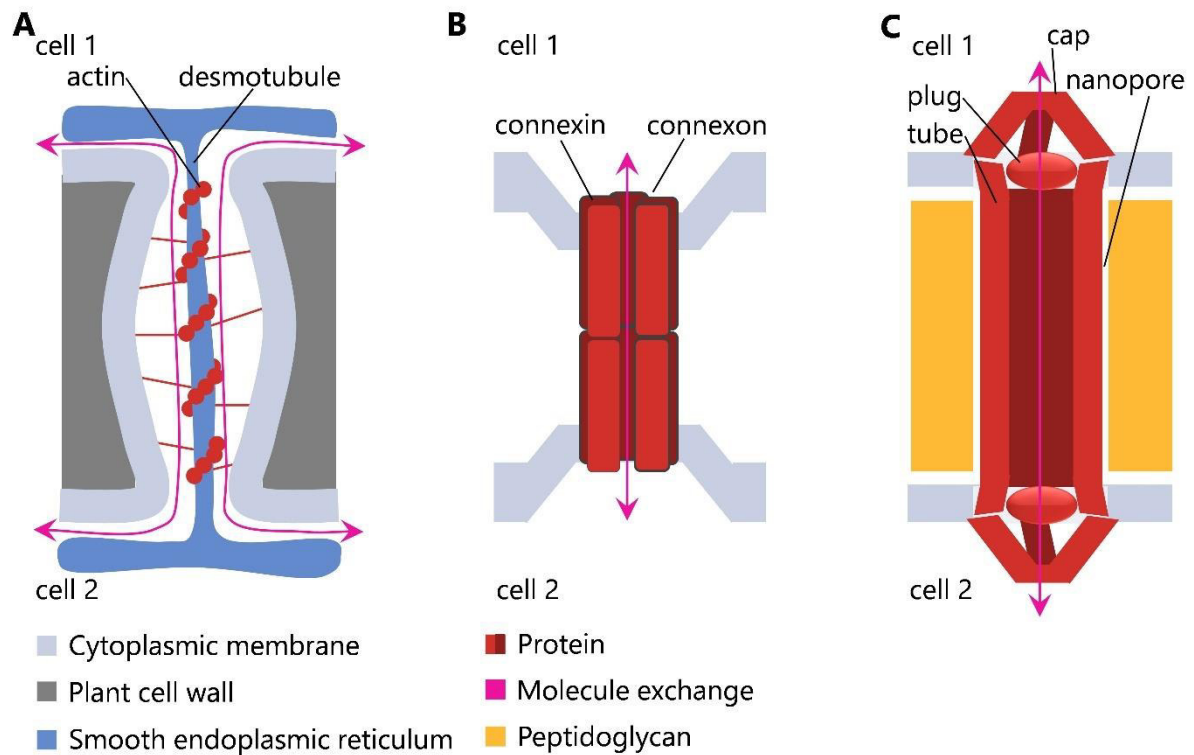


**Figure 39: Cell-cell communication structures in plants, metazoans, and filamentous cyanobacteria.** Schematic longitudinal sections through cell-cell connecting structures are shown. (A) A branch of the smooth endoplasmic reticulum (desmotubule) penetrates a channel formed by the cytoplasmic membrane to form a plasmodesma in plants. Plasmodesma are often found in groups and then called plasmodesmata (B) Metazoan gap junctions are formed out of two connexon hemichannels each consisting of six connexins. Cytoplasmic membranes of adjacent cells are in a defined and closer distance at the sites of gap junctions. (C) Proteinaceous SJs of filamentous cyanobacteria consist of caps, plugs and a length-variable tube that traverses the PG through a nanopore. Image modified from (Kieninger & Maldener, 2021).

However, assuming proteinaceous structures rather than membrane-lined channels (Wilk et al., 2011), the cell connections were eventually referred to as septal junctions (Mariscal, 2014; Flores et al., 2016). Analogy to metazoan gap junctions in terms of their proteinaceous nature and their function to allow small molecules to diffuse through was suggested (Mullineaux et al., 2008; Nieves-Mori3n et al., 2017b). At sites of gap junctions, cytoplasmic membranes of

adjacent cells are in close proximity (Söhl et al., 2005), in order to connect the cells via two hexameric hemichannels of fixed length, called connexons (Herve & Derangeon, 2013) (Figure 39B). Alteration of the distance of adjacent cytoplasmic membranes at sites of gap junctions is in contrast to SJs (Mullineaux et al., 2008). Homologs to eukaryotic connexins are absent in filamentous cyanobacteria (Kaneko et al., 2001), nevertheless, structural analogy of SJs to gap junctions was suggested (Ramos-León et al., 2017).

In this work, it was shown that SJs and gap junctions are structurally different (see 6.1). In contrast to gap junctions, SJs comprised three modules: (i) a tube traversing the PG through a nanopore to connect two adjacent cells ended at both sites in (ii) a membrane-embedded plug module, which was covered by (iii) a five-fold symmetric, cytoplasmic cap (Figure 39C). Remarkably, the tube was of variable length (Publication 1, Figure 1A, B), which is beneficial if the inconsistent thickness of the PG is considered. Instead of moving the neighboring cytoplasmic membranes closer together, the SJ tube is adjusted to bridge the gap. This implied consistence of the tube out of polymerizing protein subunits.

Here, the in-depth study of the cell-cell communication machinery was performed with the multicellular model organism *Anabaena* sp. PCC 7120. However, the three-modular SJs were also observed in cryotomograms of *Nostoc punctiforme* and *Trichodesmium erythraeum* (Publication 1, Figure S7G, H). *Nostoc punctiforme* is like *Anabaena* sp. PCC 7120 member of the heterocystous Nostocales. *Trichodesmium erythraeum* belongs to the filamentous non-heterocystous Cyanobacteria of the order Oscillatoriales, but is able to fix atmospheric nitrogen in diazocytes (Bergman et al., 2013). Strikingly, the fluorescent tracer calcein was not exchanged between cells of *Oscillatoria terebriformis*, also a member of Oscillatoriales, in FRAP experiments (Mullineaux et al., 2008). Therefore, it was concluded that SJs or SJ-like structures are absent in non-differentiating cyanobacterial strains (Mullineaux et al., 2008). Genes encoding communication-related proteins like *fraC*, *fraD*, *sjcF1*, *amiC*, and the C-terminal domain of *sepJ* are present in the genomes of *Nostoc punctiforme* and *Trichodesmium erythraeum* (Weiss et al., 2019), but absent in *Oscillatoria terebriformis*. This suggests conservation of SJs in a wide range of filamentous cyanobacteria, also including non-heterocystous species (Weiss et al., 2019), but not necessarily in an entire order. Conservation of the cell-cell connecting structures in various filamentous cyanobacteria emphasizes the importance of a gated cell-cell communication system for these organisms (Kieninger & Maldener, 2021). Moreover, structures similar to SJ tubes were observed between cells of filamentous *Streptomyces coelicolor*, a Gram-positive bacterium of the phylum Actinobacteria (Jakimowicz & van Wezel, 2012). Since the occurrence of FraD is restricted to filamentous cyanobacteria but cell-cell joining structures are present in other bacteria, cell junctions might have evolved several times in Bacteria, further pointing out the significance of such systems in filamentous organisms.

## 7.2 SJs are gated cell-cell connections

The surprisingly complex architecture of SJs (Figure 8A) strongly suggested the ability to regulate IC. The observation of ceased communication between senescent heterocysts and vegetative cells already led to speculations about a mechanism to close SJs previously (Nürnberg et al., 2015). In my work, regulation of IC dependent on various stress conditions was shown via FRAP assays after challenging cells with different compounds and conditions (see 6.1.2 and 6.2.2). The disruption of the proton motive force by treatment of the cells with the protonophore CCCP resulted in a “no communication” phenotype in the majority of analyzed cells (Publication 1, Figure 2). Interestingly, the closure of SJs could be reversed within a few hours after removal of the stress agent, also when protein biosynthesis was inhibited (Publication 1, Figure 2D). We therefore concluded, that SJs are gated cell-cell connections that function in analogy to eukaryotic gap junctions (Weiss et al., 2019). In fact, intercellular diffusion through gap junctions is likewise halted upon collapse of the proton motive force (Socolar & Politoff, 1971; Obaid et al., 1983). Intercellular communication through gap junctions is also influenced by several other changes of intracellular conditions (Herve & Derangeon, 2013). For example, by acidification of the cytoplasm, probably via intramolecular connexin interaction (Turin & Warner, 1977; Herve & Derangeon, 2013), or phosphorylation of connexins, which leads to disassembly of the junctions (Herve & Derangeon, 2013).

Interconnection between the membrane potential and the proton gradient did not allow to ascribe the trigger for closure to one of the proton motive force components. Due to the small size of bacterial cells, changes in the membrane potential could also change the chemical potential, and vice versa (Benarroch & Asally, 2020). The protonophore CCCP was the most effective compound to induce SJ gating in the WT. Besides depolarization of the membrane potential, CCCP also caused acidification of the cytoplasm (Figure 9). Acidification of the medium resulted in an even lower  $pH_i$  than by treatment with CCCP (Figure 10C). However, a larger fraction of cells exhibited a “no communication” phenotype when treated with CCCP in contrast to treatment with acidified medium (Figure 10B). It can therefore be speculated, that membrane depolarization has a higher impact on SJ gating than disruption of the proton gradient. This might be supported by delayed gating of SJs upon treatment with DCCD in comparison to CCCP (Figure 10A). The primary effect of DCCD is to inhibit the F-ATPase, but it also leads to depolarization of the membrane potential, which might be achieved only after a while. Depolarization of the membrane was also described as a result of incubating *Anabaena* strains at 4 °C (Apte & Thomas, 1986). However, incubation in the cold did not trigger SJs to close (Figure 11A). Unfortunately, the ionophores Nigericin and Valinomycin, which allow the discrimination between effects of the membrane potential or the proton gradient, did not lead to clear results and also affected the *fraCfraD* mutant (data not shown). In conclusion, the actual trigger for SJ closure still is unknown. Nevertheless, it is very likely that disruption of the membrane potential plays a major role in this process.

The “slow increase” response observed during FRAP in a fraction of cells after exposure to stress conditions might be caused by partial closed SJs, a phenomenon that was observed in gap junctions (Ek-Vitorin & Burt, 2013; Weiss et al., 2019). Another possibility would be an independent gating of single SJs within a septum and will be discussed below (7.7).

In conclusion, although structurally different, gap junctions and septal junctions are functionally analog to each other and enable multicellular organisms to gate the exchange of molecules between cells (Weiss et al., 2019). The evolution of cell-cell communication systems in multicellular organisms in all kingdoms of life emphasizes their dependence on an IC system. Regulation of intercellular diffusion seems to be highly important under filament fragmentation or predation of single cells to avoid leakage of cytoplasmic components into the exterior. Gating of SJs can therefore be seen as a survival strategy to maintain the life of a filament upon injury of single cells. Moreover, regulation of IC might also be necessary during heterocyst differentiation and will be discussed below (7.5).

### 7.3 SJ cap and plug modules are essential for gating

The three-modular architecture of SJs allows the cells to regulate IC. The transition from an open to a closed state, which inhibits molecule exchange, was accompanied by a structural rearrangement of the cap module (6.1.2). In the rearranged cap, the symmetric lateral openings were absent and its sidewalls were in closer proximity to the plug module (Figure 8). We suggested the conformational change in the cap structure might happen through a 30° rotation of each of the five arches (Publication 1, Figure S4B-E). The essentiality of the cap and plug modules to stop cell-to-cell diffusion was proven by analysis of a *fraDfraC* double mutant (6.1.2). Non-communicating cells were never observed in this mutant upon treatment with CCCP, which was linked to the absence of cap and plug modules (Publication 1, Figure 5A, D). Since structural changes in the plug module were not observed after the switch into the closed cap conformation (Publication 1, Figure 3D, E), its function remained unknown. However, a role in restriction of the particle size for passing the cell connections was assumed (Weiss et al., 2019).

In co-IPs with the SJ component FraD, SepN was the most promising candidate to interact with the former (see also 7.6), and therefore, to be involved in SJ formation itself (6.4). Indeed, a subtomogram average of electron cryotomograms revealed the absence of the plug module but an assembled cap in a *sepN* mutant (Figure 27B, C). Interestingly though, the SJ caps were reminiscent of the closed, no communication state in WT cells (Figure 27C). The combination of missing plug with present cap allowed the elucidation of the plug's function. Unexpectedly, the plug module seemed to be important for keeping the cap structure in its opened, five-fold symmetric form.

Despite the nanopore array in a *sepN* mutant was similar to the WT (Figure 26), the rate of IC was significantly reduced (Figure 24A). The missing openings in the cap modules might

be the reason for this deceleration of intercellular exchange. Moreover, although the cap structure was present in the *sepN* mutant, SJs were insensitive to treatment with CCCP. This was evidenced by CCCP-FRAP experiments, in which the majority of cells still communicated after protonophore treatment, similar to the *fraD* mutant (Figure 24B). Ongoing communication despite closed caps and inability to fully inhibit intercellular diffusion proposed an important role for the plug module in SJ gating and especially in efficient closure of the channels. Minor changes of closed-like caps in the *sepN* mutant upon CCCP treatment towards a cap module fully switched into its closed conformation was hypothesized. This is, because fluorescence recovery curves after bleaching showed a lower recovery compared to non-treated mutant cells (Figure 25).

Taken together, both, cap and plug modules are essential for proper communication and gating of SJs and form a functional unit, as already suggested previously (Weiss et al., 2019). Whereas the cap undergoes a conformational change into a closed position, the plug is important to seal the channels and might be essential for the open cap position.

#### 7.4 SJ gating is not synchronized within a filament

Regulation of IC by structural rearrangement of the SJ cap module was shown via FRAP experiments after cells were stressed. This setup, however, only allowed tracking of communication and its regulation for whole filaments, since the whole culture was challenged. How do remaining cells within a filament behave when a single cell is disrupted or upon filament fragmentation? Is communication stopped in the whole filament or just in a single cell septum?

These open questions were addressed by an advanced FRAP experiment with multiple sequential laser-bleaching, referred to as FRAMP (6.2.3). After ten sequential bleaches, half of the WT cells ceased communication completely and in the other half diffusion was impaired (Figure 12C). This was in contrast to the *fraCfraD* mutant. Usual FRAP measurements of the adjacent cells revealed “full recovery” responses. Therefore, the decision to close SJs happened on the cellular level and was not synchronized within a filament. The actual trigger for the closure in this experiment might be local permeabilization of the membrane and therefore changes in the membrane potential. Denaturation of SJs due to consecutive bleaching with a high laser intensity was at least excluded for a fraction of cells, since almost half of the before non-communicating cells recovered their fluorescence after a 2-3 h recovery time (Figure 12F). However, it needs to be mentioned, that 8 % of the multiple bleached cells died during the recovery phase, which shows the severity of the treatment.

Parallel to this work, Arévalo et al. came to a similar conclusion that communicating and non-communicating cells coexist within a filament (Arévalo et al., 2021). They observed 58-80 % non-communicating cells in a WT culture that was grown supplemented with combined nitrogen. In this work, such high fractions of non-communicating cells in the WT were never

observed and also were never described in previous FRAP studies. Nevertheless, the authors observed a drop in the fraction of non-communicating cells when the cells were shifted into nitrate-free medium (Arévalo et al., 2021). From this, they suggested that gating of SJs is dependent on the metabolic status of individual cells and that communication is only allowed in situations of metabolic imbalance.

In conclusion, gating of SJs is not synchronized in a filament, but is a very dynamic mechanism to quickly “separate” single cells from the filament. This allows a precise control of IC and protects the organism from losing cytoplasmic content and nutrients to the exterior. At the same time, exchange of fixation products and signaling molecules in the remaining filament is still maintained. Regulation of IC seems to be a tightly controlled mechanism, which we just start to understand. Further research is necessary to uncover the entire mechanisms of the cell-cell communication system.

## 7.5 FraD is a structural SJ component

The septum-localized protein FraD was identified as the first structural component of the SJ protein complex (6.1.2). Luckily, GFP fused to the N-terminus of FraD was caught in the SJ tube lumen and therefore appeared as additional density in cryo electron subtomogram averages as extension of the plug module (Publication 1, Figure 6A). Structural alteration of SJs in a *fraD* mutant was concluded from CCCP-FRAP assays, since the cells were incapable to gate IC (Publication 1, Figure 5D). Indeed, major structural alterations in a *fraD* mutant manifested in absent cap and plug modules (Publication 1, Figure 5B) explained the ungated SJs (see also 7.3).

The *fraD* mutant was complemented with different parts of FraD and characterized to gain deeper insights in the involvement of FraD on SJ assembly. Complementation of the *fraD* mutant with the membrane domain of FraD restored SJ closure upon treatment with CCCP almost to the WT-level (Figure 14A). Therefore, formation of the cap and plug modules in the presence of FraD<sub>TM</sub> seemed to be likely and was indeed confirmed by ECT (Figure 20). However, switching from the closed state back in the open state was not possible, which might suggest involvement of the C-terminal, periplasmic part of FraD in this process. Unfortunately, complementation effects of FraD<sub>PP</sub> could not be investigated, because it was not excreted into the periplasm despite a Tat signal sequence and did not localize to the septa (Figure 19). The nanopore array in the *fraD*<sub>TM</sub> strain was only slightly increased in comparison to the *fraD* mutant, which was also resembled by a communication rate in between the WT and the knockout mutant (Figure 15B, C). In conclusion, FraD<sub>TM</sub> was sufficient to compensate the mutant phenotype to a great extent. Nevertheless, minor structural changes of the SJs that account for the still reduced nanopore array and little less efficient SJ gating, might got overseen in the here achieved resolution in cryotomograms. Moreover, indirect involvement of FraD<sub>PP</sub> in drilling the nanopores for example by mediating protein-protein interactions

cannot be excluded. FraD localizes to the nascent septum in dividing cells (Merino-Puerto et al., 2011b), hence, in a state when nanopores are not drilled, yet (Bornikoel et al., 2018). This supports the suggested role of FraD, or especially FraD<sub>PP</sub>, in the recruitment or interaction with proteins involved in septum maturation and nanopore drilling, before it becomes part of the SJ complex.

As little as the first two transmembrane domains of FraD allowed at least partly assembly of plug and cap modules to the SJ tubes. This was proposed, since a fraction of 30 % of analyzed cells (about 24 % more than in the *fraD* mutant) ceased IC in CCCP-FRAP assays when FraD<sub>2TM</sub> was expressed in the *fraD* mutant background (Figure 15B). Furthermore, the “slow increase” group was enlarged by 10 % in comparison to the CCCP-treated knockout strain. To gain a more detailed view on the assembly, it would be interesting to analyze the *fraD*<sub>2TM</sub> strain via ECT. Since three more TMDs are missing compared to the FraD<sub>TM</sub> strain, differences in electron cryotomograms could be more pronounced.

Surprisingly, expression of FraD<sub>TM</sub> did not allow diazotrophic growth (Figure 16), although SJ gating was largely restored. In fact, heterocyst development was even more retarded than in the full *fraD* mutant. Heterocysts in the *fraD*<sub>TM</sub> strain developed only after 48 h in nitrate-depleted medium and just occasionally formed precipitates with TTC (Figure 17), indicative of micro-oxic conditions. The worsened process of heterocyst development gave reason to hypothesize that regulation of diffusion might be critical during cell differentiation. Assuming the need to cease IC early after depletion of nitrate, inability of the *fraD*<sub>TM</sub> strain to resume communication and therefore to exchange signaling molecules, would explain a delayed maturation of heterocysts. Eventually developed heterocyst, however, appeared identical to the heterocysts in a *fraD* mutant (Figure 18), exhibiting a widened heterocyst-vegetative cell septum as described before (Merino-Puerto et al., 2010).

In conclusion, heterocyst differentiation is highly dependent on a fully functional cell-cell communication system. An involvement of the periplasmic part of FraD in formation of the heterocyst-vegetative cell septum is furthermore conceivable.

## 7.6 SepN is involved in formation of the SJ complex

The identification of FraD as the first structural SJ component in the first part of this work (6.1.2) provided a basis to identify further components of these multimeric protein complexes. The most promising candidate was All4109, because it was co-eluted with FraD in all performed co-IPs with and without crosslinking by glutaraldehyde (Table 11). Due to its focused, septal localization similar to SepJ (Figure 22A), All4109 was named SepN.

First hints towards a role of SepN in the assembly of SJ complexes were obtained, when a WT-like nanopore array (Figure 26) combined with a severely reduced communication rate (Figure 24A) was observed in a *sepN* mutant. The presumption of a structural involvement in SJ formation was further strengthened by an insensitivity towards treatment with CCCP in

terms of SJ gating (Figure 24A). In fact, the phenotype of a *sepN* mutant in CCCP-FRAP assays was very similar to the *fraD* mutant. Analysis of a *sepN* mutant via ECT indeed revealed prominent alterations in the architecture of SJs. First, the plug but not the cap module was absent, and second, SJ caps were in a conformational state reminiscent of the closed form in WT cells (Figure 27). These observations allowed the conclusions that (i) SepN is directly or indirectly involved in the assembly of SJs, (ii) the plug domain is important for holding the cap in its open position, and (iii) the plug is essential for ceasing IC (see also 7.3). The reduced rate of molecular exchange could thus be explained by the altered cap structure that nevertheless still allowed diffusion, because of the lacking plug modules.

Surprisingly, subcellular localization of FraD was not changed in a *sepN* mutant (Figure 32), which challenges the previous conclusion of FraD being a structural part of the plug module (Weiss et al., 2019). The insights into SJ architecture revealed by the *sepN* mutant rather suggests FraD as the linker between cap, plug, and the tube module. This would explain the absence of both, cap and plug modules, in a *fraD* mutant, and at the same time the independent loss of the plug in a *sepN* mutant. It might be imaginable that the plug domain in a *fraD* mutant is absent, because SepN is dependent on FraD to localize correctly. This would fit to the lower septal fluorescence signal emitted from SepN-sfGFP in a *fraD* mutant than in the WT (Figure 33). Alternatively, the fluorescence signal caused by SepN, possibly localized to the SJs might be below the detection limit, considering the few nanopores and SJs, in a *fraD* mutant. To distinguish between these two possibilities, SepN could be immunolocalized in a *fraD* mutant with  $\alpha$ -SepN antibodies, since immunolocalization is more sensitive than detecting emission of GFP.

Since disruption of *sepN* led to slightly different heterocyst development phenotypes and morphologies in two independently created mutant clones (see 6.4.6), the impact of SepN on heterocyst development might rather be indirect. The common thread between the mutants was the ability to grow on N<sub>2</sub> without filament fragmentation (Figure 28C). Additionally, heterocyst development seemed slightly delayed, but was manifested differently. Whereas heterocysts in the earlier mutant were separated by more vegetative cells during the first days after removal of nitrate (Figure 29A) and heterocysts appeared immature after 2 days growth on N<sub>2</sub> in TEM analysis (Figure 30A), this was not observed for the second conjugants. Monitoring of the growth of both clones from the second conjugation exhibited a slight growth disadvantage compared to the WT (Figure 31). Assuming, that SJ gating is important during heterocyst differentiation (see 7.5), the minor delay in the *sepN* mutants could arise from ungated SJs.

Cryotomograms of a *sepN-sfgfp* fusion strain revealed reassembled SJ complexes with present plug modules and a cap structure with the lateral openings (Piotr Tokarz, unpublished). Unfortunately, an extra density indicating GFP, as it was the case for GFP-FraD (Publication 1, Figure 6A), was not observed in these cryotomograms. However, potential

flexibility in the position of GFP fused to the C-terminus of SepN would not allow its detection in subtomogram averages. Hence, direct structural involvement of SepN in the SJs remains to be verified. However, first hints on SepN as direct structural SJ component were gathered via ECT in a mutant in which SepN was fused to both, maltose binding protein and sfGFP (Piotr Tokarz, unpublished). In preliminary subtomogram averages, this mutant showed a plug domain with extra densities, which could arise from the larger tag. Interestingly, the majority of SJs in this mutant did not show cap modules assembled to the tube.

Apposite with the hypothesis of SepN being a structural SJ component, the rate of communication in a *sepN-sfgfp* fusion strain dropped to the same level as in the knockout mutant (Figure 24A), although SJs seemed to be correctly assembled (Piotr Tokarz, unpublished). Also, SJ gating was possible, albeit not to the full extent compared to the WT or the complemented mutant without fusion to GFP (Figure 24B). Therefore, GFP fused to SepN might interfere with molecule diffusion. However, minor changes in the SJ architecture of the *sepN-sfgfp* strain might be beyond the resolution limit of the obtained cryotomograms and hence cannot be excluded. To conclude, further research is needed to answer the detailed dependencies and functions of FraD and SepN in the assembly of the cell-cell connections.

## 7.7 FraI might be involved in formation of the nanopore array

FraI was pulled down with FraD in three crosslinked samples, and with SepN as the second and fourth most abundant protein in both, the crosslinked and non-crosslinked sample (Table 11). A mutant deficient in *fraI* exhibited a severe phenotype concerning IC and cell differentiation (6.4). Forty percent of the analyzed cells did not communicate in FRAP experiments (Figure 24), which is in line with 41 % of the analyzed septal PG discs that harbored zero to two nanopores per septum (Figure 26B). Another 45 % of the cells were assigned to the “slow increase” response group, which correlates with a fraction of 44 % of septal PG discs, in which three to ten nanopores were drilled. “Slow increase” responses in FRAP experiments were also observed in the WT, especially when only shortly treated with CCCP or with concentrations below 50  $\mu$ M (Publication 1, Figure S4I, 2C). Assuming that this response corresponds to only a few SJs in the septum, it could be hypothesized that SJs within a septum can individually be gated. Such a mechanism would allow an even more precise fine-tuning of IC than regulation on the cellular level (compare 7.4) dependent on the specific needs of the organism.

In the absence of FraI the nanopore array was reduced to average 12 % compared to the WT (Figure 26B), but gating of the remaining SJs was still possible (Figure 24B). Thus, involvement of FraI in formation of the nanopore array rather than in assembly of SJs was proposed.

Subcellular localization revealed FraI distributed over the whole septal plane in some of the cells (Figure 22A, B) reminiscent of AmiC-type amidases (Berendt et al., 2012).

Furthermore, FraI might move with the Z-ring during septum restriction, as fluorescence foci were detected in the midcell ring of some of the dividing cells (Figure 22C). Movement with the Z-ring was described for proteins that play a coordinator role in formation of the cell-cell communication machinery like FraC (Merino-Puerto et al., 2010), SepJ (Flores et al., 2007) and AmiC-type amidases (Berendt et al., 2012). Fluorescence from a FraI-sfGFP fusion was almost absent in filaments growing in nitrogen fixation conditions (Figure 23). During the time after shifting from nitrate-supplemented into nitrate-depleted medium, in which cells are not dividing but adapting to the new conditions, AmiC-GFP was not localized to the septa of vegetative cells (Berendt et al., 2012). However, after the maturation of heterocysts, AmiC-GFP was again present in the septa of now dividing vegetative cells (Berendt et al., 2012). Since the *fraI-sfgfp* strain did not survive diazotroph conditions, cells were probably not dividing after the shift in nitrate-free medium. Assuming a role for FraI in nanopore formation and relation to amidases, this might explain the non-detectable fluorescence of FraI in growth-arrested cells.

Interestingly, localization of the amidases in the septum was reduced in a *fraI* mutant (Figure 34), which further suggested a relation between FraI and one of the amidases. Regulation of AmiC expression by FraI was excluded, since the protein levels of the amidases were unaltered in crude cell extracts of a *fraI* mutant in comparison to the WT in an  $\alpha$ -AmiC Western Blot (Ana Janovic, unpublished).

FraI got its name from the severe fragmentation phenotype, which led to 91 % of filaments with a length of ten cells or less 72 h after shift in nitrate-depleted medium (Figure 28C). Importantly, the majority of filaments already consisted of less than 20 cells per filament in nitrate-supplemented medium. The reason for filament fragmentation is not fully understood, but different suggestions were made. Fragmentation in a *sepJ* mutant was suggested to be linked to involvement of SepJ in maturation of the septum (Arévalo et al., 2021). Generally, genetically programmed response to nutrient limitations was suggested, which would help cells to more easily spread to more favorable environments (Bauer et al., 1995). In this scenario, fragmentation during nitrogen fixation may improve the efficiency of distributing fixation products within a filament (Bauer et al., 1995). Since IC was nearly absent in a *fraI* mutant, metabolic imbalance between the cells in a filament might be high, especially when dependent on N<sub>2</sub>. Filament fragmentation might therefore be a stress response of cells trying to survive. Another possibility is conceivable if an inhibitory function of FraI towards the amidase activity is assumed. Since the hydrolytic activity of the amidases would be uncontrolled in the absence of FraI, the amidases might hydrolyze the whole septum instead of drilling pores. This would lead to separation of cells and therefore to filament fragmentation. This hypothesis could be investigated via an *amiCfraI* double mutant, in which filament fragmentation should be less pronounced. Similarly, a functional relation between SepJ or FraC/FraD and AmiC1 was suggested, because filaments were longer in the double

and triple mutants, respectively, than in the mutants with functional *amiC1* (Bornikoel et al., 2017).

N- and C-terminal fusions of sfGFP to FraI resulted in different phenotypes. Fusion to its C-terminus led to a nanopore array similar to the knockout mutant (Figure 26B). However, only 11 % of the isolated PG discs harbored zero to two nanopores, whereas the majority (67 %) possessed a nanopore array between three to ten pores. The slightly increased nanopore array allowed the majority of cells to fully recover in FRAP experiments (Figure 24B), albeit with a very low communication rate (Figure 24A). While gating of SJs into the closed state was possible, reopening after removal of CCCP was less efficient than in the WT and similar to the complemented *fraI* mutant DR823.847. Probably due to the very reduced nanopore array, the strain expressing FraI-sfGFP could not grow on atmospheric nitrogen (Figure 28A). Complementation of the *fraI* mutant with sfGFP-FraI, in which sfGFP was inserted between the signal peptide and FraI, enabled the cells to communicate with a WT-like rate (Figure 24A), and to grow in the absence of nitrate (Figure 28A). Strikingly though, reopening of closed SJs was not possible at all (Figure 24B).

In conclusion, the cytoplasmic C-terminus of FraI might play a role in coordinating or recruiting the nanopore-drilling proteins. However, direct interaction of FraI with AmiC-type amidases is unlikely, since only a few amino acids of FraI are predicted to range into the periplasm (Figure 21B). Nevertheless, interaction with other proteins of the cell division and nanopore drilling machineries via the TMDs or the cytoplasmic part of FraI is feasible. A possible influence of FraI, especially of a free N-terminus, on the switch from closed into open cap modules remains elusive. As also suggested for FraC and FraD (Bauer et al., 1995; Merino-Puerto et al., 2010), the inability to efficiently develop heterocysts in the absence of FraI might rather be an indirect effect caused by the severe impairment in communication than direct involvement in cell differentiation.

## 7.8 Proteins with unclear impact on cell-cell communication

Alr4788 was identified in all crosslinked samples in co-IPs directed against FraD (Table 11) and in a SepN co-IP with and without glutaraldehyde (Table 12). A fusion of sfGFP to the C-terminus of Alr4788 showed its localization to the septum in a focused manner (Figure 22), similar to the localization pattern of SepN (Figure 22) and SepJ (Flores et al., 2007). The rate of IC in an *alr4788* mutant was similar to the WT, and SJ gating was only slightly reduced reminiscent of a *sepJ* mutant (Publication 1, Figure 4D). Interestingly, septal PG discs were drilled with significantly more nanopores in comparison to the WT (Figure 26B). However, disruption of *alr4788* had no effect on heterocyst differentiation (Figure 28) or on localization of FraD (Figure 32). If so, Alr4788 plays a minor role in the cell-cell communication system or has a function in other than conditions tested here.

Another investigated mutant, in the gene *all3520*, showed a reduced communication rate (Figure 35A) but a nanopore array similar to the WT (Figure 35C). However, it's worth mentioning, that the mutation of *all3520* was created by Lechno-Yossef et al., and therefore is not in the exact same WT background (Lechno-Yossef et al., 2011). Different WT strains differ in their communication rate. So, the WT in a study from Nieves-Morion et al. showed a recovery rate constant of  $R=0.07$  (Nieves-Mori3n et al., 2017a), whereas the here investigated WT exhibited a rate of  $R=0.1$ .

An interesting protein for future studies is Alr7326, because it was highly abundant in the crosslinked and non-crosslinked co-IP directed against SepN and also present in two  $\alpha$ -FraD co-IPs.

## 8 Conclusions and outlook

The huge network of proteins involved in formation of the cell-cell communication system emphasizes its importance for the filamentous cyanobacterium. This work provided new mechanistic insights into cell-cell communication and revealed for the first time SJs as gated structures. Gating appears to be a survival strategy and as being probably important for cell differentiation. Furthermore, proteins involved in formation or structural assembly of the cell-cell communication machinery were identified and characterized.

To investigate potential regulation of IC, a CCCP-FRAP assay was established, in which cells were treated with the protonophore CCCP, which disrupts the proton motive force and thereby causes intracellular stress. Indeed, regulation of cell-to-cell diffusion could be proven and could also be induced by other stresses. Removal of the causal agent of stress and parallel inhibition of protein biosynthesis revealed the reversibility of the interrupted communication. In conclusion, this work demonstrated that SJs are gated cell-cell connections.

Analysis of untreated and CCCP-treated WT-cells via ECT, performed by our collaboration partners, supported the physiological findings and revealed the SJ architecture in a resolution never achieved before. Besides a PG-traversing tube, SJs comprised membrane-embedded plug domains and five-fold symmetric cap modules on both sites of the cell junctions. A conformational altered cap module with loss of the lateral openings allowed to conclude that the cap is essential to cease communication. The rearrangement of a macromolecular complex to regulate IC furthermore suggested functional analogy of SJs to eukaryotic gap junctions.

The established CCCP-FRAP assay turned out to be a helpful tool to screen mutants in putative cell junction proteins on their involvement in SJ assembly. In this way, and confirmed via ECT, FraD was identified as the first structural SJ component, whereas SepJ, SjcF1 and AmiC1 were excluded to be structural components of these protein complexes. Direct or indirect involvement of FraC still remains unknown.

A major aim of this work subsequently was the identification of further SJ-related proteins and the characterization of created mutants. Therefore, a co-IP using the membrane protein FraD as bait was developed and performed in sextuplicate. Interaction of FraD with All4109, named SepN, was strongly suggested, since it was detected in all of the co-IPs (Figure 40). Moreover, in a reverse co-IP with SepN, the most abundant protein was FraD. Mutation in the gene coding for the septum-localized protein SepN led to loss of SJ gating, which was caused by the absence of the SJ plug module. Structural involvement of SepN is therefore likely, nevertheless, if direct or indirect remains open for further investigation. Absence of the SJ plug in the *sepN* mutant manifested unexpected importance of the latter in retention of five-fold symmetric caps and in tightly closure of the cell-cell connections.

Another interesting protein identified via co-IPs was Alr4714, which was referred to as FraI, because of its severe fragmentation phenotype. FraI is presumably not involved in SJ assembly, but very likely plays a role in the formation of the nanopore array. Therefore, and because of its similar localization to amidases, relation to AmiC was hypothesized (Figure 40). Furthermore, Alr4788 was identified in co-IPs as putative FraD interactor and a mutant disrupted in the respective gene was created. However, no phenotype concerning IC and SJ gating was observed, which is why its role and involvement in the cell-cell communication network remains in question.

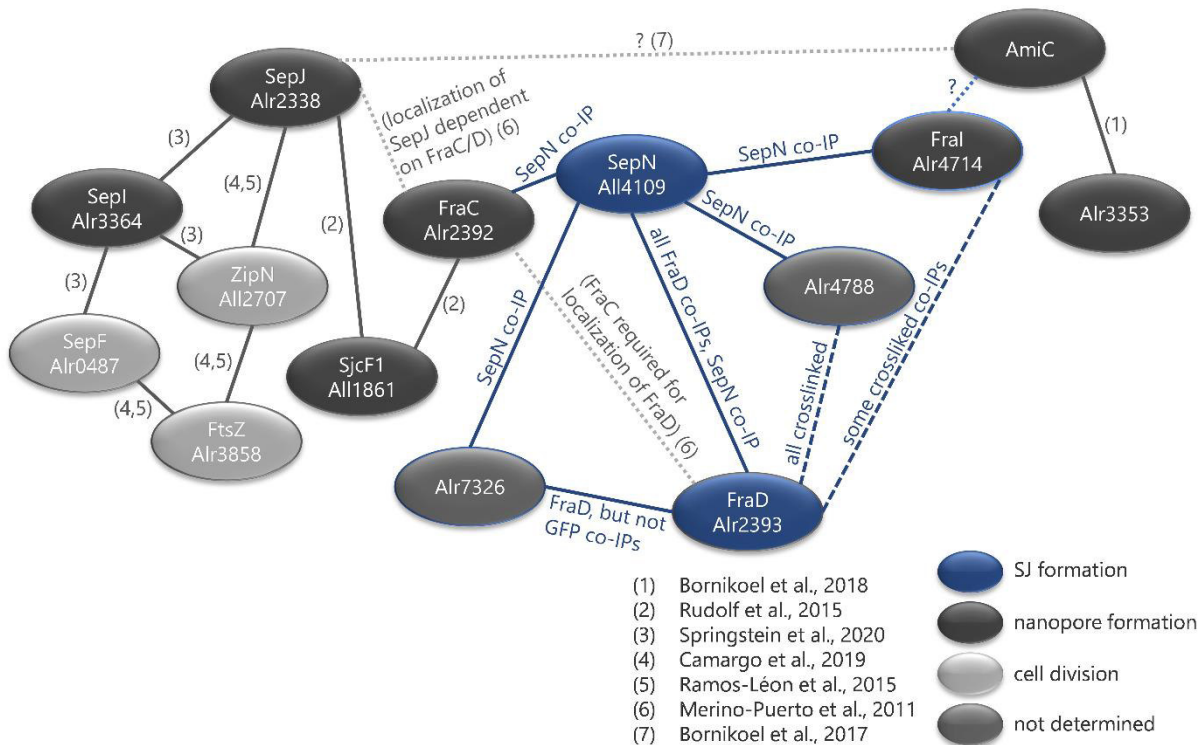


**Figure 40: Network of proteins involved in the cell-cell communication system.** Proteins that are involved in nanopore formation (dark grey) are linked to cell division (light grey) and SJ formation proteins (blue). Black lines represent confirmed protein interactions with indication of the respective publication. Dotted grey lines depict suggested but not yet identified protein interactions. Blue lines show connections suggested in this study via co-IP experiments as stated above the lines. Dashed blue lines represent suggested relation only based on crosslinked co-IP samples. Proteins with a blue border were identified in this work.

No protein-protein interactions of the here confirmed SJ component FraD with any other protein in the network could ever be shown in vitro or in vivo (Rudolf et al., 2015; Flores et al., 2019; Springstein et al., 2020). Additionally, FraC, SepJ, SjcF1 and the amidases were never detected in co-IPs using FraD as bait, and therefore, relation of FraD to these other proteins remained debatable. The here identified protein SepN might bridge the structural SJ component FraD to the nanopore formation proteins via FraC (Figure 40). Furthermore, a connection between SepN and FraI is possible regarding identified proteins of the  $\alpha$ -SepN co-IP, which in turn might directly or indirectly link the amidases to the network. Strengthening the hypothesis of SepN as the protein that connects nanopore formation to SJ formation could be the topic of future studies.

In summary, this work greatly increased the knowledge of the cell-cell communication system in filamentous cyanobacteria in structural, mechanistic and physiological aspects. Furthermore, the established CCCP-FRAP assay is a valuable tool to screen future mutants in proteins identified by the here developed co-IP workflow for (membranous) proteins involved in IC. Co-IPs directed against SepN using specific antibodies might be the first step to identify further structural SJ components. Although a wide variety of proteins were already investigated and described to be part of this network, a lot of proteins and structural SJ components are still waiting to be discovered.

## References

- Al-Haj L, Lui YT, Abed RMM, Gomaa MA, Purton S, (2016). Cyanobacteria as chassis for industrial biotechnology: Progress and prospects. *Life* 6:4, 42.
- Álvarez-Escribano I, Vioque A, Muro-Pastor AM, (2018). NsrR1, a nitrogen stress-repressed sRNA, contributes to the regulation of nbla in *Nostoc* sp. PCC 7120. *Front. Microbiol.* 9:2267.
- Angermayr SA, Hellingwerf KJ, Lindblad P, Teixeira de Mattos MJ, (2009). Energy biotechnology with cyanobacteria. *Curr. Opin. Biotechnol.* 20:3, 257-63.
- Apte SK, Thomas J, (1986). Membrane electrogenesis and sodium transport in filamentous nitrogen-fixing cyanobacteria. *Eur. J. Biochem.* 154:2, 395-401.
- Arévalo S, Flores E, (2021). Heterocyst septa contain large nanopores that are influenced by the Fra proteins in the filamentous cyanobacterium *Anabaena*. *J. Bacteriol.* JB.00081-21.
- Arévalo S, Nenninger A, Nieves-Mori6n M, Herrero A, Mullineaux CW, Flores E, (2021). Coexistence of communicating and noncommunicating cells in the filamentous cyanobacterium *Anabaena*. *mSphere* 6:1, e01091-20.
- Battesti A, Bouveret E, (2012). The bacterial two-hybrid system based on adenylate cyclase reconstitution in *Escherichia coli*. *Methods* 58:4, 325-34.
- Bauer CC, Buikema WJ, Black K, Haselkorn R, (1995). A short-filament mutant of *Anabaena* sp. strain PCC 7120 that fragments in nitrogen-deficient medium. *J. Bacteriol.* 177:6, 1520-6.
- Bekker A, Holland HD, Wang PL, Rumble D, Stein HJ, et al, (2004). Dating the rise of atmospheric oxygen. *Nature* 427:6970, 117-20.
- Benarroch JM, Asally M, (2020). The microbiologist's guide to membrane potential dynamics. *Trends Microbiol.* 28:4, 304-14.
- Berendt S, Lehner J, Zhang YV, Rasse TM, Forchhammer K, Maldener I, (2012). Cell wall amidase AmiC1 is required for cellular communication and heterocyst development in the cyanobacterium *Anabaena* PCC 7120 but not for filament integrity. *J. Bacteriol.* 194:19, 5218-27.
- Bergman B, Sandh G, Lin S, Larsson J, Carpenter EJ, (2013). Trichodesmium - a widespread marine cyanobacterium with unusual nitrogen fixation properties. *FEMS Microbiol. Rev.* 37:3, 286-302.
- Bertani G, (1951). Studies on lysogeny. I. The mode of phage liberation by lysogenic *Escherichia coli*. *J. Bacteriol.* 62:3, 293-300.
- Bok E, (2020). *The amidase AmiC2 and its peptidoglycan substrate in filamentous cyanobacteria*. Dissertation, University of Tübingen.
- Bornikoel J, Carrion A, Fan Q, Flores E, Forchhammer K, et al, (2017). Role of two cell wall amidases in septal junction and nanopore formation in the multicellular cyanobacterium *Anabaena* sp. PCC 7120. *Front. Cell. Infect. Microbiol.* 7386.
- Bornikoel J, Staiger J, Madlung J, Forchhammer K, Maldener I, (2018). LytM factor Alr3353 affects filament morphology and cell-cell communication in the multicellular cyanobacterium *Anabaena* sp. PCC 7120. *Mol. Microbiol.*
- Bradford MM, (1976). A rapid and sensitive method for the quantitation of microgram quantities of protein utilizing the principle of protein-dye binding. *Anal. Biochem.* 72:248-54.
- Brenes-Álvarez M, Vioque A, Muro-Pastor AM, (2020). The integrity of the cell wall and its remodeling during heterocyst differentiation are regulated by phylogenetically conserved small RNA Yfr1 in *Nostoc* sp. strain PCC 7120. *MBio* 11:1.

- Brilisauer K, Rapp J, Rath P, Schollhorn A, Bleul L, et al, (2019). Cyanobacterial antimetabolite 7-deoxy-sedoheptulose blocks the shikimate pathway to inhibit the growth of prototrophic organisms. *Nat. Commun.* 10:1, 545.
- Brocher J, (2015). The BioVoxel Image Processing and Analysis Toolbox. *EuBIAS-Conference*.
- Buikema WJ, Haselkorn R, (1991a). Characterization of a gene controlling heterocyst differentiation in the cyanobacterium *Anabaena* 7120. *Genes Dev.* 5:2, 321-30.
- Buikema WJ, Haselkorn R, (1991b). Isolation and complementation of nitrogen fixation mutants of the cyanobacterium *Anabaena* sp. strain PCC 7120. *J. Bacteriol.* 173:6, 1879-85.
- Burnat M, Schleiff E, Flores E, (2014). Cell Envelope Components Influencing Filament Length in the Heterocyst-Forming Cyanobacterium *Anabaena* sp. Strain PCC 7120. *J. Bacteriol.* 196:23, 4026-35.
- Büttner FM, Faulhaber K, Forchhammer K, Maldener I, Stehle T, (2016). Enabling cell-cell communication via nanopore formation: structure, function and localization of the unique cell wall amidase AmiC2 of *Nostoc punctiforme*. *FEBS J.* 283:7, 1336-50.
- Callahan SM, Buikema WJ, (2001). The role of HetN in maintenance of the heterocyst pattern in *Anabaena* sp. PCC 7120. *Mol. Microbiol.* 40:4, 941-50.
- Cardemil L, Wolk CP, (1979). The polysaccharides from heterocyst and spore envelopes of a blue-green alga. Structure of the basic repeating unit. *J. Biol. Chem.* 254:3, 736-41.
- Celler K, Koning RI, Koster AJ, van Wezel GP, (2013). Multidimensional view of the bacterial cytoskeleton. *J. Bacteriol.* 195:8, 1627-36.
- Chimileski S, Kolter R, Schaechter M, (2018). *Life at the Edge of Sight: a photographic exploration of the microbial world*. Cambridge (MA): Harvard University Press.
- Corrales-Guerrero L, Mariscal V, Flores E, Herrero A, (2013). Functional dissection and evidence for intercellular transfer of the heterocyst-differentiation PatS morphogen. *Mol. Microbiol.* 88:6, 1093-105.
- Ek-Vitorin JF, Burt JM, (2013). Structural basis for the selective permeability of channels made of communicating junction proteins. *Biochim. Biophys. Acta* 1828:1, 51-68.
- Elhai J, Wolk CP, (1988). A versatile class of positive-selection vectors based on the nonviability of palindrome-containing plasmids that allows cloning into long polylinkers. *Gene* 68:1, 119-38.
- Falkowski P, (2012). Ocean Science: The power of plankton. *Nature* 483:7387, S17-S20.
- Fay P, Stewart WDP, Walsby AE, Fogg GE, (1968). Is the heterocyst the site of nitrogen fixation in blue-green algae? *Nature* 220:5169, 810-12.
- Fay P, Kulasoorya SA, (1972). Tetrazolium reduction and nitrogenase activity in heterocystous blue-green algae. *Arch. Microbiol.* 87:4, 341-52.
- Fay P, (1992). Oxygen relations of nitrogen fixation in cyanobacteria. *Microbiol. Reviews* 56:2, 340-73.
- Fiedler G, Arnold M, Hannus S, Maldener I, (1998). The DevBCA exporter is essential for envelope formation in heterocysts of the cyanobacterium *Anabaena* sp. strain PCC 7120. *Mol. Microbiol.* 27:6, 1193-202.
- Flores E, Herrero A, Wolk CP, Maldener I, (2006). Is the periplasm continuous in filamentous multicellular cyanobacteria? *Trends Microbiol.* 14:10, 439-43.
- Flores E, Pernil R, Muro-Pastor AM, Mariscal V, Maldener I, et al., (2007). Septum-localized protein required for filament integrity and diazotrophy in the heterocyst-forming cyanobacterium *Anabaena* sp. strain PCC 7120. *J. Bacteriol.* 189:10, 3884-90.
- Flores E, Herrero A, (2010). Compartmentalized function through cell differentiation in filamentous cyanobacteria. *Nat.Rev. Microbiol.* 8:1, 39-50.

## References

- Flores E, Herrero A, Forchhammer K, Maldener I, (2016). Septal junctions in filamentous heterocyst-forming cyanobacteria. *Trends Microbiol.* 24:2, 79-82.
- Flores E, Nieves-Mori3n M, Mullineaux C, (2019). Cyanobacterial septal junctions: Properties and regulation. *Life* 9:1, 1.
- Fr3as JE, Flores E, Herrero A, (1994). Requirement of the regulatory protein NtcA for the expression of nitrogen assimilation and heterocyst development genes in the cyanobacterium *Anabaena* sp. PCC7120. *Mol. Microbiol.* 14:4, 823-32.
- Fukushima SI, Ehira S, (2018). The Ser/Thr Kinase PknH Is Essential for Maintaining Heterocyst Pattern in the Cyanobacterium *Anabaena* sp. Strain PCC 7120. *Life* 8:3.
- Gibson DG, Young L, Chuang RY, Venter JC, Hutchison CA, 3rd, Smith HO, (2009). Enzymatic assembly of DNA molecules up to several hundred kilobases. *Nature methods* 6:5, 343-5.
- Giddings T, Staehelin L, (1978). Plasma membrane architecture of *Anabaena cylindrica*: Occurrence of microplasmodesmata and changes associated with heterocyst development and the cell cycle. *Eur. J. Cell Biol.* 16, 235-49.
- Giddings TH, Staehelin LA, (1979). Changes in thylakoid structure associated with the differentiation of heterocysts in the cyanobacterium, *Anabaena cylindrica*. *Biochim. Biophys Acta Bioenerg.* 546:3, 373-82.
- Giddings TH, Staehelin LA, (1981). Observation of microplasmodesmata in both heterocyst-forming and non-heterocyst forming filamentous cyanobacteria by freeze-fracture electron microscopy. *Arch. Microbiol.* 129:4, 295-98.
- Golden JW, Robinson SJ, Haselkorn R, (1985). Rearrangement of nitrogen fixation genes during heterocyst differentiation in the cyanobacterium *Anabaena*. *Nature* 314:6010, 419-23.
- Golden JW, Yoon HS, (2003). Heterocyst development in *Anabaena*. *Curr. Opin. Microbiol.* 6:6, 557-63.
- Gupta RS, Mathews DW, (2010). Signature proteins for the major clades of Cyanobacteria. *BMC Evol. Biol.* 10:24-24.
- Hagedorn H, (1961). Untersuchungen 3ber die Feinstruktur der Blaualgenzellen. *Z. Naturforsch.* 16b:12, 825-29.
- Harish, Seth K, (2020). Molecular circuit of heterocyst differentiation in cyanobacteria. *J. Basic. Microbiol.*
- He P, Cai X, Chen K, Fu X, (2020). Identification of small RNAs involved in nitrogen fixation in *Anabaena* sp. PCC 7120 based on RNA-seq under steady state conditions. *Ann. Microbiol.* 70:1, 4.
- Herrero A, Stavans J, Flores E, (2016). The multicellular nature of filamentous heterocyst-forming cyanobacteria. *FEMS Microbiol. Rev.* 40:6, 831-54.
- Herrero A, Flores E, (2019). Genetic responses to carbon and nitrogen availability in *Anabaena*. *Environ. Microbiol.* 21:1, 1-17.
- Herve JC, Derangeon M, (2013). Gap-junction-mediated cell-to-cell communication. *Cell Tissue Res.* 352:1, 21-31.
- Hoiczuk E, Baumeister W, (1995). Envelope structure of four gliding filamentous cyanobacteria. *J. Bacteriol.* 177:9, 2387-95.
- Hoiczuk E, Hansel A, (2000). Cyanobacterial cell walls: News from an unusual prokaryotic envelope. *J. Bacteriol.* 182:5, 1191-99.
- Hopfer U, Lehninger AL, Thompson TE, (1968). Protonic conductance across phospholipid bilayer membranes induced by uncoupling agents for oxidative phosphorylation. *Proc. Natl. Acad. Sci. U. S. A.* 59:2, 484-90.

- Huergo LF, Dixon R, (2015). The emergence of 2-oxoglutarate as a master regulator metabolite. *Microbiol. Mol. Biol. Rev.* 79:4, 419-35.
- Huisman J, Codd GA, Paerl HW, Ibelings BW, Verspagen JMH, Visser PM, (2018). Cyanobacterial blooms. *Nat. Rev. Microbiol.* 16:8, 471-83.
- Jakimowicz D, van Wezel GP, (2012). Cell division and DNA segregation in *Streptomyces*: how to build a septum in the middle of nowhere? *Mol. Microbiol.* 85:3, 393-404.
- Jones KM, Haselkorn R, (2002). Newly identified cytochrome c oxidase operon in the nitrogen-fixing cyanobacterium *Anabaena* sp. strain PCC 7120 specifically induced in heterocysts. *J. Biol.* 184:9, 2491-99.
- Jüttner F, (1983). <sup>14</sup>C-labeled metabolites in heterocysts and vegetative cells of *Anabaena cylindrica* filaments and their presumptive function as transport vehicles of organic carbon and nitrogen. *J. Biol.* 155:2, 628-33.
- Kanehisa M, Goto S, (2000). KEGG: kyoto encyclopedia of genes and genomes. *Nucleic Acids Res.* 28:1, 27-30.
- Kaneko T, Nakamura Y, Wolk CP, Kuritz T, Sasamoto S, et al, (2001). Complete genomic sequence of the filamentous nitrogen-fixing cyanobacterium *Anabaena* sp. strain PCC 7120. *DNA Res.* 8:5, 205-13.
- Kieninger A-K, Forchhammer K, Maldener I, (2019). A nanopore array in the septal peptidoglycan hosts gated septal junctions for cell-cell communication in multicellular cyanobacteria. *Int. J. Med. Microbiol.* 309, 151303.
- Kieninger A-K, Maldener I, (2021). Cell-cell communication through septal junctions in filamentous cyanobacteria. *Curr. Opin. Microbiol.* 61, 35-41.
- Krisch HM, Allet B, (1982). Nucleotide sequences involved in bacteriophage T4 gene 32 translational self-regulation. *Proc. Natl. Acad. Sci. USA* 79, 4937-41.
- Kühner D, Stahl M, Demircioglu DD, Bertsche U, (2014). From cells to muropeptide structures in 24 h: Peptidoglycan mapping by UPLC-MS. *Sci. Rep.* 4:7494.
- Kumar K, Mella-Herrera RA, Golden JW, (2010). Cyanobacterial Heterocysts. *Cold Spring Harb. Perspect. Biol.* 2:a000315.
- Kumar K, Ota M, Taton A, Golden JW, (2019). Excision of the 59-kb fdxN DNA element is required for transcription of the nifD gene in *Anabaena* PCC 7120 Heterocysts. *New Zeal. J. Bot.* 57:2, 76-92.
- Kumazaki S, Akari M, Hasegawa M, (2013). Transformation of thylakoid membranes during differentiation from vegetative cell into heterocyst visualized by microscopic spectral imaging. *Plant Physiol.* 161:3, 1321-33.
- Laemmli UK, (1970). Cleavage of Structural Proteins during the Assembly of the Head of Bacteriophage T4. *Nature* 227:5259, 680-85.
- Lang NJ, Fay P, (1971). The heterocysts of blue-green algae II. Details of ultrastructure. *Proc. Roy. Soc. Lond. B.* 178, 193-203.
- Lechno-Yossef S, Fan Q, Wojciuch E, Wolk CP, (2011). Identification of ten *Anabaena* sp. genes that under aerobic conditions are required for growth on dinitrogen but not for growth on fixed nitrogen. *J. Bacteriol.* 193:14, 3482-89.
- Lehner J, Zhang Y, Berendt S, Rasse TM, Forchhammer K, Maldener I, (2011). The morphogene AmiC2 is pivotal for multicellular development in the cyanobacterium *Nostoc punctiforme*. *Mol. Microbiol.* 79:6, 1655-69.
- Lehner J, Berendt S, Dorsam B, Perez R, Forchhammer K, Maldener I, (2013). Prokaryotic multicellularity: a nanopore array for bacterial cell communication. *FASEB J.* 27:6, 2293-300.

## References

- Liu LN, (2016). Distribution and dynamics of electron transport complexes in cyanobacterial thylakoid membranes. *Biochim. Biophys. Acta* 1857:3, 256-65.
- Luque I, Forchhammer K, (2008). Nitrogen assimilation and C/N balance sensing In *The Cyanobacteria: Molecular Biology, Genomics and Evolution*, ed. Herrero A, Flores E: Norfolk, UK: Caister Academic Press.
- Maldener I, Summers ML, Sukenik A, (2014). Cellular differentiation in filamentous cyanobacteria In *The Cell Biology of Cyanobacteria*, ed. E Flores, A Herrero, pp. 239-304. Norfolk, UK: Caister Academic Press
- Maldener I, Forchhammer K, (2015). Requirement of cell wall remodeling for cell–cell communication and cell differentiation in filamentous cyanobacteria of the order nostocales. In *Biological Nitrogen Fixation*, Volume 2, ed. de Bruijn FJ: John Wiley & Sons, Inc.
- Mariscal V, Herrero A, Flores E, (2007). Continuous periplasm in a filamentous, heterocyst-forming cyanobacterium. *Mol. Microbiol.* 65:4, 1139-45.
- Mariscal V. 2014. Cell–cell joining proteins in heterocyst-forming cyanobacteria. In *The Cell Biology of Cyanobacteria*, ed. E Flores, A Herrero, pp. 239-304. Norfolk, UK: Caister Academic Press.
- Martin-Figueroa E, Navarro F, Florencio FJ, (2000). The GS-GOGAT pathway is not operative in the heterocysts. Cloning and expression of *glsF* gene from the cyanobacterium *Anabaena* sp. PCC 7120. *FEBS Lett.* 476:3, 282-6.
- Martin K, Lukas M, (2015). Cyanobacterial polyhydroxyalkanoate production: status quo and quo vadis? *Curr. Biotechnol.* 4:4, 464-80.
- Mazard S, Penesyan A, Ostrowski M, Paulsen IT, Egan S, (2016). Tiny microbes with a big impact: the role of cyanobacteria and their metabolites in shaping our future. *Mar. Drugs* 14:5, 97.
- McKinney RE, (1953). Staining bacterial polysaccharides. *J. Biol.* 66:4, 453-4.
- Meeks JC, Wycoff KL, Chapman JS, Enderlin CS, (1983). Regulation of expression of nitrate and dinitrogen assimilation by *Anabaena* species. *Appl. Environ. Microbiol.* 45:4, 1351-59.
- Merino-Puerto V, Mariscal V, Mullineaux CW, Herrero A, Flores E, (2010). Fra proteins influencing filament integrity, diazotrophy and localization of septal protein SepJ in the heterocyst-forming cyanobacterium *Anabaena* sp. *Mol. Microbiol.* 75:5, 1159-70.
- Merino-Puerto V, Mariscal V, Schwarz H, Maldener I, Mullineaux CW, et al, (2011a). FraH is required for reorganization of intracellular membranes during heterocyst differentiation in *Anabaena* sp. strain PCC 7120. *J. Bacteriol* 193:24, 6815-23.
- Merino-Puerto V, Schwarz H, Maldener I, Mariscal V, Mullineaux CW, et al, (2011b). FraC/FraD-dependent intercellular molecular exchange in the filaments of a heterocyst-forming cyanobacterium, *Anabaena* sp. *Mol. Microbiol.* 82:1, 87-98.
- Merino-Puerto V, Herrero A, Flores E, (2013). Cluster of genes that encode positive and negative elements influencing filament length in a heterocyst-forming cyanobacterium. *J. Bacteriol.* 195:17, 3957-66.
- Metzner I, (1955). Zur Chemie und zum submikroskopischen Aufbau der Zellwände, Scheiden und Gallerten von Cyanophyceen. *Arch. Mikrobiol.* 22:1, 45-77.
- Mitschke J, Vioque A, Haas F, Hess WR, Muro-Pastor AM, (2011). Dynamics of transcriptional start site selection during nitrogen stress-induced cell differentiation in *Anabaena* sp. PCC7120. *Proc. Natl. Acad. Sci. U. S. A.* 108:50, 20130-5.
- Montesinos ML, Herrero A, Flores E, (1995). Amino acid transport systems required for diazotrophic growth in the cyanobacterium *Anabaena* sp. strain PCC 7120. *J. Bacteriol.* 177:11, 3150-57.

- Mourão MA, Hakim JB, Schnell S, (2014). Connecting the dots: the effects of macromolecular crowding on cell physiology. *Biophys. J.* 107:12, 2761-66.
- Mullineaux CW, Mariscal V, Nenninger A, Khanum H, Herrero A, et al, (2008). Mechanism of intercellular molecular exchange in heterocyst-forming cyanobacteria. *EMBO J.* 27:9, 1299-308.
- Muro-Pastor AM, Valladares A, Flores E, Herrero A, (2002). Mutual dependence of the expression of the cell differentiation regulatory protein HetR and the global nitrogen regulator NtcA during heterocyst development. *Mol. Microbiol.* 44:5, 1377-85.
- Muro-Pastor AM, Maldener I, (2019). Cyanobacterial Heterocysts. In *eLS*. John Wiley & Sons, Ltd: Chichester.
- Murry MA, Wolk CP, (1989). Evidence that the barrier to the penetration of oxygen into heterocysts depends upon two layers of the cell envelope. *Arch. Microbiol.* 151:6, 469-74.
- Nayar AS, Yamaura H, Rajagopalan R, Risser DD, Callahan SM, (2007). FraG is necessary for filament integrity and heterocyst maturation in the cyanobacterium *Anabaena* sp. strain PCC 7120. *Microbiology* 153, 601-7.
- Nicolas WJ, Grison MS, Bayer EM, (2017). Shaping intercellular channels of plasmodesmata: the structure-to-function missing link. *J. Exp. Bot.* 69:1, 91-103.
- Nieves-Mori3n M, Lechno-Yossef S, Lopez-Igual R, Frias JE, Mariscal V, et al, (2017a). Specific glucoside transporters influence septal structure and function in the filamentous, heterocyst-forming cyanobacterium *Anabaena* sp. strain PCC 7120. *J. Bacteriol.* 199:7.
- Nieves-Mori3n M, Mullineaux CW, Flores E, (2017b). Molecular diffusion through cyanobacterial septal junctions. *MBio* 8e01756-16.
- Novo D, Perlmutter NG, Hunt RH, Shapiro HM, (1999). Accurate flow cytometric membrane potential measurement in bacteria using diethyloxacarbocyanine and a ratiometric technique. *Cytometry* 35:1, 55-63.
- Nürnberg DJ, Mariscal V, Bornikoel J, Nieves-Morion M, Krauss N, et al, (2015). Intercellular diffusion of a fluorescent sucrose analog via the septal junctions in a filamentous cyanobacterium. *MBio* 6:2, e02109.
- Obaid AL, Socolar SJ, Rose B, (1983). Cell-to-cell channels with two independently regulated gates in series: analysis of junctional conductance modulation by membrane potential, calcium, and pH. *J. Membrane Biol.* 73:1, 69-89.
- Oikonomou CM, Jensen GJ, (2017). Cellular electron cryotomography: toward structural biology in situ. *Ann.u Rev. Biochem.* 86:873-96.
- Olmedo-Verd E, Brenes-Alvarez M, Vioque A, Muro-Pastor AM, (2019). A heterocyst-specific antisense RNA contributes to metabolic reprogramming in *Nostoc* sp. PCC 7120. *Plant Cell Physiol.* 60:8, 1646-55.
- Omairi-Nasser A, Haselkorn R, Austin J, 2nd, (2014). Visualization of channels connecting cells in filamentous nitrogen-fixing cyanobacteria. *FASEB J.* 28:7, 3016-22.
- Omasits U, Ahrens CH, Müller S, Wollscheid B, (2013). Protter: interactive protein feature visualization and integration with experimental proteomic data. *Bioinformatics* 30:6, 884-86.
- Palinska KA, Krumbein WE, (2000). Perforation patterns in the peptidoglycan wall of filamentous cyanobacteria. *J. Phycol.* 36:1, 139-45.
- Perez R, Forchhammer K, Salerno G, Maldener I, (2016). Clear differences in metabolic and morphological adaptations of akinetes of two Nostocales living in different habitats. *Microbiology* 162:2, 214-23.

## References

- Priyadarshini R, de Pedro MA, Young KD, (2007). Role of peptidoglycan amidases in the development and morphology of the division septum in *Escherichia coli*. *J. Bacteriol.* 189:14, 5334-47.
- Ramos-León F, Mariscal V, Frias JE, Flores E, Herrero A, (2015). Divisome-dependent subcellular localization of cell-cell joining protein SepJ in the filamentous cyanobacterium *Anabaena*. *Mol. Microbiol.* 96:3, 566-80.
- Ramos-León F, Mariscal V, Battchikova N, Aro E-M, Flores E, (2017). Septal protein SepJ from the heterocyst-forming cyanobacterium *Anabaena* forms multimers and interacts with peptidoglycan. *FEBS Open Bio.*
- Rascio N, La Rocca N, (2013). Biological nitrogen fixation. In *Reference Module in Earth Systems and Environmental Sciences*. Elsevier.
- Reed RH, Rowell P, Stewart WD, (1981). Characterization of the transport of potassium ions in the cyanobacterium *Anabaena variabilis* Kutz. *Eur. J. Biochem.* 116:2, 323-30.
- Rippka R, Deruelles J, Waterbury JB, Herdman M, Stanier RY, (1979). Generic assignments, strain histories and properties of pure cultures of cyanobacteria. *Microbiology* 111:1, 1-61.
- Risser DD, Callahan SM, (2009). Genetic and cytological evidence that heterocyst patterning is regulated by inhibitor gradients that promote activator decay. *Proc. Natl. Acad. Sci.* 106:47, 19884-88.
- Rudolf M, Tetik N, Ramos-León F, Flinner N, Ngo G, et al, (2015). The peptidoglycan-binding protein SjcF1 influences septal junction function and channel formation in the filamentous cyanobacterium *Anabaena*. *MBio* 6:4, e00376-15.
- Sagan L, (1967). On the origin of mitosing cells. *J. Theor. Biol.* 14:3, 255-74.
- Sambrook J, Fritsch EF, Maniatis T, (1989). *Molecular cloning: a laboratory manual*. Cold Spring Harbor, NY: Cold Spring Harbor Laboratory Press.
- Schirmer BE, de Vos JM, Antonelli A, Bagheri HC, (2013). Evolution of multicellularity coincided with increased diversification of cyanobacteria and the Great Oxidation Event. *Proc. Natl. Acad. Sci.* 110:5, 1791-96.
- Scholl J, Dengler L, Bader L, Forchhammer K, (2020). Phosphoenolpyruvate carboxylase from the cyanobacterium *Synechocystis* sp. PCC 6803 is under global metabolic control by P(II) signaling. *Mol. Microbiol.* 114:2, 292-307.
- Sjöholm J, Oliveira P, Lindblad P, (2007). Transcription and regulation of the bidirectional hydrogenase in the cyanobacterium *Nostoc* sp. strain PCC 7120. *Appl. Environ. Microb.* 73:17, 5435-46.
- Socolar SJ, Politoff AL, (1971). Uncoupling cell junctions in a glandular epithelium by depolarizing current. *Science* 172:3982, 492-4.
- Söhl G, Maxeiner S, Willecke K, (2005). Expression and functions of neuronal gap junctions. *Nat. Rev. Neurosci.* 6:3, 191-200.
- Springstein BL, Arevalo S, Helbig AO, Herrero A, Stucken K, et al, (2020). A novel septal protein of multicellular heterocystous cyanobacteria is associated with the divisome. *Mol. Microbiol.* 113, 1140-54.
- Stanier RY, Cohen-Bazire G, (1977). Phototrophic prokaryotes: the cyanobacteria. *Annu. Rev. Microbiol.* 31:225-74.
- Stewart WDP, Haystead A, Pearson HW, (1969). Nitrogenase activity in heterocysts of blue-green algae. *Nature* 224:5216, 226-28.
- Szklarczyk D, Gable AL, Lyon D, Junge A, Wyder S, et al, (2019). STRING v11: protein-protein association networks with increased coverage, supporting functional discovery in genome-wide experimental datasets. *Nucleic Acids Res.* 47:D1, D607-d13.

- Tartof KD, Hobbs CA, (1987). Improved media for growing plasmid and cosmid clones. *Bethesda Research Labs Focus* 9:12.
- Tel-Or E, Stewart WDP, Fogg GE, (1977). Photosynthetic components and activities of nitrogen-fixing isolated heterocysts of *Anabaena cylindrica*. *Proc. Roy. Soc. Lond. B. Biol. Sci.* 198:1130, 61-86.
- Thermo Fisher Scientific, (2021). Fluo-4 AM & Fluo-4 NW Calcium Indicators. <https://www.thermofisher.com/de/de/home/industrial/pharma-biopharma/drug-discovery-development/target-and-lead-identification-and-validation/g-protein-coupled/cell-based-second-messenger-assays/fluo-4-am-fluo-4-nw-calcium-indicators.html>
- Thomas J, Meeks JC, Wolk CP, Shaffer PW, Austin SM, (1977). Formation of glutamine from [<sup>13</sup>N]ammonia, [<sup>13</sup>N]dinitrogen, and [<sup>14</sup>C]glutamate by heterocysts isolated from *Anabaena cylindrica*. *J. Bacteriol.* 129:3, 1545-55.
- Towbin H, Staehelin T, Gordon J, (1979). Electrophoretic transfer of proteins from polyacrylamide gels to nitrocellulose sheets: procedure and some applications. *Proc. Natl. Acad. Sci. U. S. A.* 76:9, 4350-4.
- Turin L, Warner A, (1977). Carbon dioxide reversibly abolishes ionic communication between cells of early amphibian embryo. *Nature* 270:5632, 56-7.
- Uehara T, Parzych KR, Dinh T, Bernhardt TG, (2010). Daughter cell separation is controlled by cytokinetic ring-activated cell wall hydrolysis. *EMBO J.* 29:8, 1412-22.
- UniProt Consortium T, (2020). UniProt: the universal protein knowledgebase in 2021. *Nucleic Acids Res.* 49:D1, D480-D89.
- Valladares A, Herrero A, Pils D, Schmetterer G, Flores E, (2003). Cytochrome c oxidase genes required for nitrogenase activity and diazotrophic growth in *Anabaena* sp. PCC 7120. *Mol. Microbiol.* 47:5, 1239-49.
- Vermaas WF, (2001). Photosynthesis and Respiration in Cyanobacteria. In *Encycl. Life Sci.* 1. London: Nature Publishing Group.
- Vollmer W, Joris B, Charlier P, Foster S, (2008). Bacterial peptidoglycan (murein) hydrolases. *FEMS Microbiol. Rev.* 32:2, 259-86.
- Walsby AE, Fogg GE, (1985). The permeability of heterocysts to the gases nitrogen and oxygen. *Proc. Roy. Soc. Lond. B. Biol. Sci.* 226:1244, 345-66.
- Walter J, Lynch F, Battchikova N, Aro E-M, Gollan PJ, (2016). Calcium impacts carbon and nitrogen balance in the filamentous cyanobacterium *Anabaena* sp. PCC 7120. *J. Exp. Bot.* 67:13, 3997-4008.
- Wang L, Lin GM, Niu TC, Zhang SR, Zhang JY, et al, (2019). *patD*, a gene regulated by NtcA, is involved in the optimization of heterocyst frequency in the cyanobacterium *Anabaena* sp. PCC 7120. *J. Bacteriol.* 201:21, e00457-19.
- Weiss GL, Kieninger A-K, Maldener I, Forchhammer K, Pilhofer M, (2019). Structure and Function of a Bacterial Gap Junction Analog. *Cell* 178:2, 374-84.e15.
- Wilk L, Strauss M, Rudolf M, Nicolaisen K, Flores E, et al, (2011). Outer membrane continuity and septosome formation between vegetative cells in the filaments of *Anabaena* sp. PCC 7120. *Cell. Microbiol.* 13:11, 1744-54.
- Wolk CP, (1968). Movement of carbon from vegetative cells to heterocysts in *Anabaena cylindrica*. *J. Bacteriol.* 96:6, 2138-43.
- Wolk CP, Thomas J, Shaffer PW, Austin SM, Galonsky A, (1976). Pathway of nitrogen metabolism after fixation of <sup>13</sup>N-labeled nitrogen gas by the cyanobacterium, *Anabaena cylindrica*. *J. Biol. Chem.* 251:16, 5027-34.

## References

- Wolk CP, Vonshak A, Kehoe P, Elhai J, (1984). Construction of shuttle vectors capable of conjugative transfer from *Escherichia coli* to nitrogen-fixing filamentous cyanobacteria. *Proc. Natl. Acad. Sci.* 81:5, 1561-65.
- Wood NB, Haselkorn R, (1980). Control of phycobiliprotein proteolysis and heterocyst differentiation in *Anabaena*. *J. Bacteriol.* 141:3, 1375-85.
- Xu X, Risoul V, Byrne D, Champ S, Douzi B, Latifi A, (2020). HetL, HetR and PatS form a reaction-diffusion system to control pattern formation in the cyanobacterium *Nostoc* PCC 7120. *eLife* 9e59190.
- Yoon HS, Golden JW, (1998). Heterocyst pattern formation controlled by a diffusible peptide. *Science* 282:5390, 935-8.
- Zhang LC, Chen YF, Chen WL, Zhang CC, (2008). Existence of periplasmic barriers preventing green fluorescent protein diffusion from cell to cell in the cyanobacterium *Anabaena* sp. strain PCC 7120. *Mol. Microbiol.* 70:4, 814-23.

## Danksagung

Ganz herzlich möchte ich mich bei PD Iris Maldener für die Betreuung meiner Dissertation über das faszinierende Projekt der Zell-Zell-Kommunikation in filamentösen Cyanobakterien bedanken. Ihre Türe stand jederzeit offen für unzählige wissenschaftliche Diskussionen, für Tipps und Ratschläge und für hilfreiches Feedback. Ebenfalls weiß ich die wissenschaftliche Freiheit, die sie mir gewährte, zu schätzen.

Ein großes Dankschön gebührt Prof. Karl Forchhammer für die Möglichkeit, meine Forschung an seinem Lehrstuhl durchzuführen. Er hat meine Arbeit mit wertvollen Ratschlägen und Vorschlägen für stichhaltige Experimente bereichert. Wissenschaftliche Probleme blieben nie ungelöst, weswegen ich nach Gesprächen mit ihm immer neue Motivation gefunden habe.

Besonderer Dank gilt unseren großartigen Kollaborationspartnern der ETH Zürich: Prof. Martin Pilhofer, Dr. Gregor Weiss und Piotr Tokarz. Ohne die Kryo-Elektronenmikroskopie und die Energie, die sie in dieses Projekt gesteckt haben, wäre diese Arbeit nicht möglich gewesen.

Bei Dr. Jan Bornikoel möchte ich mich herzlich dafür bedanken, dass er mir den Start meiner Arbeit durch unermüdliche Erklärungen von Methoden und Geräten sehr erleichtert hat. Dankeschön auch für die zahlreichen Buchungen des LSMs.

Vielen Dank an Robert Kluj, der mir durch seine Kenntnisse über die UniProt-Datenbank und durch das Schreiben eines Skripts zur Datensammlung anhand Protein-IDs sehr geholfen hat, die besten Kandidaten aus hunderten von identifizierten Proteinen zu finden.

Weiterhin möchte ich mich bei Dr. Philipp Oesterhelt für seine Hilfe am LSM und bei Prof. Samuel Wagner für die Erstellung meines Zweitgutachtens bedanken. Ein weiterer Dank gebührt den Studenten, die diese Arbeit durch gewissenhafte Forschung unterstützt haben: Sophie Schminke, Davide Paccagnella, Elisabeth Lorenz, Katharina Schmitt und Teresa Müller. Bei Claudia Menzel bedanke ich mich für die Herstellung und TEM-Aufnahmen von Ultradünnschnitten und dafür, dass ich sie jederzeit bei Problemen am TEM anrufen durfte. Michaela Kopp danke ich für alle organisatorischen Arbeiten und all die Päckchen, die sie für mich verschickt hat. Außerdem bedanke ich mich bei Dr. Carolina Nishi und Nelli Deobald, die dafür gesorgt haben, dass immer genügend Medien vorhanden waren. Des Weiteren möchte ich mich bei der gesamten AG Forchhammer und AG Maldener für gemeinsame Mittagessen, amüsante Kuchen-Freitage sowie für wissenschaftlichen Input und Hilfestellungen bedanken.

Abschließend bedanke ich mich bei Freunden und meiner Familie für die bedingungslose Unterstützung, für Aufmunterungen und für den starken Glauben an mich und meine Arbeit. Vielen Dank!

## Appendix

## Appendix 1 Segregation and integration PCRs

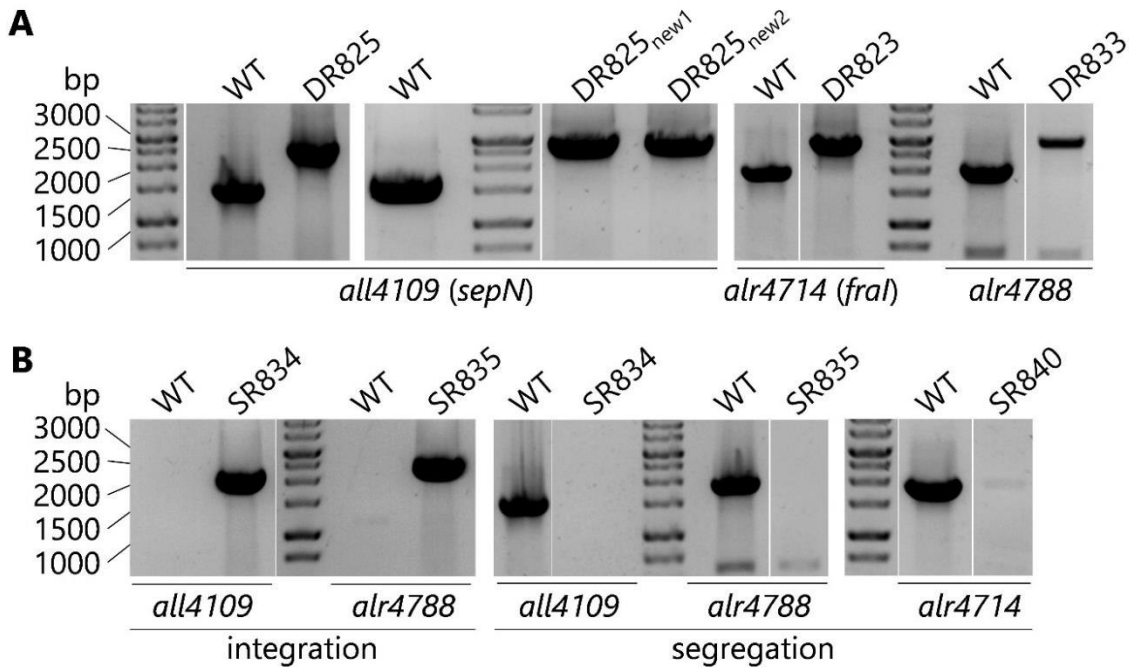


**Figure 41: Agarose gels of segregation and integration PCRs.** (A) Segregation of the integrated C.K3t4 cassette in the respective genes (indicated below the gel) via double homologous recombination was tested with primer pairs specified in Table 8. Expected lengths of PCR products: *all4109* ~1580 bp (WT), ~2600 bp (DR825); *alr4714* ~1950 bp (WT), ~2780 bp (DR823); *alr4788* ~1920 bp (WT), ~2870 bp (DR833). (B) Integration and segregation of pRL277 plasmids for translational *gfp* fusion to the indicated genes was tested with primer pairs specified in Table 8. PCRs to check for integration did not lead to PCR products in the WT, because one primer was located within the vector backbone. Fully segregated single recombinant insertion did not lead to PCR products in the mutants, because of the length of the whole plasmid. Expected lengths of PCR products: *all4109* ~2500 bp (integration), ~1920 bp (segregation); *alr4788* ~2360 bp (integration), 1920 bp (segregation); *alr4714* ~1950 bp (segregation).

## Appendix 2 ImageJ Macro scripts

```

1 //The scale is set from  $\mu\text{m}$  to nm.
2 getPixelSize(unit, pw, ph, pd);
3 print(pw);
4 pixel = getInfo("log");
5 run("Set Scale...", "distance"+pixel+" known=1000 pixel=1 unit=nm");
6
7 //Transformation from a 16-bit into a 8-bit image and slection of the septal disc makes the script faster.
8 run("8-bit");
9 waitForUser("Please make a selection of the septum including all nanopores.");
10 setTool("dropper");
11 setTool("rectangle");
12 setBackgroundColor(0, 0, 0);
13 run("Clear Outside");
14
15 //The name of the opened image is retrieved.
16 originalImage = getTitle();
17 run("Duplicate...", "title=[dup_" + originalImage + "]");
18 duplicateImage = getTitle();
19 run("Duplicate...", " ");
20
21 //Preparation for detection of the nanopores are made.
22 run("Median...", "radius=2");
23 run("Convolved Background Subtraction", "convolution=Median radius=50");
24 run("Median...", "radius=2");
25
26 //Now you need to find the best threshold for detection of the nanopores for this image.
27 waitForUser(
28   "Choose a treshold and apply.\nFor this, click the BioVoxel Toolbox and then Treshold check.\nKeep in mind the name of the best
29   treshold and apply it to the image\nvia clicking the hammer symbol and Auto Treshold.\nIf possible, take the treshold Minimum.");
30 //The applied threshold is calculated and particles are selected.
31 run("Options...", "iterations=1 count=1 black do=Nothing");
32 run("Fill Holes");
33 roiManager("reset");
34 run("Analyze Particles...", "size=50-Infinity circularity=0.20-1.00 show=Nothing add exclude");
35 updateResults();
36 selectWindow("Results");
37 run("Close");
38 selectWindow(duplicateImage);
39
40 //Detected nanopores are shown and need to be carefully checked.
41 waitForUser(
42   "Please check ROIs and eventually edit some, then click on update in ROI manager.\nTo change a selection, mark one and use the sel
43   ection brush tool.\nIf additional ROIs need to be added, it's good to use wand tool or free hand selection.\nPress t to add select
44   ion to ROI manager.");
45 updateResults();
46 selectWindow("Results");
47 run("Close");
48 selectWindow(duplicateImage);
49
50 //The mask with the nanopores will be saved. You need to choose the folder, where to save.
51 for(i=0; i<roiManager("count"); i++) {
52   roiManager("Select", i);
53   run("Measure");
54   updateResults();
55 }
56 roiManager("Show All with labels");
57 run("Overlay Options...", "stroke=none width=0 fill=none show");
58 run("From ROI Manager");
59
60 dir = getDirectory(originalImage);
61 selectWindow(duplicateImage);
62 saveAs("tiff", dir + duplicateImage)
63
64 //Largest and smallest diameter of all nanopores are measured and printed.
65 Feret = newArray(nResults());
66 MinFeret = newArray(nResults());
67 print("Feret \t MinFeret");
68 for (i=0; i<nResults(); i++){
69   Feret[i] = getResult("Feret", i);
70   MinFeret[i] = getResult("MinFeret", i);
71   print(Feret[i], "\t", MinFeret[i]);
72 }
73
74 waitForUser("Copy Log Window into Excel.");
75 waitForUser("Close all images? Sure?");
76 run("Close All");

```

**Figure 42: ImageJ Macro script for counting and measurement of nanopores.** Script in the IJ1 Macro language for use in ImageJ version 1.51j including the BioVoxel toolbox (Brocher, 2015) for semi-automated analysis of the septal nanopore array.

## Appendix

```
1 //Changes scale from  $\mu\text{m}$  to nm and enhances the contrast for better visualization.
2 getPixelSize(unit, pw, ph, pd);
3 print(pw);
4 pixel = getInfo("log");
5 run("Set Scale...", "distance"+pixel+" known=1000 pixel=1 unit=nm");
6 roiManager("Show all with labels");
7 run("Enhance Contrast", "Auto");
8 setTool("oval");
9
10 //3-6 Lines that traverse the center of the circle needs to be drawn. Press t to add to ROI manager.
11 waitForUser("insert a circle and lines for measuring the septum diameter");
12 roiManager("Select", 0);
13 roiManager("Delete");
14
15 //Measuring the length of the lines, which correspond to the diameter of the septum.
16 for(i=0; i<roiManager("count"); i++) {
17     roiManager("Select", i);
18     run("Measure");
19 }
20
21 Length = newArray(nResults());
22 // print("Length");
23 for (i=0; i<nResults(); i++){
24     Length[i] = getResult("Length", i);
25     print(Length[i]);
26 }
27
28 run("Close All");
```

**Figure 43: ImageJ Macro script for measurement the diameter of septal PG discs.** Script in the IJ1 Macro language for use in ImageJ version 1.51j to measure the diameter of septal discs.

Appendix 3 ImageJ Macro Scripts

**A**

① Before running the macro: Analyze (in Fiji toolbar) – Set measurements – select Feret's diameter.

② Selection of a region including all nanopores is sufficient.

④

⑤ The region outside the selection is filled with black, inside, the background will be removed.

**B**

①

Image after rolling ball background subtraction.

②

③

④

Calculated thresholds are shown as image stack. Blue is recognized as background, yellow as nanopores. Scroll through the stack to find the best threshold. If possible, choose 'Minimum'. Very small detected regions will not be considered as nanopore in the following step. Close this window, do not press OK in the 'action required' window, yet.

Legend on page 114.

**C**

In the Fiji toolbar, click on the hammer symbol to choose 'Auto Treshold'.

Select the best threshold from the threshold check.

Binary mask derived from threshold.

①

②

③

④

The screenshot shows the Fiji software interface. At the top, the menu bar includes File, Edit, Image, Process, Analyze, Plugins, Window, and Help. Below the menu bar is a toolbar with various icons. A circled '1' points to the hammer icon in the toolbar. An arrow points from this icon to the text 'In the Fiji toolbar, click on the hammer symbol to choose 'Auto Treshold''. Below the toolbar is the 'Auto Threshold' dialog box. The dialog box has a title bar 'Auto Threshold' and a close button. Inside, it says 'Auto Threshold v1.16.4'. There is a 'Method' dropdown menu set to 'Minimum', with a circled '2' next to it. Below this are several checkboxes: 'Ignore black', 'Ignore white', 'White objects on black background' (checked), 'SetThreshold instead of Threshold (single images)', and 'Show threshold values in log window'. At the bottom of the dialog box are 'OK' and 'Cancel' buttons, with a circled '3' next to 'OK'. To the right of the dialog box is a window titled 'dup\_Rio9 0561.dm4 - C=...' showing a binary mask with white spots on a black background. An arrow points from the 'OK' button in the dialog box to the text 'Select the best threshold from the threshold check.'. Below the binary mask window is the text 'Binary mask derived from threshold.'. At the bottom of the screenshot is an 'Action Required' dialog box with the text: 'Choose a treshold and apply. For this, click the BioVoxel Toolbox and then Treshold check. Keep in mind the name of the best treshold and apply it to the image via clicking the hammer symbol and Auto Treshold. If possible, take the treshold Minimum.' and an 'OK' button with a circled '4' next to it.

**D**

Please check ROIs and eventually edit some, then click on update in ROI manager. To change a selection, mark one and use the selection brush tool. If additional ROIs need to be added, it's good to use wand tool or free hand selection. Press t to add selection to ROI manager.

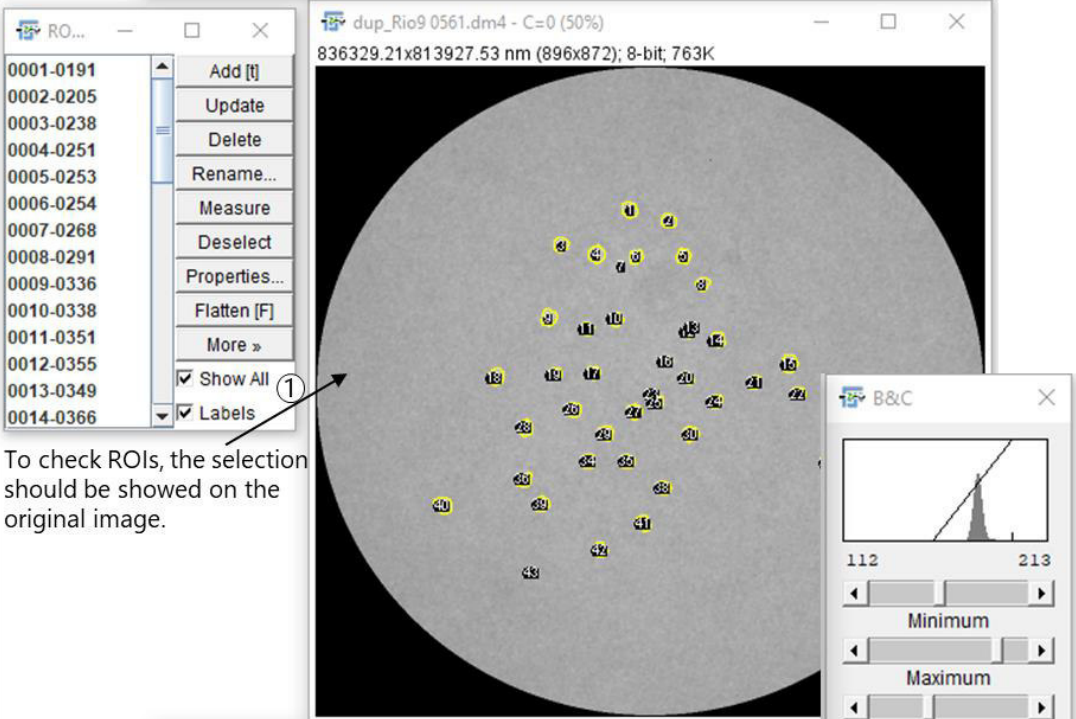
Next, this textbox pops up. How to check the ROIs is explained on the following page.

OK

The screenshot shows an 'Action Required' dialog box with a close button in the top right corner. The text inside the dialog box reads: 'Please check ROIs and eventually edit some, then click on update in ROI manager. To change a selection, mark one and use the selection brush tool. If additional ROIs need to be added, it's good to use wand tool or free hand selection. Press t to add selection to ROI manager.' At the bottom right of the dialog box is an 'OK' button.

Legend on page 114.

**E** ROI manager shows selections.



0001-0191  
0002-0205  
0003-0238  
0004-0251  
0005-0253  
0006-0254  
0007-0268  
0008-0291  
0009-0336  
0010-0338  
0011-0351  
0012-0355  
0013-0349  
0014-0366

Add [t]  
Update  
Delete  
Rename...  
Measure  
Deselect  
Properties...  
Flatten [F]  
More »  
 Show All  
 Labels

dup\_Rio9 0561.dm4 - C=0 (50%)  
836329.21x813927.53 nm (896x872); 8-bit; 763K

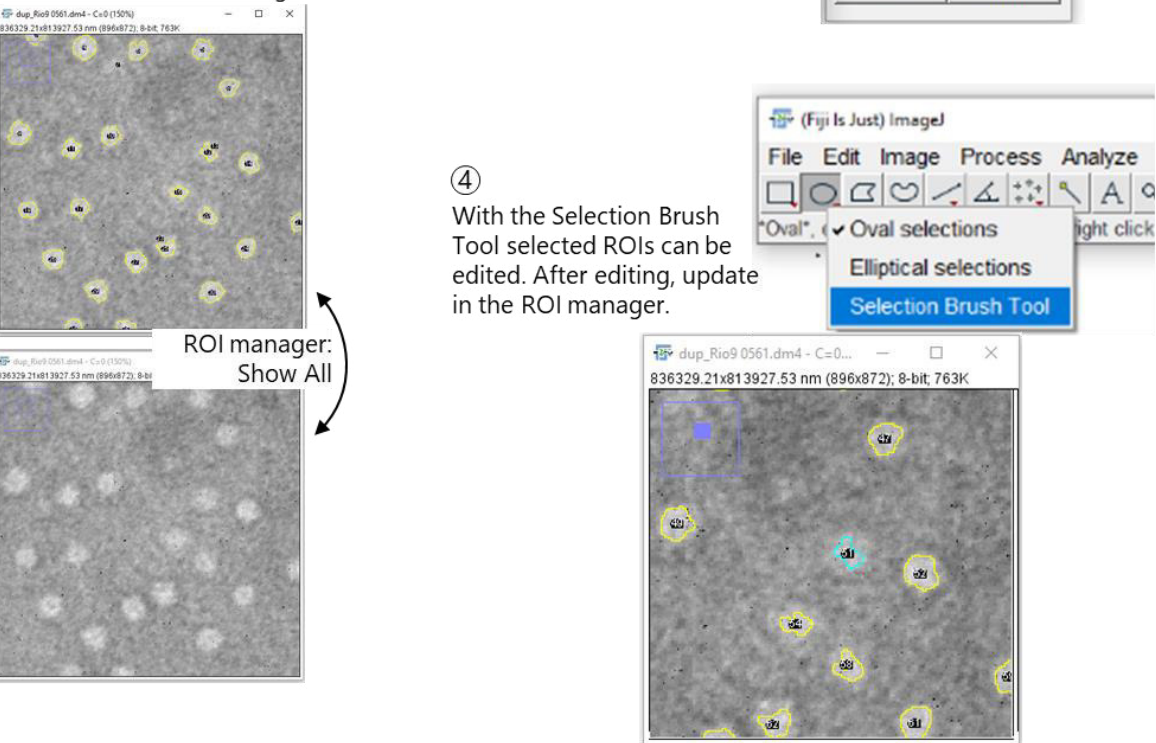
B&C  
112 213  
Minimum  
Maximum  
Brightness  
Contrast  
Auto Reset  
Set Apply

① To check ROIs, the selection should be showed on the original image.

② For better visualization of the nanopores, brightness and contrast can be adjusted (Hammer symbol – Brightness/Contrast).

③ Falsely recognized particles can be removed by selecting them (blue rim) and press 'Delete' in the ROI manager.

④ With the Selection Brush Tool selected ROIs can be edited. After editing, update in the ROI manager.



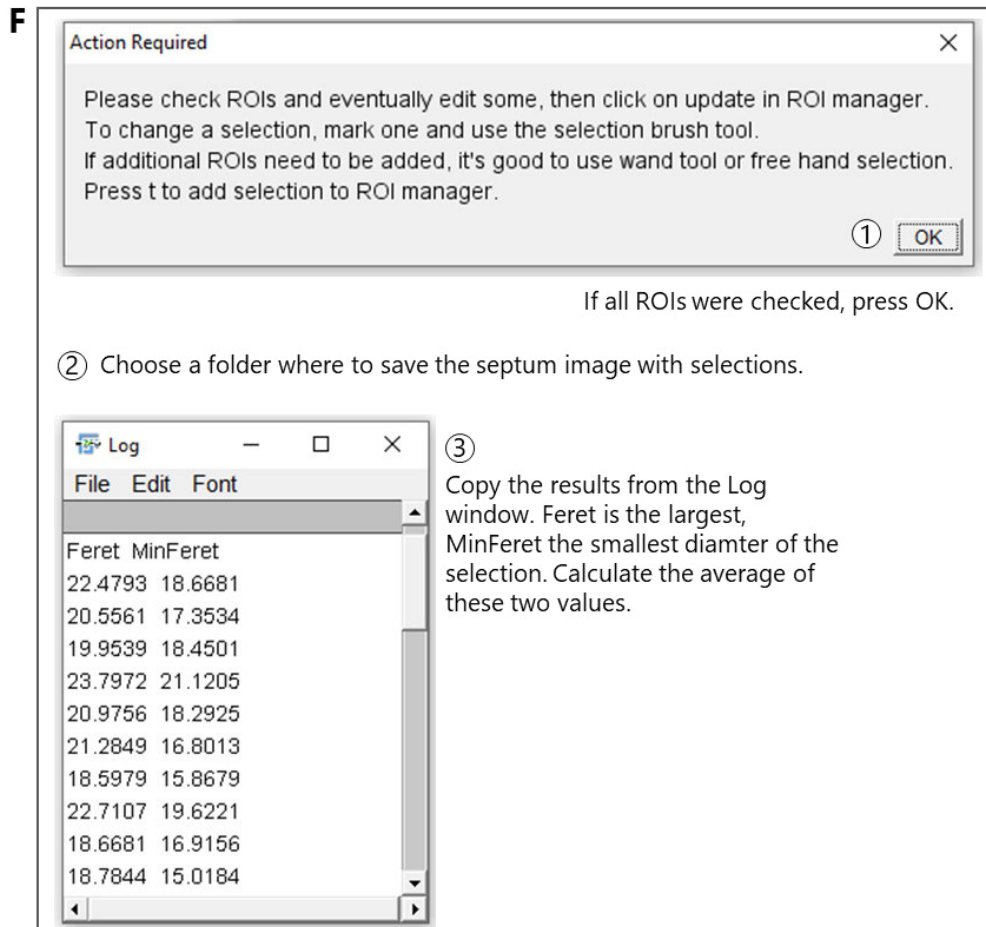
dup\_Rio9 0561.dm4 - C=0 (50%)  
836329.21x813927.53 nm (896x872); 8-bit; 763K

ROI manager: Show All

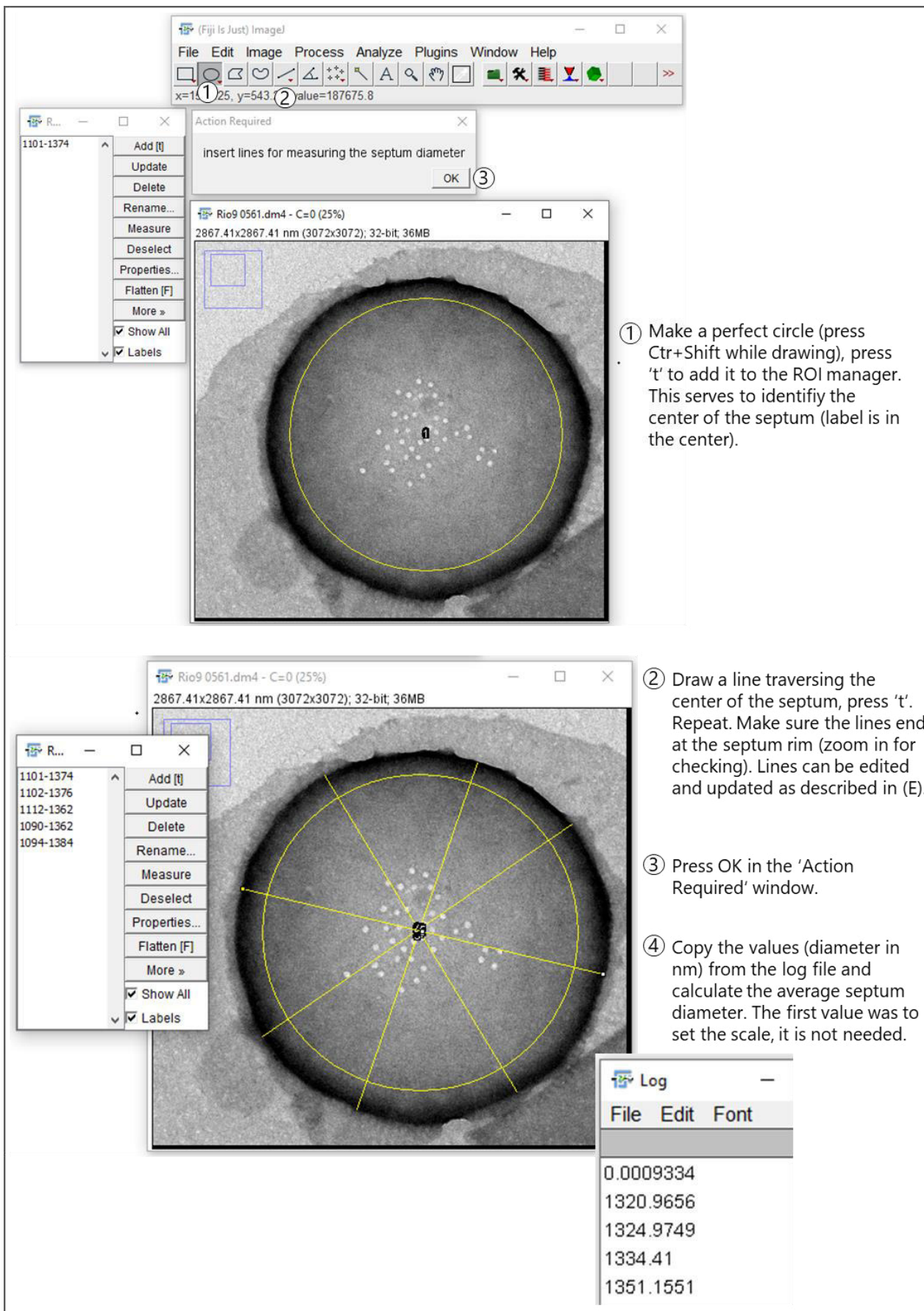
Fiji Is Just ImageJ  
File Edit Image Process Analyze  
Oval\* Oval selections  
Elliptical selections  
Selection Brush Tool

dup\_Rio9 0561.dm4 - C=0...  
836329.21x813927.53 nm (896x872); 8-bit; 763K

Legend on page 114.



**Figure 44: Step-by-step manual for analysis of the nanopore array.** A macro for use in ImageJ for semi-automated analysis of the septal nanopore array was written in the IJ1 Macro language (Figure 42). The BioVoxel toolbox (Brocher, 2015) is necessary to run the program. (A) A region comprising the nanopores is selected. (B) Rolling ball background subtraction is performed and a suitable threshold chosen. (C) A binary mask is created by applying the threshold. (D) Information for the user appears how to adjust the ROIs. (E) The individual ROIs need to be checked and potentially edited. (F) Min and max diameter of each nanopore can be extracted to calculate an average diameter.

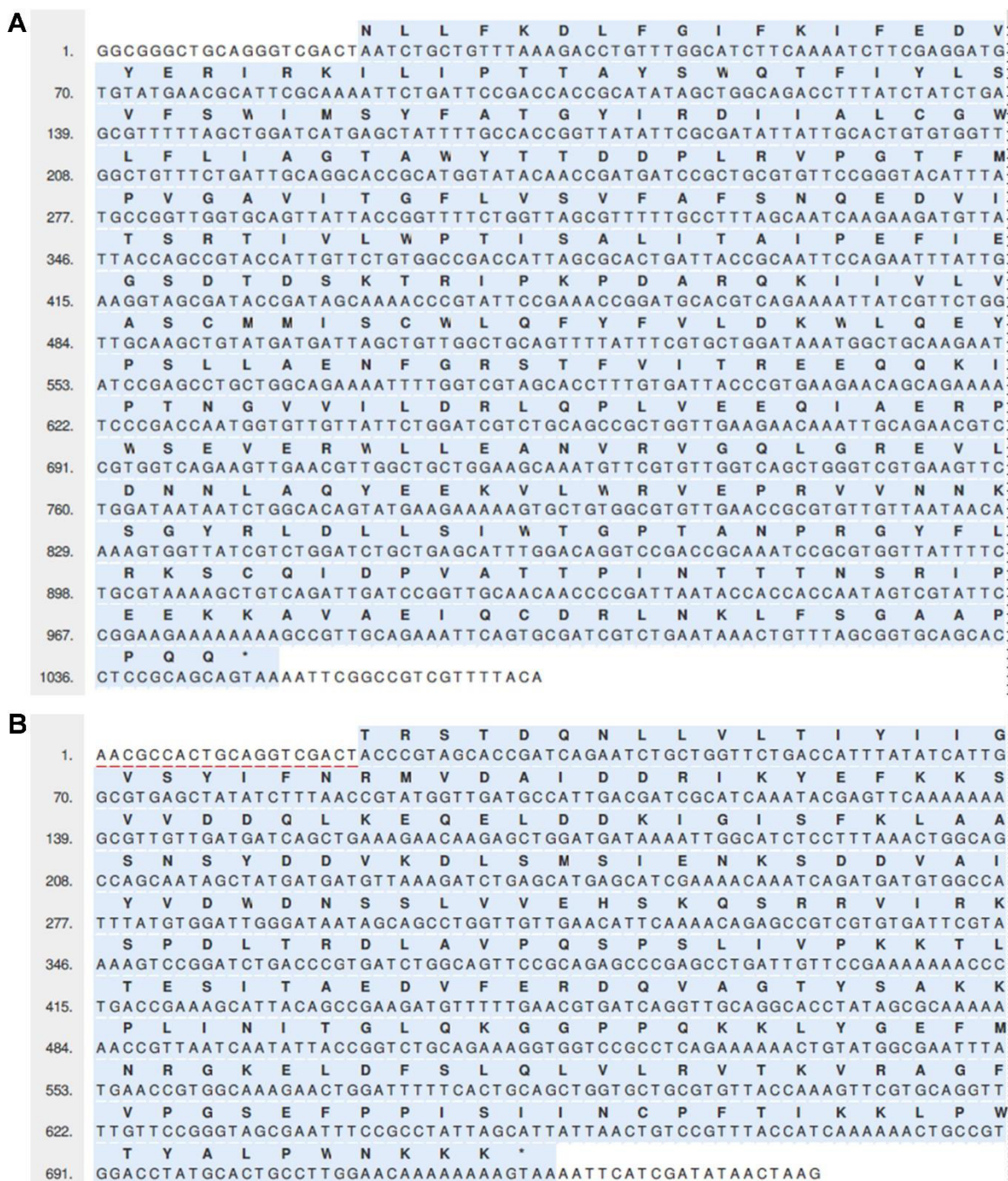


**Figure 45: Manual for measurement of the septum diameter.** Corresponds to the script in Figure 43. First, a circle is drawn to indicate the center of the septum. Lines from one rim of the septum to the opposing rim traversing the center of the septum are drawn. The average length of the lines gives the average septum diameter.

## Appendix 4 Identified proteins in co-IPs with FraD as bait

**Table 15: Proteins identified at least two times in independent co-IPs directed against FraD.**

Protein	Detected in co-IP	LC-MS/MS
All1678	GFP-FraD 1, only in crosslinked sample	1 peptide, low sequence coverage
	GFP-FraD 2	low sequence coverage
All3032	GFP-FraD 1, only in crosslinked sample	
	GFP-FraD 2	1 peptide
All3541	GFP-FraD 1	
	GFP-FraD 2	
All7195	FraD co-IP 1	
	FraD co-IP 3	
Alr0198	FraD co-IP 1	1 peptide
	FraD co-IP 3	1 peptide
Alr0248	GFP-FraD 1	1 peptide, low sequence coverage
	GFP-FraD 3	1 peptide, low sequence coverage
Alr0302	FraD co-IP 1	1 peptide, low sequence coverage
	FraD co-IP 3	1 peptide, low sequence coverage
Alr2762	GFP-FraD 1	1 peptide
	FraD 1	1 peptide
Alr3365	GFP-FraD 2	
	FraD 1	
Alr3990	GFP-FraD 1, only in crosslinked sample	1 peptide
	GFP-FraD 3, only in crosslinked sample	
Alr5087	FraD 1	1 peptide
	FraD 2	1 peptide
Alr7017	FraD 2	
	FraD 3	
Alr7019	FraD 2	
	FraD 3	
Alr7233	FraD 1	
	FraD 3	
Alr7326	FraD 2	
	FraD 3	
Alr7384	FraD 2	
	FraD 3	

Appendix 5 Codon-optimized *fraD* and *all4109* sequences for expression in *E. coli*

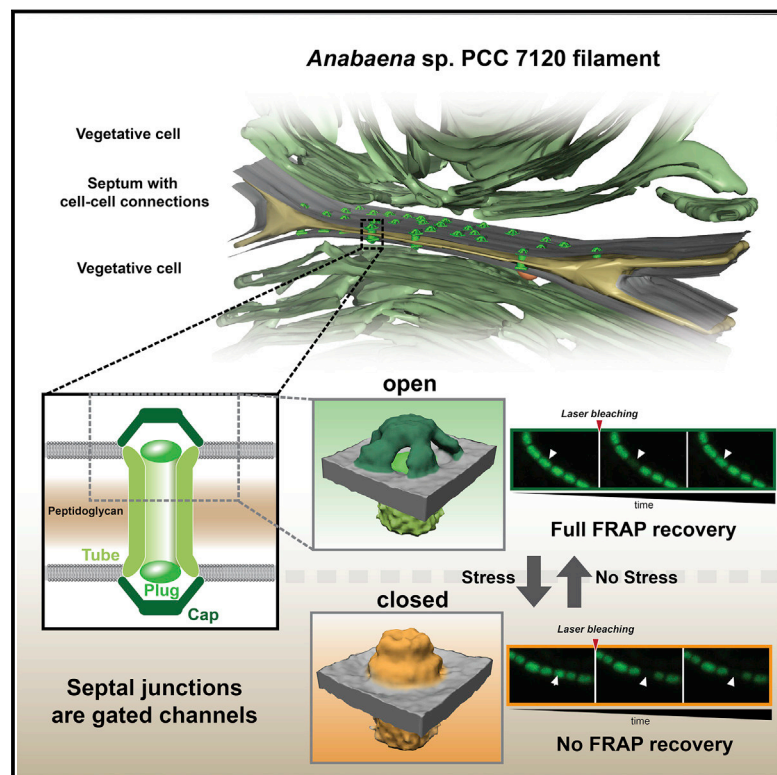
**Figure 46: Synthesized codon-optimized sequences for BACTH.** Synthetic genes coding for (A) FraD or (B) All4109 were codon-optimized for *E. coli* using the GeneArt tool offered by Thermo Fisher Scientific. Genes were synthesized by Thermo Fisher Scientific. ORFs are highlighted in blue.

Appendix

Appendix 6      Publication 1

# Structure and Function of a Bacterial Gap Junction Analog

## Graphical Abstract



## Highlights

- The *in situ* architecture of septal junctions reveals cap, plug, and tube modules
- Septal junctions reversibly control cell-cell communication upon stress
- FraD is a structural element of the septal junction plug module
- Bacterial septal junctions are mechanistically analogous to metazoan gap junctions

## Authors

Gregor L. Weiss, Ann-Katrin Kieninger, Iris Maldener, Karl Forchhammer, Martin Pilhofer

## Correspondence

iris.maldener@uni-tuebingen.de (I.M.), pilhofer@biol.ethz.ch (M.P.)

## In Brief

The *in situ* architecture of cyanobacterial septal junctions reveals a gated intercellular communication channel that evolutionarily predates eukaryotic gap junctions by a billion years.



Weiss et al., 2019, *Cell* 178, 374–384  
July 11, 2019 © 2019 The Author(s). Published by Elsevier Inc.  
<https://doi.org/10.1016/j.cell.2019.05.055>

# Structure and Function of a Bacterial Gap Junction Analog

Gregor L. Weiss,<sup>1,3</sup> Ann-Katrin Kieninger,<sup>2,3</sup> Iris Maldener,<sup>2,\*</sup> Karl Forchhammer,<sup>2</sup> and Martin Pilhofer<sup>1,4,\*</sup>

<sup>1</sup>Department of Biology, Institute of Molecular Biology & Biophysics, Eidgenössische Technische Hochschule Zürich, Otto-Stern-Weg 5, 8093 Zürich, Switzerland

<sup>2</sup>Interfaculty Institute of Microbiology and Infection Medicine Tübingen, Organismic Interactions, University of Tübingen, Auf der Morgenstelle 28, 72076 Tübingen, Germany

<sup>3</sup>These authors contributed equally

<sup>4</sup>Lead Contact

\*Correspondence: [iris.maldener@uni-tuebingen.de](mailto:iris.maldener@uni-tuebingen.de) (I.M.), [pilhofer@biol.ethz.ch](mailto:pilhofer@biol.ethz.ch) (M.P.)

<https://doi.org/10.1016/j.cell.2019.05.055>

## SUMMARY

**Multicellular lifestyle requires cell-cell connections. In multicellular cyanobacteria, septal junctions enable molecular exchange between sister cells and are required for cellular differentiation. The structure of septal junctions is poorly understood, and it is unknown whether they are capable of controlling intercellular communication. Here, we resolved the *in situ* architecture of septal junctions by electron cryotomography of cryo-focused ion beam-milled cyanobacterial filaments. Septal junctions consisted of a tube traversing the septal peptidoglycan. Each tube end comprised a FraD-containing plug, which was covered by a cytoplasmic cap. Fluorescence recovery after photobleaching showed that intercellular communication was blocked upon stress. Gating was accompanied by a reversible conformational change of the septal junction cap. We provide the mechanistic framework for a cell junction that predates eukaryotic gap junctions by a billion years. The conservation of a gated dynamic mechanism across different domains of life emphasizes the importance of controlling molecular exchange in multicellular organisms.**

## INTRODUCTION

The evolution of multicellular organisms required the invention of structures mediating intercellular molecular exchange to allow division of specialized tasks among sister cells (Brunet and King, 2017). Metazoan cells communicate via gap junctions, which are multimeric protein complexes that form two hemi-channels and can control molecular exchange by a dynamic conformational change (Hervé and Derangeon, 2013; Unwin and Zampighi, 1980). In plants, plasmodesmata generate continuity between the cytoplasm of neighboring cells. However, they are mainly composed of membranes, their structure is highly heterogeneous, and closing is possible

by polysaccharide (callose) deposition on a timescale of only hours to days (Oparka et al., 1999; Sager and Lee, 2014).

Filamentous cyanobacteria are true multicellular organisms that exhibit cell-cell communication (Mullineaux et al., 2008). Under nitrogen limiting conditions, strains of the order *Nostocales* differentiate N<sub>2</sub>-fixing heterocysts in a semiregular pattern along the filament, which supply the neighboring vegetative cells with nitrogen-fixation products in form of glutamine and the dipeptide β-aspartyl-arginine (Burnat et al., 2014; Thomas et al., 1977). Vegetative cells, in turn, fix CO<sub>2</sub> via oxygenic photosynthesis and provide heterocysts with sucrose as a carbon and energy source (Cumino et al., 2007; Jüttner, 1983). In addition to metabolites, signaling molecules need to be exchanged to establish the correct pattern of differentiated cells along the filament (Flores and Herrero, 2010; Flores et al., 2016; Maldener et al., 2014).

Exchanged molecules need to traverse the septum between two adjacent cells in a filament. In multicellular cyanobacteria, this septum contains one peptidoglycan (PG) disc and two cytoplasmic membranes (Hoiczuk and Baumeister, 1995; Lehner et al., 2013). The outer membrane, however, continuously surrounds the entire filament without entering the septum (Flores et al., 2006). The existence of pores in the septal PG has been known for decades (Metzner, 1955). Investigation of the septal PG of *Nostoc punctiforme* and *Anabaena* sp. PCC 7120 (hereafter *Anabaena*) by conventional electron microscopy (EM) methods revealed the presence of 80–150 nanopores, each ~20 nm in diameter. These so-called nanopore arrays were shown to be required for cell-cell communication (Lehner et al., 2013; Nürnberg et al., 2015). AmiC-type cell wall-lytic amidases were suggested to drill nanopores into septal PG. Consistently, AmiC mutants were affected in cell-cell communication and cell differentiation (Berendt et al., 2012; Bornikoel et al., 2017; Lehner et al., 2011, 2013).

The nanopores in the septal PG were proposed to accommodate cell-cell joining structures that traverse the septal space between neighboring cells (for reviews, see Flores et al., 2016, 2019). Early studies observed structures perpendicular to the cytoplasmic membranes of adjacent cells and referred to them as microplasmodesmata, in analogy to plasmodesmata in plants, suggesting cytoplasmic continuity (Giddings and Staehelin, 1978, 1981; Lang and Fay, 1971). Later studies visualized



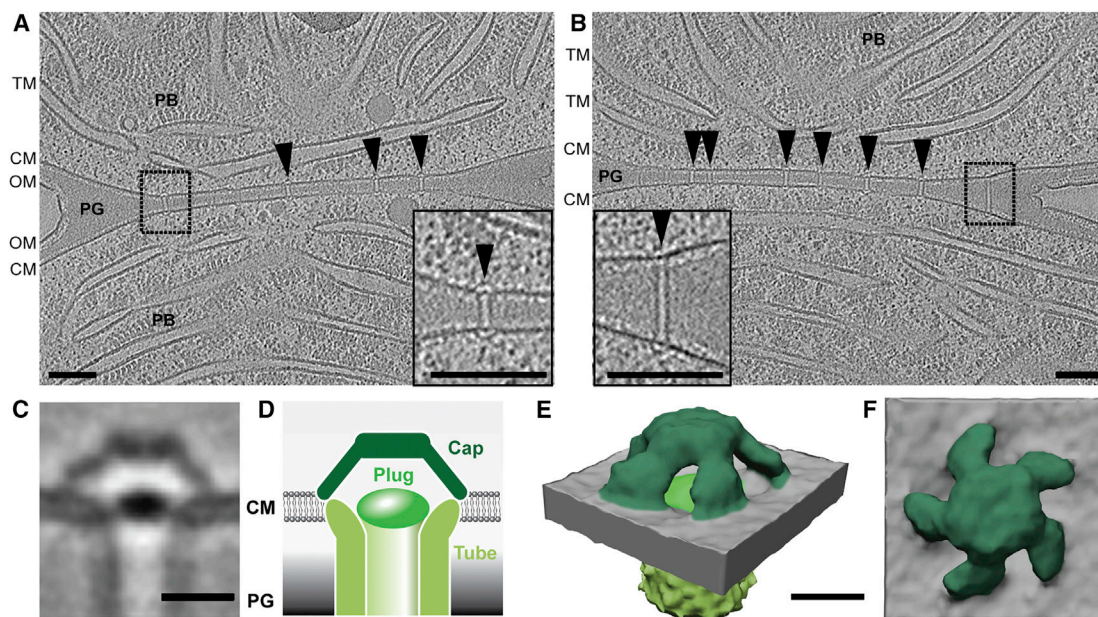


**Figure 1. In Situ Architecture of Septal Junctions Reveals Tube, Plug, and Cap Modules**

(A and B) Cryotomograms (magnified views in boxes) of a FIB-milled *Anabaena* filament. The two different slices at different Z-heights show the septum between adjacent vegetative cells. Multiple SJs were seen crossing the septum (arrowheads). The SJ lengths were precisely adjusted to the septum thickness. CM, cytoplasmic membrane; OM, outer membrane; PB, phycobilisomes; PG, septal peptidoglycan; TM, thylakoid membranes. Bars, 100 nm. Shown are projections of 13.5 nm-thick slices.

(C–F) Subtomogram averaging of SJ ends revealed three structural modules: tube, cap, and plug. Shown is a 0.68 nm-thick tomographic slice through the average (C), a schematic representation of SJ modules (D; modules segmented in different shades of green), and oblique (E) and top (F) views of a surface representation (modules were segmented to match colors in D). The cap consisted of a ceiling that was held by five arches. Bars, 10 nm.

See also [Figures S1](#) and [S2](#) and [Videos S1](#) and [S2](#).

channels in the septum between cells by electron tomography and suggested that they were proteinaceous (Omairi-Nasser et al., 2014; Wilk et al., 2011). The field has now settled on the widely used term “septal junctions” (SJs), describing cell-cell joining structures in multicellular cyanobacteria that might establish a direct connection between the cytoplasm of neighboring cells (Mariscal, 2014; Flores et al., 2016).

The structural components of SJs are still unknown. However, the predicted membrane proteins FraC, FraD, and SepJ (also termed FraG) are considered as possible candidates (for reviews, see Flores et al., 2016, 2019; Herrero et al., 2016). They were all shown to localize to the septum between vegetative cells by fusion with GFP and/or immuno-labeling (Flores et al., 2007; Merino-Puerto et al., 2010, 2011). Mutants in these proteins are impaired in filament integrity and cell-cell communication, and they possess a significantly reduced number of nanopores (Bauer et al., 1995; Mariscal et al., 2011; Nayar et al., 2007; Nürnberg et al., 2015). Furthermore, AmiC1 is necessary for the correct localization of SepJ at the septum (Bornikoel et al., 2017), indicating a functional link between FraC/D, SepJ, and AmiC. More recently, the PG-binding protein SjcF1 was described as an additional factor involved in the formation of nanopores and septal junctions via the interaction of SjcF1 with FraC and SepJ. A SjcF1 mutant was also impaired in intercellular transport (Rudolf et al., 2015).

Molecular exchange through SJs occurs by diffusion (Mullineaux et al., 2008; Nieves-Morión et al., 2017), but it remains

unclear whether and how SJs can control cell-cell communication under certain conditions or in stress situations (Flores et al., 2019). Single cells within a cyanobacterial filament can burst or die due to predator attack, shear force or senescence. Furthermore, the filaments fragment when the intercalated heterocysts die (Nürnberg et al., 2015). Little is known how the organism can ensure the survival of the remaining filament in such settings. Here, we set out to uncover the architecture and mechanism of this primordial type of cell-cell junction.

## RESULTS AND DISCUSSION

### In Situ Architecture of Septal Junctions Reveals Tube, Plug, and Cap Modules

We imaged *Anabaena* cells by electron cryotomography (ECT) to reveal the architecture of SJs *in situ* and in a near-native state. To obtain a sample that was thin enough for ECT imaging, we plunge-froze cells on EM grids and prepared lamellae using cryo-focused ion beam (FIB) milling (Figure S1) (Marko et al., 2007; Medeiros et al., 2018; Rigort et al., 2010; Schaffer et al., 2017). Despite the generally relatively low throughput of the FIB milling approach, for this study we generated a comprehensive dataset of ~480 tomograms that were recorded on an unprecedented total number of ~120 lamellae. Tomograms of septa between vegetative cells revealed numerous putative SJs that appeared as tubular structures traversing the septum (Figures 1A and 1B; Video S1). In a

200 nm thick lamella, an average of 9.8 SJs were clearly visible ( $n = 22$  tomograms), consistent with the reported number of  $\sim 80$  nanopores in a septum (Bornikoel et al., 2017). Structures resembling SJs were never observed in the lateral cell wall. The cross-sectional density plot of a SJ suggests that a tube structure was embedded into the septal PG (rather than the PG nanopore being empty), and the tube lumen density was relatively low compared to the PG (Figures S2A and S2B). Depending on the thickness of the septum, the length of the tube module varied between 26 and 79 nm (average  $37.9 \text{ nm} \pm 7.1 \text{ nm}$ ,  $n = 208$ , Figure S2C), suggesting a multimeric nature of the tube.

In addition to the tube module, the tomograms revealed a cytoplasmic cap-like structure, as well as a plug-like density in the cytoplasmic membrane (CM) (Figures 1A and 1B). Both ends of each SJ comprised cap and plug modules, without any recognizable differences between both ends. To increase contrast and resolution, we performed subtomogram averaging of 446 SJ ends (Figures 1C–1F and S2D; Video S2). The average resolved that the 11 nm-wide tube (lumen of 7 nm) made direct contact with the CM. No bilayer-like density was observed in the SJ tube wall, supporting an earlier report (Wilk et al., 2011) that suggested that the periplasm-spanning tube was assembled of proteinaceous subunits. The plug ( $7 \text{ nm} \times 2.5 \text{ nm}$ ) was sitting at the end of the tube at the level of the CM. The cap module was a 5-fold rotationally symmetric (Figure S2E) dome (8 nm height) covering the tube end. The ceiling had a diameter of 9.5 nm and was held by five arches with lengths of 8.5 nm.

### Intercellular Communication Ceases upon Ionophore Treatment in a Reversible Manner

The structural complexity of the SJ ends led us to speculate that the assembly might allow the control of intercellular molecular diffusion. Cyanobacterial intercellular communication was studied previously by monitoring the exchange rate of fluorescent tracers, like calcein, 5-carboxyfluorescein diacetate and esculin by fluorescence recovery after photobleaching (FRAP) (Mullineaux et al., 2008; Nürnberg et al., 2015). We therefore monitored the molecular exchange rate of calcein by FRAP after challenging the proton motif force. We treated cells with carbonyl cyanide 3-chlorophenylhydrazone (CCCP), a protonophore that dissipates the proton gradient across membranes (Hopfer et al., 1968) and measured the FRAP response. Upon treatment with  $50 \mu\text{M}$  CCCP, 83% of the analyzed cells ceased to exchange calcein, showing a “no communication” response after bleaching (Figures 2A and 2B; Video S3). This is in contrast to the control experiment (control cells were treated with DMSO to exclude effects of the solvent), where all cells displayed “full recovery” of fluorescence (Figure 2A). Seven percent of CCCP-treated cells were assigned to a “slow increase” response, because fluorescence recovery was delayed (started only 20–60 s after bleaching) and reached only  $<50\%$  of the initial fluorescence (Figures 2A and 2B). In further 7% of the cells, exchange took place only with a single neighboring cell. Only 3% of CCCP-treated cells showed a normal “full recovery” FRAP response (Figures 2A and 2B). The fraction of non-communicating cells was dependent on the concentration of CCCP (Figures 2C and S3A), which had no effect below  $0.5 \mu\text{M}$ . Con-

centrations above  $50 \mu\text{M}$  did not further enhance the inhibition of molecular exchange.

To test whether CCCP inhibited cell-cell communication in a reversible manner, cells were washed after a  $50 \mu\text{M}$  CCCP treatment and incubated in fresh medium for 2.5 h at room temperature. Eighty-five percent of the cells resumed communication, suggesting that the inhibition of molecular exchange was indeed reversible (Figures 2D and S3B) and cells were still viable after recovering from CCCP treatment (Figure S3C). We then set out to explore whether the re-opening of SJs required the synthesis of new proteins. Hence, cells were treated with CCCP, washed, and incubated for 2.5 h in fresh medium supplemented with  $50 \mu\text{g/mL}$  chloramphenicol (inhibiting protein synthesis) before monitoring the FRAP response (Figures 2D and S3B). Because 72% of the tested cells were able to restore communication (showing “full recovery” response), we concluded that the reversibility of communication was based on an opening mechanism of SJs that was independent of *de novo* protein synthesis. To check whether the ATP level within the cells was altered by CCCP treatment, we analyzed the ATP content of *Anabaena* cells after CCCP treatment. No significant differences between the control (DMSO-treated cells) and CCCP-treated cells were detected (Figure S3D), indicating that the cellular ATP level was not a signal for gating communication.

### Ceased Intercellular Communication after Ionophore Treatment Coincides with a Major Structural Rearrangement of the Septal Junction Cap

To investigate whether a structural change in the macromolecular architecture of SJs was involved in the gating of cell-cell communication, we plunge froze CCCP-treated *Anabaena* cells and acquired tomograms of septal areas. Differences were hardly detectable in individual tomograms ( $n = 13$  tomograms, Figure 3A). However, subtomogram averaging ( $n = 188$  SJ ends) revealed a striking conformational change in the cap module, whereas the tube and plug modules remained unchanged (Figures 3B–3D; Video S4). Compared to the cap structure in untreated cells (Figure 3E), the individual arches were not anymore detectable, and the cap did not reveal any detectable openings (Figures 3B and S4A; Video S5). The structural rearrangement also resulted in a tightening of the cap by 6 nm and the introduction of a small cavity on the ceiling of the cap. It is possible that the closed conformation of the cap could arise from rotations of the individual arches (Figures S4B–S4E). The reversibility of SJ closing upon CCCP treatment that was seen by FRAP was confirmed by ECT imaging of cells that were CCCP-treated, washed, and incubated in fresh medium for 2.5 h before plunge freezing. The SJ architecture from these recovered cells matched the untreated (open) conformation without detectable differences ( $n = 8$  tomograms, 66 SJ ends, Figures S4F–S4H). In order to further examine the time frame in which SJ closure was observed, we incubated *Anabaena* with CCCP for the shortest possible duration prior to FRAP and ECT imaging. FRAP experiments indicated that intercellular communication already ceased in  $<4$  min after CCCP treatment (Figure S4I). ECT and subtomogram averaging ( $n = 5$  tomograms, 28 SJ ends) revealed SJs in the closed conformation already after 45 s of CCCP treatment (Figures S4J–S4L).

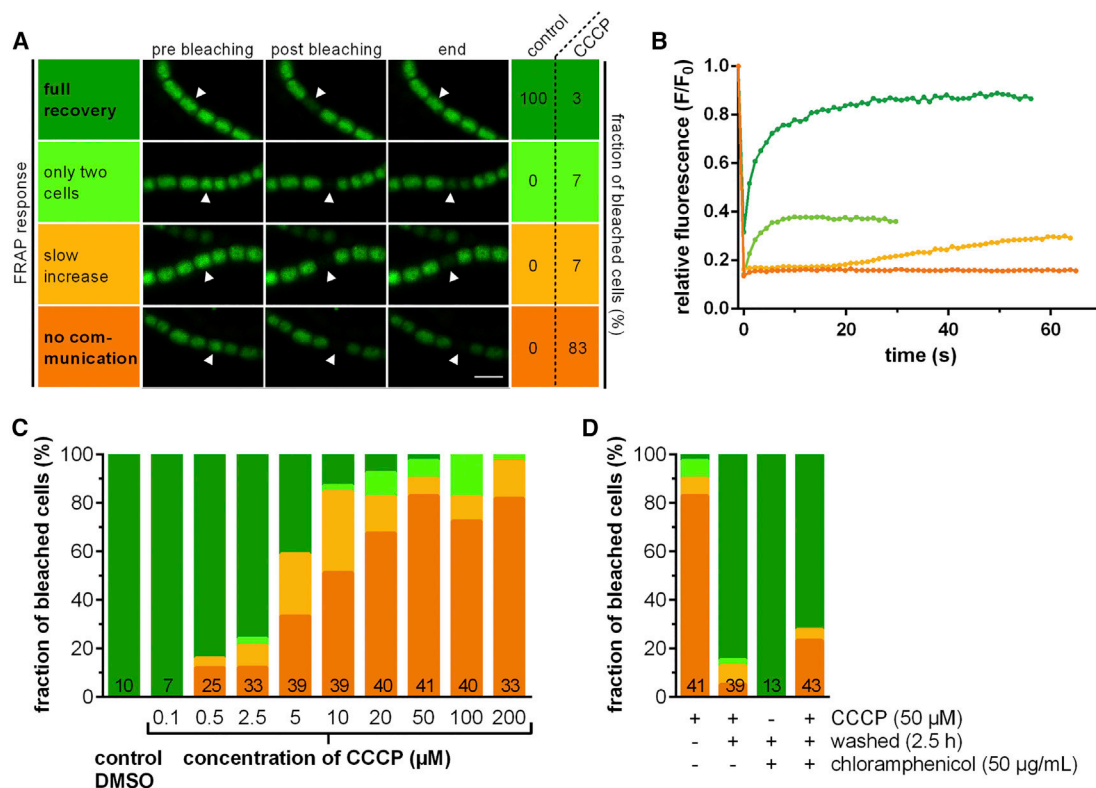


**Figure 2. Intercellular Communication Ceases upon Ionophore Treatment in a Reversible Manner**

(A) FRAP analysis of cells that were stained with fluorescent calcein. In the control experiment (control cells were treated with DMSO to exclude effects of the solvent), all cells showed full recovery of fluorescence after bleaching. After treatment with the ionophore CCCP (50  $\mu\text{M}$  in DMSO), the bleached cells showed four different types of FRAP responses: “full recovery,” “slow increase” (delayed recovery to <50% of original fluorescence), “only two cells” (exchange of calcein only with one neighboring cell), and “no communication” (no recovery). For each FRAP response, representative images are shown at three time points (5 s before bleaching,  $\sim$ 0.5 s after bleaching, 30–60 s after bleaching). Arrowheads point to the bleached cells. *Anabaena* was apparently able to control communication upon challenging the proton motive force, because the majority of CCCP-treated cells showed “no communication.” Bar, 5  $\mu\text{m}$ .

(B) Fluorescence recovery curves corresponding to the four FRAP responses that were observed in (A) (color scheme identical to A). Time point  $t = 0$  shows the analyzed cell directly after bleaching.

(C) Cell-cell communication after increasing the concentration of CCCP (color scheme identical to A). The effect of CCCP on cell-cell communication was concentration-dependent for CCCP concentrations between 0.5–50  $\mu\text{M}$ . In the control experiment, cells were treated with 0.002% DMSO. Numbers within the bars indicate the number of analyzed cells ( $n$ ) from different filaments and represent cumulated results from at least two independent cultures (except for 0.1  $\mu\text{M}$  CCCP).

(D) Recovery of cell-cell communication after incubation in fresh medium lacking CCCP and in the presence of chloramphenicol (color scheme identical to A). Regaining cell-cell communication was independent of *de novo* protein synthesis, “+” and “–” indicate the presence and absence of CCCP, washing in fresh medium, and chloramphenicol. Numbers in bars indicate number of analyzed cells ( $n$ ). Shown are cumulated results from at least two independent cultures.

See also Figure S3 and Videos S3, S4, and S5.

### AmiC1, SepJ, and SjcF1 Mutants Are Impaired in Intercellular Communication but Nevertheless Able to Control Molecular Exchange

AmiC1, SepJ, and SjcF1 were proposed to play important roles in the formation of nanopores and SJs (Flores et al., 2016). We therefore analyzed the mutants’ SJ architectures (Figures 4A–4C) as well as their ability to control intercellular molecular exchange (Figure 4D). The number of SJs was significantly reduced in all tested mutants, except for  $\Delta\text{sjcF1}$ , which is consistent with previous quantifications of nanopore arrays (Bornikoe et al., 2017; Nürberg et al., 2015; Rudolf et al., 2015). The septa of all mutants were also wider, which was reflected in the increased SJ average length (Figure S5A).

A subtomogram average of the *amiC1* mutant SR477 ( $n = 6$  to-mograms, 156 SJ ends, Figure 4A) showed SJs in the open state and did not reveal any structural differences compared to the wild type. When we monitored intercellular molecular exchange by FRAP, we found that only 52% of SR477 cells showed “full recovery,” likely based on the low number of SJs. Upon CCCP treatment, 87% of the analyzed cells showed a “no communication” response (Figures 4D and S5B), suggesting that the low number of SJs could mostly still switch to the closed state. The amidase AmiC1 is therefore unlikely a major structural component of SJs and does not play a role in the gating mechanism, which is consistent with previous data (Bornikoe et al., 2017, 2018; Lehner et al., 2013; Nürberg et al., 2015).

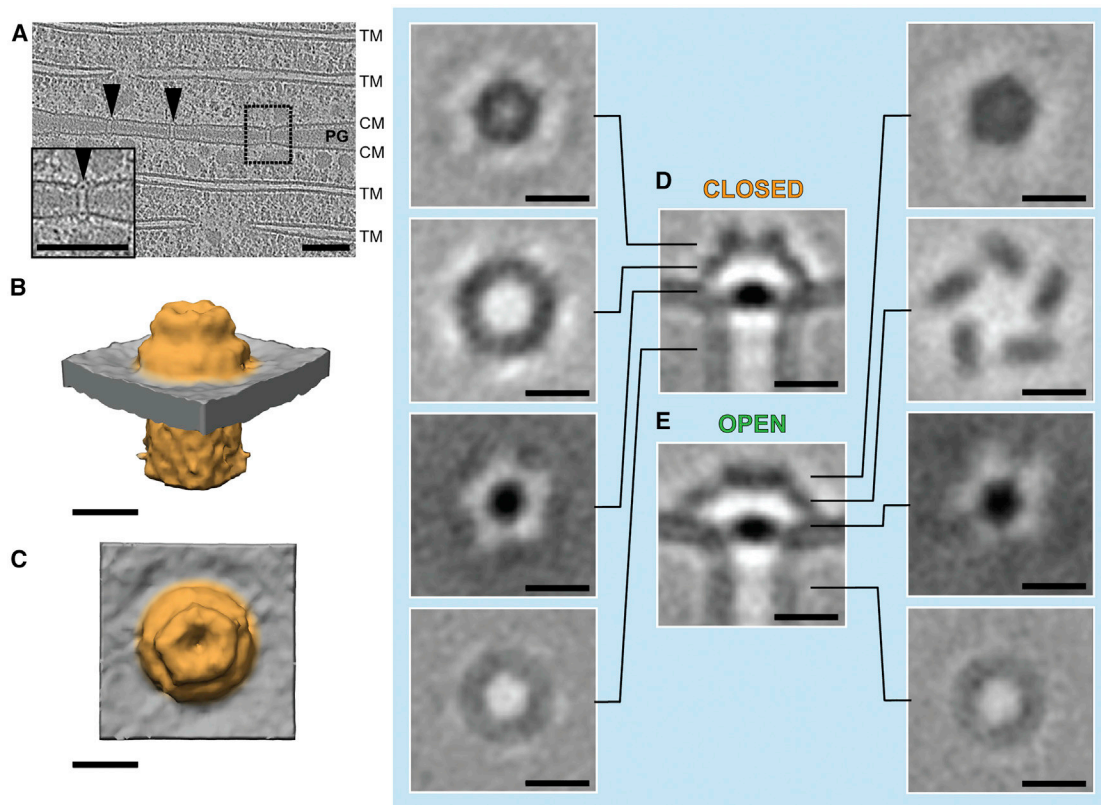


**Figure 3. Ceased Intercellular Communication after Ionophore Treatment Coincides with a Major Structural Rearrangement of the Septal Junction Cap**

(A) Shown is a 13.5 nm-thick slice through a cryotomogram (magnified view in box) of the septal area of a CCCP-treated *Anabaena* filament. SJs are indicated by arrowheads. CM, cytoplasmic membrane; PG, septal peptidoglycan; TM, thylakoid membranes. Bar, 100 nm.

(B–E) Subtomogram averaging of SJs in the CCCP-treated non-communicating “closed” state (B–D) revealed major structural rearrangements in the cap module, compared to the “open” state (E). Shown are surface representations (B and C), and longitudinal and cross-sectional slices (0.68 nm) through the averages (D and E). Sliced positions are indicated in (D) and (E). Bars, 10 nm.

See also [Figure S4](#) and [Videos S4](#) and [S5](#).

The subtomogram average of SJs of a  $\Delta sepJ$  strain ( $n = 6$  tomograms, 62 SJ ends) revealed wild type architecture in the open state ([Figure 4B](#)). Compared to the wild type,  $\Delta sepJ$  cells showed impaired intercellular communication, possibly based on the lower total number of SJs. Upon CCCP treatment, 65% of  $\Delta sepJ$  cells showed a “no communication” response, which indicates that SJs could still close ([Figures 4D](#) and [S5B](#)). The presence of SJs in the  $\Delta sepJ$  mutant is consistent with previous conventional EM studies that detected cell-cell connections in this mutant ([Omairi-Nasser et al., 2015](#); [Wilk et al., 2011](#)). The overexpression of SepJ was reported to result in an increased number of nanopores ([Mariscal et al., 2016](#)). Other studies suggested a role of the divisome for the subcellular localization of SepJ ([Ramos-León et al., 2015](#)) and found that a SepJ-GFP fusion migrates with the FtsZ ring during cell division and is finally found in a central localized spot within the septum ([Flores et al., 2007](#)). Taken together, SepJ is likely not a major structural component of SJs, but rather plays a role in coordinating septum maturation and precise amidase-dependent placement of nanopores.

A subtomogram average of SJs of *sjcF1* mutant cells ( $n = 7$  tomograms, 116 SJ ends) also revealed wild type architecture in

the open state ([Figure 4C](#)). 75% of the mutant cells showed a “no communication” response upon CCCP treatment, which is comparable to the wild type ([Figures 4D](#) and [S5B](#)). These findings are consistent with a previous study, suggesting that SjcF1 is not an essential component of SJs, but rather plays a regulatory role in nanopore formation ([Rudolf et al., 2015](#)).

#### The Cap and Plug Modules Are Required to Control Intercellular Communication upon Ionophore Treatment

FraC and FraD were also reported to be related to SJs and important for filament integrity ([Merino-Puerto et al., 2010, 2011](#)). We therefore analyzed the architecture of SJs in different mutants. SJs in  $\Delta fraC$ - $\Delta fraD$  ( $n = 7$  tomograms) ([Figures 5A](#) and [S5C](#)) and  $\Delta fraD$  ( $n = 7$  tomograms) ([Figures 5B](#) and [S5C](#)) mutants were missing the cap and plug modules. By contrast, the  $\Delta fraC$  mutant showed a heterogeneous phenotype, exhibiting a mixture of fully assembled SJs, SJs without cap and plug, and presumably misassembled SJs ( $n = 11$  tomograms) ([Figures 5C](#) and [S5C](#)). Importantly, none of the analyzed  $\Delta fraC$ - $\Delta fraD$  cells and only 7% of the  $\Delta fraD$  cells showed a “no communication” response upon CCCP treatment, even at high CCCP

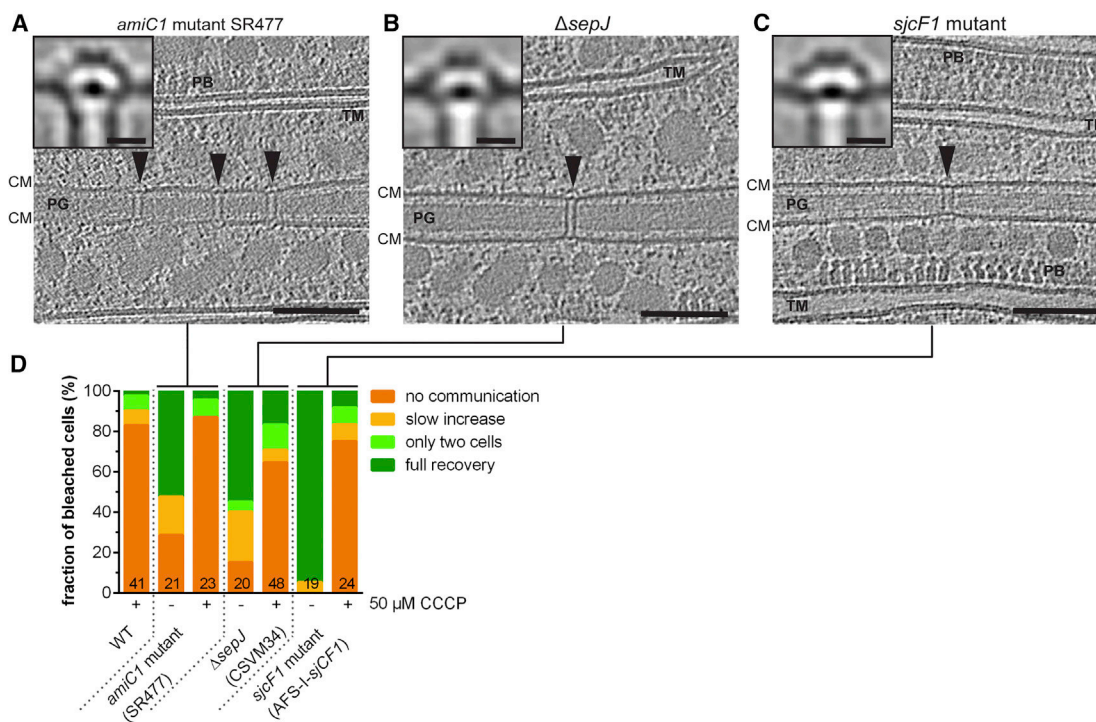


**Figure 4. AmiC1, SepJ, and SjcF1 Mutants Are Impaired in Intercellular Communication but Nevertheless Able to Control Molecular Exchange**

(A–C) Cryotomograms (shown are 13.5 nm-thick projections; bars, 100 nm) of different *Anabaena* mutants. Subtomogram averages of SJs (insets in A–C; bars, 10 nm) showed that neither the *amiC1* mutant SR477 (A), nor  $\Delta sepJ$  (B), nor the *sjcF1* mutant (C) were missing structural modules. CM, cytoplasmic membrane; PB, phycobilisomes; PG, septal peptidoglycan; TM, thylakoid membranes.

(D) FRAP responses of the wild type and the mutants shown in (A)–(C). The *amiC1* mutant SR477 and the *sepJ* mutant showed that compared to the wild type, a reduced fraction of cells was able to communicate already in the absence of CCCP (likely based on the lower total number of SJs). However, the open SJs of these mutants were able to close upon CCCP treatment, consistent with the unaltered SJ structure. The *sjcF1* mutant was not impaired in closing its SJs upon CCCP treatment. “+” and “–” indicate the presence and absence of CCCP. Numbers within the bars indicate the number of analyzed cells (n) from different filaments. Results from at least two independent cultures were cumulated.

See also Figure S5.

concentrations (Figures 5D and S5B), whereas in the  $\Delta fraC$  filaments, a fraction of 26% of the cells were still able to control communication. Taken together, our data suggest that the cap and/or plug structures are required to close SJs and thereby terminate intercellular molecular diffusion. FraC might be important for correct localization and assembly of SJ components, as proposed earlier (Merino-Puerto et al., 2011). FraD, on the other hand, emerges as a possible candidate for a SJ major structural component. This is supported by the presence of five predicted transmembrane helices, as well as the localization of FraD across the entire septum in GFP-fusion and Immunogold labeling experiments (Merino-Puerto et al., 2010, 2011).

#### FraD Localizes to the SJ Plug

We continued to investigate whether FraD was indeed a structural component of SJs. Because there are no widely used protein localization tags suitable for ECT, other studies visualized GFP as an extra density within subtomogram averages (Chang et al., 2016; Hu et al., 2017). We therefore generated a subtomogram average of SJs in a mutant expressing an N-terminal fusion of GFP to FraD. Strikingly, the average (n = 17 tomograms, 220

SJ ends) revealed an extra density in the lumen of the SJ tube, directly adjacent to the plug (Figures 6A, S6A, and S6B; Video S6). A difference map that was generated using the wild type and GFP-FraD SJ averages identified the density in the tube lumen as the major difference and indicated an otherwise similar architecture (Figures 6B and 6C). Our data suggest that FraD localized to the SJ plug, with the N terminus likely facing the tube lumen. Without knowledge of the detailed SJ architecture, an earlier study suggested that the FraD C terminus was located in the periplasm (shown by Immunogold labeling), while the N terminus was predicted to be in the cytoplasm (because of structure predictions and because an N-terminal GFP fusion would likely not be fluorescent in the periplasm) (Merino-Puerto et al., 2011). Our data are compatible with these predictions and together with the previous study they suggest that (1) the FraD C terminus extends from the plug into the periplasm, and (2) the tube lumen has in fact cytoplasmic characteristics that allow for the maturation of the N-terminal GFP-fusion.

FRAP analyses of the GFP-FraD expressing mutant revealed that this strain was still able to close SJs after CCCP treatment; however, the reopening was less efficient (Figure 6D). Interestingly,

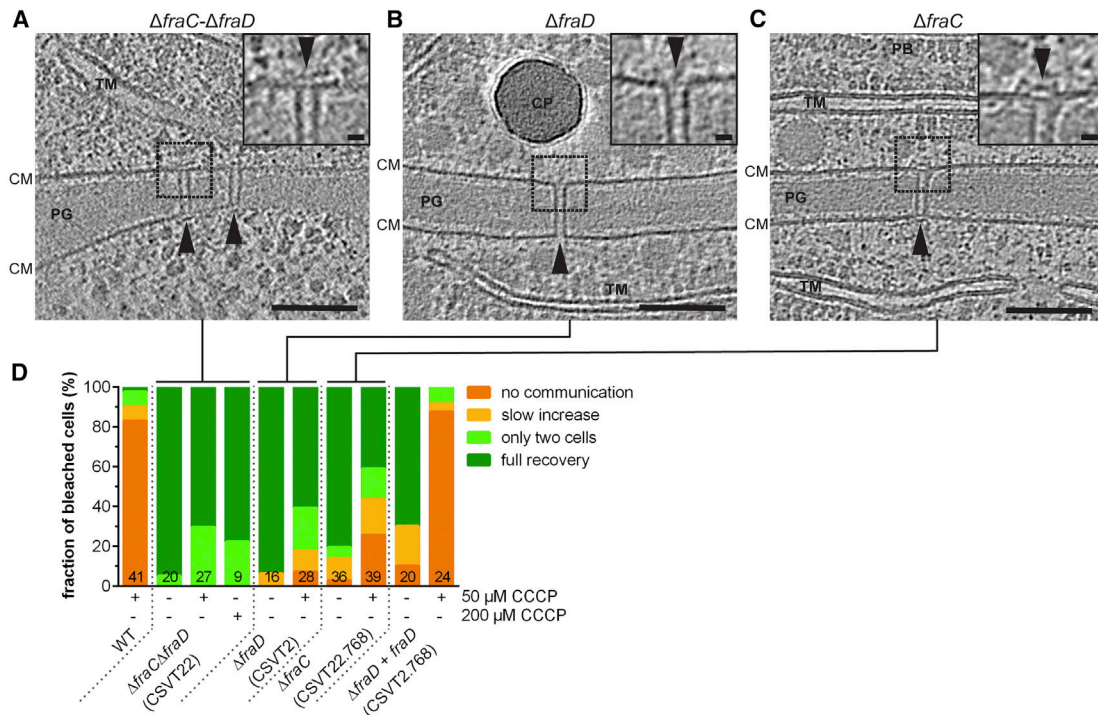


**Figure 5. The Cap and Plug Modules Are Required to Control Intercellular Communication upon Ionophore Treatment**

(A–C) SJs from the  $\Delta fraC\text{-}\Delta fraD$  (A) and  $\Delta fraD$  (B) mutants were missing the cap and plug modules. SJs from  $\Delta fraC$  (C) showed a mixture of fully assembled and misassembled SJs (insets show magnified views; bars, 10 nm). Shown are 13.5 nm-thick sections through cryotomograms; bars, 100 nm. CM, cytoplasmic membrane; CP, cyanophycin; PB, phycobilisomes; PG, septal peptidoglycan; TM, thylakoid membranes.

(D) FRAP experiments of the wild type and the mutants shown in (A)–(C). The CCCP-treated  $\Delta fraD$  and  $\Delta fraC$  single mutants showed a much smaller fraction of non-communicating cells than in the CCCP-treated wild type, indicating that the mutants were unable to gate communication. Strain CSVT2.768 is a complementation of the  $\Delta fraD$  mutant and showed wild type behavior. “+” and “-” indicate the presence and absence of CCCP. Numbers within the bars indicate the number of analyzed cells (n) from different filaments. Results from at least two independent cultures were cumulated (except for  $\Delta fraC\text{-}\Delta fraD$  treated with 200  $\mu\text{M}$  CCCP).

See also Figure S5.

the fluorescence recovery rate constant  $R$  was significantly reduced in  $gfp\text{-}fraD$  cells compared to the wild type and the complemented  $\Delta fraD\text{+}fraD$  mutant (Figure 6E), indicating a diminished diffusion rate through the SJs. This agrees with a reduced diffusion area caused by the presence of GFP ( $\sim 2.5\text{ nm} \times 5\text{ nm}$ ) within the tube lumen (7 nm).

Taken together, FraD is likely a major structural component of SJs, localized to the plug module. The analyses of mutants indicate that cap and plug form a functional unit that provides a size cutoff and gating mechanism for intercellular communication. It remains to be seen how these tasks are distributed between both modules. Our study will also serve as a framework for future efforts to identify other SJ building blocks.

### SJs Close in Response to Different Stress Factors

Because gating of intercellular communication is likely to be important under different environmental conditions, we analyzed other stress factors for their ability to induce SJ closure. Oxidative stress was imposed by treatment with 5 mM and 10 mM  $\text{H}_2\text{O}_2$  for 3 h. It was shown that  $\text{H}_2\text{O}_2$  affects the electron transport chain and therefore the activity of photosystems I and II in cyanobacteria (Samuilov et al., 2001). Similar to CCCP treat-

ments, the fraction of cells showing the FRAP response “full recovery” dropped from 100% to 30% upon treatment with 5 mM  $\text{H}_2\text{O}_2$  (Figure S7A). Cells were still viable after this treatment (Figure S7B). Nevertheless, only a small fraction of cells reopened SJs after washing (Figure S7A), indicating secondary effects of the  $\text{H}_2\text{O}_2$  treatment, which is also visible in the impaired growth of  $\text{H}_2\text{O}_2$ -treated and washed cells (Figure S7B). Consistent with the above data is the observation that the  $\Delta fraC\text{-}\Delta fraD$  mutant was impaired in ceasing molecular exchange upon  $\text{H}_2\text{O}_2$  treatment (Figure S7A).

We then tested the effect of the absence of light on gating of intercellular communication. After incubation of wild type cells for 28 h in the dark, the “full recovery” FRAP response dropped from 100% to only 5% (Figure S7C). ECT imaging after incubation in the dark for 24 h revealed SJs in the closed conformation (Figures S7D–S7F). Incubation of the  $\Delta fraC\text{-}\Delta fraD$  mutant in the dark resulted in a 6-fold higher number of “full recovery” FRAP response compared to the wild type (Figure S7C). The fraction of non-communicating cells in this mutant probably arose from secondary effects caused by the long period in the dark. Nevertheless, there is a clear difference in the regulation of molecular exchange between the wild type and mutant cells.

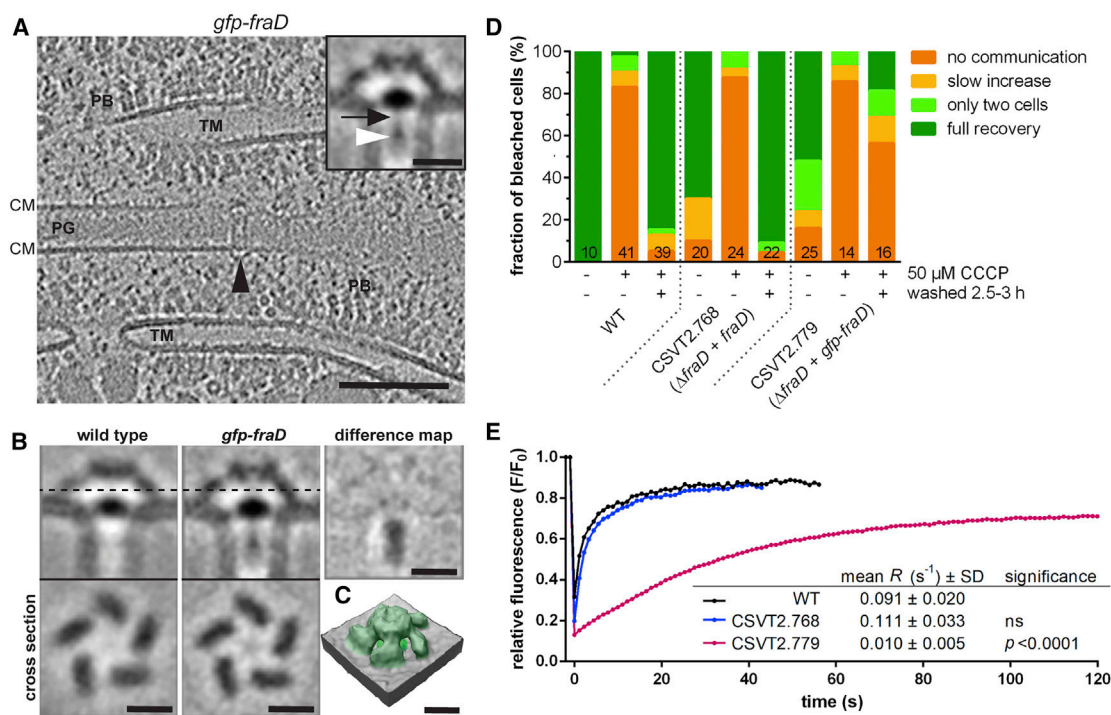


### Figure 6. FraD Localizes to the SJ Plug

(A) Cryotomograms of *Anabaena* expressing *gfp-fraD* showed SJs with partially filled tubes (black arrowhead). Shown is a 13.5 nm-thick slice; bar, 100 nm. Subtomogram averaging (inset; bar, 10 nm) revealed an extra density (white arrowhead) situated in the SJ lumen and connected to the SJ plug (black arrow). CM, cytoplasmic membrane; PB, phycobilisomes; PG, septal peptidoglycan; TM, thylakoid membranes.

(B) The difference map between subtomogram averages of septal junctions from *Anabaena* wild type and *gfp-fraD* expressing cells showed that the only major difference between these two structures was the extra density within the tube lumen, most likely corresponding to the GFP fusion. The cross sectional views (location indicated by dashed line) through the caps revealed that SJs from *gfp-fraD* expressing cells are in the open state. Bar, 10 nm.

(C) Surface representation of the average of the SJ from the *gfp-fraD*-expressing mutant showed that the cap was in the open state and similar to the wild type structure. Bar, 10 nm.

(D) The  $\Delta$ *fraD* mutant CSVT2 complemented with *gfp-fraD* (CSVT2.779) or *fraD* (CSVT2.768) expressed from a plasmid was investigated by the FRAP assay under the stated conditions (“+” and “-” indicate the presence and absence of CCCP and washing in fresh medium). The *gfp-fraD* strain (CSVT2.779) was still able to control communication, even though reopening was less efficient. Numbers within the bars indicate the number of analyzed cells (n) from different filaments. Results from at least two independent cultures were cumulated.

(E) The fluorescence recovery rate constant *R* was calculated from non-treated cells, showing a “full recovery” FRAP response. (n(WT) = 10, n(CSVT2.768) = 14, n(CSVT2.779) = 13). The *gfp-fraD* strain (CSVT2.779) showed a significantly reduced fluorescence recovery rate constant compared to wild type and the complemented  $\Delta$ *fraD*+*fraD* mutant (CSVT2.768). Significance was determined using Student’s *t* test in comparison to the wild type. A representative FRAP curve (bleaching at *t* = 0) for each strain is shown.

See also Figure S6 and Video S6.

In summary, we showed that challenging the proton motif force, oxidative stress, and darkness all induce the closure of SJs and therefore allow the cell to gate molecular exchange. It is likely that gating can be induced by a wide range of environmental factors.

### Conclusions

In conclusion, our data suggest that cyanobacterial SJs are dynamic, gated cell-cell connections, which reversibly block intercellular molecular diffusion along the filament upon different types of stress (Figure 7). This challenges the concept that the cyanobacterial filament is a symplast, with SJs providing cytosolic continuity between the cells—analogue to plasmodesmata. SJs rather reveal striking similarities to metazoan gap junctions, because they are both gated by a dynamic conformational change

of a proteinaceous macromolecular complex. Furthermore, just like SJs, gap junction closure is triggered by disruption of the proton motif force (Hervé and Derangeon, 2013; Obaid et al., 1983; Socolar and Politoff, 1971). Interestingly, the closure of gap junctions can be only partial (Ek-Vitorin and Burt, 2013), a phenomenon that might also exist in SJs, considering the “slow increase” FRAP response (Figure 2B). Finally, gap junction and SJ closure operates on a similar timescale of only seconds (Figures S4I–S4L). Despite the functional analogy between SJs and gap junctions, the involved proteins do not have a last common ancestor, which is reflected in differences in architecture. Gap junctions are composed of two hexameric connexon hemichannels of a fixed length that bridge plasma membranes (Hervé and Derangeon, 2013; Söhl et al., 2005); in contrast to SJs, featuring a 5-fold symmetric cap, a plug module, and a tube of variable length.

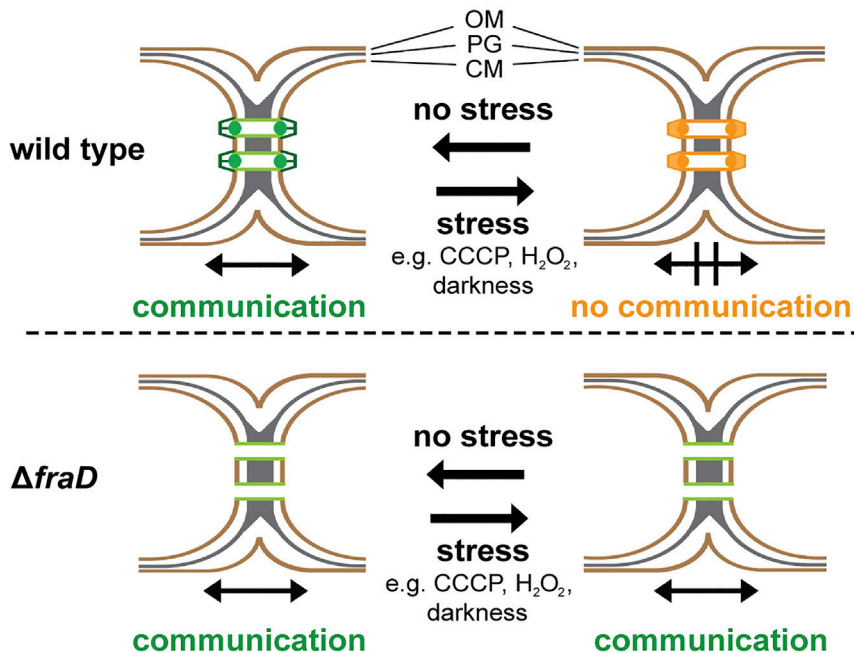


**Figure 7. SJs Reversibly Gate Cell-Cell Communication by a Conformational Change**  
SJs (green, open; orange, closed) of *Anabaena* are dynamic, gated cell-cell connections, which reversibly block intercellular molecular diffusion along the filament upon different types of stress. The  $\Delta fraD$  mutant was missing the cap and plug modules, consistent with the inability to close SJs upon stress. FraD was shown to localize to the plug module. See also Figure S7.

In the bacterial domain of life, multicellularity is found in diverse phylogenetic clades. It will be exciting to investigate whether cell-cell connections are conserved among diverse bacteria. Importantly, we imaged two further cyanobacterial model organisms, *Nostoc punctiforme* PCC 73102 and *Trichodesmium erythraeum* IMS101, and revealed that they had similar SJ architectures (Figures S7G and S7H). Together with the conservation of *fraC*, *fraD*, *amiC*, *sjcF1*, and the C-terminal domain of *sepJ* genes in their genomes, this points toward a conserved SJ mechanism at least across diverse multicellular cyanobacteria. The branching of the cyanobacterial order *Nostocales* (comprising the genus *Anabaena*) was estimated to date back more than two billion years ago (Schirmer et al., 2013). Our data thus provide a mechanistic framework for an ancient cell-cell connection structure, predating metazoan gap junctions by more than a billion years. The convergent evolution of a dynamic gated mechanism in such divergent lineages emphasizes the importance of controlling molecular exchange in multicellular organisms in order to stop communication under certain metabolic conditions, or, upon predation or fragmentation. Upon stress, the closure of the septal junctions prevents leakage of cytoplasmic components into damaged cells and thereby avoids deterioration of the entire multicellular organism, which appears as a universal survival strategy across different domains of life.

## STAR★METHODS

Detailed methods are provided in the online version of this paper and include the following:

- KEY RESOURCES TABLE
- LEAD CONTACT AND MATERIALS AVAILABILITY

## ● EXPERIMENTAL MODEL AND SUBJECT DETAILS

- Microbe strains

## ● METHOD DETAILS

- Construction of mutant strains
- FRAP assays and treatment with CCCP and  $H_2O_2$
- Plunge freezing of *Anabaena* cells
- Cryo-Focused Ion Beam milling
- Electron Cryotomography
- Tomogram reconstruction and subtomogram averaging
- ATP determination

## ● QUANTIFICATION AND STATISTICAL ANALYSIS

## ● DATA AND CODE AVAILABILITY

## SUPPLEMENTAL INFORMATION

Supplemental Information can be found online at <https://doi.org/10.1016/j.cell.2019.05.055>.

## ACKNOWLEDGMENTS

We thank Peter Tittmann and Christian Zaubitzer for technical support as well as ScopeM for instrument access at ETH Zürich. We thank Hannah Minas for help with preparing samples and analyzing the data. Jörn Piel and Anna Vagstaad are acknowledged for providing *Anabaena* and *Nostoc punctiforme* cultures for preliminary observations. We thank Ulrike Pfreundt and Roman Stocker for providing *Trichodesmium erythraeum* cultures. We thank Enrique Flores for providing plasmid pCSV56, mutants CSV2, CSV22, and CSV34, Enrico Schleiff for providing strain AFS-1-*sjcF1*, and Peter Wolk for pRL-plasmids. Fabian Eisenstein is acknowledged for help with movies. We thank João Medeiros, Tobias Zachs, and Andreas Schertel for help with preparing lamellae at Zeiss, Oberkochen. G.L.W. was supported by a Boehringer Ingelheim Fonds PhD fellowship. Work in Tübingen was supported by the Deutsche Forschungsgemeinschaft (SFB766). M.P. was supported by the Swiss National Science Foundation

(31003A\_179255), the European Research Council (679209), and the Helmut Horten Foundation.

#### AUTHOR CONTRIBUTIONS

G.L.W. and A.-K.K. contributed equally. I.M., K.F., and M.P. conceptualized the study. All authors designed experiments. G.L.W. and A.-K.K. performed experiments. All authors analyzed data. All authors participated in writing the manuscript.

#### DECLARATION OF INTERESTS

The authors declare no competing interests.

Received: October 29, 2018

Revised: March 4, 2019

Accepted: May 29, 2019

Published: July 11, 2019

#### REFERENCES

- Bauer, C.C., Buikema, W.J., Black, K., and Haselkorn, R. (1995). A short-filament mutant of *Anabaena* sp. strain PCC 7120 that fragments in nitrogen-deficient medium. *J. Bacteriol.* *177*, 1520–1526.
- Berendt, S., Lehner, J., Zhang, Y.V., Rasse, T.M., Forchhammer, K., and Maldener, I. (2012). Cell wall amidase AmiC1 is required for cellular communication and heterocyst development in the cyanobacterium *Anabaena* PCC 7120 but not for filament integrity. *J. Bacteriol.* *194*, 5218–5227.
- Black, T.A., and Wolk, C.P. (1994). Analysis of a Het<sup>-</sup> mutation in *Anabaena* sp. strain PCC 7120 implicates a secondary metabolite in the regulation of heterocyst spacing. *J. Bacteriol.* *176*, 2282–2292.
- Bornikol, J., Carrión, A., Fan, Q., Flores, E., Forchhammer, K., Mariscal, V., Mullineaux, C.W., Perez, R., Silber, N., Wolk, C.P., and Maldener, I. (2017). Role of two cell wall amidases in septal junction and nanopore formation in the multicellular cyanobacterium *Anabaena* sp. PCC 7120. *Front. Cell. Infect. Microbiol.* *7*, 386.
- Bornikol, J., Staiger, J., Madlung, J., Forchhammer, K., and Maldener, I. (2018). LytM factor Alr3353 affects filament morphology and cell-cell communication in the multicellular cyanobacterium *Anabaena* sp. PCC 7120. *Mol. Microbiol.* *108*, 187–203.
- Brunet, T., and King, N. (2017). The origin of animal multicellularity and cell differentiation. *Dev. Cell* *43*, 124–140.
- Burnat, M., Herrero, A., and Flores, E. (2014). Compartmentalized cyanophycin metabolism in the diazotrophic filaments of a heterocyst-forming cyanobacterium. *Proc. Natl. Acad. Sci. USA* *111*, 3823–3828.
- Chang, Y.-W., Rettberg, L.A., Treuner-Lange, A., Iwasa, J., Søgaard-Andersen, L., and Jensen, G.J. (2016). Architecture of the type IVa pilus machine. *Science* *351*, aad2001.
- Cumino, A.C., Marcozzi, C., Barreiro, R., and Salerno, G.L. (2007). Carbon cycling in *Anabaena* sp. PCC 7120. Sucrose synthesis in the heterocysts and possible role in nitrogen fixation. *Plant Physiol.* *143*, 1385–1397.
- Ek-Vitorin, J.F., and Burt, J.M. (2013). Structural basis for the selective permeability of channels made of communicating junction proteins. *Biochim. Biophys. Acta* *1828*, 51–68.
- Elhai, J., and Wolk, C.P. (1988). Conjugal transfer of DNA to cyanobacteria. *Methods Enzymol.* *167*, 747–754.
- Flores, E., and Herrero, A. (2010). Compartmentalized function through cell differentiation in filamentous cyanobacteria. *Nat. Rev. Microbiol.* *8*, 39–50.
- Flores, E., Herrero, A., Wolk, C.P., and Maldener, I. (2006). Is the periplasm continuous in filamentous multicellular cyanobacteria? *Trends Microbiol.* *14*, 439–443.
- Flores, E., Pernil, R., Muro-Pastor, A.M., Mariscal, V., Maldener, I., Lechno-Yossef, S., Fan, Q., Wolk, C.P., and Herrero, A. (2007). Septum-localized protein required for filament integrity and diazotrophy in the heterocyst-forming cyanobacterium *Anabaena* sp. strain PCC 7120. *J. Bacteriol.* *189*, 3884–3890.
- Flores, E., Herrero, A., Forchhammer, K., and Maldener, I. (2016). Septal junctions in filamentous heterocyst-forming cyanobacteria. *Trends Microbiol.* *24*, 79–82.
- Flores, E., Nieves-Mori6n, M., and Mullineaux, C.W. (2019). Cyanobacterial septal junctions: Properties and regulation. *Life (Basel)* *9*, E1.
- Giddings, T.H., and Staehelin, L.A. (1978). Plasma membrane architecture of *Anabaena cylindrica*: Occurrence of microplasmodesmata and changes associated with heterocyst development and the cell cycle. *Cytobiologie* *16*, 235–249.
- Giddings, T.H., and Staehelin, L.A. (1981). Observation of microplasmodesmata in both heterocyst-forming and non-heterocyst forming filamentous cyanobacteria by freeze-fracture electron microscopy. *Arch. Microbiol.* *129*, 295–298.
- Herrero, A., Stavans, J., and Flores, E. (2016). The multicellular nature of filamentous heterocyst-forming cyanobacteria. *FEMS Microbiol. Rev.* *40*, 831–854.
- Herv6, J.-C., and Derangeon, M. (2013). Gap-junction-mediated cell-to-cell communication. *Cell Tissue Res.* *352*, 21–31.
- Hoiczky, E., and Baumeister, W. (1995). Envelope structure of four gliding filamentous cyanobacteria. *J. Bacteriol.* *177*, 2387–2395.
- Hopfer, U., Lehninger, A.L., and Thompson, T.E. (1968). Protonic conductance across phospholipid bilayer membranes induced by uncoupling agents for oxidative phosphorylation. *Proc. Natl. Acad. Sci. USA* *59*, 484–490.
- Hu, B., Lara-Tejero, M., Kong, Q., Gal6n, J.E., and Liu, J. (2017). In situ molecular architecture of the salmonella type III secretion machine. *Cell* *168*, 1065–1074.
- Iancu, C.V., Tivol, W.F., Schooler, J.B., Dias, D.P., Henderson, G.P., Murphy, G.E., Wright, E.R., Li, Z., Yu, Z., Briegel, A., et al. (2006). Electron cryotomography sample preparation using the Vitrobot. *Nat. Protoc.* *1*, 2813–2819.
- Jüttner, F. (1983). <sup>14</sup>C-labeled metabolites in heterocysts and vegetative cells of *Anabaena cylindrica* filaments and their presumptive function as transport vehicles of organic carbon and nitrogen. *J. Bacteriol.* *155*, 628–633.
- Kremer, J.R., Mastronarde, D.N., and McIntosh, J.R. (1996). Computer visualization of three-dimensional image data using IMOD. *J. Struct. Biol.* *116*, 71–76.
- Lang, N.J., and Fay, P. (1971). The heterocysts of blue-green algae II. Details of ultrastructure. *Proc. R. Soc. Lond. B Biol. Sci.* *178*, 193–203.
- Lehner, J., Zhang, Y., Berendt, S., Rasse, T.M., Forchhammer, K., and Maldener, I. (2011). The morphogene AmiC2 is pivotal for multicellular development in the cyanobacterium *Nostoc punctiforme*. *Mol. Microbiol.* *79*, 1655–1669.
- Lehner, J., Berendt, S., D6rsam, B., Perez, R., Forchhammer, K., and Maldener, I. (2013). Prokaryotic multicellularity: a nanopore array for bacterial cell communication. *FASEB J.* *27*, 2293–2300.
- Maldener, I., Summers, M.L., and Sukenik, A. (2014). Cellular differentiation in filamentous cyanobacteria. In *The Cell Biology of Cyanobacteria*, E. Flores and A. Herrero, eds. (Caister Academic Press), pp. 239–304.
- Mariscal, V. (2014). Cell-cell joining proteins in heterocyst-forming cyanobacteria. In *The Cell Biology of Cyanobacteria*, E. Flores and A. Herrero, eds. (Caister Academic Press), pp. 293–304.
- Mariscal, V., Herrero, A., Nenninger, A., Mullineaux, C.W., and Flores, E. (2011). Functional dissection of the three-domain SepJ protein joining the cells in cyanobacterial trichomes. *Mol. Microbiol.* *79*, 1077–1088.
- Mariscal, V., Nürnberg, D.J., Herrero, A., Mullineaux, C.W., and Flores, E. (2016). Overexpression of SepJ alters septal morphology and heterocyst pattern regulated by diffusible signals in *Anabaena*. *Mol. Microbiol.* *101*, 968–981.
- Marko, M., Hsieh, C., Schalek, R., Frank, J., and Mannella, C. (2007). Focused-ion-beam thinning of frozen-hydrated biological specimens for cryo-electron microscopy. *Nat. Methods* *4*, 215–217.

- Mastronarde, D.N. (2005). Automated electron microscope tomography using robust prediction of specimen movements. *J. Struct. Biol.* 152, 36–51.
- Mastronarde, D.N. (2008). Correction for non-perpendicularity of beam and tilt axis in tomographic reconstructions with the IMOD package. *J. Microsc.* 230, 212–217.
- Medeiros, J.M., Böck, D., Weiss, G.L., Kooger, R., Wepf, R.A., and Pilhofer, M. (2018). Robust workflow and instrumentation for cryo-focused ion beam milling of samples for electron cryotomography. *Ultramicroscopy* 190, 1–11.
- Merino-Puerto, V., Mariscal, V., Mullineaux, C.W., Herrero, A., and Flores, E. (2010). Fra proteins influencing filament integrity, diazotrophy and localization of septal protein SepJ in the heterocyst-forming cyanobacterium *Anabaena* sp. *Mol. Microbiol.* 75, 1159–1170.
- Merino-Puerto, V., Schwarz, H., Maldener, I., Mariscal, V., Mullineaux, C.W., Herrero, A., and Flores, E. (2011). FraC/FraD-dependent intercellular molecular exchange in the filaments of a heterocyst-forming cyanobacterium, *Anabaena* sp. *Mol. Microbiol.* 82, 87–98.
- Metzner, I. (1955). [Chemistry and submicroscopic structure of cell walls, sheaths, and gelatin of Cyanophyceae. II. Cell morphology and cell physiology of Cyanophyceae]. *Arch. Mikrobiol.* 22, 45–77.
- Mullineaux, C.W., Mariscal, V., Nenninger, A., Khanum, H., Herrero, A., Flores, E., and Adams, D.G. (2008). Mechanism of intercellular molecular exchange in heterocyst-forming cyanobacteria. *EMBO J.* 27, 1299–1308.
- Nayar, A.S., Yamaura, H., Rajagopalan, R., Risser, D.D., and Callahan, S.M. (2007). FraG is necessary for filament integrity and heterocyst maturation in the cyanobacterium *Anabaena* sp. strain PCC 7120. *Microbiology* 153, 601–607.
- Nicastro, D., Schwartz, C., Pierson, J., Gaudette, R., Porter, M.E., and McIntosh, J.R. (2006). The molecular architecture of axonemes revealed by cryoelectron tomography. *Science* 313, 944–948.
- Nieves-Mori6n, M., Mullineaux, C.W., and Flores, E. (2017). Molecular diffusion through cyanobacterial septal junctions. *MBio* 8, e01756-16.
- Nürnberg, D.J., Mariscal, V., Bornikoel, J., Nieves-Mori6n, M., Krauß, N., Herrero, A., Maldener, I., Flores, E., and Mullineaux, C.W. (2015). Intercellular diffusion of a fluorescent sucrose analog via the septal junctions in a filamentous cyanobacterium. *MBio* 6, e02109.
- Obaid, A.L., Socolar, S.J., and Rose, B. (1983). Cell-to-cell channels with two independently regulated gates in series: analysis of junctional conductance modulation by membrane potential, calcium, and pH. *J. Membr. Biol.* 73, 69–89.
- Omairi-Nasser, A., Haselkorn, R., and Austin, J., 2nd. (2014). Visualization of channels connecting cells in filamentous nitrogen-fixing cyanobacteria. *FASEB J.* 28, 3016–3022.
- Omairi-Nasser, A., Mariscal, V., Austin, J.R., 2nd, and Haselkorn, R. (2015). Requirement of Fra proteins for communication channels between cells in the filamentous nitrogen-fixing cyanobacterium *Anabaena* sp. PCC 7120. *Proc. Natl. Acad. Sci. USA* 112, E4458–E4464.
- Oparka, K.J., Roberts, A.G., Boevink, P., Santa Cruz, S., Roberts, I., Pradel, K.S., Imlau, A., Kotlizky, G., Sauer, N., and Epel, B. (1999). Simple, but not branched, plasmodesmata allow the nonspecific trafficking of proteins in developing tobacco leaves. *Cell* 97, 743–754.
- Pettersen, E.F., Goddard, T.D., Huang, C.C., Couch, G.S., Greenblatt, D.M., Meng, E.C., and Ferrin, T.E. (2004). UCSF Chimera—a visualization system for exploratory research and analysis. *J. Comput. Chem.* 25, 1605–1612.
- Ramos-Le6n, F., Mariscal, V., Frías, J.E., Flores, E., and Herrero, A. (2015). Divisome-dependent subcellular localization of cell-cell joining protein SepJ in the filamentous cyanobacterium *Anabaena*. *Mol. Microbiol.* 96, 566–580.
- Rigort, A., Bäuerlein, F.J.B., Leis, A., Gruska, M., Hoffmann, C., Laugks, T., Böhm, U., Eibauer, M., Gnaegi, H., Baumeister, W., and Plitzko, J.M. (2010). Micromachining tools and correlative approaches for cellular cryo-electron tomography. *J. Struct. Biol.* 172, 169–179.
- Rippka, R., Deruelles, J., Herdman, M., Waterbury, J.B., and Stanier, R.Y. (1979). Generic assignments, strain histories and properties of pure cultures of cyanobacteria. *Microbiology* 117, 1–61.
- Rudolf, M., Tetik, N., Ramos-Le6n, F., Flinner, N., Ngo, G., Stevanovic, M., Burnat, M., Pernil, R., Flores, E., and Schleiff, E. (2015). The peptidoglycan-binding protein SjcF1 influences septal junction function and channel formation in the filamentous cyanobacterium *Anabaena*. *MBio* 6, e00376.
- Sager, R., and Lee, J.-Y. (2014). Plasmodesmata in integrated cell signalling: insights from development and environmental signals and stresses. *J. Exp. Bot.* 65, 6337–6358.
- Sambrook, J., Fritsch, E.F., and Maniatis, T. (1989). *Molecular cloning: A laboratory manual* (Cold Spring Harbor Laboratory Press).
- Samuilov, V.D., Bezryadov, D.B., Gusev, M.V., Kitashov, A.V., and Fedorenko, T.A. (2001). Hydrogen peroxide inhibits photosynthetic electron transport in cells of cyanobacteria. *Biochemistry (Mosc.)* 66, 640–645.
- Schaffer, M., Engel, B.D., Laugks, T., Mahamid, J., Plitzko, J.M., and Baumeister, W. (2015). Cryo-focused ion beam sample preparation for imaging vitreous cells by cryo-electron tomography. *Bio. Protoc.* 5, e1575.
- Schaffer, M., Mahamid, J., Engel, B.D., Laugks, T., Baumeister, W., and Plitzko, J.M. (2017). Optimized cryo-focused ion beam sample preparation aimed at in situ structural studies of membrane proteins. *J. Struct. Biol.* 197, 73–82.
- Schindelin, J., Arganda-Carreras, I., Frise, E., Kaynig, V., Longair, M., Pietzsch, T., Preibisch, S., Rueden, C., Saalfeld, S., Schmid, B., et al. (2012). Fiji: an open-source platform for biological-image analysis. *Nat. Methods* 9, 676–682.
- Schirmeister, B.E., de Vos, J.M., Antonelli, A., and Bagheri, H.C. (2013). Evolution of multicellularity coincided with increased diversification of cyanobacteria and the Great Oxidation Event. *Proc. Natl. Acad. Sci. USA* 110, 1791–1796.
- Socolar, S.J., and Politoff, A.L. (1971). Uncoupling cell junctions in a glandular epithelium by depolarizing current. *Science* 172, 492–494.
- S6hl, G., Maxeiner, S., and Willecke, K. (2005). Expression and functions of neuronal gap junctions. *Nat. Rev. Neurosci.* 6, 191–200.
- Thomas, J., Meeks, J.C., Wolk, C.P., Shaffer, P.W., and Austin, S.M. (1977). Formation of glutamine from [13n]ammonia, [13n]dinitrogen, and [14C]glutamate by heterocysts isolated from *Anabaena cylindrica*. *J. Bacteriol.* 129, 1545–1555.
- Tivol, W.F., Briegel, A., and Jensen, G.J. (2008). An improved cryogen for plunge freezing. *Microsc. Microanal.* 14, 375–379.
- Unwin, P.N.T., and Zampighi, G. (1980). Structure of the junction between communicating cells. *Nature* 283, 545–549.
- Weiss, G.L., Medeiros, J.M., and Pilhofer, M. (2017). In situ imaging of bacterial secretion systems by electron cryotomography. *Methods Mol. Biol.* 1615, 353–375.
- Wilk, L., Strauss, M., Rudolf, M., Nicolaisen, K., Flores, E., Kühlbrandt, W., and Schleiff, E. (2011). Outer membrane continuity and septosome formation between vegetative cells in the filaments of *Anabaena* sp. PCC 7120. *Cell. Microbiol.* 13, 1744–1754.
- Wolk, C.P., Vonshak, A., Kehoe, P., and Elhai, J. (1984). Construction of shuttle vectors capable of conjugative transfer from *Escherichia coli* to nitrogen-fixing filamentous cyanobacteria. *Proc. Natl. Acad. Sci. USA* 81, 1561–1565.
- Zheng, S.Q., Keszhelyi, B., Branlund, E., Lyle, J.M., Braunfeld, M.B., Sedat, J.W., and Agard, D.A. (2007). UCSF tomography: an integrated software suite for real-time electron microscopic tomographic data collection, alignment, and reconstruction. *J. Struct. Biol.* 157, 138–147.

## STAR★METHODS

## KEY RESOURCES TABLE

REAGENT or RESOURCE	SOURCE	IDENTIFIER
<b>Bacterial and Virus Strains</b>		
<i>Anabaena</i> sp. PCC 7120	Rippka et al., 1979	PCC 7120
<i>Nostoc punctiforme</i> PCC 73102	Rippka et al., 1979	PCC 73102
<i>Trichodesmium erythraeum</i> IMS101	Stocker Lab, ETH Zürich	IMS101
<i>E. coli</i> NEB 10-beta (electrocompetent)	NEB	Cat#C3020K
<i>E. coli</i> HB101	Sambrook et al., 1989	N/A
<i>E. coli</i> J53 (RP-4)	Wolk et al., 1984	N/A
Strain details	This study	see Table S1
<b>Chemicals, Peptides, and Recombinant Proteins</b>		
Calcein, AM	Invitrogen	Cat#C3099
CCCP (Carbonyl cyanide 3-chlorophenylhydrazone)	Sigma-Aldrich	Cat#C2759; CAS: 555-60-2
30% hydrogen peroxide	Carl Roth	Cat#CP26; CAS: 7722-84-1
Chloramphenicol	Carl Roth	Cat#3886; CAS: 56-75-7
Spectinomycin dihydrochloride pentahydrate	Sigma-Aldrich	Cat#S4014; CAS: 22189-32-8
Neomycin sulfate	Sigma-Aldrich	Cat#PHR1491; CAS: 1405-10-3
Streptomycin sulfate	Sigma-Aldrich	Cat#S1400000; CAS: 3810-74-0
Kanamycin sulfate	Carl Roth	Cat#T832; CAS: 25389-94-0
<b>Critical Commercial Assays</b>		
Monarch Plasmid Miniprep Kit	NEB	Cat#T1010S
Monarch DNA Gel Extraction Kit	NEB	Cat#T1020S
Monarch PCR & DNA Cleanup Kit	NEB	Cat#T1030S
ATP Determination Kit (A22066)	Invitrogen	Cat#10700345
<b>Deposited Data</b>		
<i>Anabaena</i> sp. PCC 7120 reference genome, CyanoBase	Kazusa DNA Research Institute (KDRI)	<a href="http://genome.microbedb.jp/cyanobase/">http://genome.microbedb.jp/cyanobase/</a>
<i>Anabaena</i> sp. PCC 7120 example tomogram	This study	EMDB: EMD-4949
<i>Anabaena</i> sp. PCC 7120 CCCP treated example tomogram	This study	EMDB: EMD-4957
<i>Anabaena</i> sp. PCC 7120 $\Delta$ SepJ example tomogram	This study	EMDB: EMD-4952
<i>Anabaena</i> sp. PCC 7120 $\Delta$ SjcF1 example tomogram	This study	EMDB: EMD-4951
<i>Anabaena</i> sp. PCC 7120 $\Delta$ AmiC1 example tomogram	This study	EMDB: EMD-4956
<i>Anabaena</i> sp. PCC 7120 $\Delta$ FraD example tomogram	This study	EMDB: EMD-4953
<i>Anabaena</i> sp. PCC 7120 $\Delta$ FraC example tomogram	This study	EMDB: EMD-4955
<i>Anabaena</i> sp. PCC 7120 $\Delta$ FraCD example tomogram	This study	EMDB: EMD-4954
<i>Anabaena</i> sp. PCC 7120 GFP-FraD example tomogram	This study	EMDB: EMD-4950
Subtomogram average of septal junctions of <i>Anabaena</i> sp. PCC 7120	This study	EMDB: EMD-4969
Subtomogram average of septal junctions of <i>Anabaena</i> sp. PCC 7120 after 24h in the dark	This study	EMDB: EMD-4968
Subtomogram average of septal junctions of <i>Anabaena</i> sp. PCC 7120 after CCCP treatment	This study	EMDB: EMD-4962
Subtomogram average of septal junctions of <i>Anabaena</i> sp. PCC 7120 after washing out CCCP	This study	EMDB: EMD-4963
Subtomogram average of septal junctions of <i>Anabaena</i> sp. PCC 7120 $\Delta$ SepJ	This study	EMDB: EMD-4965

(Continued on next page)

<b>Continued</b>		
REAGENT or RESOURCE	SOURCE	IDENTIFIER
Subtomogram average of septal junctions of <i>Anabaena</i> sp. PCC 7120 ΔSjcF1	This study	EMDB: EMD-4966
Subtomogram average of septal junctions of <i>Anabaena</i> sp. PCC 7120 ΔAmiC1	This study	EMDB: EMD-4964
Subtomogram average of septal junctions of <i>Anabaena</i> sp. PCC 7120 FraD-GFP	This study	EMDB: EMD-4967
Subtomogram average of septal junctions of <i>Anabaena</i> sp. PCC 7120 after 45 s CCCP treatment	This study	EMDB: EMD-4961
Experimental Models: Organisms/Strains		
<i>Anabaena</i> sp. PCC 7120 SR477	<a href="#">Berendt et al., 2012</a>	N/A
<i>Anabaena</i> sp. PCC 7120 CSV22	<a href="#">Merino-Puerto et al., 2011</a>	N/A
<i>Anabaena</i> sp. PCC 7120 CSV2	<a href="#">Merino-Puerto et al., 2010</a>	N/A
<i>Anabaena</i> sp. PCC 7120 CSV22 pIM496	B. Jan, I.M., and K.F., unpublished data	N/A
<i>Anabaena</i> sp. PCC 7120 CSVM34	<a href="#">Mariscal et al., 2011</a>	N/A
<i>Anabaena</i> sp. PCC 7120 AFS-I- <i>sjcF1</i>	<a href="#">Rudolf et al., 2015</a>	N/A
<i>Anabaena</i> sp. PCC 7120 CSV22.768	This study	N/A
<i>Anabaena</i> sp. PCC 7120 CSV2.768	This study	N/A
<i>Anabaena</i> sp. PCC 7120 CSV2.779	This study	N/A
Strain details	This study	see <a href="#">Table S1</a>
Oligonucleotides		
Primer 1998: GATATCCCGCAAGAGGCCCTTTCGTCCTT CAAGAATTCTGCCGTTCCCTTGTCATCTG	This study	N/A
Primer 2000: ATGAGTAAAGGAGAAGAACTTTTC	This study	N/A
Primer 2001: ACTCCAGTGAAAAGTTCTTCTCCTTTACT CATAGACACTCAACAAAAAGGGAAACTGTAG	This study	N/A
Primer 2040: CCCTTTTTGTTGAGTGTCTTGCTAACTC GTTAAGTTAC	This study	N/A
Primer 2041: GTAACCTAACGAGTTAGCAAGACTCAA CAAAAAGGGAAAC	This study	N/A
Primer 2042: CACTATAGGGAGACCACAACGGTTCCCT CTACCGGGATCCTCACTGCTGCGGTGGCGCTG	This study	N/A
Primer 2092: GGCATGGATGAACATACAAGCTTAATTTA TTATTTAAAGACC	This study	N/A
Primer 2093: AGCTTGATAGTTCATCCATGCC	This study	N/A
Recombinant DNA		
Plasmid: pRL1049	<a href="#">Black and Wolk, 1994</a>	N/A
Plasmid: pIM496	<a href="#">Berendt et al., 2012</a>	N/A
Plasmid: pIM768	This study	N/A
Plasmid: pIM779	This study	N/A
Plasmid: pIM759	This study	N/A
Plasmid: pRL528	<a href="#">Wolk et al., 1984</a>	Addgene Plasmid #58495
Plasmid: pCSV56	<a href="#">Merino-Puerto et al., 2010</a>	N/A
Plasmid details	This study	see <a href="#">Table S1</a>
Software and Algorithms		
ImageJ version 1.51j	Rasband, W.S., ImageJ, U. S. National Institutes of Health, Bethesda, Maryland, USA	<a href="https://imagej.nih.gov/ij">https://imagej.nih.gov/ij</a>
ZEN 2.3 (blue edition)	ZEISS	<a href="https://www.zeiss.de/mikroskopie/downloads.html?vaURL=www.zeiss.de/mikroskopie/downloads/zen.html">https://www.zeiss.de/mikroskopie/downloads.html?vaURL=www.zeiss.de/mikroskopie/downloads/zen.html</a>

(Continued on next page)

**Continued**

REAGENT or RESOURCE	SOURCE	IDENTIFIER
GraphPad PRISM version 6.01 for Windows	La Jolla, CA, USA	<a href="https://www.graphpad.com/">https://www.graphpad.com/</a>
ImageJ Time Series Analyzer V3	Balaji, J., Department of Neurobiology, UCLA	<a href="https://imagej.nih.gov/ij/plugins/time-series.html">https://imagej.nih.gov/ij/plugins/time-series.html</a>
IMOD	<a href="#">Kremer et al., 1996</a>	<a href="http://bio3d.colorado.edu/imod/">http://bio3d.colorado.edu/imod/</a>
UCSF Tomography	<a href="#">Zheng et al., 2007</a>	<a href="http://msg.ucsf.edu">http://msg.ucsf.edu</a>
SerialEM	<a href="#">Mastronarde, 2005</a>	<a href="http://bio3d.colorado.edu/SerialEM/">http://bio3d.colorado.edu/SerialEM/</a>
PEET	<a href="#">Nicastro et al., 2006</a>	<a href="http://bio3d.colorado.edu/PEET/">http://bio3d.colorado.edu/PEET/</a>
Other		
Confocal microscope	ZEISS	LSM 800
Plunge freezing robot Vitrobot Mk IV	Thermo Fisher	Vitrobot Mk IV
Dual Beam FIB/SEM microscope Helios NanoLab 600i	Thermo Fisher	Helios Nanolab600i
300kV Cryo-transmission electron microscope Titan Krios	Thermo Fisher	Titan Krios
Luminometer	Berthold Detection System	Sirius

**LEAD CONTACT AND MATERIALS AVAILABILITY**

Further information and requests for resources and reagents should be directed to and will be fulfilled by the Lead Contact, Martin Pilhofer ([pilhofer@biol.ethz.ch](mailto:pilhofer@biol.ethz.ch)).

**EXPERIMENTAL MODEL AND SUBJECT DETAILS****Microbe strains**

The bacterial strains used in this study are described in the [Key Resource Table](#) and in [Table S1](#). All cyanobacteria strains were cultivated in liquid Bg11 media in 100 mL flasks at 28°C with constant illumination at 30–40  $\mu\text{E m}^{-2} \text{s}^{-1}$ , shaking at 100–120 rpm or grown on Bg11 medium solidified with 1.5% (w/v) Difco agar. Stock cultures of the wild-type strain were kept in BG11<sub>0</sub> medium, void of a nitrogen source ([Rippka et al., 1979](#)). Indicated mutant strains (see [Table S1](#)) were cultured in Bg11 media supplemented with antibiotics at the following concentrations: 50  $\mu\text{g mL}^{-1}$  neomycin, 5  $\mu\text{g mL}^{-1}$  spectinomycin, and 5  $\mu\text{g mL}^{-1}$  streptomycin.

*Escherichia coli* (*E. coli*) strains were used for cloning and conjugation and were cultured in LB media at 37°C supplemented with antibiotics at concentrations of 50  $\mu\text{g mL}^{-1}$  kanamycin, 100  $\mu\text{g mL}^{-1}$  spectinomycin, and 25  $\mu\text{g mL}^{-1}$  streptomycin when indicated.

**METHOD DETAILS****Construction of mutant strains**

Plasmids (see [Table S1](#)) were introduced into *Anabaena* sp. strains by triparental mating (conjugation) using the *E. coli* strains J53 (RP-4) ([Wolk et al., 1984](#)) and HB101 (pRL528) ([Wolk et al., 1984](#); [Sambrook et al., 1989](#)) carrying the respective cargo plasmid ([Elhai and Wolk, 1988](#)). Reference sequences were obtained from Cyanobase (<http://genome.microbedb.jp/cyanobase/>) and amplified performing colony PCR using *Anabaena* sp. PCC 7120 culture as template. PCR fragments and plasmid DNA were purified using the Monarch Kits (New England Biolabs, Frankfurt). Plasmids were inserted into *E. coli* cells via electroporation (1.8 kV, 25  $\mu\text{F}$ , 200  $\Omega$ ) and sequences were verified by sequencing (GATC biotech AG, Konstanz, Germany).

Cloning of the plasmid pIM768 was done by amplification of a 344 bp upstream region of the *fraCDE* operon using oligonucleotides 1998/2041. Via overlap extension PCR (OE-PCR) using oligonucleotides 1998/2042, this fragment was fused to the *fraD* ORF, which was amplified with oligonucleotides 2042/2040. The PCR product was fused into EcoRI/BamHI-digested pRL1049 ([Black and Wolk, 1994](#)) via Gibson Assembly cloning resulting in pIM768. The plasmid was transferred into strain CSVT22 ([Merino-Puerto et al., 2011](#)) for construction of a  $\Delta$ *fraC* mutant and in CSVT2 ([Merino-Puerto et al., 2010](#)) for complementation of the *fraD* gene as expression control strain.

For construction of a GFP-FraD fusion, the *fraCDE* upstream region was amplified with oligonucleotides 1998/2001. *Gfp-mut2* was amplified from plasmid pCSV56 ([Merino-Puerto et al., 2010](#)) via standard PCR using oligonucleotides 2000/2093. The two PCR fragments were fused via OE-PCR with oligonucleotides 1998/2093. The *fraD* ORF was amplified using oligonucleotides 2092/2042 and fused via OE-PCR to the latter construct using oligonucleotides 1998/2042. The fused PCR fragment was introduced into EcoRI/BamHI-digested pRL1049 ([Black and Wolk, 1994](#)) via Gibson Assembly cloning resulting in pIM779, which was then transferred into strain CSVT2 ([Merino-Puerto et al., 2010](#)).

### FRAP assays and treatment with CCCP and H<sub>2</sub>O<sub>2</sub>

*Anabaena* filaments were taken after growth for 3 days on Bg11 agar plates and resuspended to an optical density of OD<sub>750</sub> = 1.2 in 500  $\mu$ L liquid Bg11. Cells were washed three times with Bg11 medium and stained with the fluorescent dye calcein acetoxymethyl-ester (1 mg/mL in DMSO) for 90 min in the dark at 28°C with gentle agitation as previously described (Merino-Puerto et al., 2011; Mullineaux et al., 2008). Thereafter, the cells were washed again three times with Bg11 medium. Either 0.25-1  $\mu$ L CCCP (carbonyl cyanide 3-chlorophenylhydrazone; stock 0.1 mM, 10 mM or 100 mM in DMSO) or 1  $\mu$ L DMSO as control was added to the cells, whereby the concentration of DMSO never exceeded a final concentration of 0.002%. After another 90 min of incubation with gentle shaking in the dark, the cells were spotted onto Bg11 agar and covered with a coverslip for imaging at room temperature. In order to test for reversibility of the closure of SJs after CCCP treatment, cells were washed three times with CCCP-free Bg11 medium and incubated for 2.5 h at room temperature in the light. For the H<sub>2</sub>O<sub>2</sub> assay, cells were treated with 10 mM H<sub>2</sub>O<sub>2</sub> instead of CCCP and incubated 3 h prior to FRAP (fluorescence recovery after photobleaching) measurements. All FRAP measurements were performed with a 63x/1.4 oil-immersion objective of a Zeiss LSM 800 confocal microscope and the ZEN 2.3 (blue edition) software as described previously (Bornikoel et al., 2017). The sample was excited using the 488 nm line of a 10 mW laser at 0.2% intensity. Chlorophyll auto-fluorescence (emission detection at 650-700 nm) and calcein fluorescence (emission detection at 400-530 nm) were imaged simultaneously using a 191  $\mu$ m confocal pinhole (4.49 airy units) resulting in a point-spread of about 3  $\mu$ m in the Z-direction. Further imaging settings are listed hereafter: frame size 36.2  $\times$  36.2  $\mu$ m, pixel size 0.07  $\mu$ m, pixel dwell time 1.52  $\mu$ s, averaging 1x line averaging. Five images of pre-bleached cells were captured before the laser intensity was increased by at least a factor of 10 for bleaching a region of interest using the 'fast-bleach' option. Images at 1 s intervals were taken for 30-120 s in order to record the fluorescence recovery in the bleached cell. Data were processed via ImageJ and Excel (see section QUANTIFICATION AND STATISTICAL ANALYSIS). Obtained fluorescence recovery curves were assigned into one of the four groups and percentage distribution was calculated for cumulated results from at least 2 independent experiments.

### Plunge freezing of *Anabaena* cells

*Anabaena* cultures sedimented for  $\sim$ 45 min and were concentrated by removing 2/3 of the medium. 3.5  $\mu$ L of cell suspension was applied on glow-discharged copper or molybdenum EM grids (R2/2, Quantifoil) and automatically blotted from the back (Weiss et al., 2017) for 4-6 s and plunged into liquid ethane/propane (Tivol et al., 2008) using a VitroBot plunge freezing robot (ThermoFisher) (Iancu et al., 2006). Frozen grids were subsequently stored in liquid nitrogen.

### Cryo-Focused Ion Beam milling

CryoFIB milling was used to thin plunge frozen *Anabaena* filaments for subsequent ECT analysis and was done according to (Medeiros et al., 2018). Frozen grids were clipped into modified autoloader grids (provided by J. Plitzko, Max Planck Institute of Biochemistry) (Schaffer et al., 2015), clamped into a 40° pre-tilted TEM grid holder (Leica Microsystems) and transferred from the loading station to the dual beam instrument using the VCT100 cryo-transfer system (Leica Microsystems). The holder was mounted on a custom-built cryo-stage on a Helios NanoLab600i dual beam FIB/SEM instrument (ThermoFisher). Grid quality and targeting of the cells was done by scanning EM (SEM) imaging (3-5 kV, 21 pA). After coating with Platinum precursor gas, 8-9  $\mu$ m wide lamellae through *Anabaena* filaments were prepared in several steps using the focused ion beam. This size allowed covering roughly two septa per bacterial filament. The current of the ion beam was gradually reduced from 43 nA to 24 pA according to lamella thickness until a final lamella thickness of  $\sim$ 250 nm was achieved. 9 – 24 lamellae were produced in a 12 h session and the holder was subsequently brought back to the loading station using the VCT100 transfer system. Grids were unloaded and stored under liquid nitrogen until loaded to the TEM. Lamella for the 45 s CCCP-treated *Anabaena* cells (Figures S4J–S4L) were prepared on a Crossbeam 550 (Zeiss), equipped with a cryo-stage (Leica Microsystems). The workflow was identical to the one described above, except that a lamella width of 11  $\mu$ m and a final lamella thickness of 200 nm was targeted. For transfer of cryo-samples between the FIB/SEM microscope and the loading station, a VCT500 cryo-transfer system (Leica Microsystems) was used.

### Electron Cryotomography

CryoFIB processed *Anabaena* filaments were examined by electron cryotomography. Images were recorded on a Titan Krios 300kV FEG transmission electron microscope (ThermoFisher) equipped with a Quantum LS imaging filter (slit width 20 eV) and K2 Summit direct electron detector (Gatan). A low magnification overview of the grid was recorded using SerialEM (Mastronarde, 2005). Tilt series were collected automatically using UCSF Tomo (Zheng et al., 2007) and covered an angular range from  $-60^\circ$  to  $+60^\circ$  with  $2^\circ$  increment with a defocus of  $-7$  to  $-9$   $\mu$ m. The total dose of a tilt series accumulated to 120-140  $e^- / \text{\AA}^2$  and the pixel size at the specimen level was 3.38  $\text{\AA}$ .

### Tomogram reconstruction and subtomogram averaging

Tilt series were drift-corrected using alignframes, and CTF correction and three-dimensional reconstructions were generated using the IMOD package (Kremer et al., 1996; Mastronarde, 2008). Subtomogram averaging was done according to (Weiss et al., 2017) using PEET (Nicastro et al., 2006). Briefly, SJs were identified visually in individual tomograms and their periplasm-spanning axes were modeled with open contours in 3dmod (Mastronarde, 2008) to generate model points, the initial motive list and particle rotation axes. For the open state of the septal junctions, 446 particles were averaged with a box size of 22  $\times$  22  $\times$  22 pixels and a pixel size of

1.35 nm. The average indicated a 5-fold rotational symmetry. To exclude other symmetries, 3-, 4-, 5-, 6- and 8-fold rotational symmetries were imposed on the average. The averages indicated the strongest reinforcement with 5-fold symmetry. The final 5-fold symmetrized average resulted, in 1802 particles (after removal of duplicated or misaligned particles), with a box size of  $44 \times 44 \times 44$  pixels and a pixel size of 0.67 nm. A similar approach was applied to CCCP-treated SJs, resulting in 312 particles and a final average of 1471 particles after 5-fold symmetrization and the removal of duplicated particles. The box size was  $44 \times 44 \times 44$  pixels with 0.67 nm pixel size. For the subtomogram averages of SJs from *Anabaena* PCC7120 *gfp-fraD*, 220 particles were initially selected and the final subtomogram average represents 1100 particles after 5-fold symmetrization and removal of duplicate particles with a box size of  $44 \times 44 \times 44$  pixels and 0.67 nm pixel size. The difference map between subtomogram averages from wild-type and *gfp-fraD* was generated in Chimera (Pettersen et al., 2004) with the “vop map## subtract map##” command. For subtomogram averages of SJs from *Anabaena* PCC 7120 wild-type (45 s CCCP treatment; 270 particles after 5-fold symmetrization), wild-type (90 min CCCP treatment, 3 times washed and 2.5 h incubation in fresh medium; 660 particles after 5-fold symmetrization), wild-type (24 h incubation in the dark; 200 particles after 5-fold symmetrization), *amiC1* mutant SR477 (780 particles after 5-fold symmetrization),  $\Delta sepJ$  (310 particles after 5-fold symmetrization) and  $\Delta sjcF1$  (504 particles after 5-fold symmetrization) the pixel size was 1.34 nm and box size was  $26 \times 26 \times 26$  pixels. 3D rendering, segmentations and movies were done with IMOD or Chimera. The density plot was generated with FIJI (Schindelin et al., 2012). Coloring of the different SJ modules was done with Adobe Photoshop.

### ATP determination

Sample preparation for ATP determination was performed identically to CCCP-FRAP experiments. *Anabaena* cells grown four days on Bg11 agar were resuspended to an  $OD_{750} = 1.2$  in 0.5 mL Bg11 medium. In order to mimic addition of calcein solved in DMSO, 10  $\mu$ L DMSO were added to each sample (except for no treatment control) and incubated for 90 min at 28°C in the dark. After washing the cells three times with Bg11 medium, either different concentrations of CCCP or 1  $\mu$ L DMSO (maximum volume added with CCCP) were added to the samples, followed by another 90 min incubation period at 28°C in the dark.

For ATP extraction, the samples were filled to 1 mL with Bg11 medium and immediately frozen in liquid nitrogen, followed by thawing at 99°C and shaking at 1400 rpm in a heating block. After three freeze/thaw cycles, the samples were centrifuged 3 min at 25,000 g and 4°C. The ATP quantification was performed using the ATP determination kit (Invitrogen) following the manufacturer’s protocol using 50  $\mu$ L of the sample supernatant in a 500  $\mu$ L reaction. The principle of the measurement relies on detection of bioluminescence generated by a recombinant firefly luciferase from its substrate D-luciferin and ATP. Luminescence was detected using a luminometer (Sirius Luminometer; Berthold Detection System) and ATP content was calculated using a generated ATP standard curve.

### QUANTIFICATION AND STATISTICAL ANALYSIS

For detailed information for software used in this study, see the [Key Resources Table](#). FRAP imaging was performed using the ZEN 2.3 blue edition software (ZEISS). Fluorescence intensity of a FRAP sequence was measured using the ImageJ plugin ‘Time series analyzer V3’ and normalized to the fluorescence intensity  $F_0$  prior to bleaching via the Excel software (Microsoft). The percentage distribution of bleached cells in the four groups was calculated for cumulated results from at least 2 independent experiments using GraphPad PRISM. The number of analyzed cells  $n$  is indicated within the bar graphs. All bleached cells  $n$  are from different filaments. Distribution of the groups in single FRAP experiments are shown in the Supplement and referred to in the figure legends. The fluorescence recovery rate constant  $R$  of a bleached cell was calculated as previously described using the formula  $C_B = C_0 + C_R(1 - e^{-2Rt})$ , with  $c_B$  being the fluorescence of the bleached cell,  $C_0$  the fluorescence directly after bleaching tending toward  $(C_0 + C_R)$  during fluorescence recovery,  $C_R$  the fluorescence during recovery,  $2R$  the recovery rate constant due to molecular exchange from both neighboring cells, and  $t$  the time (Merino-Puerto et al., 2011; Nürnberg et al., 2015).

### DATA AND CODE AVAILABILITY

Example tomograms and subtomogram averages of all *Anabaena* mutants described in this study were deposited in the Electron Microscopy Data Bank (accession numbers EMDB: EMD-4949–EMD-4957 for tomograms and EMDB: EMD-4961–EMD-4969 for subtomogram averages).

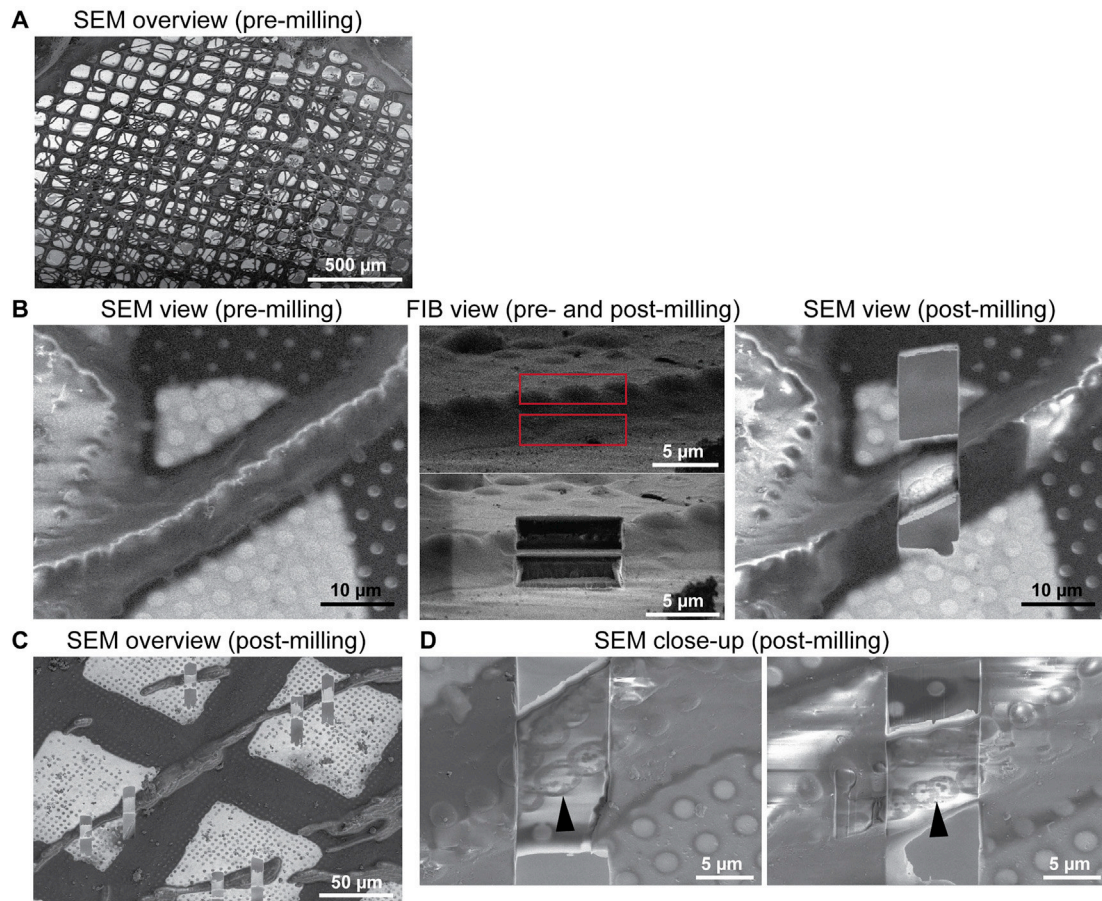


**Figure S1. CryoFIB-Milling of *Anabaena* Filaments, Related to Figure 1**

- (A) Shown is a cryo-scanning electron microscopy (SEM) image of an EM grid with plunge-frozen *Anabaena* filaments.
- (B) Shown is one example for the preparation of a lamella through a filament. The target was identified in SEM view (SEM view, pre-milling). The focused ion beam (FIB) was used to inspect the same filament from a shallow angle (FIB view) and to choose a milling pattern (red box, upper panel). Material was then removed using the FIB and inspected again (FIB view, lower panel). The final lamella was inspected again by SEM (SEM view, post-milling).
- (C) The procedure was repeated for 9-24 lamellae. Shown is a SEM overview image of a grid area with seven lamellae.
- (D) Two examples of cryoFIB-milled lamellae through *Anabaena* filaments. Details like cell outline (arrowheads) or thylakoid membranes are already detectable.

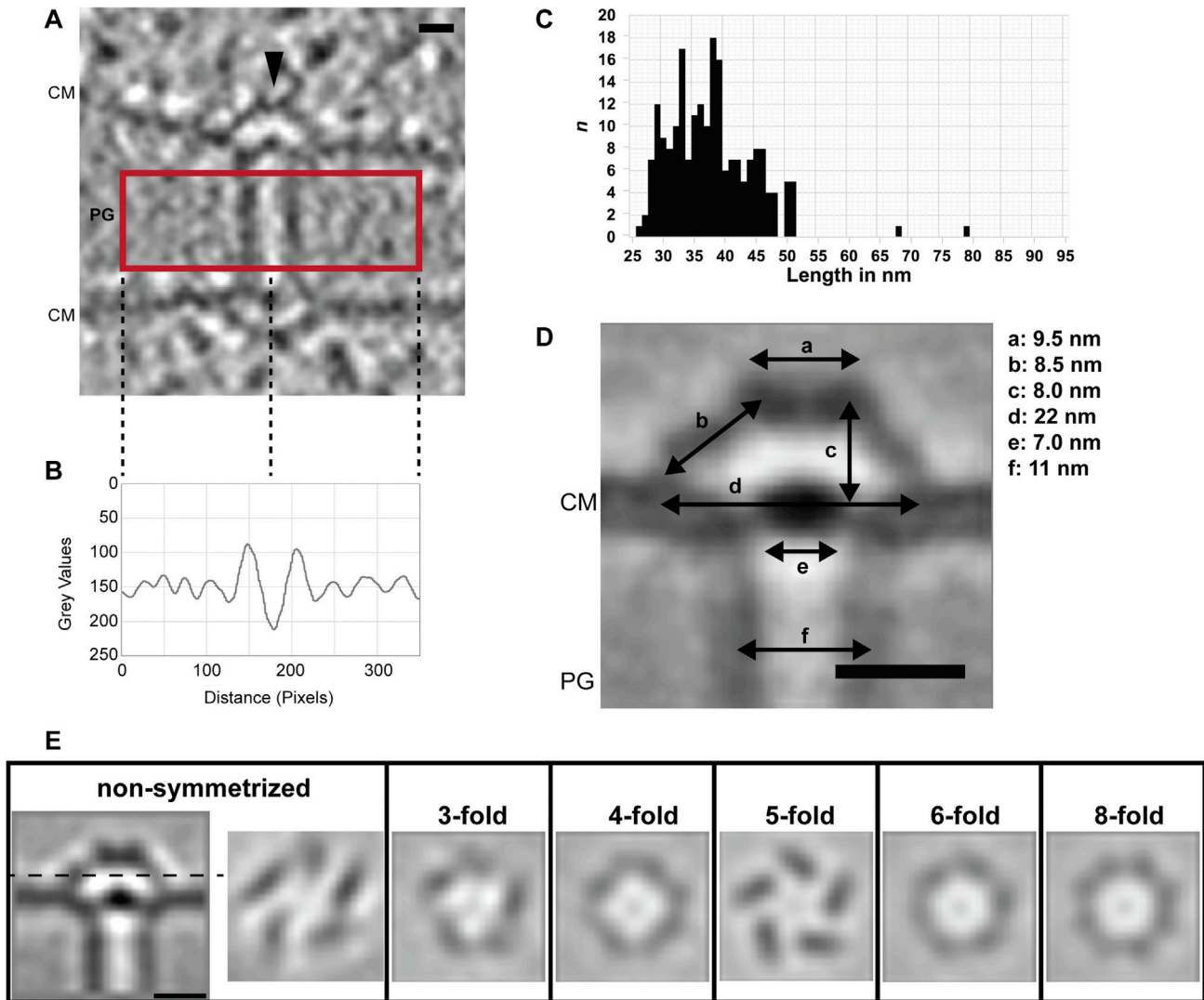


**Figure S2. Analysis of SJs in *Anabaena* Wild Type, Related to Figure 1**

(A) Shown is a cryotomogram (9.45 nm-thick slice) of a SJ (arrowhead). The area indicated by the red box was used to calculate a density plot. CM, cytoplasmic membrane; PG, septal peptidoglycan. Bar, 10 nm.

(B) The density plot of the area indicated in (A) revealed that the SJ tube had a higher density than the surrounding PG and the tube lumen had a lower density than the PG.

(C) SJ length distribution in *Anabaena* PCC 7120 wild-type. SJ lengths were measured from plug to plug and their occurrence was plotted in the graph.  $n = 208$  SJs

(D) Measurements of SJ structural features. The indicated measurements were performed using the subtomogram average of the SJ end shown in Figure 1 C/E/F. CM, cytoplasmic membrane; PG, septal peptidoglycan. Bar, 10 nm.

(E) The SJ cap module has 5-fold rotational symmetry. The cross-sectional view (position indicated in the longitudinal view by dashed line) of the non-symmetrized subtomogram average indicated a rotational 5-fold symmetry of the cap module. To further investigate this, different symmetries (indicated) were applied to the non-symmetrized subtomogram average (1.35 nm pixel size). The strongest reinforcement of densities was seen in the 5-fold symmetrized average. Bar, 10 nm.

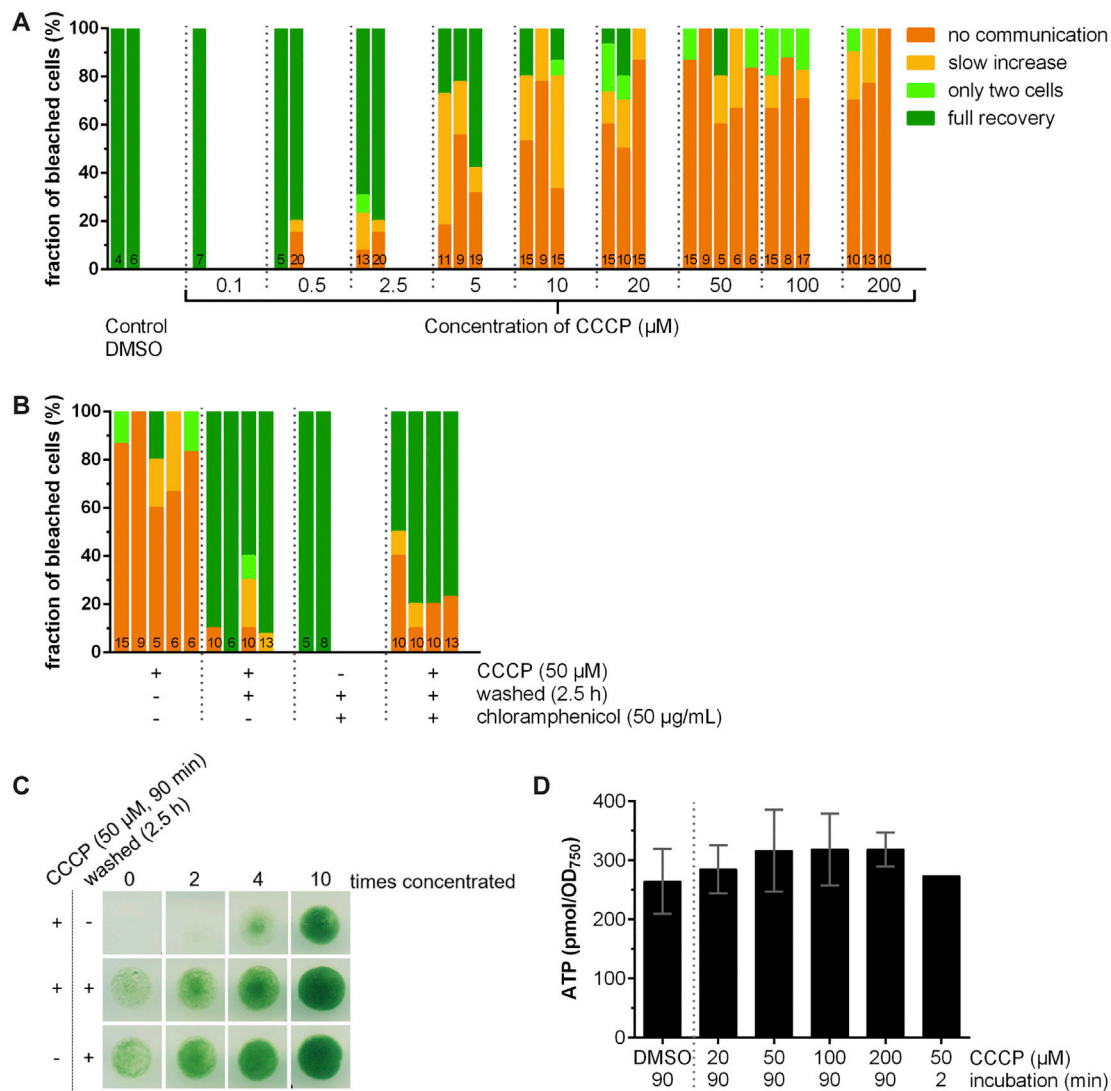


**Figure S3. FRAP Response Distributions of Independent Cultures and Viability after CCCP Treatment, Related to Figure 2**

(A and B) Shown are the distributions of FRAP responses of independent cultures (one bar represents one culture), to complement the cumulative results that are shown in Figure 2. Numbers within the bars indicate the number of analyzed cells  $n$  from different filaments. The shown graph in (A) corresponds to Figure 2C. The shown graph in (B) corresponds to Figure 2D.

(C) Cells that were washed after CCCP treatment were viable. *Anabaena* was grown for three days on a Bg11 agar plate, resuspended to  $\text{OD}_{750} = 1.2$ , split and processed by different treatments (indicated on the left, details described in STAR Methods). Subsequently, 10  $\mu\text{L}$  of different concentrations of the cultures were spotted onto a solid Bg11 agar plate and incubated for two days before taking a picture of the plate (shown). No difference in viability was observed between the control (no CCCP treatment) and CCCP-treated/washed cells. All spots were grown on the same plate, white lines were introduced for a clear view.

(D) The ATP level of *Anabaena* cells is not affected by CCCP treatment. The ATP content of *Anabaena* cells was determined in cells treated with only DMSO (control to mimic the addition of calcein and CCCP), and cells treated with DMSO and different concentrations of CCCP for 90 min or 2 min as indicated in graph. The measured ATP level was normalized to  $\text{OD}_{750} = 0.6$ . Bars show the mean  $\pm$  SD of two biological replicates with two technical replicates (one biological replicate for 2 min incubation with 50  $\mu\text{M}$  CCCP). Differences between CCCP treated cells compared to DMSO control cells were not significant (Student's  $t$  test).

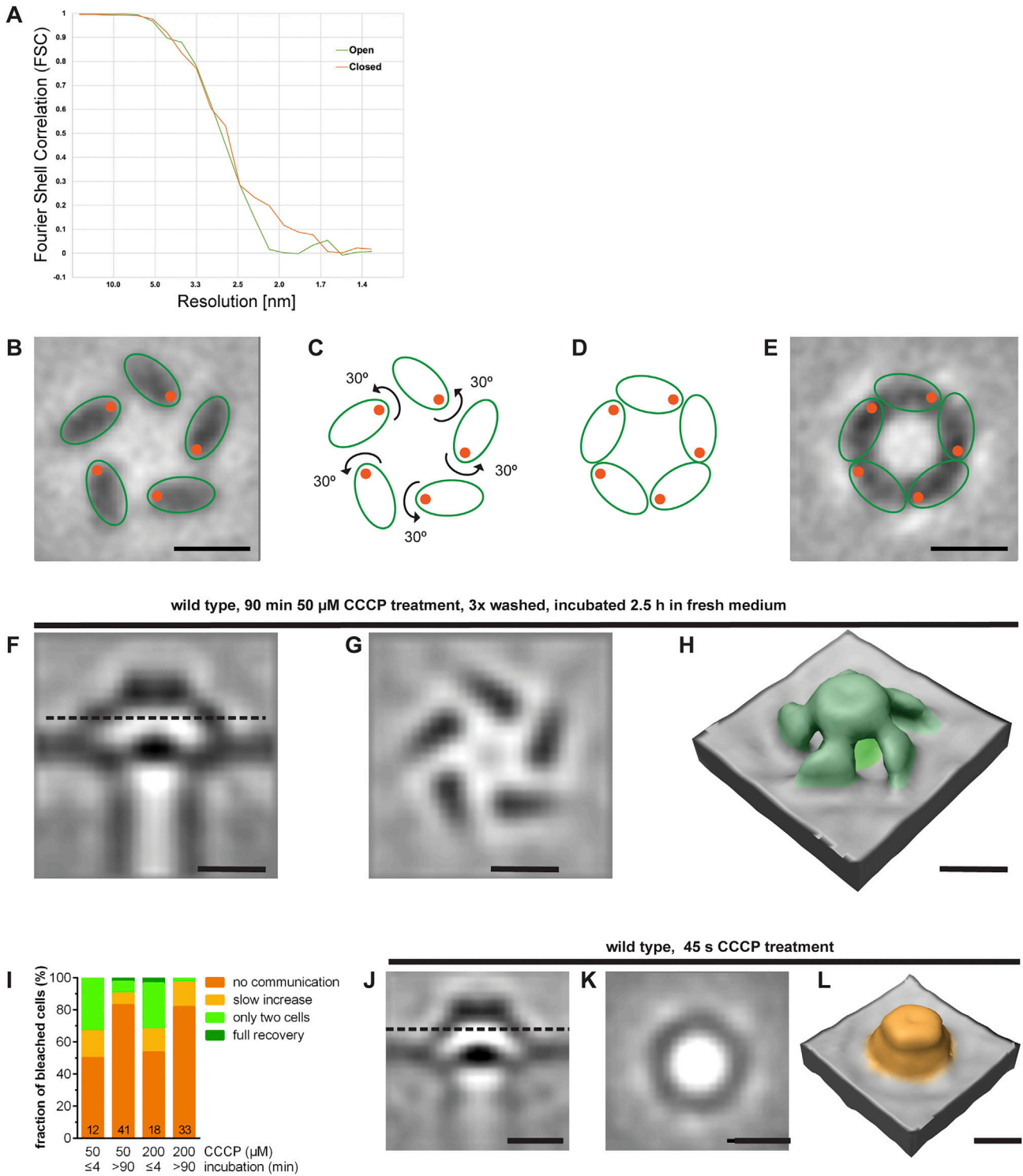


**Figure S4. SJ Gating Is Fast and Reversible, Related to Figure 3**

(A) Shown are Fourier Shell Correlation (FSC) curves of two half-datasets of subtomogram averages of SJs in open (green) and closed (orange) states, respectively. The estimated resolution of the averages was  $\sim 28$  Å.

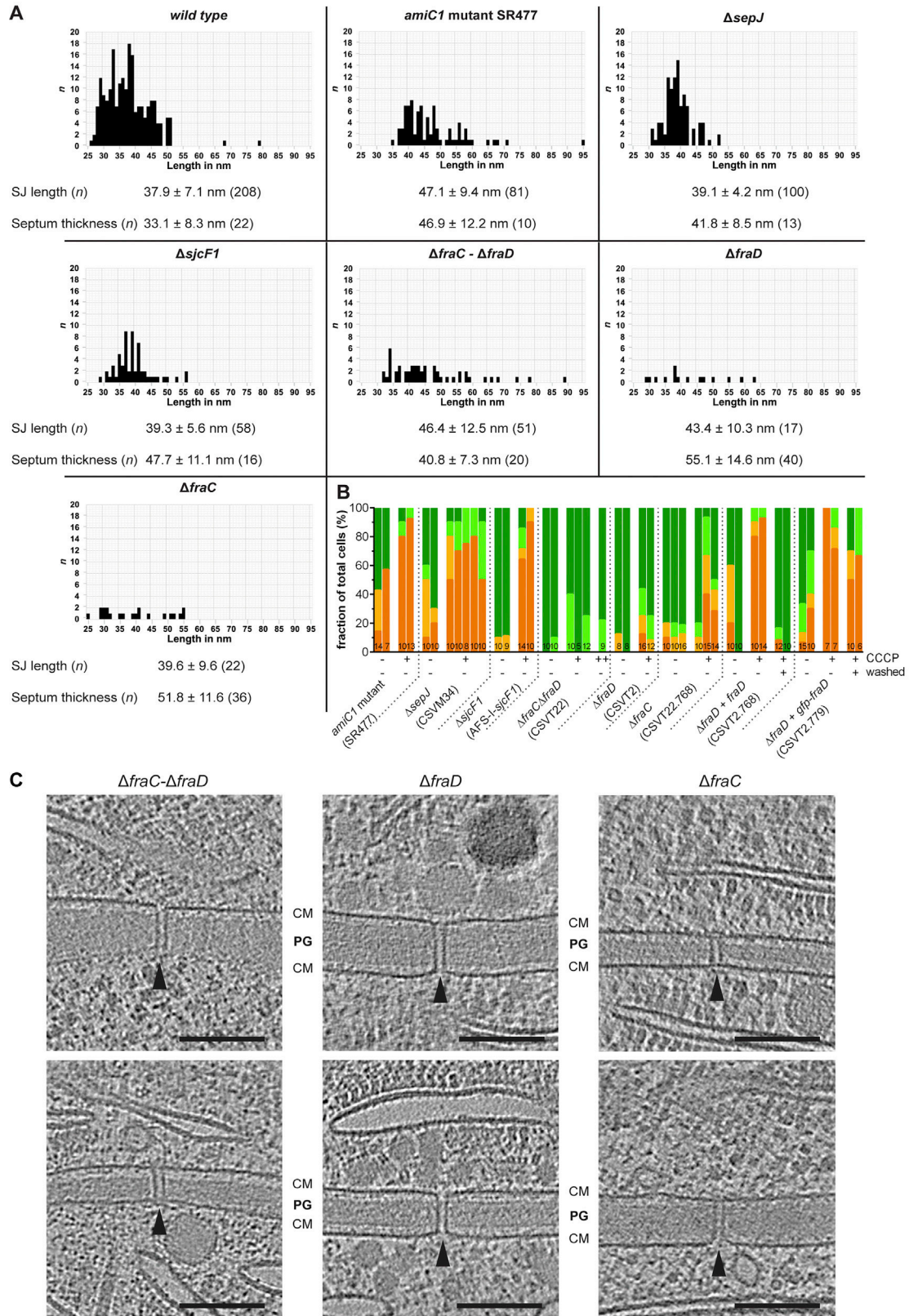
(B–E) Speculative model of cap closure by arch rotations. (B) Perpendicular cross-section (0.68 nm thickness) of the subtomogram average of the SJ in the open conformation. The arches are represented by green ellipses. (C) Schematic indicating a 30° rotation of each arch around a rotation center (orange). (D) Schematic

(legend continued on next page)

indicating the arches after the rotation indicated in (C). The result was a closed circle. (E) Overlay of the model in the closed state with a perpendicular cross-section (0.68 nm thickness) of the SJ in the closed conformation. Bars, 10 nm.

(F–H) The structural rearrangement of SJs upon ionophore treatment is reversible. Wild-type *Anabaena* cells were incubated for 90 mins with 50  $\mu$ M CCCP. Afterward, cells were washed three times, incubated in fresh medium for 2.5 h and plunge frozen. The subtomogram average revealed SJs in their open state (F/G). Dashed line in (F) indicates the position of the cross sectional view shown in (G). The five arches of the SJ cap, a hallmark for the SJ open state, are detectable. Surface representation (H) of the SJ cap generated from the subtomogram average shown in (F/G). Bars, 10 nm.

(I–L) Intercellular communication is impaired within seconds upon CCCP treatment. Wild-type *Anabaena* cells were incubated with CCCP. FRAP analyses [shown in (I)] were performed either between 1.5 min and 4 min after the addition of CCCP, or more than 90 min after the addition of CCCP (data from [Figure 2](#)). Already after the short incubation time of  $\leq 4$  min, the majority of cells already ceased communication. Numbers within the bars indicate the number of analyzed cells  $n$  from different filaments. (J–L) show a subtomogram average (J/K) and surface representation (L) of SJs from *Anabaena* wild-type cells that were treated with CCCP (50  $\mu$ M) for 45 s. The average [longitudinal view in (J); cross section in (K)] shows SJs in their closed state [dashed line indicates the position of the cross sectional view in (K)]. No individual arches are detectable. Bars, 10 nm.



(legend on next page)

---

**Figure S5. Details and Examples of Analyzed SJ Mutants and Their FRAP Response Distribution of Independent Cultures, Related to Figures 4 and 5**

(A) SJ lengths in wild-type and mutant strains were measured from plug to plug and their frequency was plotted in the graphs. The data were also used to calculate the average SJ length. We also measured the septum thickness (as the shortest distance between the inner membranes within a tomogram of a septal region), showing an increase for all mutant strains.

(B) Shown are the distributions of FRAP responses of independent cultures (one bar represents one culture), to complement the cumulative results that are shown in Figures 4 and 5. Numbers within the bars indicate the number of analyzed cells  $n$  from different filaments. +: 50  $\mu\text{M}$  CCCP; ++: 200  $\mu\text{M}$  CCCP

(C) Further examples of cryotomograms showing SJs (black arrowheads) from different mutant strains. Shown are 13.5 nm thick slices. CM, cytoplasmic membrane; PG, septal peptidoglycan. Bars, 100 nm.

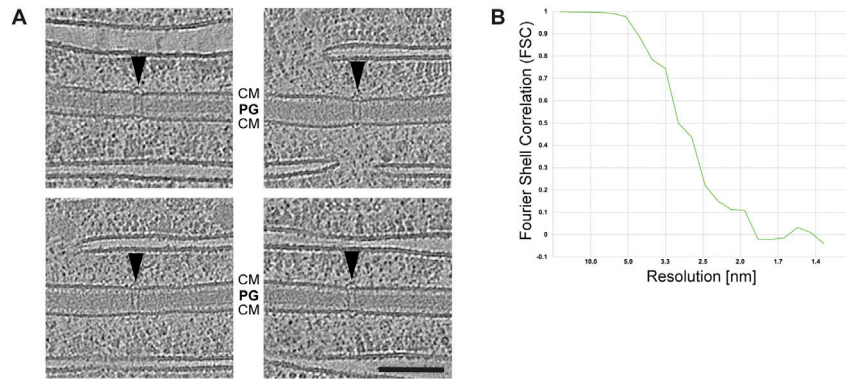


**Figure S6. Examples of Cryotomograms Showing SJs of *Anabaena* Expressing *gfp-fraD*, Related to Figure 6**

(A) Further examples of cryotomograms showing SJs (black arrowheads) from *gfp-fraD* expressing mutant. Shown are 13.5 nm thick slices. CM, cytoplasmic membrane; PG, septal peptidoglycan. Bars, 100 nm.

(B) Shown is a Fourier Shell Correlation (FSC) curve of two half-datasets of the subtomogram average in Figure 6A, showing SJs from *gfp-fraD* expressing mutant.

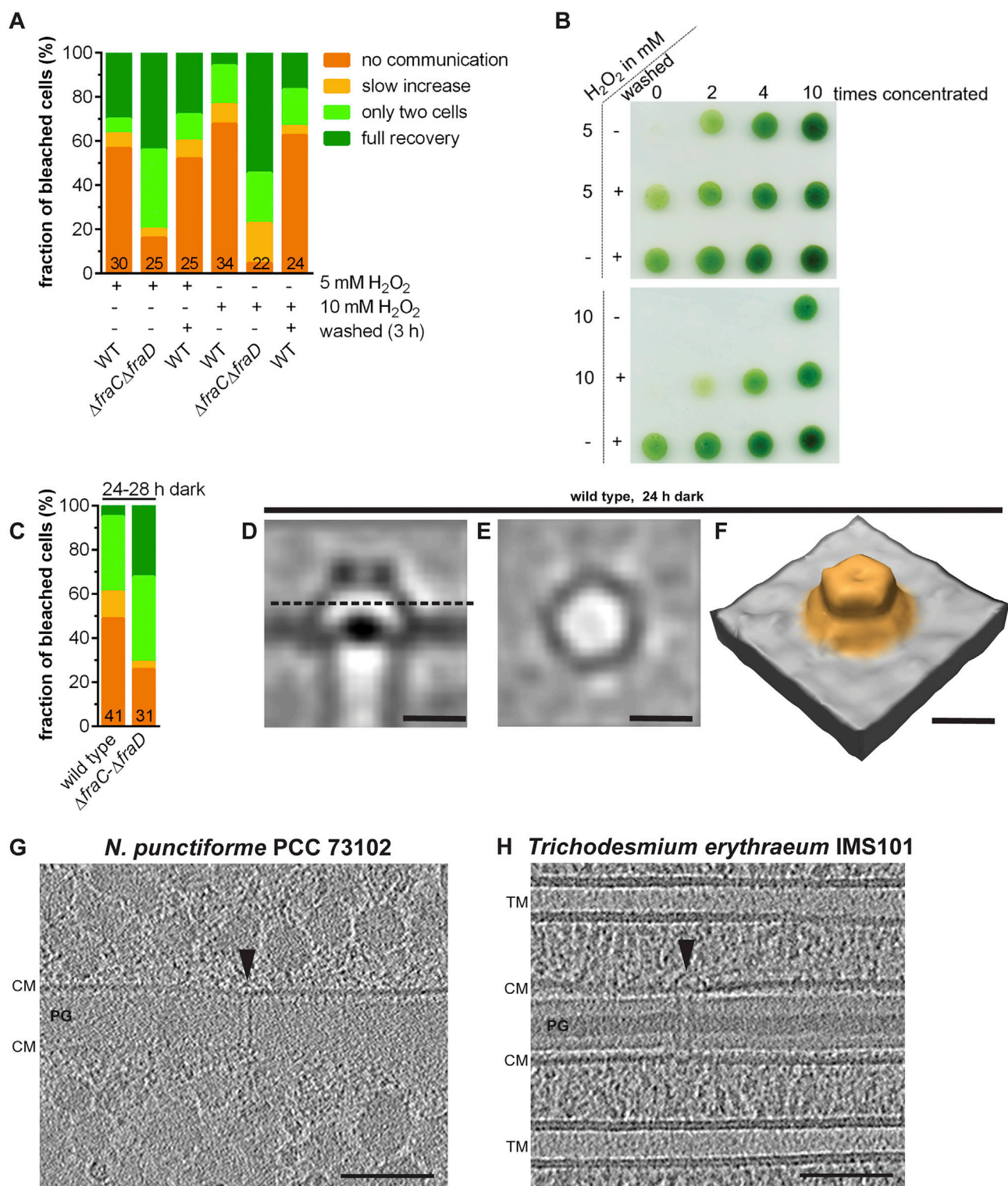


**Figure S7. Intercellular Communication Was Reduced upon Different Types of Stress, and SJs in Other Cyanobacteria Share Similar Architecture, Related to Figure 7**

(A and B) Treatment with H<sub>2</sub>O<sub>2</sub> was tested as an alternative stress. Calcein-stained cells were treated with 5 mM or 10 mM H<sub>2</sub>O<sub>2</sub>, followed by washing with fresh medium and further incubation for 3 h when indicated. Molecular exchange of the treated cells was analyzed by FRAP (A). Similar to CCCP treatment, wild-type cells showed a reduced level of communication upon H<sub>2</sub>O<sub>2</sub> treatment, while the  $\Delta fraC\Delta fraD$  mutant was impaired in ceasing molecular exchange upon H<sub>2</sub>O<sub>2</sub>

(legend continued on next page)

treatment. Shown are cumulated results from at least two independent experiments. Numbers within the bars indicate the number of analyzed cells  $n$  from different filaments. To check the viability of wild-type cells after  $H_2O_2$  treatment, 10  $\mu$ L spots were placed onto a Bg11 agar plate and incubated for three days (B). Cells treated with 5 mM  $H_2O_2$  and washed afterward grew comparable to the untreated control. (C–F) Incubation in the dark was tested as an alternative stress. Cells were incubated in the dark for 28 h prior to FRAP analyses (C). FRAP indicated that a significant fraction of wild-type cells ceased to communicate upon incubation in the dark, while the  $\Delta fraC-\Delta fraD$  mutant was less effective in ceasing molecular exchange. Shown are cumulated results from at least two independent FRAP experiments. Numbers within the bars indicate the number of analyzed cells  $n$  from different filaments. The color code is identical to (A). For ECT imaging (D–E), cells were incubated in the dark for 24 h prior to plunge freezing. Shown is a subtomogram average of SJs from *Anabaena* wild-type cells. The average shows SJs in the closed state (no individual arches are detectable). The dashed line in (D) indicates the position of the cross sectional view of the cap shown in (E). A surface representation of the subtomogram average is shown in (F). Bars, 10 nm. (G and H) SJs in other cyanobacteria share a similar architecture. We also cryoFIB-milled and imaged two further cyanobacterial representatives, revealing the presence of SJs (arrowheads) without fundamentally different SJ architecture as compared to *Anabaena*. Importantly, SJ-related genes (*amiC*, *fraC/fraD*, *sjcF1* and the C-terminal domain of *sepJ*) are also present in the genomes of these cyanobacteria. CM, cytoplasmic membrane; PG, septal peptidoglycan; TM, thylakoid membrane. Bars, 100 nm.